

**CHARACTERIZATION OF FRACTURE BEHAVIOR OF
CONCRETE STRUCTURAL ELEMENTS USING
ACOUSTIC EMISSION TECHNIQUE**

ARASH BEHNIA

**THESIS SUBMITTED IN FULFILMENT OF THE
REQUIREMENTS FOR THE DEGREE OF DOCTOR OF
PHILOSOPHY**

**DEPARTMENT OF CIVIL ENGINEERING FACULTY OF
ENGINEERING
UNIVERSITY OF MALAYA
KUALA LUMPUR**

SEPTEMBER 2015

UNIVERSITY OF MALAYA
ORIGINAL LITERARY WORK DECLARATION

Name of Candidate: **ARASH BEHNIAI.C/Passport No: P95425630**

Registration/Matric No: **KHA120041**

Name of Degree: **DOCTOR OF PHILOSOPHY**

Title of Project Paper/Research Report/Dissertation/Thesis (“this Work”):

**CHARACTERIZATION OF FRACTURE BEHAVIOR OF CONCRETE
STRUCTURAL ELEMENTS USING ACOUSTIC EMISSION TECHNIQUE**

Field of Study: **STRUCTURAL ENGINEERING & MATERIALS**

I do solemnly and sincerely declare that:

- (1) I am the sole author/writer of this Work;
- (2) This Work is original;
- (3) Any use of any work in which copyright exists was done by way of fair dealing and for permitted purposes and any excerpt or extract from, or reference to or reproduction of any copyright work has been disclosed expressly and sufficiently and the title of the Work and its authorship have been acknowledged in this Work;
- (4) I do not have any actual knowledge nor do I ought reasonably to know that the making of this work constitutes an infringement of any copyright work;
- (5) I hereby assign all and every rights in the copyright to this Work to the University of Malaya (“UM”), who henceforth shall be owner of the copyright in this Work and that any reproduction or use in any form or by any means whatsoever is prohibited without the written consent of UM having been first had and obtained;
- (6) I am fully aware that if in the course of making this Work I have infringed any copyright whether intentionally or otherwise, I may be subject to legal action or any other action as may be determined by UM.

Candidate’s Signature

Date: 06.03.2015

Subscribed and solemnly declared before,

Witness’s Signature

Date:

Name:

Designation:

UNIVERSITI MALAYA
PERAKUAN KEASLIAN PENULISAN

Nama: **ARASH BEHNI**No. K.P/Pasport: **P95425630**

No. Pendaftaran/Matrik: **KHA120041**

Nama Ijazah:**DOCTOR FALSAFAH**

Tajuk Kertas Projek/Laporan Penyelidikan/Disertasi/Tesis (“Hasil Kerja ini”):

Pencirian Kelakuan Patah Elemen Struktur Konkrit Menggunakan Teknik Pancaran Akustik

Bidang Penyelidikan:**STRUKTUR DAN BAHAN**

Saya dengan sesungguhnya dan sebenarnya mengaku bahawa:

- (1) Saya adalah satu-satunya pengarang/penulis Hasil Kerja ini;
- (2) Hasil Kerja ini adalah asli;
- (3) Apa-apa penggunaan mana-mana hasil kerja yang mengandungi hakcipta telah dilakukan secara urusan yang wajar dan bagi maksud yang dibenarkan dan apa-apa petikan, ekstrak, rujukan atau pengeluaran semula daripada atau kepada mana-mana hasil kerja yang mengandungi hakcipta telah dinyatakan dengan sejasanya dan secukupnya dan satu pengiktirafan tajuk hasil kerja tersebut dan pengarang/penulisnya telah dilakukan di dalam Hasil Kerja ini;
- (4) Saya tidak mempunyai apa-apa pengetahuan sebenar atau patut semunasabahnya tahu bahawa penghasilan Hasil Kerja ini melanggar suatu hakcipta hasil kerja yang lain;
- (5) Saya dengan ini menyerahkan kesemua dan tiap-tiap hak yang terkandung di dalam hakcipta Hasil Kerja ini kepada Universiti Malaya (“UM”) yang seterusnya mula dari sekarang adalah tuan punya kepada hakcipta di dalam Hasil Kerja ini dan apa-apa pengeluaran semula atau penggunaan dalam apa jua bentuk atau dengan apa juga cara sekalipun adalah dilarang tanpa terlebih dahulu mendapat kebenaran bertulis dari UM;
- (6) Saya sedar sepenuhnya sekiranya dalam masa penghasilan Hasil Kerja ini saya telah melanggar suatu hakcipta hasil kerja yang lain sama ada dengan niat atau sebaliknya, saya boleh dikenakan tindakan undang-undang atau apa-apa tindakan lain sebagaimana yang diputuskan oleh UM.

Tandatangan Calon

Tarikh: 06.03.2015

Diperbuat dan sesungguhnya diakui di hadapan,

Tandatangan Saksi

Tarikh:

Nama:

Jawatan:

I hereby declare that this thesis is based on the results found by myself. Materials of work found by other researcher are mentioned by references. This thesis is neither in whole nor in part has been previously submitted for any degree.

Date: 28.08.2015

Signature

ABSTRACT

In this study, basically, acoustic emission technique was applied to develop its application in concrete structural members. Four different types of experimental sets were conducted to study the structural concrete members fracture and condition monitoring. The first experiment set was carried out for pure torsion fracture analysis to characterize fracture parameters under pure torsion by means of acoustic emission incorporated with statistical approach (Weibull method). As a first study, the damage Weibull parameters for torsional fracture were calibrated by acoustic emission so that damage probability function was proposed.

In the next study, a pattern recognition technique, kernel fuzzy c-means (KFCM), was applied to cluster different damage stages so that a novel damage index called spatial intelligent b-value was proposed to quantify damage in an unsupervised approach. Thereafter, the second experiment was conducted for large scales multi-cells beams subjected to pure torsional loading. The fracture process was qualitatively and qualitatively characterized by means of AE analysis. The third set of experiment aims to study the concrete slab fracture behaviour and provide early warning of occurrence of damage whilst the type of failure can be characterized by means of AE. AE could quantify stiffness reduction in composite slabs under concentrated loading other than offering an early warning system. In the next step, by means of statistical process control and autoregressive method a novel structural health monitoring scheme was proposed to detect damage and analyse reliability of failure in composite slabs. The last experiments utilized fiber reinforced concrete beams subjected to flexural loading to investigate the combination of AE with travel time tomography technique to provide a robust global and local technique.

Innovatively, global and local structural condition could be evaluated by integration acoustic emission signal strength and velocity of time tomography in a combined plot.

ABSTRAK

Oleh itu, dalam kajian ini satu kaedah NDT bernama “acoustic emission” telah digunakan untuk membangunkan aplikasi dalam struktur kejuruteraan awam. Untuk tujuan ini, empat jenis eksperimen telah dijalankan untuk mengkaji keretakan struktur konkrit dan kerosakan untuk jenis ujian beban yang kritikal dan jenis umum daripada ahli dalam struktur konkrit. Oleh itu, set eksperimen pertama telah dijalankan untuk analisis patah kilasan tulen untuk mencirikan parameter patah di bawah kilasan tulen dengan menggunakan “acoustic emission” digabungkan dengan pendekatan statistik (kaedah Weibull). Dalam kajian seterusnya, keamatan kerosakan yang dikenakan kepada struktur dikuantifikasikan melalui aplikasi kaedah tanpa pengawasan dipanggil “kernel fuzzy c-means” (KFCM). Sebuah indeks kerosakan dinamakan spatial pintar daripada b-value telah dicadangkan untuk mengukur kerosakan dalam pendekatan tanpa pengawasan. Selepas itu, eksperimen kedua dijalankan untuk skala besar multi-sel rasuk yang biasanya digunakan dalam jambatan dan mereka terdedah kepada beban kilasan. Proses patah telah dicirikan secara kualitatif dan secara kualitatif karakter melalui analisis AE. Penggunaan “acoustic emission” untuk mengukur tahap kerosakan telah diperiksa. Set ketiga eksperimen bertujuan untuk mengkaji kelakuan konkrit daripada keretakan papak dan memberikan amaran awal berlakunya kerosakan “whist” dengan jenis kegagalan boleh dicirikan melalui AE. Kelakuan keretakan papak komposit telah disiasat secara menyeluruh dan AE telah menunjukkan potensi yang besar untuk menganalisis dan mencirikan kelakuan patah daripada pelbagai lapisan papak komposit. AE boleh mengukur pengurangan kekakuan dalam papak komposit di bawah pembebanan tertumpu selain menawarkan sistem amaran awal.

Dalam langkah seterusnya, melalui kawalan proses statistik dan kaedah autoregresif daripada satu skim pemantauan kesihatan struktur telah dicadangkan untuk mengesan kerosakan dan menganalisis kebolehpercayaan kegagalan dalam papak komposit. Eksperimen yang terakhir menggunakan lepas serat rasuk konkrit bertetulang tertakluk kepada bebanan lenturan untuk menyiasat gabungan AE dengan teknik tomografi masa perjalanan untuk menyediakan teknik global dan tempatan yang teguh. Keputusan dan perbincangan yang berkaitan dengan kajian ini menunjukkan potensi kaedah “acoustic emission” yang akan digunakan dalam pemantauan struktur konkrit selain daripada analisis keretakan struktur konkrit.

DEDICATION

There are a number of people without whom this thesis might not have been written, and to whom I am greatly indebted. This thesis is dedicated to my beloved parents, sister, and brother for their endless love and supports. I dedicate this thesis to my father who has always troubled himself to make a shield around me. I dedicate this thesis to my mother whom I cannot find any words to thank her. I dedicate this thesis to her for her support, encouragement, love that sustained me throughout my life. I also dedicate this thesis to my beloved sister, Armaghan for her endless support and engorgement. I also dedicate this thesis to my beloved brother, Nima who has burdened himself to take all my responsibility to take care of our family when I was not around.

My sincere thanks should be given to my best friends Mahyar, Navid, Saba, Elaheh, Maria for their constant kind supports. Special thanks to Navid with whom I spent these years at UM to work together and being for each other in rainy days.

ACKNOWLEDGEMENT

I would like to first express my profound gratitude and appreciation to Dr. Hwa Kian Chai. His guidance, enthusiasm, encouragement, and support during my doctoral studies have been invaluable. All our discussions about the subjects of my dissertation were extremely helpful, but above all, his understanding, trust, and flexibility to my personal opinions could allow me to grow professionally and be productive.

Now after spending all these three years with its difficult and happy days, I learnt that I have made a valuable friend with a person who was my PhD supervisor.

I also thank my co-supervisor, Professor. Dr Zamin for his kind helps in conducting research and experiments.

My deep appreciations and earnest thanks to all staff members from department of Civil Engineering and also Dr Abeer for her contribution in preparation and testing some samples of this research.

My special thanks to Maria, one of my best friend and colleague for her kind help in conducting test and spending great time in our office.

I also would like to thank Mr Ahmad Zaki and Dr Maziza for their helps in editing the abstract of this thesis.

I would also wish to express my profound and deep thanks and appreciation to my best friend, Navid who has shared his great and pure knowledge and experience.

Finally, I express my sincere thanks to the most important people in my life, my father, mother, sister, and brother who have given me their endless support and love.

TABLE CONTENT

DECLARATION FORM	i
ABSTRACT	iii
ABSTRAK	iv
DEDICATION	vi
ACKNOWLEDGMENT	x
TABLE OF CONTENT	xi
LIST OF FIGURES	xvii
LIST OF TABLE	xxiii
LIST OF SYMBOLES AND ABBREVIATION	xxiv
CHAPTER 1: INTRODUCTION	1
1.1. Deterioration of concrete structures.....	1
1.2. Non-destructive testing (NDT).....	1
1.2.1. Acoustic emission (AE).....	3
1.3. Problem statement.....	4
1.4. Objectives.....	7
1.5. Scope and outline of this study.....	7
2.1. Introduction.....	9
2.2. Potential Structural Assessment Approaches Based on AE.....	10
2.3. Parametric Analysis.....	11
2.4. Fundamental Studies on AE Technique in Concrete.....	14
2.5. Damage Assessment of RC Structures by AE.....	14
2.6. Damage Localization Process.....	14
2.6.1. Zonal or One Dimensional Approach.....	15
2.6.2. Two Dimensional Approach.....	15
2.6.3. Three Dimensional Approach.....	15
2.7. Source Discrimination and Crack Classification.....	16

2.7.1. Moment Tensor Analysis	16
2.7.2. Crack Classification Based on Parametric Approach	17
2.8. Clustering of Acoustic Emission Data for the Purpose of Damage Mode Identification in Concrete Structures	19
2.9. Damage Severity Evaluation for Concrete Structures	25
2.10. AE Applicable Parameters	27
2.10.1. AE Energy Parameter Analysis.....	27
2.10.2. AE Signals Amplitude	28
2.10.3. AE Hit Application in Crack Monitoring	29
2.10.4. AE Count Application in Concrete Monitoring	30
2.10.5. b-value Analysis to Assess the Damage Severity	32
2.10.6. Improved b-value Analysis	33
2.10.7. Sifted b-value Analysis	33
2.10.8. Minimum b-value Approach in Bridges	34
2.11. AE Application in Global and Local Monitoring	36
2.12. Recent Trends and Modern AE Research	37
2.12.1. AE Application in Monitoring Corrosion	37
2.12.2. Fatigue Analysis by Acoustic Emission Technique.....	38
2.12.3. Monitoring by AE During Simple Bending	39
2.12.4. Creep Defect Analysis by Acoustic Emission Technique.....	40
3.1. Introduction.....	41
3.2. General Material Properties	41
3.2.1. Cement and Water.....	41
3.2.2. Mixing Water	41
3.2.3. Aggregates	42
3.2.3.1. Fine Aggregates (Sand).....	42
3.2.3.2. Normal Gravel.....	42
3.2.4. Fly ash.....	43

3.2.5. Rubber.....	43
3.3. Torsional Fracture Test.....	44
3.3.1. Mechanical Properties and Torsion Tests.....	44
3.3.2. Acoustic Emission System and Measurements.....	46
3.4. Large Scale Multi-cells Girders Subjected to Pure Torsion.....	47
3.4.1. Tests and Procedures.....	47
3.4.2. Steel reinforcement bars.....	49
3.4.3. Molding and Casting.....	51
3.4.4. Torsion Test Procedure.....	52
3.4.5. AE Monitoring and Instrumentation.....	54
3.5. AE Monitoring of Ferrocement Composite Slabs.....	55
3.5.1. Experimental Program.....	55
3.6. Fiber reinforced concrete beams in flexural behaviour.....	58
3.6.1. Casting, Sensor instruments, Loading Procedure.....	58
4.1. Introduction.....	61
4.2. Damage Detection of SFRC Concrete Beams Subjected to Pure Torsion by Integrating Acoustic Emission and Weibull Damage Function.....	62
4.2.1. Analysis Theory: Quantification of Damage and fracture process.....	62
4.2.1.1. b-value Analysis.....	62
4.2.1.2. Gaussian Smoothing Filter.....	64
4.2.1.3. Principal Component Analysis (PCA).....	65
4.2.2. Weibull Damage Function Calibrated with AE Data for Torsion Damage Behavior...	65
4.2.2.1. Weibull Function for Damage Behavior.....	65
4.2.2.2. Weibull damage function calibration with detected AE events.....	67
4.2.2. Results and Discussion.....	68
4.2.2.1. Mechanical Effect of Inclusion of Steel fiber in Torsion Behavior.....	68
4.2.4.2. Damage Evolution Process Analysis by b-value.....	69
4.2.4.3. Principal component analysis (PCA).....	76

4.2.4.4. Fracture Process Analysis by b-value	78
4.2.4.5. Weibull Damage Function and Mechanical Loading Correlation to AE Data.....	81
4.2.4.6. AE Parameters and Activity Correlation to Structural Behaviour	86
4.2.4.7. AE Average Frequency and RA Variation in Fracture Process	87
4.2.4.8. AE Signal Amplitude Variation in Fracture Process	92
4.2.5. Conclusion	95
4.3. Acoustic Emission Monitoring of Multi-Cell Reinforced Concrete Box Girders Subjected to Torsion.....	96
4.3.1. Cumulative Signal Strength (CSS)	96
4.3.2. Intensity Analysis (IA).....	96
4.3.3. b-value Analysis.....	97
4.3.4. Test Result and Discussion	98
4.3.4.1. Crack development	98
4.3.4.2. Damage localization process.....	102
4.3.4.3. Qualitative AE Analysis by AE Hit	104
4.3.4.4. Qualitative Analysis by AE Signal Strength.....	106
4.3.4.5. Quantitative AE Analysis by Intensity Analysis (IA).....	108
4.3.4.6. Damage Quantification by b-value Analysis	110
4.3.5. Conclusion	114
4.4. Unsupervised Acoustic Emission Damage Detection Technique Incorporating Kernel Fuzzy C-Mean for Structural Concrete Subjected to Pure Torsion	115
4.4.1. Theory and Procedure of Application of Pattern Recognition in AE	115
4.4.2. Principal Component Analysis (PCA)	118
4.4.3. Kernel Fuzzy C-mean (KFCM)	118
4.4.4. Spatial Intelligent b-value (SIb) analysis	122
4.4.5. Results and discussion	124
4.4.5.1. Mechanical Behavior Correlation with AE Activity.....	124
4.4.6. Unsupervised Acoustic Emission Data Clustering	124

4.4.6.1. Qualitative Damage Analysis.....	124
4.4.6.2. Quantitative damage analysis by Spatial Intelligent b-value	132
4.4.7. Conclusion	135
4.5. Acoustic Emission Fracture Monitoring of Multi-Layered Wire Mesh-Reinforced Cementitious Composite Slabs	136
4.5.1. Introduction and Theory.....	136
4.5.2. Mechanical Behavior of Ferrocement Slabs	138
4.5.3. Generalized Behaviour of Ferrocement Composite Slabs	145
4.5.4. AE parametric Analysis and Material Properties Correlation.....	147
4.5.5. AE Technique for Structural Behavior Analysis	157
4.5.6. Early warning failure system	163
4.5.7. Conclusion	165
4.6. Damage Detection and Monitoring of Ferrocement Composite Slabs by Means of Acoustic Emission Technique.....	166
4.6.1. Theory of Application of Damage Sensitive Feature and Control Charts in AE.....	166
4.6.2. Statistical Process Controlling of AE Energy to Evaluate Damage State.....	169
4.6.3. Damage-sensitive Feature Extraction With an AR Model.....	169
4.6.4. EWMA and Shewhart Control Charts for Statistical Process Controlling (SPC) Model	170
4.6.5. Data Compression on AR Model by Means of Linear and Quadratic Projection.....	173
4.6.6. Results and Discussion	176
4.6.6.1. Mechanical Behaviour of Composite Slabs	176
4.6.6.2. AE Signal Strength Analysis.....	177
4.6.6.3. Feature extraction and damage detection analysis	180
4.6.6.4. Intensity Analysis (IA).....	190
4.6.6.5. Conclusion	194
4.7. Integrated non-destructive assessment of concrete structures under flexure by acoustic emission and travel time tomography	196

4.7.1. Theory of Global and Local Monitoring	196
4.7.1.2. Theory of Travel Time Tomography (TTT)	196
4.7.2. Results and Discussion	199
4.7.4.1. Damage mapping by TTT	199
4.7.4.2. AE Evaluation and Crack Propagation	205
4.7.4.3. AE Count Rate Analysis	209
4.7.4.4. AE Signal Strength Analysis.....	212
4.7.4.5. AE Frequency Analysis	215
4.7.4.6. Damage Classification Based on AE Parameters.....	218
4.7.4.7. ISA Evaluation and Elastic Wave Velocity Tomography.....	220
4.7.5. Conclusion	225
5.1. Conclusions and Recommendations	227
REFERENCES	232
APENDIX	247

LIST OF Figures

Figure 2.1: Basic parameters of an acoustic emission waveform	12
Figure 2.2: Crack type classification with a combination of average frequency and RA values: a) pure tension and combined crack, b) pure tension and pure shear (Aggelis, 2011a).....	19
Figure 2.3: U -matrix resulting from the application of the SOM	22
Figure 2.4: Gaussian mixture model for crack classification: a. dominance is with tensile crack, b. dominance is with shear cracks	23
Figure 2.5: Cumulative AE hits versus time for RC beams	29
Figure 2.6: AE amplitude distributions in reinforced concrete beams under cyclic loading.....	31
Figure 2.7: Algorithm of S_b -value analysis	34
Figure 2.8: Examples of continuous b -values for an overload: a) and a simulated test truck, b) over the course of one complete load cycle.....	35
Figure 3.1: CHO80/60NB collated steel fiber hooked end	45
Figure 3.2: Torsion tests on concrete beams and AE sensor placement	45
Figure 3.3: Geometrical detail and reinforcement of girder specimens: a) Single cell box, b) Double cell box, c) Triple cell box	48
Figure 3.4: Steel tensile reinforcement test.....	50
Figure 3.5: Molds, polystyrene and reinforcement cages overview	51
Figure 3.6: Specimen casting overview	52
Figure 3.7: Torsion testing system loading and instrumentation	53
Figure 3.8: the arrangement of AE sensors mounted on surface of two sides of girders	54
Figure 3.9: Test setup and of flexural strength test of ferrocement slab and AE sensor placement	57

Figure 3.10: Schematic diagrams of beam specimens and location of AE sensors (units in mm).....	60
Figure 4.1: Torque moment versus twist angle in concrete specimens.....	69
Figure 4.20: b-values results for the entire dataset before filtering process for #1.....	70
Figure 4.3: Smoothed b-value results for the entire dataset after filtering for #1.....	71
Figure 4.4: b-value variation trend based on smoothed curve for different sensors in #1: a) S1, b) S2, c) S5, d) S6.....	73
Figure 4.5: 3D event localization of damage progress with respect to progressive damage evolution for #1 (a: $t_1 = 0-1000$ sec, b: $t_2 = 1001-2000$ sec, $t_3 = 2001-3000$ sec, $t_4 = 3001-4700$ sec).....	76
Figure 4.6: Principal components visualization AE data considering S1 and S2 for #1	77
Figure 4.7: Torque moments versus time and event rate for #2.....	80
Figure 4.8: Correlation between mechanical response and AE accumulative hits for #2	81
Figure 4.9: Description of mechanical damage behavior with acquired AE data for the #2 Specimen with comparison between cumulative AE hits and the Weibull distribution function curve based on rotation measurement, with Weibull distribution function parameters	83
Figure 4.10: Influence of Weibull parameters on damage evolution.....	86
Figure 4.11: Mechanical description of SFRC and plain concrete specimens correlated to AE activity	87
Figure 4.12: a) Average frequency variation versus data set in fracture process, b) Smoothed average frequency for specimen #7 versus data	89
Figure 4.13: a) RA variation versus data set in fracture process, b) Smoothed RA for specimen #7 versus data.....	91

Figure 4.14: Amplitude distribution for plain and SFRC beams	93
Figure 4.15: Typical AE amplitude distribution versus duration, a) specimen #2, b) Specimen #6, c) specimen #7	94
Figure 4.16: Torque-Angle of twist: a) Single cell section girder, b) Double cell section girder, c) Triple cell section girder	101
Figure 4.17: 3D even localization of damage progress with respect to progressive damage evolution. a) Stage I, b) Stage II, c) Stage III, d) Stage IV.....	103
Figure 4.18: Cumulative Hits for all three girders, the plot of torque moment is imposed. a) Single cell section girder, b) Double cell section girder c) Triple cell section girder	105
Figure 4.19: AE signal strength analysis for DC specimen. a) Historic index as a function of time. The plot of the cumulative signal is superimposed. b) Magnified portion of plot.....	108
Figure 4.20: Severity index as a function of time for DC specimen. The plot of the cumulative signal is superimposed.....	108
Figure 4.21: Intensity chart for double cell specimen at each stage of damage. a) Stage I, b) stage II, c) stage III, d) stage IV	110
Figure 4.22: Values results for the entire data set before smoothing process for TC specimen.....	112
Figure 4.23: Smoothed b-values results for entire data set of TC specimen.....	113
Figure 4.24: Flowchart of determination of number of required clusters by application of k-means	121
Figure 4.25: Flow chart of SIb analysis	123
Figure 4.26: The percent of the total variability explained by each principal component for specimen: a) #2, b) #4, and c) #7	126

Figure 4.27: PCA visualization of the kernel fuzzy c-means clustering: a) #2, b) #4, and c) #7.....	128
Figure 4.28: Peak Frequency distribution of the patterns belonging to each cluster at different stages for specimen: a) #2, b) #4, and c) #7. S1: matrix micro cracking, S2: visible macro cracking, S3: fiber pull-out/tension softening (plain concrete).....	131
Figure 4.29: A) Load- deflection curves for ferrocement slab specimens: a) Normal mortar series (NM), b) Self-compact mortar series (SCMR0), B) Ib-value	139
Figure 4.30: A) Load- deflection curves for ferrocement slab specimens: a) Self-compact 5% rubberized mortar series (SCMR5), b) Self-compact 10% rubberized mortar series (SCMR10), B) Ib-value	140
Figure 4.31: a) S.E.M. images of interface surface of rubber (10%) and cement paste (A) Rubber particle; (B) Cement paste, b) Schematic illustration of ITZ	145
Figure 4.32: General types of failure modes: a) Punching failure, b) Flexural failure	147
Figure 4.33: Cumulative AE hits along the loading, a) Normal mortar, b) SCM, c) SCMR5, d) SCMR10	149
Figure 4.34: AE hits rate against loading: a) Punching failure, b) Flexural failure..	152
Figure 4.35: AE hit rates against loading: a) SC6LR10, b) SC8LR10	153
Figure 4.36: Cumulative AE hits and stiffness versus time for NM6.....	155
Figure 4.37: Loss of stiffness versus normalized cumulated AE hits, a) NM6, b) SC4LR0, c) SC8LR5.....	156
Figure 4.38: RA and Average frequency variation against loading for NM6.....	159
Figure 4.39: Trend of variation of AE features in different type of failures: a) RA, b) AF.....	161
Figure 4.40: Failure type classification based on average frequency versus RA.....	163
Figure 4.41: Proposed damage detection scheme flowchart.....	168

Figure 4.42: AE energy level distribution against AE events distribution for NM6 .	178
Figure 4.43: Acoustic emission event source localization with respect to different energy classes: a) Class A, b) Class B, c) Class C, d) Class D	180
Figure 4.44: X-bar control chart using first AR coefficient, a) Damage level I (25%), b) Damage level II (50%)	183
Figure 4.45: X-bar control chart using first AR coefficient, a) Damage level III (75%), b) Damage level IV (100%)	184
Figure 4.46 Comparisons of structural damage detection schemes: a) Damage sensitivity of different schemes, b) Increment in damage indicator in different schemes	187
Figure 4.47: Effect of AR model order on damage indicator sensitivity	189
Figure 4.48: Intensity analysis for composite slabs: a) Severity versus Historic index, b) Historic index profile	191
Figure 4.49: Bathtub curve for hazard rate function	194
Figure 4.50: Load-displacement curves of beam specimens.....	200
Figure 4.51: Failure pattern of PFRC specimen at ultimate load	201
Figure 4.52: Variations of measured velocity in accordance to specimen type	202
Figure 4.53: Velocity distribution results of the beam center cross sections, perpendicular to transverse direction	203
Figure 4.54: 3D wave velocity mapping in different damage level for the PFRC specimen.....	203
Figure 4.55: Relation between wave attenuation and travel distance	205
Figure 4.56: Load- displacement of RC beam specimen: damage categories.....	206
Figure 4.57: 2D localization by acoustic emission events activity in: a) micro-elastic crack formation, b) macro crack formation stage, c) crack localization stage.....	209

Figure 4.58: AE activity (count) versus strain in steel; a) PFRC, b) SFRC, and c) RC	211
Figure 4.59: Cumulative signal strength versus loading in: a) PFRC; b) SFRC; and c) RC	214
Figure 4.60: Signal strength versus loading in PFRC beam	215
Figure 4.61: Trend of variation of frequency versus damage level; a) PFRC, b) SFRC, and c) RC	217
Figure 4.62: Crack type classification in different Damage Level based on average frequency versus RA; a) damage level I, b) damage level II, c) damage level III, d) damage level IV	220
Figure 4.63: Intensity signal analysis versus elastic wave velocity for the entire length of PFRC beam specimen.....	222
Figure 4.64: Zonal based damage severity assessment based on elastic wave velocity distribution map	223
Figure 4.65: Intensity signal analysis versus elastic wave velocity for PFRC beam specimen at region C.....	224

LIST OF TABLES

Table 2.1: Acoustic Emission techniques Applications in Source Events Information..	13
Table 3.1: Concrete specimen's specification.....	45
Table 3.2: Mix proportion of concrete	49
Table 3.3: Reinforcing steel properties	50
Table 3.4: Mechanical properties of concrete specimens	52
Table 3.5: Proportion of constituent materials and rheological properties of mortar mixes and slabs	56
Table 3.6: Mix proportion of concrete specimens	60
Table 4.1: Summary of subsequent sections and references of related experiments ...	61
Table 4.2: b-value and fractal dimension results	80
Table 4.3: Parameters for Weibull damage functions.....	85
Table 4.4: Ultimate Torque and corresponding twist angle of specimens.....	102
Table 4.5: The average b-values for each stage of damage	113
Table 4.6: SIb-value and b-value related to each stage of damage.....	134
Table 4.7: Test results for ultimate load, flexural strength, ultimate deflection and fracture mod	141
Table 4.9: Acoustic emissions events and the recorded AE energy	178
Table 4.10: Outlier of X-bar control charts by using different AR coefficients	185
Table 4.11: Outlier of Shewhart X-bar control chart by Linear and Quadratic projection.....	186
Table 4.12: Intensity Analysis Description	224
Table 4.13: Elastic Wave Velocity Distribution for PFRC beam (m/s).....	224

LIST OF SYMBOLES

ϕ_j	AR coefficient
A_{db}	Peak amplitude of the AE events in decibels
AF	Average Frequency
Amp	Amplitude
AR	Auto regressive mode
AR(p)	AR model of order p
<i>bAEAE</i> -based b-value	
c	A constant of proportionality
D	Fractal dimension
D(x)	Bayes 'decision rule
DI	Damage indicator
D_K	Dimensionality of the transformed feature in kernel fuzzy c-mean
$d_K(x_i, x_k)$	Kernel-based distance between the ith and kth feature vectors
E	Expected vector in AR model projection
E^{AE}	AE energy
e(t)	Random error
E_u^{AE}	Maximum AE energy
EWMA	Exponentially Weighted Moving Average
EWMA0	Mean of historical data (target)
f	Frequency
f(t)	Time history at time t
F(x)	Gaussian smoothing
f(ϵ)	Probability density function of the microelement
g	Gravity constant
HI	Historic index

Ib	Improved b-value
k	Shape parameter in the Weibull modulus
K	Stiffness
K_r	Stiffness reduction
K_{ru}	Maximum stiffness loss
l	Length
L	Length of ray path
LCL	Lower center line limit
m	Weibull elastic properties parameter in torsional fracture
ma	Mean vector of class A
mb	Mean vector of class B
n	Weibull dimension parameter in torsional fracture
N (M)	The number of AE hits (or events) of magnitude $\geq M$
N_{tot}	Total AE events
N_{θ}	The number of cumulated AE for torsional angle
PFRC	Polypropolyn fiber reinforced concrete
Q	Quadratic projection matrices
RA	Rise time/amplitude
RBF	Radial-basis-function
RC	Reinforced concrete
RSCC	Rubberized self-compact concrete
S	Covariance matrix in AR model projection
SCC	Self-compact concrete
SFRC	Steel fiber reinforced concrete
SIb	Spatial intelligence b-value
SIRT	Simultaneous iterative reconstruction technique

SPC	Statistical process control
Sr	Severity index
t	Time
U	Fuzzification parameter
UCL	Upper center line limit
UPV	Ultrasonic pulse velocity
v	Velocity of signal
V	Linear projection matrices
x	Vector in kernel fuzzy c-mean
$Z_{\alpha/2}$	Percentage point in the normal distribution with zero mean
θ	Angle of twist in the beam
λ	Scale parameter in the Weibull modulus
μ	A dummy in Gaussian filter
σ	Standard deviation
Φ	Nonlinear mapping function in kernel fuzzy c-mean
(θ)	Weibull damage function in torsional fracture
$f(,;)$	The typical probability density function of a Weibull random
Σ_A	Covariance matrices of class A
Σ_B	Covariance matrices of class B
η	Constant that determines the depth of memory of the EWMA

CHAPTER 1

INTRODUCTION

1.1. Deterioration of concrete structures

Concrete is one of the most common and popular materials currently being used in construction of all scales and for all purposes mainly because of its distinctive advantages over some other materials. Structures made of concrete with reinforcement such as steel bars are known to be very versatile and able to fulfil major strength and serviceability requirements. Although proper design approach may increase the level of performance in terms of strength and durability, concrete structures should not be considered as maintenance free because they deteriorate under physical and environmental stressors. Deterioration can pose loss of strength and cause unsafe conditions. For instance, in many concrete structures the emergence of cracks is a common issue that triggers degradation process of concrete (Chen et al., 2006). The presence of cracks may either cause significant reduction of concrete structure strengths or pose durability problems. Small flaws that might be initially present in the material and eventually develop can be the main cause of formation of large cracks. Thus, they may begin as small cracks which can actively grow to become large ones.

Apart from concrete structures deterioration, there are several issues that can disturb the normal structural performance. Examples are earthquake, flood, over loading, fatigue, environmental attack, and aging.

1.2. Non-destructive testing (NDT)

Structural deterioration in concrete structure can occur in different forms such as loss of stiffness (loss of strength), cracks, corrosion, creep, overloading, etc. The deterioration posed by the concrete portion of the structure can disturb the overall structural integrity.

Therefore, by means of various non-destructive testing methods, the integrity of deteriorated structure can be assessed both locally and globally.

There are several methods such as vibration based test or stress wave techniques that can be used for structural integrity assessment (Shin, 2008). These techniques can be categorized in two classes: Global methods such as vibration or modal technique and local method such as ultrasonic pulse velocity. Most of the available local NDT methods require that the part of the structure under inspection is accessible or the damage location has been already identified. It is noted that when the structural damage is in the interior of the medium, it is not possible to localize the damage visually from the exterior. In such cases, vibration based methods can be beneficial. The most important feature of vibration based method is that location of damage can be identified even though it is unknown in advance. Second, sensors can be placed arbitrarily along the structure and do not need to be mounted on the structure in the vicinity of the damage (Shin, 2000). However, these vibration based methods are based on dynamic properties of the structure such as natural frequency, and minor damages or fracture might not cause sufficient significant changes in these properties to be noticeable. Therefore, in such cases the result of inspection might be doubtful.

Conversely, due to their sensitivity to even small localized damages, stress wave based methods can be used as local damage detection methods (McCann and Ford, 2003). Many different local NDT methods are being extensively used in concrete structure assessment tasks for crack and strength measurement.

For instance, among the stress wave methods ultrasonic pulse velocity (UPV) or impact echo are widely being utilized in concrete structure assessments as a common local technique because of their straightforward implementation (Shin, 2008). However, in these types of local methods a prior knowledge of damage location is required.

On the other hand, among the stress wave methods, acoustic emission (AE) might be used as a global and local online monitoring tool without need of prior knowledge of damage location. That is because AE is a passive NDT method which can capture stress waves generated from active cracks. Therefore, due to several advantages of AE technique, AE application is turning out to be a potential NDT technique which can be employed either independently or in combination with other NDT tools for structural assessment.

1.2.1. Acoustic emission (AE)

Phenomenon of emission of elastic stress waves in solids due to the occurrence of irreversible changes in material is called acoustic emission (AE). AE is somewhat unique among non-destructive testing techniques. The main difference between AE and other NDT techniques is the method of data acquisition. In contrast to other NDT methods, AE should be applied during loading period, unlike other NDT techniques which are implemented either before or after loading period (Grosse and Ohtsu, 2008). This has raised the question of whether or not AE should be categorized as a NDT method. However, considering the way that AE signals are captured and recorded, AE can be considered truly as a NDT method. As long as the material is tested on the working load without imposing any additional load, AE can be used as a NDT technique.

In addition, AE is capable to provide early warning of failure long before the ultimate failure. AE sensors record elastic waves released from a growing fracture. Thus, acoustic emission is classified as a passive NDT technique, because AE detects defects while growing and propagating. The main difference in the essence of active and passive methods refers to the way through which the source emits.

In active methods like scanning technique, the source is applied externally into the medium to generate waves, whereas in AE as a passive method sensor receives waves which were generated from a source within the medium (Grosse and Ohtsu, 2008).

AE features have being widely studied in concrete engineering for around five decades (Miller and McIntire 1987; Ruesch, 1959). Effort has been put forward to bring AE applications beyond laboratory studies (Ohtsu, 1987) and it is gaining attention in practical applications such that codes have been issued to standardize AE procedure for field monitoring usages (NDIS2421, 2000).

However, with an ever-increasing demand for concrete structure assessment, AE techniques have drawn a great deal of attention for use as a problem-solving structural assessment technique.

1.3. Problem statement

Assessment of concrete structure deterioration involves two different factors. The First factor is related to the characteristic of material properties and its failure criteria according to the fracture properties. The second factor is the overall performance and condition of structures.

In other words, it is often required to study the fracture mechanism of concrete structures and quantify its mechanical properties after the concrete has hardened to find out if the structure meets the requirements for its design use, other than regular inspections to ensure the integrity of the structure in service. In ideal conditions, it is desirable that these tests and inspections be accomplished without imposing any sort of damage to the structure.

Therefore, assessment of concrete structures requires drawing attention to the development of techniques which are capable of characterizing the fracture properties and assessing the overall performance of structures.

Among the other NDT techniques, unique AE characteristics provide a great potential toward practical application of AE for examining either one or both of the above mentioned factors in structural assessment. This is because the use of AE makes it possible to monitor changes in a materials behavior over a long period of time without moving one of its components i.e. sensors. Second, AE can trace crack propagations occurring both on the surface and deep inside a material (Grosse and Ohtsu, 2008).

Therefore, AE technique has become an important addition to NDT methods by enabling the active survey of a structure by scanning for geometric defects as well as the employment of visual inspection methods for observation of a materials surface.

However, while there have been several successful applications of AE in monitoring different structures (Grosse and Ohtsu, 2008) there is no guarantee that AE can be easily implemented, particularly for concrete structures in which the level of uncertainty is considerably high. In this regard, there are various concerns which demand careful and comprehensive study so that application of AE in regards to both fracture analysis and overall performance assessment can be facilitated. For instance, AE waveform variation with respect to different types of loading, e.g. torsional loading which has not been investigated yet, combination of AE and other NDT methods to provide a robust global and local monitoring technique, finding reliable AE signal parameters to discriminate fracture sources, precise damage quantification parameters along with damage progress. Consequently, the importance of developing a reliable monitoring method in which the afore-mentioned concerns could be dealt with inspired the following objectives for this study.

As stated, there are various imperative concerns with regard to application of AE technique for assessing concrete structures which need to be answered. There are several issues which have yet to be answered such as effect of torsional fracture on AE parameters, quantitative correlation between AE parameters and torsional fracture, unsupervised separation of different level of damages, quantification of damage by AE hit, obtaining a global and local method with AE sensors, a general and comprehensive online monitoring and failure reliability system.

Therefore, to explore the possibility of attaining suitable answers to above questions, four different laboratory experimental projects were conducted so that each particular test could provide suitable background to answer either one or more specific objectives.

1.4. Objectives

1. Characterise torsional fracture process of concrete structural elements by means of AE monitoring
2. Quantify progressive damage of concrete structural elements by acoustic emission
3. Provide pattern recognition algorithm for online monitoring systems using AE technique
4. Introduce a global and local monitoring scheme for assessment and failure reliability analysis of concrete structural elements.

1.5. Scope and outline of this study

To attain the objectives of this research, four different experiment sets were conducted and along with analysis of the experiments data through AE monitoring, some statistical and numerical analyses were carried out. The scope of this research which is accomplished in five chapters includes:

1. Chapter 1 which briefly addresses the characteristics of concrete structures and current state of NDT methods to monitor these structures.
2. Chapter 2 which provides a comprehensive literature review of AE study on concrete structures to show the trend and direction of studies in this field.
3. Chapter 3 which describes materials and methodologies of four different experiments through which the objectives of this research were studied. The procedures and testing methods were described in detail.
4. Chapter 4 which discusses results, analysis and discussions associated with the experiments and numerical techniques carried out in this research. Chapter 4 is in the form of articles that presenting a part of this research objectives. The specific objectives related to each sections are presented herewith.

5. Chapter 5 which draws the final conclusions and makes recommendations for further research.

CHAPTER 2

LITERATURE REVIEW

2.1. Introduction

The phenomenon of acoustic emission is defined as the propagation of elastic waves due to the release of localized internal energy, such as a micro-fracture in elastic material (Shiotani and Ohtsu, 1999; Behniaet al., 2014; Shiotani, 2006; Fowler, 1986; Ohtsu and Yuyama, 2000). Sources of AE activities include structural deformation processes as plastic deformation, crack expansion and other kinds of material degradation. The AE process involves the use of sensors to detect released strain energy generated from growing cracks (Seto et al., 1992; Luo et al., 2002).

AE technique has been widely used in the field of civil engineering for structural health monitoring (SHM) (Ohtsu and Yuyama, 2000; Shiotani, 2006; Carpinteri et al., 2011; Shiotani et al. 2001; Ohtsu, 1991; Capeneri et al., 2007a; Capeneri et al., 2007b; Capeneri et al., 2007c). The advantages of using AE technique compared to other non-destructive techniques are that the position of the developing cracks can be determined and the entire structure can be tested without interrupting the performance of the structure. Classification and crack direction can be calculated through different approaches such as b- value analysis of AE (Shiotani et al., 1999; Mogi, 1963; Scholz, 1968; Ohno and Ohtsu, 2010; Shiotani et al., 2000; Shiotani, Bisschop, & Van Mier, 2003; Shiotani, 2006a, Shiotani, 2006b). AE activities are categorized in two groups namely 'primary AE activity' and 'secondary AE activity'. The former considers crack growth or crack formation while in the latter crack growth has been stopped and the intended activity is based on friction between crack surfaces.

Two typical crack modes should be considered when investigating the cracking behavior in structures with AE parameters since the fracture cracking mode in concrete structure changes as the fracture progresses from the tensile type (mode I) to the shear type (mode II). Usually AE activities associated with mode I type cracks are registered when the fracture growth is in the stable stage. Upon reaching final failure, most recorded AE activities are related to mode II type cracks.

On the other hand, in loading and unloading system, during unloading process in the early stages, few AE events are expected. Approaching final failure, during the unloading process AE activities would be considerably increased. Therefore AE activity during unloading process has potential to show the damage degree. As a result, different aspects of structural defect including damage intensity, crack mode and health level of the structure are measurable using parameters extracted from AE signals.

2.2. Potential Structural Assessment Approaches Based on AE

AE technique is extensively used for real-time damage monitoring. The premise of AE refers to the generation of transient elastic waves during the rapid release of energy from a localized source within a material. The fundamental concept of AE brings some unique features for this technique as an applicable non-destructive testing technique. Among these features the most important ones are (1) real time capability, (2) high sensitivity. (3) global monitoring capability, (4) source location, (5) sensitivity to any process or mechanism that generates stress waves, (6) passive nature (no need to supply energy from outside, but energy from damage source itself is utilized).

Considering AE features, the application of AE might be divided in two core categories; (1) Global structural health monitoring which can provide total insight into the situation of the structure and focuses on overall health of structure. For example, analysis of AE parameters or waveform may result in a general perception of damage severity or identification of the nature of damage through entire dataset of all sensor arrays (2) Local structural health monitoring which focuses on a specific location in the structure. Examples include monitoring to assess growth of a known crack, corrosion at specific locations with a specific number of sensors. Hence, recording and analysing AE signals can be divided into parameter-based approach (classical) and signal-based approach (quantitative) (Shiotani et al., 1999; Mogi, 1963; Scholz, 1968; Ohno and Ohtsu, 2010; Shiotani et al., 2001; Shiotani et al., 2003). Both above mentioned approaches can be applied to both categories, i.e. Global and Local structural health monitoring. Civil engineers who work in the field of concrete structure might use both approaches for different purposes. As a result, considering the existing literature, this literature aims to provide comprehensive information of fundamental and advanced concepts of these two above mentioned approaches and highlight the current application of AE and its drawbacks.

2.3. Parametric Analysis

Waveform and parametric data are two basic forms of recordable AE data. The hardware and software are required to be fast enough in order to avoid losing AE data and provided storage must be significant. In the case of huge amounts of AE activity in a short period of time, waveform is not a practicable test. On the other hand, in parametric approach a series of parameters characterize the AE signals.

In parametric based approach, signal characteristic are utilized to evaluate the grade of damage as well as identification of nature of damage. Therefore parametric data are more feasible and tractable.

The definitions of basic AE parameters are schematically described in Figure2.1. However, a summary of AE parameters and their contribution to provide information about the source event is listed in Table 2.1.

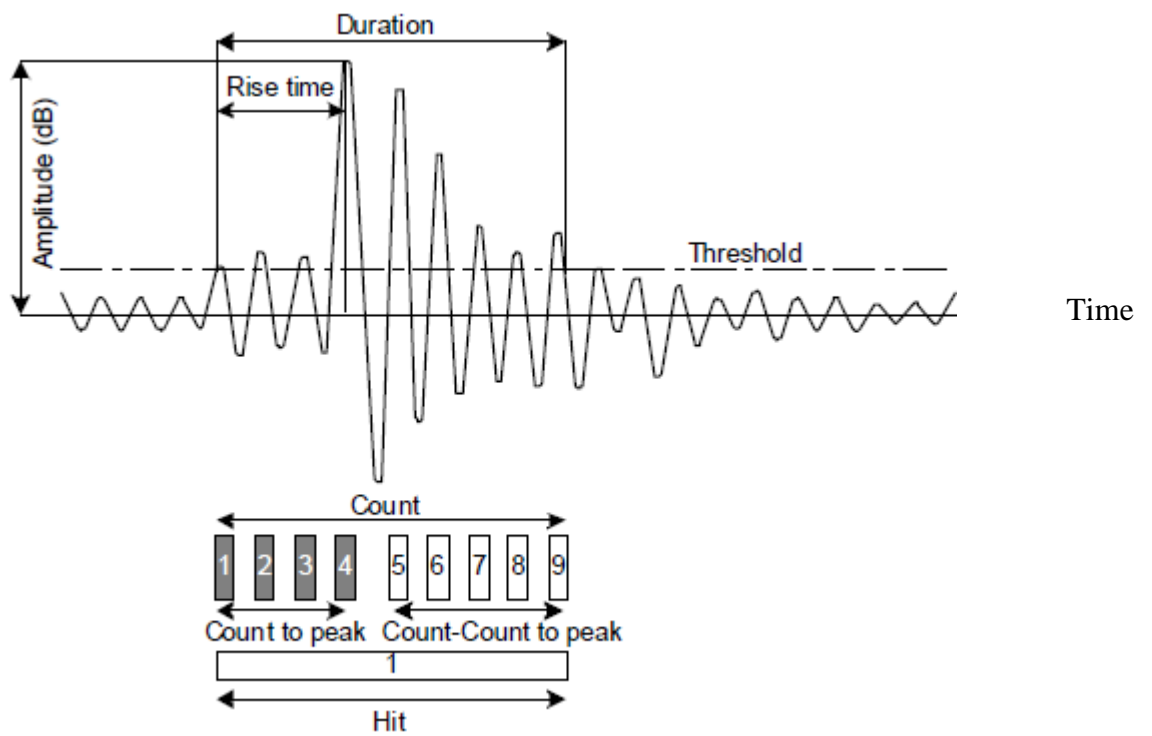


Figure 2.1: Basic parameters of an acoustic emission waveform

Table 2.1: Acoustic Emission techniques Applications in Source Events Information

Variables	Parameter	Obtained Information
Time Domain	Rate	Rate of Damage Occurring
	Peak Amplitude	Intensity of Source Event
	Relative Arrival Time	Source Location
	Duration	Energy of Source Event
	Count	Energy of Source Event
	Waveform	Structure of Source Event
	Energy	Energy of Source Event, Type of Damage
Frequency Domain	Frequency Spectrum	Nature of Source Event
Time- Frequency Domain	Spectrogram	Energy Distribution of Source Event Through Time
	The Time Variation of Each Frequency Component	The Intensities of Source Frequency Component

2.4. Fundamental Studies on AE Technique in Concrete

AE testing has a history spanning more than 50 years. Kishinouye's report was the first statement containing an experiment on AE (Chang and Liu, 2003; Obert and Duvall, 1945; Obert, 1977; Drouillard, 1990). AE researches culminated in fundamental concepts and subsequently a phenomenon called 'Kaiser Effect' was introduced (Kaiser, 1953). Further, Schofield achieved some progress for AE testing by publishing a report entitled "Acoustic Emission under Applied Stress" in 1954 (Schofield, 1954).

The American Society of Non-destructive Testing also published a comprehensive description of AE testing (Miller and McIntire, 1987). Ohtsu (Ohtsu, 1996; Ohtsu, 1989) has accomplished surveys in the application of AE testing methods in the field of civil engineering, specifically in concrete structures (Grosse and Ohtsu, 2008). In general, application of AE in concrete structures might include three major aims: 1. Localizing the damage, 2. Quantifying the severity of damage, 3. Characterizing the nature of source. Then in following sections the concepts and recent developments for each specific AE application will be discussed.

2.5. Damage Assessment of RC Structures by AE

Damage assessment of concrete structures includes different stages: localization of damage, identification the type of damage, and damage severity assessment. The following sections briefly address these stages.

2.6. Damage Localization Process

Localization technique is required for quantitative methods in acoustic emission analysis in order to accurately obtain the source coordinates of the AE events. In practice, there are a variety of ways for AE localization to obtain the required resolution in one, two, or three dimensions.

The principal of acoustic emission source localization arose from modified earthquake source localization (Aid and Richards, 1980; Schweitzer et al., 2002; Shearer, 1999; Finck and Manthei, 2004). Damage localization process may be divided in three categories. These categories will be discussed in the following sections.

2.6.1. Zonal or One Dimensional Approach

The Zonal location method is the simplest way to locate the AE source for a one-dimensional structure. This method is often used in monitoring large scale structures such as buildings, pipes, etc.

In this method sensors should be installed over a wide area on the structure's surface and/or specifically focus on the most critical locations. If AE is recorded by a particular sensor, the technician should inspect the area nearby this sensor (Lovejoy, 2006).

2.6.2. Two Dimensional Approach

The planar localization technique applies to two-dimensional structures in which the structure's thickness is small compared to the length size of the object and source coordinates are only required in two directions.

Since only three unknowns (the two source coordinates and the time of origin) have to be determined, recordings from only three sensors are sufficient (Lovejoy, 2006; Labuz et al., 1988; Köppel and Grosse, 2000).

2.6.3. Three Dimensional Approach

Many specialists have employed 3D AE localization methods in the field of civil engineering (Lovejoy,2006; Labuz et al.,1988; Köppel and Grosse,2000). The principal is quite similar to the determination of earthquake hypocentres in seismology and uses the recorded arrival waves of an earthquake at multiple seismometers.

2.7. Source Discrimination and Crack Classification

Another major problem behind successful AE monitoring is to discriminate the nature of source in a medium. There are two different approaches based on waveform and parametric analysis. The former one which is called Moment Tensor Analysis was developed from seismic engineering application for structural and material engineering applications (Ohtsu et al., 2010).

The latter approach (parametric based analysis) utilizes signal parameter definitions including Rise time, Amplitude, and Average Frequency.

2.7.1. Moment Tensor Analysis

Moment tensor analysis is a post-processing analysis method for identification of crack mechanism which classifies the crack based on AE signals. It is known that the crack mechanisms associated with AE generation include crack kinetics and crack kinematics (Ohtsu et al., 1998).

Crack kinetics might be determined by using deconvolution analysis, while moment tensor analysis (MTA) may be promising for crack kinematics (Ohtsu et al., 1998; Shigeishi and Ohtsu, 2001). By using this visualizing approach the cracking modes can be shown by an arrow vector indicating crack-motion vector and the circular plate corresponding to the crack surface which is perpendicular to crack normal vector (Yuyama et al., 1995; Minemura et al., 1998).

The most distinct feature of this analysis is that the procedure can give quantitative information on three-dimensional 3-D location of cracks, crack types, crack orientations, and directions of crack motion.

However, not all the recorded waveforms are useful for moment tensor analysis intentions, since many sets do not have six clear P-waves. Furthermore, some waveform sets that give readable P-wave arrivals fail in locating sources by using a set of five arrival time difference values. It is known that accurate source location requires accurate arrival time differences values, which require ideal structures.

In general, reinforced concrete specimens may have reinforcing bars, cracks, and boundaries which can result in conflicting arrival time values for the calculation of location. These are the reasons why only small percentages of the recorded waveform sets were applicable to the analysis. Thus only some part of the detected information can be used in moment tensor analysis (Yuyama et al., 1999).

2.7.2. Crack Classification Based on Parametric Approach

As stated previously, in some cases the application of moment tensor analysis might not be the most proper method. The main reason might be the number of minimum required sensors to detect each cracking event (at least six).

Since the crack location is not known beforehand, the sensors have to be distributed evenly to cover the largest area of material volume. Consequently, the distance between neighbouring sensors does not allow capturing one single cracking event by the necessary number of sensors. This matter is an irrefutable hindrance in long structures like bridges. The sensors are placed in a straight line to cover as much of the structure's dimension and length as possible (Shiotani et al., 2009).

This placement enables only linear location of the damage zones but is not suitable for MTA. Therefore, simple classification patterns have been introduced to utilize signal parameters for the sake of characterization of the cracking mode based on the information of a small number of sensors (Shiotani et al., 2009; Shiotani and Aggelis, 2009).

Considering the analogy between different crack propagation events, it can be deduced that there might be a different signature for each specific type of crack. Cracks with inherent tensile cause opposing movement of the crack sides and subsequently results in AE waveforms with short rise time and high frequency. In contrast, shear type of cracks usually emerge in longer waveforms which results in signals with lower frequency and longer rise time (Aggelis et al., 2012a; Aggelis et al., 2012b). This might be owing to the fact that larger part of energy is transmitted in the form of shear waves, which are slower; therefore, the maximum peak of the waveform is considerably delayed compared to the onset of the initial longitudinal arrivals. This has been already demonstrated in many studies in different material, particularly concrete medium (Ohno and Ohtsu, 2010; Shahidan et al., 2013; Soulioti et al., 2009), fiber composites (Philippidis et al, 1998; Aggelis et al., 2010, Aggelis et al., 2012c; Aggelis et al., 2012d) and rock (Shiotani, 2006).

In conclusion, considering the aforementioned concept the tensile crack types might be differentiated from shear type crack by drawing the following graph (Figure 2.2a). However, in recent studies this method has been highly investigated and the new result might discriminate pure tensile crack from combined crack which are the most dominant cracks in the time of final failure and fracture (Figure 2.2b).

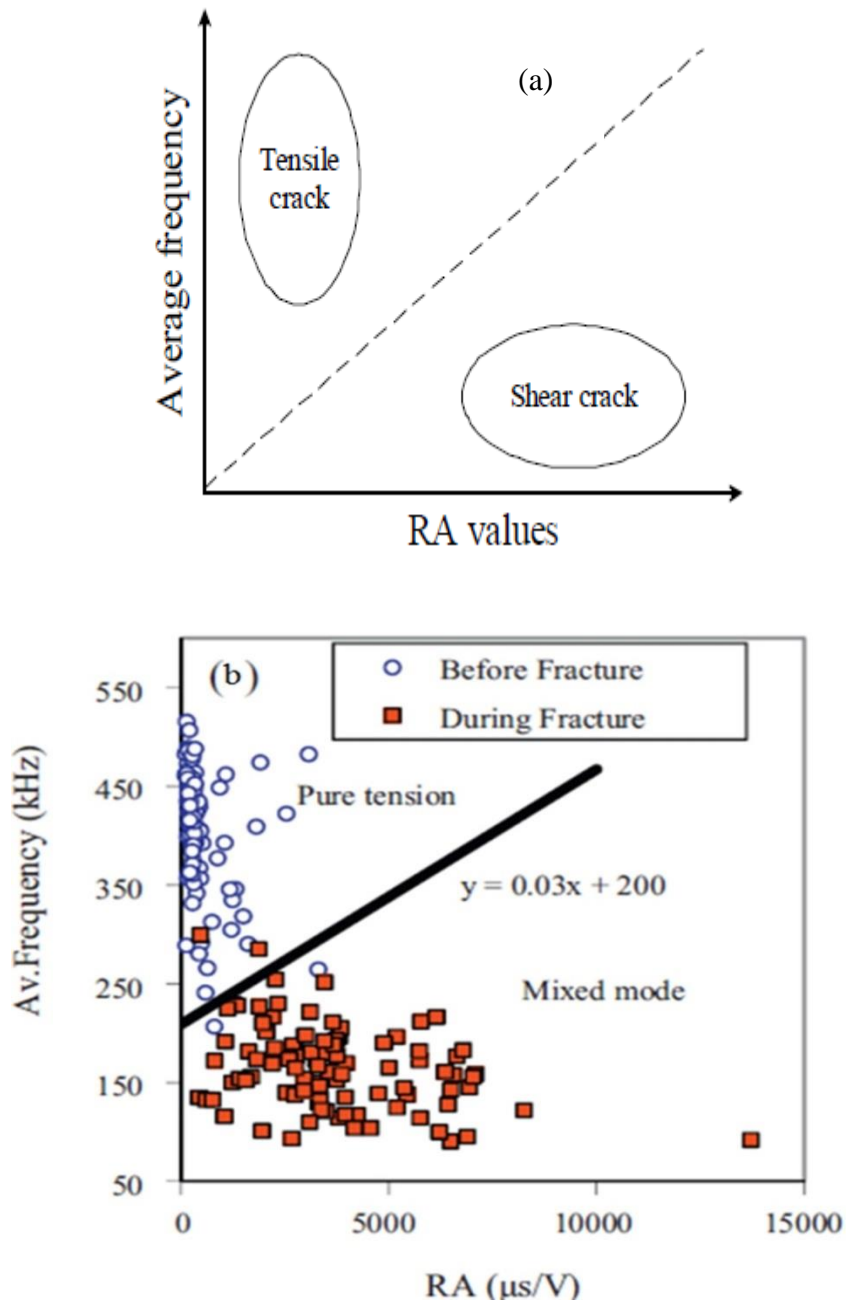


Figure 2.2: Crack type classification with a combination of average frequency and RA values: a) pure tension and combined crack, b) pure tension and pure shear (Aggelis, 2011a)

2.8. Clustering of Acoustic Emission Data for the Purpose of Damage Mode

Identification in Concrete Structures

As mentioned in earlier sections, one of the main targets of AE data analysis is identifying the nature of AE sources. In the preceding section it was found that there is a relation between the magnitude of different AE parameters and damage mechanisms.

Thus, each signal can be considered as the acoustic signature of a damage mode. However, even by introducing simplified AE parametric analysis as an alternative strategy for moment tensor, there are still some drawbacks. These drawbacks are sometimes related to discrepancy in AE data parameters or the huge amount of AE parameters.

Thus as a solution using multi-parametric analysis seems to be essential to improve the identification of damage modes. One well-known technique for the classification of AE events is pattern recognition (Johnson, 2002). A methodology involving descriptor selection, cluster analysis and cluster validity with no information on the attended cluster is called unsupervised pattern recognition. K-means algorithm is a popular example of clustering method (Likas et al., 2003). Another method of multivariate analysis is called Principal Component Analysis (PCA) (Jolliffe, 2002).

PCA is a mathematical algorithm by which the dimensionality of a data set is reduced in order to allow better pattern recognition and data interpretation. Through this algorithm, a p -dimensional data vector X is transferred into a new q -dimensional data vector Z , containing the data 'principal components' (Johnson, 2002). If the p -coordinates are a linear combination of $q < p$ variables, the first q principal components will completely characterize the data and the remaining $p - q$ components will be zero. This method is based on achieving a specified cumulative percentage of total variance extracted by successive factors. The purpose is to ensure practical significance for the derived factors by ensuring that they explain at least a specified amount of variance (Johnson, 2002; Likas et al., 2003; Jolliffe, 2002; Sharma, 1995; Manson et al., 2001; Mustapha et al., 2005).

Another method for data classification is Kohonen's Self Organizing Map (SOM) which separates data numerically by neural network procedures. The self-organizing map (SOM) is one of the most prominent artificial neural network models adhering to the unsupervised learning paradigm. The model consists of a number of neural processing elements, i.e. units. Each unit i is assigned an n dimensional weight vector m_i , $m_i \in \mathbb{R}^n$. The training process of self-organizing map may be described in terms of input pattern presentation and weight vector adaptation. Each training iteration t starts with the random selection of one input pattern $x(t)$. This input pattern is presented to the self-organizing map and each unit determines its activation. Euclidean distance between the weight vector and the input pattern was used to calculate a unit's activation. In SOM an incoming signal pattern of arbitrary dimension is transferred into a one or two dimensional discrete map which plots the similarities of the data by grouping similar data items together (Godin et al., 2004; Kohonen, 1990). Thus SOM accomplishes two tasks; it reduces dimensions and displays similarities. The result of the Kohonen algorithm is called U-matrix which shows distances between neighbouring units and thus visualizes the cluster structure of the map (Figure 2.3). SOM is adopted to identify clusters and relate them to the A patterns. U-matrix can be calculated for each individual parameter. Comparing maps with each other and a combination of different clustering methods such as PCA and SOM help practitioners in quantifying the damage severity (Calabrese et al., 2013a; Calabrese et al., 2013b).

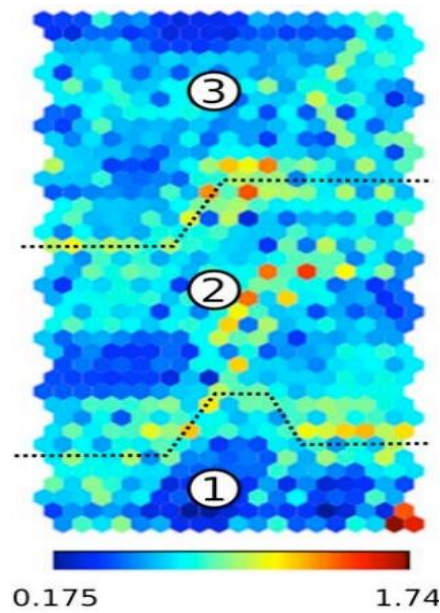


Figure 2.3: U -matrix resulting from the application of the SOM (Calabrese et al., 2013a)

On the other hand, for crack type classification there are also some proper methods which are known as pattern recognition technique that can discriminate shear and tensile type cracks by application of supervised and unsupervised machine learning approach (Aggelis, 2011b; Beck et al., 2003; Calabrese et al., 2012; Shigeishi and Ohtsu, 2001; Farhidzadeh et al., 2013).

In general, pattern recognition problems are categorized based on the type of learning that generates the output, i.e., supervised and unsupervised. Supervised learning exploits a set of training data that consists of a set of labels clarifying to which class each training data belongs to. This training set is used to train (learn) a classifier as well as possible. In unsupervised learning, on the other hand, the training data does not have labels. Therefore, it attempts to discover the inherent patterns in the training data that can then be used to determine the hidden class boundaries. Towards providing a solution for uncertainty in AE data other than existing supervised method, a novel approach was proposed to discriminate shear and tensile crack by aid of an unsupervised method which is called Gaussian mixture modelling (GMM).

As illustrated in Figure 2.4, the tensile and shear cracks have been differentiated by GMM method. In fact, for this study (Farhidzadeh et al, 2013) a full scale shear wall was subjected to low frequency cyclic lateral loads in 10 steps called LS1 to LS10. In the first few load steps the dominant cracks were tensile type, e.g. LS2, and as damage progressed in the last load steps, e.g. LS9, the shear crack turned out to be dominant. These classes were properly identified by application of GMM.

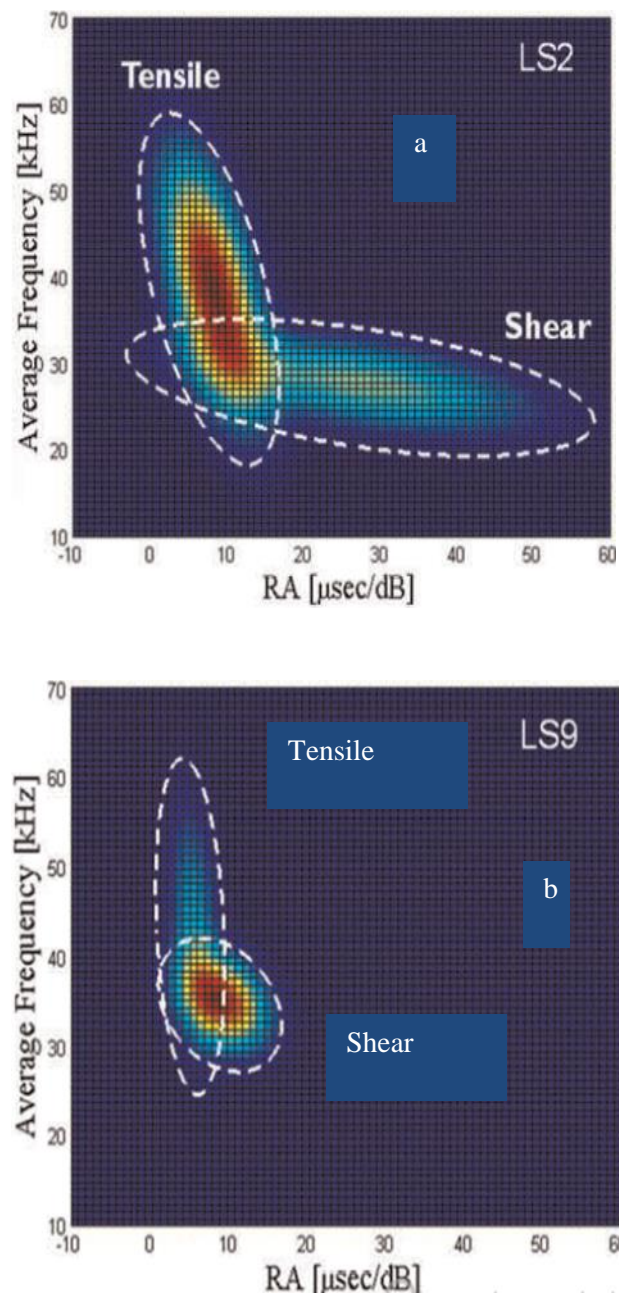


Figure 2.4: Gaussian mixture model for crack classification: a. dominance is with tensile crack, b. dominance is with shear cracks (Farhidzadeh et al, 2013)

Nevertheless, although pattern recognition methods have been utilizing in AE data analysis, there are still some major issues to be solved. One of the main problems may refer to the labelling process in supervised methods. Since this process involves visual inspection analysis, it might lead to spurious labelling.

Therefore, application of unsupervised method such as Fuzzy-c mean in conjunction with separate experimental studies might direct the works to have an independent classification of failure stages, correlating each specific stage of failure to the AE raw data like frequency etc. In fact, Fuzzy c-means (FCM) is a data clustering technique wherein each data point belongs to a cluster to some degree that is specified by a membership grade. This technique was originally introduced by Jim Bezdek (1981) as an improvement on earlier clustering methods. It provides a method that shows how to group data points that populate some multidimensional space into a specific number of different clusters. Consider an n set sample data to classify in c classes, $X = \{x_1, x_2, \dots, x_n\}$.

Each data sample x_i , is defined by m features, i.e., $x_i = \{x_i^1; x_i^2; \dots; x_i^m\}$, where x_i in the set X (X is an m – dimensional space). Because the m features can all have different units in general, the normalization for each of the features to a unified scale before classification should be taken.

Finally, other than above mentioned problem, there is another obvious drawback in the available methods. This problem is related to having certain limits for crack classification modes, i.e. fracture process analysis is limited to diagnose mode I and mode II by utilizing available methods. Hence, utilizing more powerful unsupervised pattern recognition techniques such as Density-based spatial clustering of applications with noise (DBSCAN) or kernel fuzzy c-mean (KFCM) may enable researchers to come up with a robust solution.

For example, replacing k-means approach with DBSCAN can be an alternative, since for k-means method the numbers of clusters are required to be determined beforehand whereas in DBSCAN technique this drawback is eliminated. In fact, the k-means aims at partitioning datasets into k disjoint subsets (clusters) based on minimization of a criterion. The most common clustering criterion is the summation of square distance of each data point in a subset to the center of the subset in which it is partitioned (Farhidzadeh et al., 2012). On the other hand, DBSCAN is a density-based clustering algorithm because it finds a number of clusters starting from the estimated density distribution of corresponding nodes. DBSCAN's definition of a cluster is based on the notion of density reachability. Basically, a point q is directly density-reachable from a point p if it is not farther away than a given distance ϵ (i.e., is part of its ϵ -neighbourhood) and if p is surrounded by a sufficient number of points such that one may consider p and q to be part of a cluster.

Note that q is called density-reachable (note the distinction from "directly density-reachable") from p if there is a sequence p_1, \dots, p_n of points with $p_1 = p$ and $p_n = q$ where each p_{i+1} is directly density-reachable from p_i (Ester et al., 1996). Hence, considering k-means and DBSCAN criteria, it can be realized that DBSCAN does not require one to specify the number of clusters in the data, as opposed to k-means. Therefore, classes will be formed based on the judgment of analysis rather than visual observation.

2.9. Damage Severity Evaluation for Concrete Structures

Many researchers have attempted to evaluate the damage level of RC structures applying AE parameters. Five methods pertaining to assess the damage in concrete structures were presented by aid of AE. Yuyama et al. (1999) and Ohtsu et al. (2002) correlated the calm and felicity ratio which was the first main damage evaluation method.

These above studies formed a testing standard (NDIS-2421) for AE monitoring applications. The second method was based on the “b-value” theory proposed by Pollock (1981) and afterward Ohtsu and Watanabe (2001) and Colombo et al.(2003) modified the presented method. The third method was demonstrated by Fowler, Blessing and Conlisk (1989) who employed the historic index versus severity index (intensity analysis).

This method has been applied in the field of concrete bridges by Golaski et al. (2002) to measure the level of deterioration, and was also applied on full-size pre-stressed concrete girders with the Texas Department of Transportation monitoring the structure.

The fourth method which applied “relaxation ratio”, determining the residual strength of concrete bridges, was proposed by Colombo et al. (2005). This method is based on the theory in which normal release of AE energy during the unloading phase of AE testing is a sign of structural damage.

Final method recommended by Ziehl and Ridge (2006) entitled “cumulative signal strength ratio”, distinguished the damage level of RC beams strengthened by FRP. This ratio evaluates the Kaiser or Felicity effect and is in a positive relationship with the growth in the level of damage. Emissions generated by structures increase as the damage level increases. This method modified the first method in which calm ratio and felicity ratio used to be calculated based on the number of hits. In the first method Calm ratio was initially defined based on the total number of hits during unloading to the total number of hits during the whole period period. Since the number of hits would not be able to differentiate between weak and strong hits, the first method was then modified by considering signal strength instead of number of hits in the last method.

2.10. AE Applicable Parameters

In the following sections the most useful AE parameters will be discussed.

2.10.1. AE Energy Parameter Analysis

Elastic energy released through an AE event is identified as AE energy. AE energy is regarded as the area under the purified AE signal. Occurring AE events cause the generation and propagation of elastic waves in all directions through the surface. The root mean square values of AE signals have been used by some researchers.

The relation between the energy of the signal received at transducer and the released strain energy can be influenced through a variety of factors such as the distance from the source, attenuation due to the material medium, and the coupling medium (Salinas et al., 2010; Labuz et al., 1988; Köppel and Grosse, 2000).

AE energy (MARSE) is defined as follows (Miller and McIntire, 1987):

$$E_i = \int_{t_0}^{t_1} V_i^2(t) dt \quad (2.1)$$

where V_i is the voltage transient of an i_{th} channel, t_0 and t_1 are the start and end times of the voltage transient record, respectively. Aldahdooh et al. (2012) used energy counts as the values given to the energy by the testing equipment.

It is noteworthy that when the term energy is discussed in AE, it is commonly referring to Measured Area of the Rectified Signal Envelope (a measurement of the area under envelope of the rectified linear voltage time signal from the sensor, as mentioned in Equation 2.1). This quantity is preferred over counts because it is sensitive to both amplitude and duration. It is also less sensitive to operating frequency and threshold setting. MARSE is well suited for specifying the overall cumulative acoustic emissions activity.

On the other hand, the term energy might sometimes refer to the energy contained in a detected acoustic emission burst signal, with units usually reported in joules and values which can be expressed in logarithmic form (dB, decibels). The energy is defined as:

$$E = \frac{1}{2} \int_{t_1}^{t_2} f^2 + (t) dt + \frac{1}{2} \int_{t_1}^{t_2} f^2 - (t) dt \quad (2.2)$$

where

f_+ = positive signal envelope function

f_- = negative signal envelope function

t_1 = time at first threshold crossing

t_2 = time at last threshold crossing

The AE energy can be applied to verify both fresh and hardened concrete properties. AE sensor should be attached directly to the outer surface of the concrete mixer body to evaluate the coherence of fresh concrete through AE measurement.

2.10.2. AE Signals Amplitude

One of the most significant AE parameters applied by researchers to evaluate structural damage is AE signal Amplitude. Damage in concrete can be assessed by b-value which is an important parameter. This parameter (b-value) calculates amplitude distribution data following the same methods used in seismology (Ohtsu, 1996; Farhidzadeh, et al., 2012; Pollock, 1981; Rao and Lakshmi, 2005).

2.10.3. AE Hit Application in Crack Monitoring

AE has shown a high potential in the monitoring of cracks ranging from nucleation phases of micro cracking in concrete structures to macro-crack opening stage. AE monitoring was applied on reinforcement concrete by Yoon et al. (2000) to assess the defects of steel reinforcement corrosion. Figure 2.5 shows a plot of cumulative hits versus time under cyclic load.

Observation from the Figure 2.5 shows that by increasing the degree of corrosion, AE counts decrease. Determination of deterioration level due to corrosion in RC beams can be accomplished through AE testing (Yoon et al., 2000).

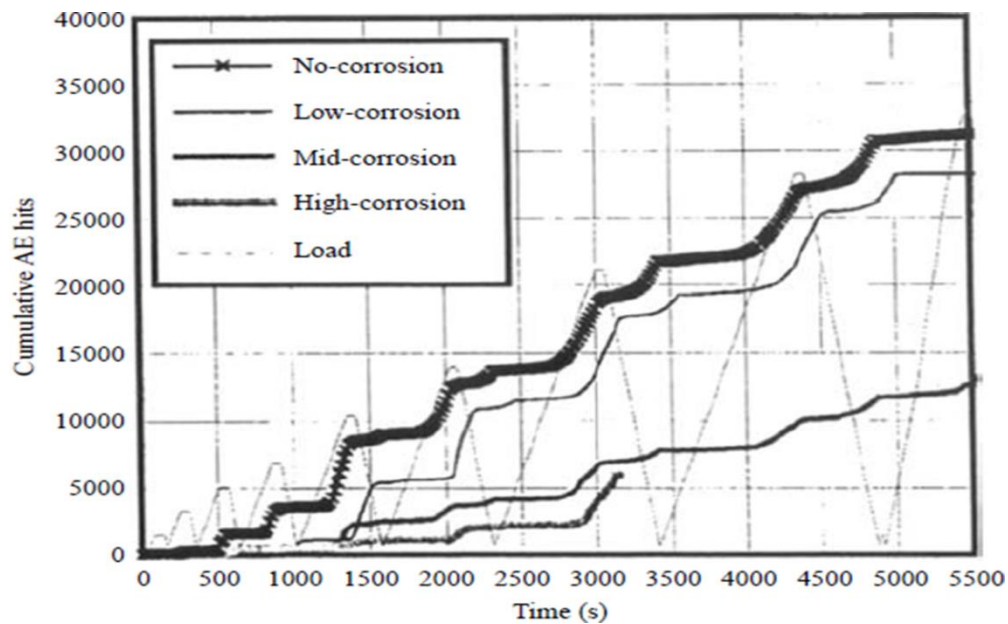


Figure 2.5: Cumulative AE hits versus time for RC beams (Yoon et al., 2000)

Formation of micro and macro cracks is described by Rao et al. (2009) correlating AE hit rate and stress level on quasi-brittle materials. In this study it was concluded that due to crack nucleation, AE activity increases slowly and steadily. Yoon et al. (2000) used AE hits to assess RC beams under cyclic load. Through his observation a variety of AE hits with different percentages have been recorded during the test.

The AE hit can be applied in other assessments of concrete structures including fracture tests. Valuable information can be obtained by measuring different fracture parameters such as CMOD or CTOD versus AE hits.

2.10.4. AE Count Application in Concrete Monitoring

Count Rate is defined as the set of times, within duration, when one signal exceeds a present threshold (Miller and McIntire, 1987). AE count rate reflects the intensity of the AE event.

The condition of increase in AE activity should be taken as an initial concern while the other types of parameters should be included for quantitative damage analysis, since AE hit or count rate itself may not provide conclusive information of signal strength to assess the damage level quantitatively (Ohtsu et al., 2002). However, observations have shown that AE count rate increases exponentially in an under-reinforced beam due to sliding between reinforcement and concrete. On the other hand, in an over-reinforced beam, AE count rate remains constant until final failure (Ohtsu et al., 2002). Thus, it was established that AE count is also a significant parameter.

Count measurement can be also a suitable approach when it is used in conjunction with the other AE parameters during the deterioration process of concrete structures. Figure 2.6 shows amplitude distributions recorded for reinforced concrete beams under bending.

These beams were deteriorated by a given load level of cyclic loading. The beam was statically loaded up to the service-load limit after a particular loading cycle, and AE counts were measured. The beam was frequently loaded at 85% static load bearing capacity until final failure. After several cycles of loading, amplitude distributions of AE signals were measured under monotonous loading.

With the increase in loading cycles, amplitude distributions shift to a different distribution where AE signals of the larger amplitudes are dominant (Grosse and Ohtsu, 2008).

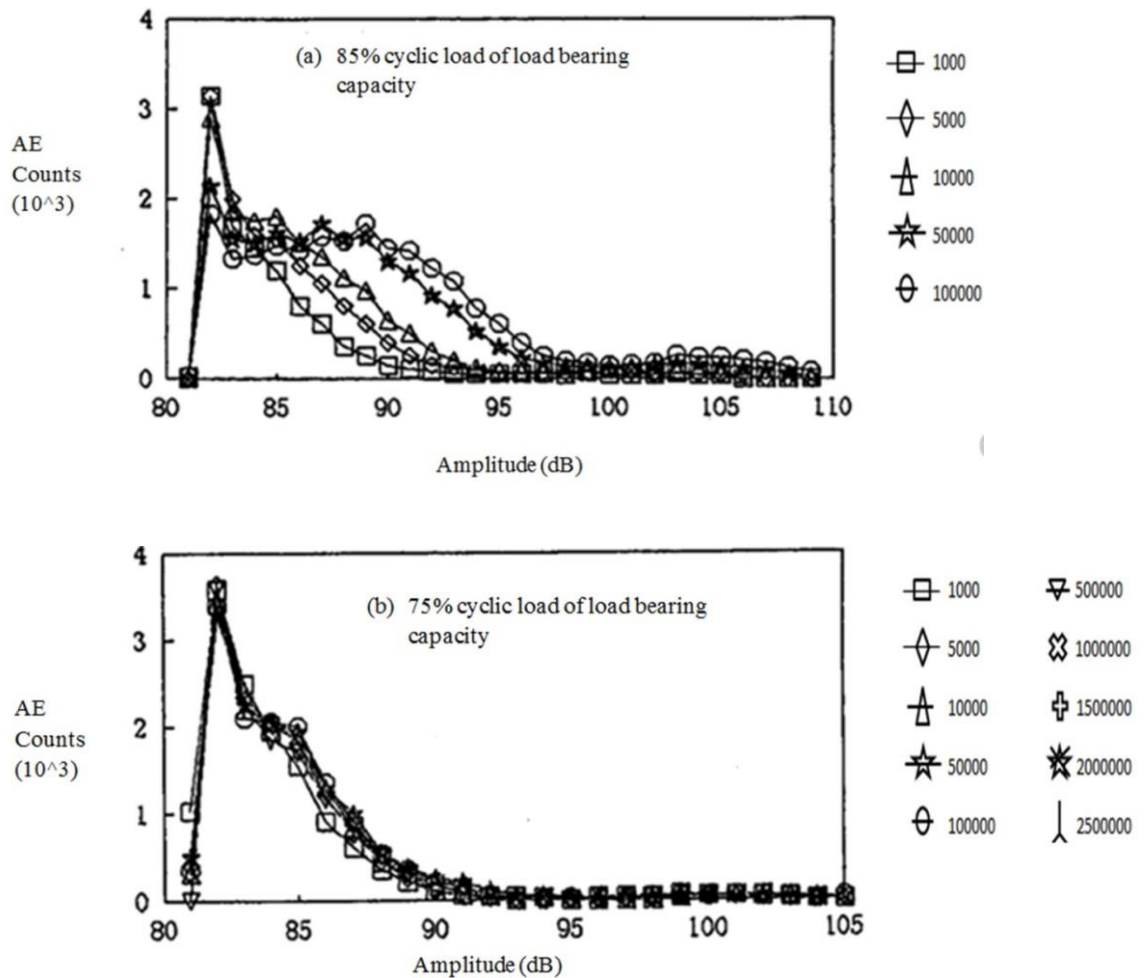


Figure 2.6: AE amplitude distributions in reinforced concrete beams under cyclic loading (Grosse and Ohtsu, 2008)

Conversely, no change of the amplitude distribution was observed in the beam which was frequently loaded at only 75% until 2,500,000 cycles (Figure 2.6b). It should be noted that the beam did not break at any point during the testing. Hence, this may suggest that amplitude distribution might be applied to usual inspection, investigating the variation of the distribution without imposing serious damage to the structure.

Moreover, the amplitude distribution is possible to be quantitatively computed from the gradient of the slope to quantify the damage level. This gradient of the slope in amplitude distribution is called b value (Grosse and Ohtsu, 2008).

2.10.5. b-value Analysis to Assess the Damage Severity

The b-value is a well-known macro and micro structural crack identification method. Drawing on the basics of seismology, it is defined as the negative gradient of the log-linear plot of earthquake frequency magnitude (Grosse and Ohtsu, 2008). Many studies were carried out to relate the b-value with the strains in concrete and steel at different stages of damage and loading. Gutenberg–Richter has defined the relationship between magnitude and frequency as below:

$$\log_{10}N(M) = a - b \left[\frac{A_{db}}{20} \right] \quad (2.3)$$

in which A_{db} is the peak amplitude of the AE events in decibels, b_{AE} is AE-based b-value and $N(M)$ is the number of AE hits (or events) of magnitude $\geq M$.

Many researches regarding diagnosis of concrete and masonry structures by b-value analysis have been accomplished (Carpinteri and Lacidogna, 2007; Carpinteri et al., 2006). It was stated by Colombo et al. (2003) that larger b-values represent the stage of micro crack occurrence and vice versa. They also proposed that since b-value originates from seismology, its application in engineering material will be problematic. Hence, the improved b-value was introduced.

2.10.6. Improved b-value Analysis

The calculation of Ib-value is based on the slope of the peak amplitude distribution of AE signals. The statistical values of amplitude distribution of acoustic emission are considered in the calculation of Ib-value since during experiments it was observed that the AE amplitude values vary with time (Shiotani and Ohtsu, 1999). The Ib-value is given in equation below.

$$Ib = \frac{\log_{10}N(\mu-\alpha_1\sigma)-\log_{10}N(\mu+\alpha_2\sigma)}{(\alpha_1+\alpha_2)\sigma} \quad (2.4)$$

where μ is the mean amplitude, σ is the standard deviation and α_1 and α_2 are user-defined constants which would represent coefficients of lower and upper limits of the amplitude range to yield a proper straight line.

Shiotani, Yuyama et al. (2000) studied the damage quantification for concrete structures by Ib-value analysis. The differences in monitoring conditions in each application sometimes lead to non-quantitative results.

The Ib-value is known to be unaffected by monitoring conditions, and it uniquely varies depending on the damage level.

Shiotani et al. studied the Ib-value to quantify the damage in concrete piers due to an earthquake (Shiotani et al., 2001). The calculated Ib-value based on the AE events located within the pier was obtained and as a result, the damage degree was quantified by the Ib-value.

2.10.7. Sifted b-value Analysis

Sifted b-value is a method developed by Farhidzadeh et al. (2012) to monitor and assess the damage in concrete structures. In the suggested algorithm, the information about crack evaluation and structural integrity is provided through correlation between b-value analysis and cluster analysis.

The flow chart in Figure 2.7 illustrates the Sb-value analysis algorithm. The steps can be explained as: 1) Sieve crack modes by systematic AE clustering (i.e., k-means); 2) calculate the b-values for each cluster; 3) apply Gaussian filtering to highlight the micro to macro transition stage for each crack mode. It should be mentioned that the authors later developed their method using a Bayesian-based probabilistic approach, Gaussian Mixture Modelling (Farhidzadeh et al., 2013).

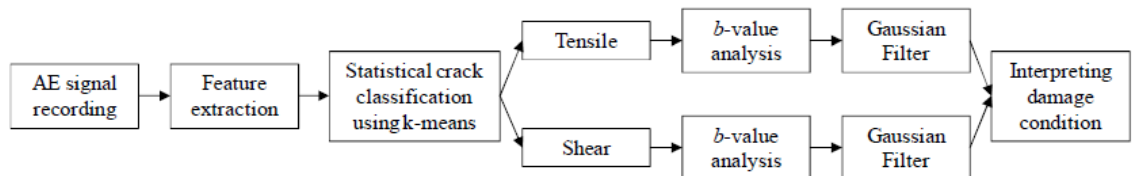


Figure 2.7: Algorithm of Sb -value analysis (Farhidzadeh et al., 2012)

2.10.8. Minimum b-value Approach in Bridges

To monitor in-service bridges, a method was used to inspect and quantify the influence of a passing vehicle on a monitored bridge component or section. This method was named minimum b-value (Schumacher et al., 2011).

As explained before, reductions in the b-value may indicate the macro crack occurrence. Such information may be used in conjunction with knowledge about the applied loading, that is, passing vehicles (ambient or test trucks) to help in estimating the current operating load level of a bridge component along with some information about the past lifetime loading history. The minimum b-value is determined by following these steps:

- (1) Determine lowest b-values from one complete load event for each of the AE sensors (defined by the TT load effect)

(2) Compute sensor network mean and standard deviation for all values obtained from step 1.

For repeated load events of the same magnitude, minimum b-values are determined over all cycles, for example, if there are three load cycles and eight sensors, the mean and standard deviation are taken over 24 estimated b-values. Figure 2.8 illustrates two examples of applied loads in the laboratory.

Figures 2.8a & 2.8b show an applied OL (load that exceeds all maximum previous experienced loads) and a service-level load (load to be expected under everyday conditions), respectively. The b-values are shown with dashed lines and the total applied force is highlighted through a solid line with diamonds. For example, the minimum b-values (and standard deviation) were 0.55 (0.06) and 1.33 (0.31) for the OL and the simulated test truck (TT), respectively.

The approach presented in this article intends to give an averaged representation of ongoing deterioration from within a region or section of interest, for example, an existing crack or a cracked region.

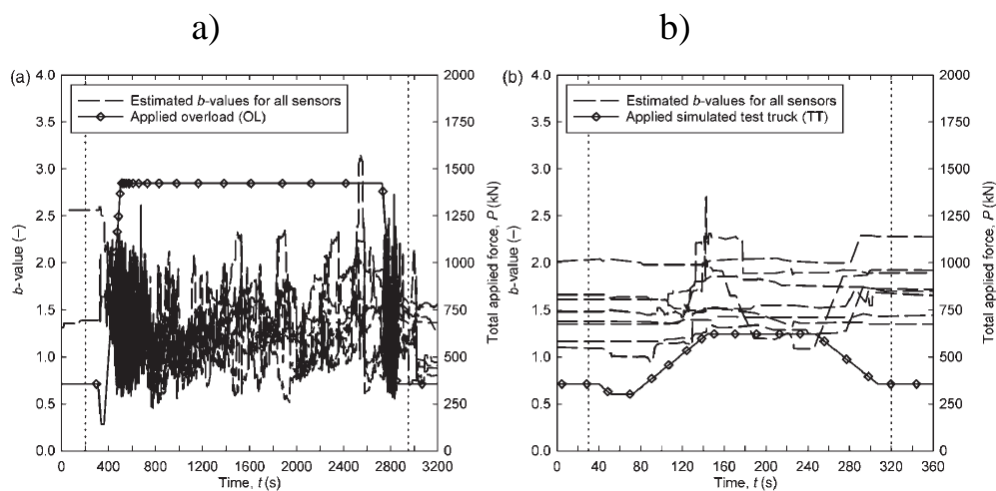


Figure 2.8: Examples of continuous b-values for an overload: a) and a simulated test truck, b) over the course of one complete load cycle (Schumacher et al., 2011)

2.11. AE Application in Global and Local Monitoring

Infrastructure, specifically deteriorated areas which need more accurate investigation, could be monitored with sparsely arrayed AE sensors with low frequency. An appropriate type of AE sensor which depends on specific requirements can be applied to the objective area to provide high resolution monitoring. AE monitoring was applied on large bridges (Shiotani, 2012) and preliminary observations showed little deterioration in a 45-m bridge span by both surface-crack observation and physical tests of excavated cores.

Sensors were placed in a linear arrangement spaced 1.5 m apart over a 45 m span in a longitudinal direction in order to assess the damaged area for the longitudinal structure. Detailed investigations were applied on those parts of the structure that were suspected of higher damage levels based on AE activity, and parts which had no AE activity ended up in the first monitoring. In the first case, the area with active AE was measured once more with a denser sensor array in 2D. The P-wave velocity was investigated by applying a surface ultrasonic examination on the area of interest. The characteristic of low velocity zone was developed due to application of velocity tomogram.

The low velocity zone might be recognized as a subsurface defect, although it is quite difficult to determine the depth.

It can be concluded that concrete cracks, delamination of different layers (e.g. asphalt on concrete) or friction between the tendon ducts and matrix concrete are the possible origins of inducing AE activity due to loading, considering the fact that the AE events were generated in an extremely low velocity zone. It is observed that this sequential investigation started with global AE monitoring, then local AE monitoring, followed by detailed measurements of ultrasonic P wave velocity. The conclusion could be that sequential investigation for larger scale beams with different material properties may be required in order to characterize the quality of large-scale concrete structures.

2.12. Recent Trends and Modern AE Research

A brief description on the recent researches considering possible applications of AE in concrete structures will be given in the following subsections.

2.12.1. AE Application in Monitoring Corrosion

Reinforced concrete beams were monitored to study corrosion of reinforcing steel by AE testing (Mangual et al., 2013; Kawasaki et al., 2013; Elfergani et al. 2013; Calabrese et al., 2013b). During the observation it was concluded that the degree of corrosion of reinforcing steel had an enormous influence on the rate of AE events and trend of AE activity generation. In other words, the total count of AE events decreases with an increase in the degree of corrosion. Therefore, the level of deterioration of RC structures could be evaluated for corrosion. The relationship between AE activity and half-cell potential results was studied experimentally.

An acoustic emission (AE) technique was also used to detect and locate corrosion induced failure in pre-stress concrete bridges (Yuyama et al., 2007). It was found that steel wire and bar failures produce significant AE signals with extremely high amplitudes.

Moreover, active corrosion could be localized successfully through experimental characterization of wave speed. The results showed that AE is a functional, nonintrusive technique to detect and quantify the corrosion damage. AE may be developed as a structural prognostic tool for maintenance prioritization (Mangual et al., 2013). In addition, there are copious studies which successfully studied different aspects of corrosion analysis by aid of AE for pre-stress and SCC structures.

These studies investigated detection of triggering time of corrosion, early corrosion detection, and univariate and multivariate statistical analysis during long term acoustic emission monitoring to identify corrosion mechanisms on a pre-stressed concrete beam and post-tensioned steel strands (Kawasaki et al., 2013; Elfergani et al., 2013).

2.12.2. Fatigue Analysis by Acoustic Emission Technique

One of the popular subjects in the field of AE application is fatigue analysis and life span prediction. There are many researchers who have contributed to develop different aspects of fatigue analysis by means of AE instrumentation (Shah et al., 2012; Shah and Kishen, 2010; Benavent et al., 2010; Benavent et al., 2009; Wang et al., 2010; Antonaci et al., 2011; Sagar, 2011). For instance, by comparison of the results of laboratory and experimental studies it was shown that by understanding the relation between the loading phase and AE activity, the final stages of the fracture process can be evaluated by detecting AE signals generated near the minimum loading phase (Yuyama et al., 2001). In another study, it could be seen that AE evaluation criterion of peak CSS ratio could provide information on safety margins of residual strength of a structure and results were compared to the traditional method (CLT method). AE technique demonstrated an even better performance than CLT method (Ridge and Ziehl, 2006). In addition, the ability of AE to assess low-cycle fatigue loading was investigated by Benavent et al. (2009). They assessed the damage in RC exterior beam-column sub assemblages. Observations proved that when plastic deformations exist in steel reinforcement, AE activity increases. By making use of AE improved b-value, it was showed that macroscopic fracture processes generally occur during the loadings paths.

2.12.3. Monitoring by AE During Simple Bending

Ohtsu et al. (1999) applied acoustic emission and the boundary element method (BEM) during study of crack extension of mixed-mode in concrete. The crack extension of mixed-mode failure was studied in bending tests of notched concrete beams.

However, application of AE was recognized as a powerful method to analyse the bending behavior of normal and FRC beams. Extensive information on the time, location, and nature of progressive damage were provided for normal and fiber reinforced concrete by incorporation of AE data into mechanical test results (Soulioti et al., 2009; Finck and Manthei, 2002; Momoki et al. 2009).

On the other hand, by aid of AE and simple bending test method (with or without notch) the characteristics of concrete material have been investigated. Signals generated from the deformation or fracture of materials under external loading were analysed to study and determine the damage process in concrete structures (Dai et al., 2012; Sagar, 2011), ductility and mechanical properties of concrete specimens (Nair and Cai, 2010; Rossi et al., 1990; Haneef et al., 2013; Aggelis et al., 2012d), characterization of corrosion (Mangual et al., 2013; Kawasaki et al., 2013), fatigue and fracture analysis (Shah et al., 2012; Benavent et al., 2010; Wang et al., 2010; Antonaci et al., 2011; Yuyama et al., 2001), classification of failure modes (Ohtsu et al., 1999), behavior of strengthened concrete beams by FRP like material (Ridge and Ziehl, 2006; Degala, 2008; Degala et al., 2009; ElBatanouny et al., 2014; Chen and Liu, 2008; Carpinteri et al. 2007b), bending strength of concrete and SFRC and PFRC specimens (Uppal et al., 2002; Holford et al., 1999; Pullin et al., 1999; Pullin et al., 2008; Nair and Cai, 2010; Finck, 2002; Aggelis et al., 2008) and fire resistance during explosive spalling in high-strength concrete at high temperature (Ozawa et al., 2012).

2.12.4. Creep Defect Analysis by Acoustic Emission Technique

The Acoustic Emission (AE) technique was used in order to investigate creep effects and micro cracking phenomena. Carpinteri et al. (2007a) suggested an analogy between the snap-back instability of the FRP delamination and that occurring during fault growth regarding the self-similarity of the AE phenomenon and seismicity. Rossi et al. (2012) conducted a case study concerning an investigation of the physical mechanisms of basic creep behavior of concrete by applying acoustic emission. It was found that micro-cracks created during creep step generate water transfer which causes some additional self-drying shrinkage.

CHAPTER 3

EXPERIMENTAL PROGRAM

3.1. Introduction

This chapter introduces the properties of materials and their preparation prior to casting, mixture proportioning, and test methods which were used toward accomplishing the current research.

As stated in Chapter 1, this research was carried out to obtain various objectives so that there were specific testing schemes to obtain objectives of this research. As a result, four independent experiments were conducted which will be presented in this chapter, respectively.

3.2. General Material Properties

The main material properties used in this research will be briefed in the following sections.

3.2.1. Cement and Water

For all types of concrete in this research, the mix proportions were prepared by ASTM Type I cement of 350-500 kg/m³. The specific gravity of the used cement was 3.14 g/cm³. In addition, this cement Blaine's specific surface area was 2400 cm²/g. The physical and chemical properties tables of cement used in this research were presented in appendix. It was found that based on the tests results the cement properties conformed to the British standards for ordinary Portland cement.

3.2.2. Mixing Water

Water used in this research was portable water free from chemical contaminants and impurities.

3.2.3. Aggregates

Aggregates used in this research were mainly normal coarse aggregate (gravel) and fine aggregates (sand). Due to important role of aggregates and their properties in the mix design, required tests related to aggregate properties according to the code of practices were carried out so that it can be assured that they comply with the standards definitions.

3.2.3.1. Fine Aggregates (Sand)

Local sand was used as fine aggregates in these experiments. The obtained sand was sieved at sieve size (4.75 mm) dispose coarse aggregates. The sand was then washed and cleaned by water several times, thereafter the clean sands were spread out and left to dry in the air, after which it was ready to be used in concrete mixture. The grading of sand was evaluated through sieve analysis so that it could be assured the grading would conform to the standard codes of practices.

Table 3.3 shows the results of the sieve analysis and it was found that the grading of fine aggregates was in the range of Malaysian Specification (MS 30 Part 4: 1995) for Particle Size Distribution (Sieving Method). Physical and chemical properties of fine aggregates are presented in Table Physical and chemical properties of fine aggregates are presented in appendix.

3.2.3.2. Normal Gravel

Concrete mixtures used in this study utilize crushed granite (excluding mortar mixtures) as normal coarse aggregate with the maximum size of 10 to 12 mm.

3.2.4. Fly ash

It is imperative to enhance the amount of pastry in the SCM because it is an agent that carries the aggregates, especially when the rubber tires powder is added in the mortar. To achieve this, FA was used in those cases where the rubber powder was added to the SCC mortar. Low calcium FA (class F) used in this research was supplied by Lafarge Malayan Cement Bhd, Malaysia.

3.2.5. Rubber

The locally provided tire rubber particles, with 200 μm average particle size and density of $1.152 \pm 0.001 \text{ g.cm}^{-3}$ have been used in the RSCM mixtures. The chemical composition and physical properties of rubber is presented in appendix.

3.3. Torsional Fracture Test

This set of experiment was carried out toward obtaining objectives introduced in chapter1. This experiment is used for analysis of sections 4.2 and 4.4. To this end, the following specimens were prepared.

3.3.1. Mechanical Properties and Torsion Tests

Seven types of specimens were prepared by varying water-to-cement ratio (W/C) and steel fiber volume fraction (FVF) in concrete. Table 3.1 shows the details and physical properties of specimens. Each type consisted of two specimens for testing. The specimens have uniform cross section of 100mm x 100mm and length of 500 mm. In all cases, mix design was in accordance with ASTM standards which used ordinary Portland cement and coarse aggregates with a maximum size of 10 mm.

The target compressive strength at 28 days for #2 was opted to 38Mpa. The ratio of coarse aggregates to fine aggregates was 60/40.

The steel fibers used were of type CHO80/60NB, which were 60 mm long with diameter of 0.75 mm (Figure3.1).After demolding, the specimens were placed into a water tank inside the laboratory for curing up to 28 days.

Figure3.2 shows the testing condition and AE sensors placement scheme. This research used a GT-704-C (from Gotech Testing Machines Inc.) torsion testing machine and the twist angle rate was kept constant within the tests at the rate of 0.5 degree/min.

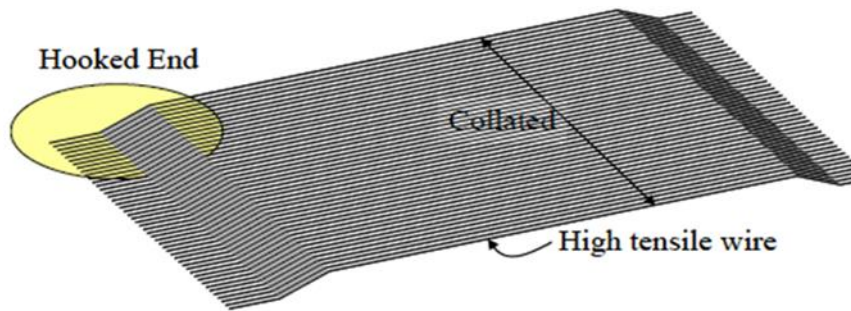


Figure 3.1: CHO80/60NB collated steel fiber hooked end

Table 3.1: Concrete specimen's specification

Specimen	W/C	FVF%	$f_{cu}(MPa)$	*E(GPa)	*G(GPa)
#1	0.45	0	60.3	42.2	16.23
#2	0.55	0	38.8	30.9	11.88
#3	0.65	0	26.81	21.3	8.19
#4	0.55	0.5	44.42	31.5	12.11
#5	0.55	1	48.8	32.6	12.4
#6	0.65	1	36.9	30.6	11.77
#7	0.55	2	51.3	39.3	15.16

*E: Modulus of Elasticity

*G: Shear Modulus

*FVF: Fiber volume fraction

* f_{cu} : 28-day Compressive strength



Figure 3.2: Torsion tests on concrete beams and AE sensor placement

3.3.2. Acoustic Emission System and Measurements

The AE measurement system (by Mistras Group Inc) consisted of PCI-2 data acquisition boards that accommodate six AE sensors and a windows-based AE data operation program known as AEwin. The AE sensors used have a resonant excitation frequency of 60 kHz (R6I). In the measurements, the sampling rate was set to 2 MHz, with the pre trigger was set as 250.000 μ s. The hit definition time (HDT), hit lockout time (HLT), and wave velocity were configured as 2000 μ s , 300 μ s and 3900 m/s, respectively. To eliminate electrical and mechanical noise, the threshold level was set at 50 dB.

3.4. Large Scale Multi-cells Girders Subjected to Pure Torsion

This set of experiment was carried out to obtain the fourth objective introduced in the chapter1. This experiment is used for analysis of sections 4.3. To this end, the following specimens were prepared.

3.4.1. Tests and Procedures

This experimental program was conducted to monitor damage evolution in large scale multi-cells girders box up to ultimate torsional capacity.

The experimental task dealt with testing, under pure torsion, different classes of hollow box girders, extensively instrumented with focus on torsion behavior. There are three classes of girders which include single, double, and triple boxes. Figure 3.3 shows the geometries and reinforcement details of the specimens. All the specimens have a uniform length of 3000 mm and accommodated single (SC), double (DC) and triple (TC) box cells, respectively.

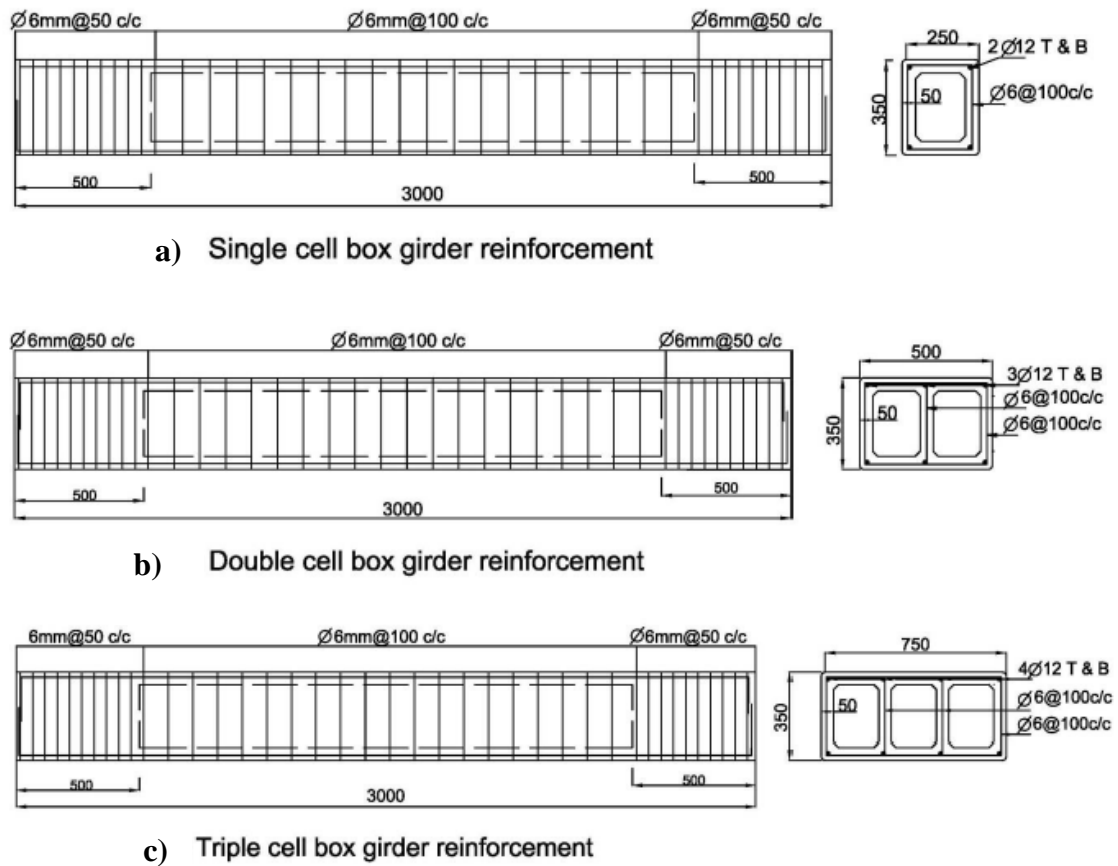


Figure 3.3: Geometrical detail and reinforcement of girder specimens: a) Single cell box, b) Double cell box, c) Triple cell box

In RC beams subjected to torsion, cover spalling occurs due to excessive axial thrust on concrete at regions close to beam edges. In order to prevent cover spalling the thickness of the concrete cover should not exceed 30% of A_c/P_c , where A_c and P_c are the area and perimeter of concrete cross section, respectively (MacGregor and Ghoneim, 1995). Therefore all the reinforced specimens prepared with constant concrete cover of 20mm. The cell wall thickness was fixed at 50 mm, which fulfilled the requirement in resisting axial thrust using the Modified Softened Truss Model Theory (MSTMT). The wall interior corners were provided with haunches for increased stiffness. In order to apply torque at the end of the specimen, the cross section of the ends was prepared as solid (fully-filled) rectangular with length of 500 mm.

This configuration resembled the fixed connection of the practical support condition, with which the girders were supported rigidly at the ends by columns and transverse beams. In order to obtain the hollow section inside the specimens, polystyrene blocks were placed into the specimen mould before casting with their edges were sliced accordingly to provide interior hunches of 30mm long at four corners of each cell cross section. After demolding the specimens were covered with dampen sponge sheets and cured for 28 days.

Table 3.2 gives the mix proportion of the concrete used. Concrete with a designed 28-day compressive strength of 40 MPa was used preparing all the specimens. The mix design complied with (BS 5328:1997) specifications which adopted ordinary Portland cement and coarse aggregates with maximum size of 10 mm. Ready mix concrete with designed compressive strength of 40MPa were used for all beams.

The steel bars used, on the other hand, were of type hot roll deformed bars which gave characteristic strengths of 460 N/mm², and 250 N/mm², for main bars and shear links, respectively.

Table 3.2: Mix proportion of concrete

Material	Fine aggregate (kg/m ³)	Coarse aggregate (kg/m ³)	W/C ratio	Super plasticizer, R1100 (litre/m ³)	Water reducer, P218R (litre/m ³)
	890	800	0.42	3.6	1.0

3.4.2. Steel reinforcement bars

For all beams, two sizes of steel reinforcing bars were used. Deformed Bars of size (ϕ 12 mm) were used as longitudinal reinforcement and plain bars of size (ϕ 6 mm) were used as closed stirrups.

Values for yield and ultimate strength for each bar are given in Table 3.3 Results are compatible with the British Standard BS-4449 1997. Figure3.3 illustrates the tensile test system for steel reinforcements.

Table 3.3: Reinforcing steel properties

Bar size (mm)	Yield strength (MPa)	Yield strain	Ultimate strength (MPa)	Ultimate strain
12	605.5	0.0026	663.5	0.198
6	402	0.0024	550.3	0.184

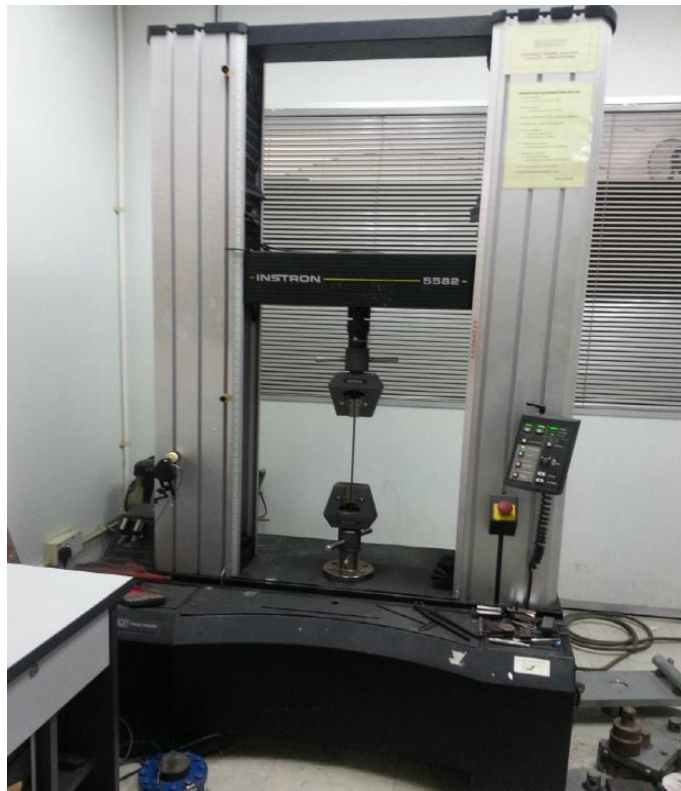


Figure 3.4: Steel tensile reinforcement test

3.4.3. Molding and Casting

For casting purpose the wooden molds were prepared. To obtain a measurement of the compressive strength of concrete, eight standard cubes of 150X150X150 mm were used. Four standard cylinders of 100mm diameter by 200 mm height to test the splitting tensile test, for rupture test four standard prisms of 100X100X500 mm were used. In order to get the modulus of elasticity of concrete, four standard cylinders of 150mm diameter and 300 mm height were cast from the same concrete batch used for specimens. Concrete was poured in the molds in two layers, and each layer was compacted using electrical handle vibrator. The tested molds were filled with concrete into three equal layers. Each layer was vibrated on a table vibrator of (3000 vibrations per minutes) for 30 seconds. The upper surface of concrete was smoothly finished half-hour after casting was completed using hand trowel.

All specimens were left in the laboratory until they were de-molded after 24 hours, and then covered with sponge sheets and place water daily for 28 days.

For the standard molds, they were open after 24 hours of casting and placed in tap water until the date of test; after 7 days of casting and after 28 days of casting (Figures 3.5 and 3.6).



Figure 3.5: Molds, polystyrene and reinforcement cages overview



Figure 3.6: Specimen casting overview

After demolding sample specimens the results of mechanical properties of concrete specimens were obtained that is presented in Table 3.4.

Table 3.4: Mechanical properties of concrete specimens

Day	Compressive strength (MPa)	Splitting tensile strength (MPa)	Modulus of Elasticity (MPa)	Rupture Strength (MPa)
7-day	33.72	2.34	27466	4.65
28-day	45.06	2.72	31750	4.86

3.4.4. Torsion Test Procedure

Loading was conducted by a hydraulic actuator setup as shown in Figure 3.7. A load cell with 450 kN capacity (Interface 1232 AJ-4550kN-B) was connected to the actuator to measure loading values. The specimens were simply supported by steel rollers with clear span of 2000 mm. Two specially fabricated steel frames with rotating hinges were fixed to both ends of specimens to provide rigid grips.

The vertical load applied to the center of a steel spreader beam would be transferred to the steel frame and specimen ends, causing rotation of steel frames about the hinges and induce torsion loading to the specimens. The specimens were tested under monotonically increased torque up to failure. The lateral displacements were measured using LVDTs (Liner Variable Differentiable Transformers). The angle of twist was calculated based on measurements of two installed LVDTs at the top and bottom of the specimen. The specimen elongation was found using two LVDTs fixed at center of specimen cross section at both ends.

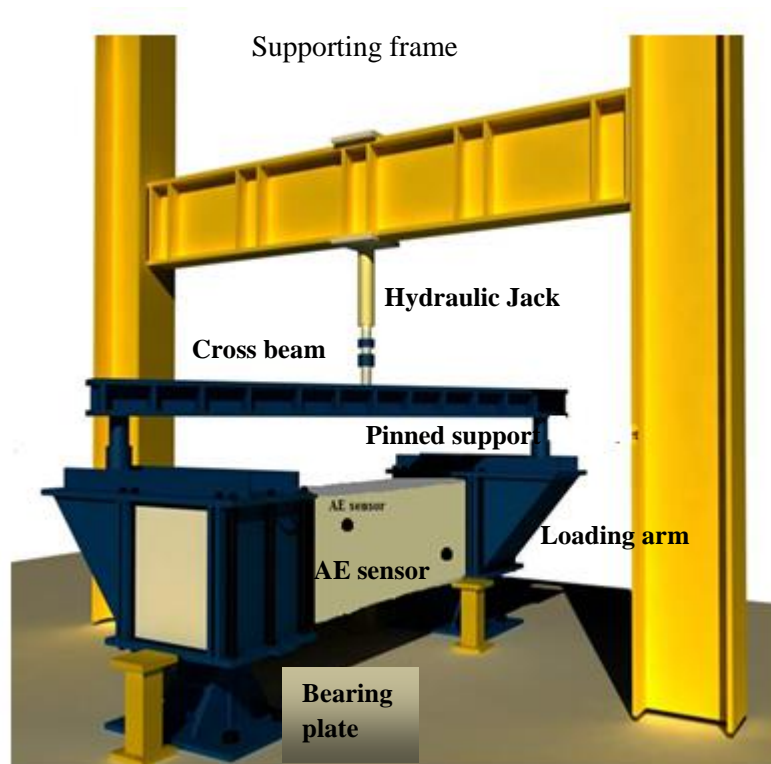


Figure 3.7: Torsion testing system loading and instrumentation

3.4.5. AE Monitoring and Instrumentation

The AE measurement system used in this experiment and its instrumentation is set as previous experiment procedures as presented in section 3.3.2 with a change in the threshold level which was set at 45 dB.

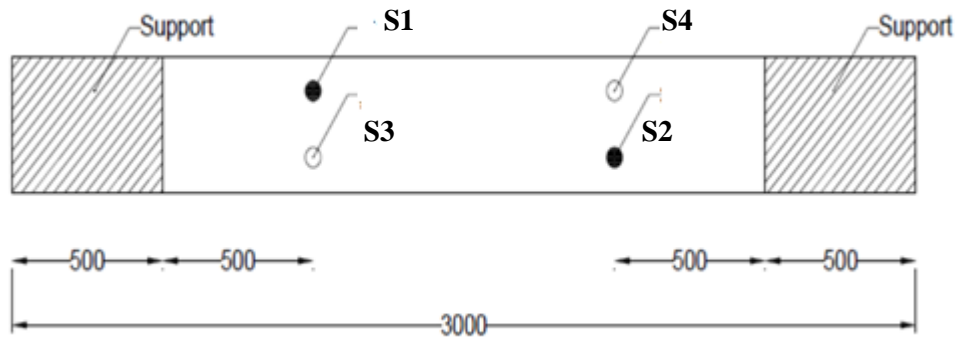


Figure 3.8: the arrangement of AE sensors mounted on surface of two sides of girders

3.5. AE Monitoring of Ferrocement Composite Slabs

This set of experiment was carried out to obtain the fourth objective introduced in the chapter1. This experiment is used for analysis of sections 4.5 and 4.6. To this end, the following specimens were prepared

3.5.1. Experimental Program

Locally sourced ASTM Type I Portland Cement (PC) was used as the key binder material. Locally available river sand with grading in accordance with the limit values specified by BS 882 (1992) was used as aggregate for the mortar mixes.

The river sand was washed prior to mixing to remove its natural silt and clay in the raw stock pile. The mixed design used for this study is presented in Table 3.5.

It can be noted that four different types of mortar were prepared for this study; normal cement mortar (NM), self-compact (SC), and rubberized self-compact (SCR) mortar. During the fabrication of fresh SCC, all aggregates were firstly mixed in dry state. Next, fly ash (FA) and cement were added. After a homogeneous dry mixture was prepared, 80% of mixture water by volume was added to the mixture. Before, chemical admixture was dissolved in the rest of the mixing water and this solution was included to the mixture. Mixing process was until the mixture was consistent in self-compatibility. This duration has been continued not less than 3 min.

A total of four, six, and eight layers of welded galvanized steel square mesh with a wire diameter of 1 mm and spacing of 13 mm were provided as internal reinforcement for each fabricated ferrocement slab. The mesh was tested in the laboratory according to the design guide on construction and repair of ferrocement reported by the ACI committee 549 (1993). The yield strength of the wire mesh was determined to be 300 MPa and the average ultimate strength of the wire mesh was found to be 335 MPa.

Table 3.5: Proportion of constituent materials and rheological properties of mortar mixes and slabs

Series	Cement	Sand	W/C ratio	Fly ash (FA) (%)	Super plasticizer (%)	Rubber Powder (%)	Wire Mesh Layers	Specific surface cm ² /cm ³	Type of Mortars
NM4	1	1.5	0.35	0	0	0	4	0.7112	NM
NM6	1	1.5	0.35	0	0	0	6	1.0668	NM
NM8	1	1.5	0.35	0	0	0	8	1.4224	NM
SCL4R0	1	1.5	0.35	20	1	0	6	0.7112	SC
SCL6R0	1	1.5	0.35	20	1	0	6	1.0668	SC
SCL8R0	1	1.5	0.35	20	1	0	8	1.4224	SC
SCL4R5	1	1.5	0.35	20	1.1	5	4	0.7112	SC
SCL6R5	1	1.5	0.35	20	1.1	5	6	1.0668	SCR
SCL8R5	1	1.5	0.35	20	1.1	5	8	1.4224	SCR
SCL4R10	1	1.5	0.35	20	1.5	10	4	0.7112	SCR
SCL6R10	1	1.5	0.35	20	1.5	10	6	1.0668	SCR
SCL8R10	1	1.5	0.35	20	1.5	10	8	1.4224	SCR

SCM mortar: Self-compacted mortar

RSCM mortar: Rubberize self-compacted mortar

For the slab specimens, steel moulds having top and bottom faces opened were used, which have dimensions of 500 mm*500 mm* 30 mm. For each specimen initially, a thin layer of mortar was poured to achieve the desired cover thickness before the chicken wire mesh layers were positioned in the slab over the mortar layer.

The mortar has been evenly spread into the reinforcement cage by trowels for full penetration through the wire mesh layers. In the last step, to ensure the smooth top surface, finishing step was performed on the top by levelling a thin layer of mortar, the specimens were left for 24 hours to set after casting. The testing machine and schematic detail of the test procedure is given in Figure 3.9. A total of twelve slab specimens were prepared, with variations given in Table 3.5.

For each type of mortar, three different specimens by varying the number of mesh layers in four, six, and eight layers. To study the behavior of different specimens, a concentrated monotonic loading through a steel disc was applied on the center of specimens.

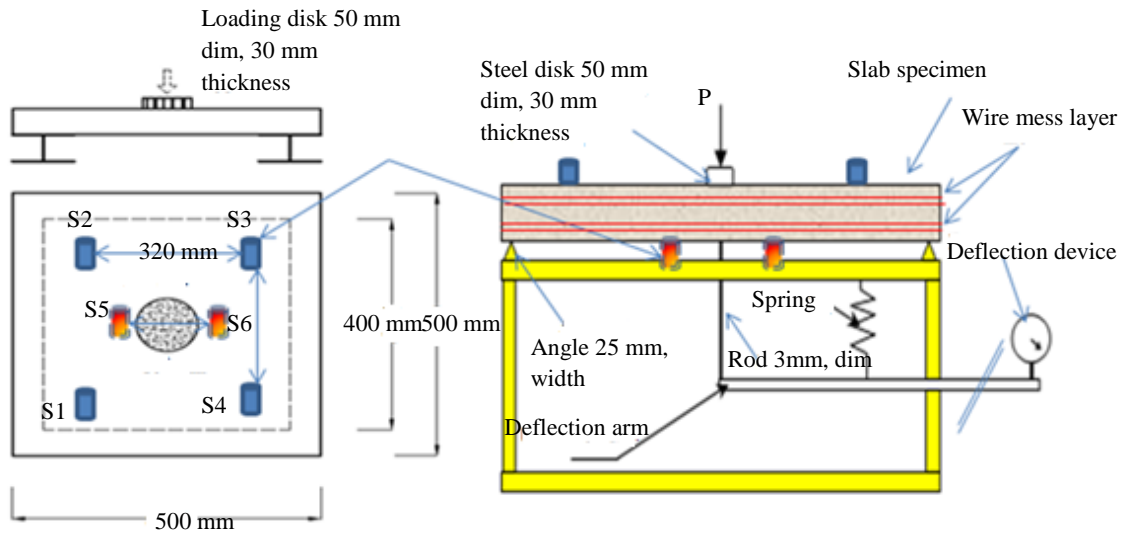


Figure 3.9: Test setup and of flexural strength test of ferrocement slab and AE sensor placement

The AE measurement system and its instrumentation followed set up presented in section 3.3.2 with a change in the threshold level to 45 dB.

3.6. Fiber reinforced concrete beams in flexural behaviour

This set of experiment was carried out to obtain a global and local monitoring system. This experiment is used for analysis of sections 4.6. To this end, the following specimens were prepared.

3.6.1. Casting, Sensor instruments, Loading Procedure

All the three specimens have uniform cross section of 250 mm x 200 mm and length of 2500 mm. The concrete was designed to achieve a 28-day compressive strength of 36 MPa using ordinary Portland cement and a water-to-cement ratio of 0.55. The mix proportion of concrete is given in Table 3.6. The SFRC and PFRC specimens were incorporated with steel fibers and polypropylene fibers at 1% concrete volume fraction (FVF), respectively. The steel fibers were 30 mm long with a diameter of 0.62 mm, while the polypropylene fibers were 40 mm long with cross sectional dimensions of 0.5 mm x 0.9 mm. For tension reinforcement, two D13 (SD295) steel bars were included in all the three specimens, respectively. Figure 3.10 gives schematic drawings of the specimens. A total of sixteen AE sensors (R6I by Mistras Group Inc.), which have resonant frequency of 60 kHz were mounted on the top, left and right sides of each specimen as shown in the Figure. The sensors were used for both AE and travel time tomography (TTT) measurements. A sixteen-channel AE acquisition system was used for the measurement. The system was set to 'AE mode' when undertaking AE monitoring and 'TRA mode' when conducting wave propagation measurement for TTT. The specimens were loaded in flexure with an effective span of 2000 mm. Compression load was distributed from a hydraulic jack to two points on the top surface of specimen, each separated 200 mm from the center of specimen to both the left and right sides. In the experiment, the loading was first applied in the pattern of 0 kN – 11.2 kN – 0 for three cycles.

Following the same loading-unloading pattern, the load was then increased to 30 kN. In the third step, load was increased from zero to the maximum, at which specimen would fail.

The wave measurements for TTT were conducted at several steps: 1) before start of loading, 2) at third cycle of 11.2 kN, 3) at the third cycle of 30 kN and 4) after failure.

During the wave measurement for TTT in steps 2) and 3), the AE monitoring was temporarily terminated and would resume after the measurement with loading being resumed. In the measurements, stress waves were generated using two different means, namely by mechanical impact from a 5 mm steel ball impactor and an electric pulser that emitted ultrasonic pulse. The wave generation was carried out by placing the impact or pulser adjacent to a sensor that acted as the trigger. The sensor would detect incoming waves and trigger simultaneous recording of signal for the other sensors, which acted as the wave receivers. The acquisition was made at a time interval of 1 μ s for a data length of 5120 to reproduce waveform data. For each set of measurement, five excitations were made and the waveforms were stacked to increase signal-to-noise ratio for facilitating pick-up of the wave arrival time. The trigger was subsequently shifted to another sensor to repeat the wave generation and acquisition exercise. The sixteen sensor arrangement has resulted in a total of 240 waveforms to be processed for obtaining data of travel time difference. The processed data was later used to compute velocity distributions of the measured volume using a tomographic reconstruction program. As for the AE monitoring, the acquisition system was configured by setting the sampling rate to 1×10^6 . The wave velocity for signal localization was set as 4200 m/s, which was the average value measured experimentally from the concrete specimens. Throughout the monitoring, the threshold level of AE signal was fixed at 45 dB as an attempt to avoid acquisition of signals due to electrical and mechanical disturbances.

Table 3.6: Mix proportion of concrete specimens

Specimen	W/C %	kg/m ³			
		Water	cement	Fine aggregate	Coarse aggregate
RC	55	165	300	860	965
SFRC					
PFRC					

W/C: Water/Cement ratio

W: Water, C: Cement, S: Sand, G: Coarse aggregate

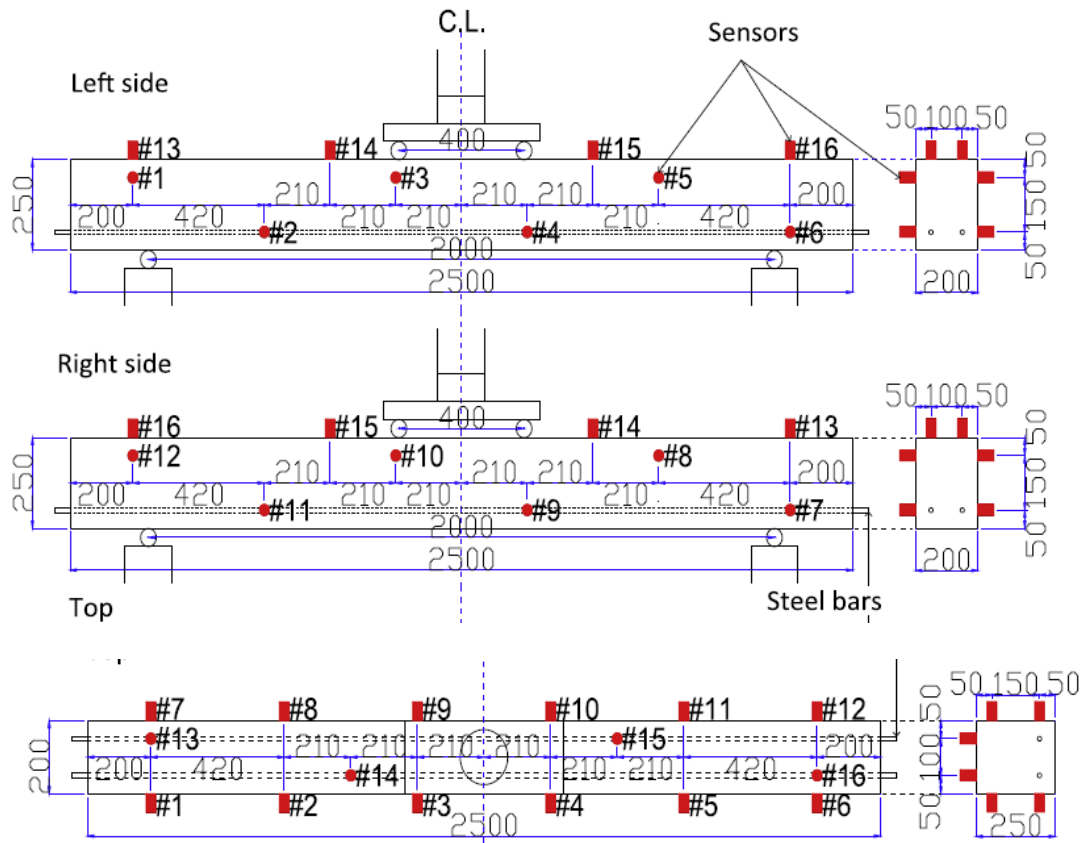


Figure 3.10: Schematic diagrams of beam specimens and location of AE sensors (units in mm)

CHAPTER 4

RESULTS AND DISCUSSIONS

4.1. Introduction

This chapter presents and discusses the results obtained for objectives listed in chapter 1. Each section of this chapter will be in the form of one SCI article. The specific methodology for each paper is given in chapter 3. The pertaining publications are listed in Table 4.1.

Table 4.1: Summary of subsequent sections and references of related experiments

Number	Article title	Experimental Reference in Chapter 3	Section no
1	Damage detection of SFRC concrete beams subjected to pure torsion by integrating acoustic emission and Weibull damage function	3.3	4.2
2	Acoustic Emission Monitoring of Multi-Cell Reinforced Concrete Box Girders Subjected to Torsion	3.4	4.3
3	Unsupervised Acoustic Emission Damage Detection Technique Incorporating Kernel Fuzzy C-Mean for Structural Concrete Subjected to Pure Torsion	3.3	4.4
4	Acoustic Emission Fracture Monitoring of Multi-Layered Wire Mesh-Reinforced Cementitious Composite Slabs	3.5	4.5
5	Damage Detection and Monitoring of Ferrocement Composite Slabs by Means of Acoustic Emission Technique	3.5	4.6
6	Integrated non-destructive assessment of concrete structures under flexure by acoustic emission and travel time tomography	3.6	4.7

4.2. Damage Detection of SFRC Concrete Beams Subjected to Pure Torsion by Integrating Acoustic Emission and Weibull Damage Function

In the following the theories, analysis, results and conclusions is given for this article.

The related experimental references are presented in section 3.3.

4.2.1. Analysis Theory: Quantification of Damage and fracture process

In the following theories related to damage quantification and fracture process will be discussed.

4.2.1.1. b-value Analysis

The b-value is a well-known macro and micro structural crack identification method. Drawing on the basics of seismology, it is defined as the negative gradient of the log-linear plot of earthquake frequency magnitude (Grossi and Ohstu, 2008).

Many studies have been carried out to relate the b-value with strain in concrete and steel at different stages of damage and loading. Gutenberg–Richter has defined the relationship between magnitude and frequency as below:

$$\log_{10}N(M) = a - b \left[\frac{A_{db}}{20} \right] \quad (4.1)$$

in which A_{db} is the peak amplitude of the AE events in decibels, b_{AE} is AE-based b-value and $N(M)$ is the number of AE hits (or events) of magnitude $\geq M$.

Diagnosis of concrete and masonry structures by b-value analysis was conducted in some researches (Carpinteri and Lacidogna, 2007; Carpinteri et al., 2006; Carpinteri et al., 2007a). It was stated by Colombo et al. (2003) that larger b-values represent the stage of micro crack occurrence and vice versa.

There are copious studies which showed that during the fracture process of concrete structure, a relation can be made between types of cracks and evolution of b-value.

Mostly, the b-value decreases during the different stages of fracture that lead to the formation and localization of macro-cracks (Colombo et al., 2003).

Moreover, size effect in fracture analysis can be studied by means of b-value analysis (Carpinteri et al., 2007b).

On the other hand, a statistical interpretation to the variation of the b-value during the evolution of damage detected by AE has been proposed by Carpinteri et al. (2008).

This proposed method is based on a different model of b-value calculation treatment (Carpinteri et al., 2008). The proposed model captures the transition from the condition of diffused criticality to that of imminent failure localization (Carpinteri et al., 2013).

Considering seismic analogy, the application of b-value and AE signal magnitude was drawn to connect between magnitude m and size L of the defect associated with an AE event (Carpinteri et al., 2013). Equation 4.2 shows the validity of relation where the fractal dimension is also correlated to b-value.

$$N(\geq L) = cL^{2b} \quad (4.2)$$

where N is the cumulative number of AE events generated by source defects with a characteristic linear dimension L , c is a constant of proportionality, and $2b = D$ is the fractal dimension of the damage domain.

Although numerous studies have been accomplished on the application of b-value, few if any such methods have been applied for torsion fracture analysis. As a result, in this study, fracture process and damage evolution in pure torsion loading is correlated to b-value results. Moreover, to overcome the fluctuation of b-value and provide a transparent vision of b-value in each stage of fracture, a Gaussian filter has been utilized.

4.2.1.2. Gaussian Smoothing Filter

Gaussian filters can be used to smooth a signal prior to extracting primary features. Farhidzadeh et al. (2012) used this filtering method for AE signals to propose Sifted b-value (Sb) analysis.

It is noteworthy that there are some properties in Gaussian functions which have made them useful in smoothing filters. These features can be listed as follows: 1) the Gaussian function is symmetric about the mean, and the weights assigned to signal values decrease gradually with distance from the mean; 2) the width of the Gaussian function is determined by its spread parameter, i.e., the standard deviation.

As the standard deviation decreases, the Gaussian function does less smoothing; in contrast, as the spread parameter increases, the amount of smoothing is increased. 3) The local extrema (e.g., b-value drop caused by overloads) observed at one standard deviation is also observable at the smaller standard deviations and no additional local extrema are created as the spread parameter increases. This property plays a key role when analysing the change of local extrema across different spread parameters. Generally, Gaussian smoothing is the convolution of a Gaussian window and a 1-D vector of data.

The Gaussian smoothing $F(x)$ of a signal, $f(x)$, is defined as:

$$F(x) = f(x) * g(x, \sigma) = \int_{-\infty}^{\infty} f(\mu) g(x - \mu, \sigma) d\mu = \int_{-\infty}^{\infty} f(\mu) (1/\sqrt{2\pi\sigma^2}) \exp[-\frac{(x-\mu)^2}{2(\sigma^2)}] d\mu \quad (4.3)$$

where "*" denotes convolution with respect to x , $g(x, \sigma)$ is the Gaussian function with the standard deviation σ , and μ is a dummy variable. These filtering parameters, other than window span, should be well chosen to show the correct and clear trend of b-value.

4.2.1.3. Principal Component Analysis (PCA)

PCA is known as a mathematical algorithm that could be implemented to decrease the dimensionality of a data set for compression, pattern recognition and data interpretation. The algorithm is obtained by a linear transformation, a p -dimensional data vector X into a new q -dimensional data vector Z , containing what is addressed as the data's 'principal components' (Rippengill et al., 2003).

Given the data $X_i = (x_{1i}, x_{2i}, \dots, x_{pi})$ with $i = 1, \dots, N$, the new data vector $Z_i = (z_{1i}, z_{2i}, \dots, z_{qi})$ where: z_1 is the linear combination of the original x_j ($j = 1, \dots, p$) with maximal variance; z_2 is the linear combination that describes most of the remaining variance and so on.

If the p -coordinates are a linear combination of $q < p$ variables, the first q principal components may completely characterize the data and the remaining $p-q$ components is zero (Rippengill et al., 2003).

4.2.2. Weibull Damage Function Calibrated with AE Data for Torsion Damage

Behavior

The theory behind Weibull damage function and its correlation to acoustic emission will be presented in this section.

4.2.2.1. Weibull Function for Damage Behavior

According to the statistical theory of damage of quasi-brittle materials, concrete can be considered to be composed of many microelements. Under external load, the rupture probability of each microelement is different but the damage probability of materials with heterogeneous properties complies with a Weibull distribution (Weibull, 1951).

The typical probability density function of a Weibull random is shown as:

$$f(x; \lambda, k) = \frac{k}{\lambda} \left(\frac{x}{\lambda}\right)^{k-1} e^{-(x/\lambda)^k} \quad x \geq 0 \quad (4.4)$$

The cumulative distribution function for the Weibull distribution is:

$$f(x; \lambda, k) = 1 - e^{-(x/\lambda)^k} \quad x \geq 0 \quad (4.5)$$

where x is defined as a random variable, the shape parameter k is the Weibull modulus, and λ is a scale parameter.

Chen and Liu (2004) have shown that under uniform uniaxial tensile strain, the rupture probability density function of the microelement could be described as follows:

$$f(\varepsilon) = nm(\varepsilon - \varepsilon_0)^{m-1} \exp[-n(\varepsilon - \varepsilon_0)^m] \quad (4.6)$$

where ε_0 is determined by experimental results and parameters of n and m are related to the dimensions and elastic properties of the specimens.

It should be noted that in probability theory, a probability density function (pdf), or density of a continuous random variable, is a function that describes the relative likelihood for this random variable to take on a given value. The probability of the random variable falling within a particular range of values is given by the integral of this variable's density over that range. Therefore, by integrating Equation 4.6 which is the probability density function of rupture, the rupture probability will be given.

Therefore, the rupture probability of the microelement occurring in the material which is described up to the strain level ε is given in Equation 4.7 whereby it is correlated to the Weibull distribution function and is given as:

$$F(\varepsilon) = \int f(\varepsilon) = \int nm(\varepsilon - \varepsilon_0)^{m-1} \exp[-n(\varepsilon - \varepsilon_0)^m] = 1 - \exp[-n(\varepsilon - \varepsilon_0)^m] \quad (4.7)$$

4.2.2.2. Weibull damage function calibration with detected AE events

The ratio of $dN_{\theta}/d\theta$ to the total AE events N_{tot} acquired by the AE system can describe the rupture probability density as given in the equation below:

$$f(\theta) = \frac{\frac{dN_{\theta}}{d\theta}}{N_{tot}} \quad (4.8)$$

where θ is angle of twist in the beam and N_{θ} is defined as the number of cumulated AE events. Therefore, the Weibull damage function is given as:

$$F(\theta) = \frac{N_{\theta}}{N_{tot}} \quad (4.9)$$

Equating Equations 4.6 and 4.8, the relations below can be obtained by substituting ε for θ :

$$f(\theta) = (dN_{\theta}/d\theta)/N_{tot} = nm(\theta - \theta_0)^{m-1} \exp[-n(\theta - \theta_0)^m] \quad (4.10)$$

The bi-logarithmic regression analysis of the acquired AE data with respect to the θ was conducted to determine the n and m values for the SFRC specimen. Combination of the two previous equations yields:

$$\ln \left[-\ln \left(1 - \frac{N_{\theta}}{N_{tot}} \right) \right] = m \ln(\theta - \theta_0) + \ln n \quad (4.11)$$

The standard expression of the linear regression with logarithm terms x and y is:

$$y = ax + b \quad (4.12)$$

Where $y = \ln \left[-\ln \left(1 - \frac{N_{\theta}}{N_{tot}} \right) \right]$; $x = \ln(\theta - \theta_0)$; $a = m$ and $b = \ln n$ and θ_0 is defined as the rotation of the supports when the first AE signal is emitted and the acoustic emission measurements can determine the n and m parameters. These parameters influenced fracture resistance in terms of crack events of a specimen.

4.2.2. Results and Discussion

In this section pertaining results are given and discussed.

4.2.2.1. Mechanical Effect of Inclusion of Steel fiber in Torsion Behavior

Some physical and mechanical characteristics of the investigated specimens have experimentally been determined through conducting two different series of specimens: (1) plain concrete specimens (specimens #1 to #3), (2) SFRC specimens (specimens #4 to #7). As indicated in Table 3.8, the compressive strength depends significantly on the water/cement ratio, showing a decrease equal to about 44% by increasing w/c from 0.45 to 0.65. In the case of torsional strength, which is due to indirect tensile stress, the water/cement ratio effect was also apparent because by increasing w/c from 0.45 to 0.65, a considerable decrease corresponding to about 37% was observed.

As illustrated in Figure 4.1, the addition of steel fiber has caused an increase in torsion resistance and improvements in the post-failure behavior of concrete specimens. It can be confirmed that the inclusion of fiber has restrained cracking.

It is observed that in the test for plain concrete specimen, when the matrix started to rupture, cracks would immediately develop spirally around the specimen, and loading would drop abruptly as the specimen failed. In the presence of fibers, crack propagation would be restrained and the load did not drop straight away due to contribution of material in the absorption of energy.

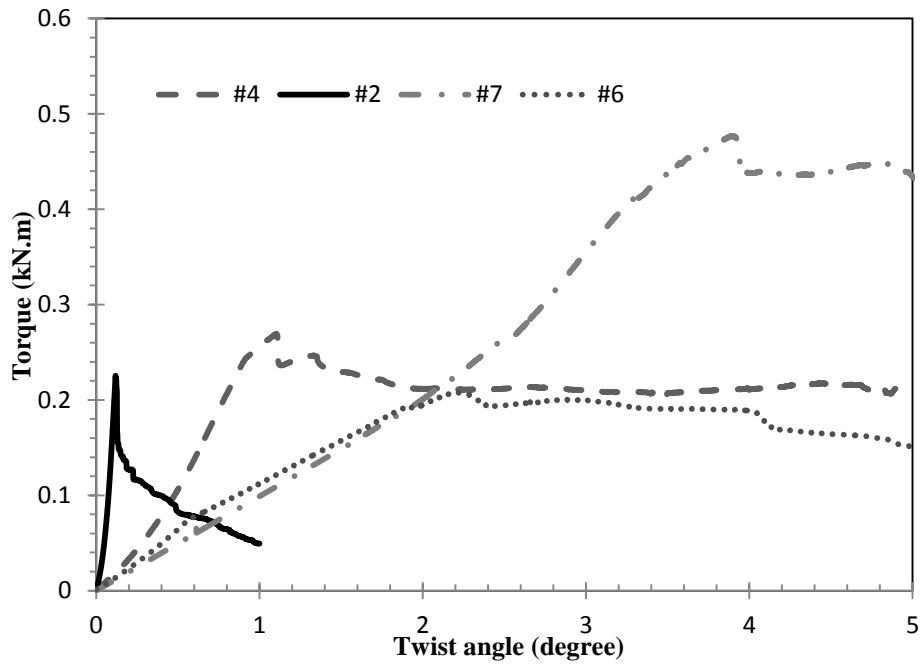


Figure 4.1: Torque moment versus twist angle in concrete specimens

4.2.4.2. Damage Evolution Process Analysis by b-value

Figure 4.2 illustrates the b-value data based on groups of $n=100$ AE signals recorded for the entire data set of specimens #1. In addition, the estimated probability density function is placed at the top left side of Figure 4.2. It is noted that Inverse Gaussian distribution fits this function properly.

Although the general decreasing trend of b-value indicates the evolution of damage, it is difficult to identify a trend in each particular stage of damage. However, the difficulty in identifying b-value trend might pose as a drawback in real time monitoring. Therefore, in order to provide a precise elaboration of variation in b-value trend, a Gaussian filtering was introduced to the b-value results.

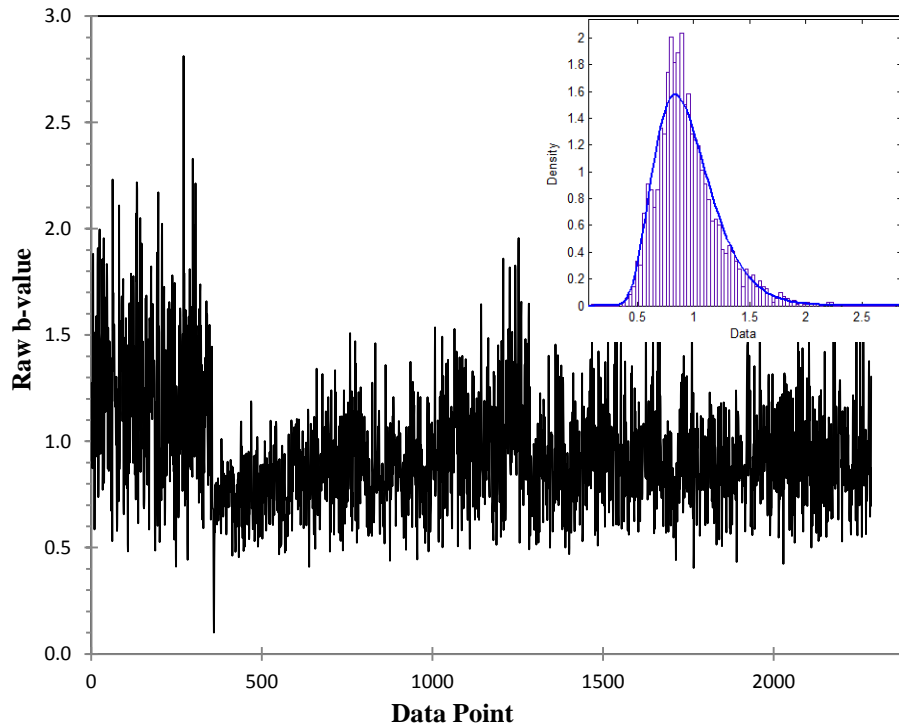


Figure 4.20: b-values results for the entire dataset before filtering process for #1

It should be noted that the window span selected was about 5% of the length of the data vector. In addition, the standard deviation was set to a quarter of window span. Figure 4.3 shows the smoothed b-value data after being processed by Gaussian filtering method. In addition, the corresponding damage states are indicated in the graph. As can be seen, after filtering the raw b-value data, the trend of variation of b-value corresponding to each level of damage is fairly well distinguished. Considering Figure 4.3, it can be realized that there are three distinct stages of damage which can impact the trend of b-value.

In general observation, during stage I b-value shows a general increase which is pertinent to nucleation of micro-cracks. Approaching the peak load coincided with the start of macro-crack formation and localization stage (stage II). In this stage, initially a significant drop occurs in b-value and thereafter slight increase with fluctuation can be observed.

Finally, in stage III which is also called macro-crack opening (softening branch for plain concrete or fiber pull out branch for SFRC), a general decrease could be observed in b-value.

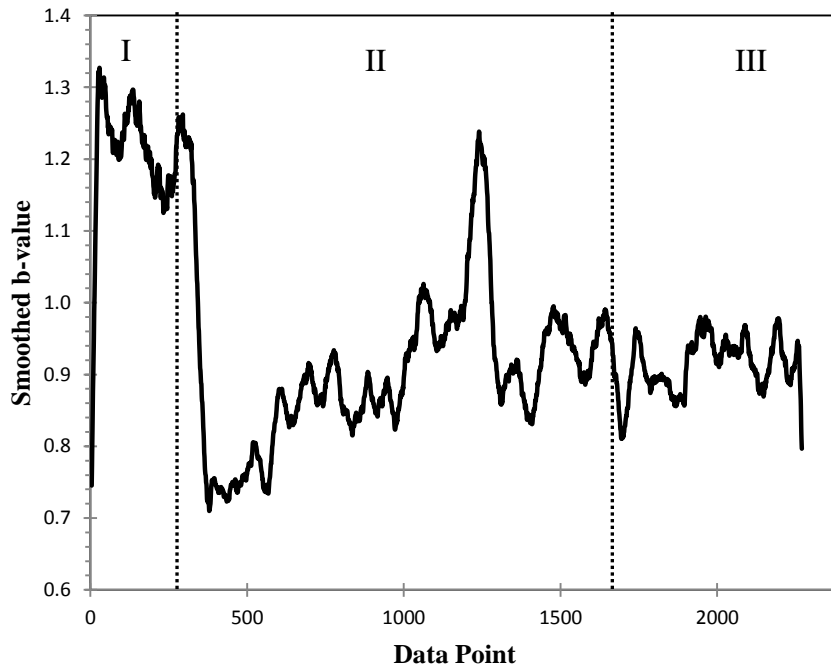
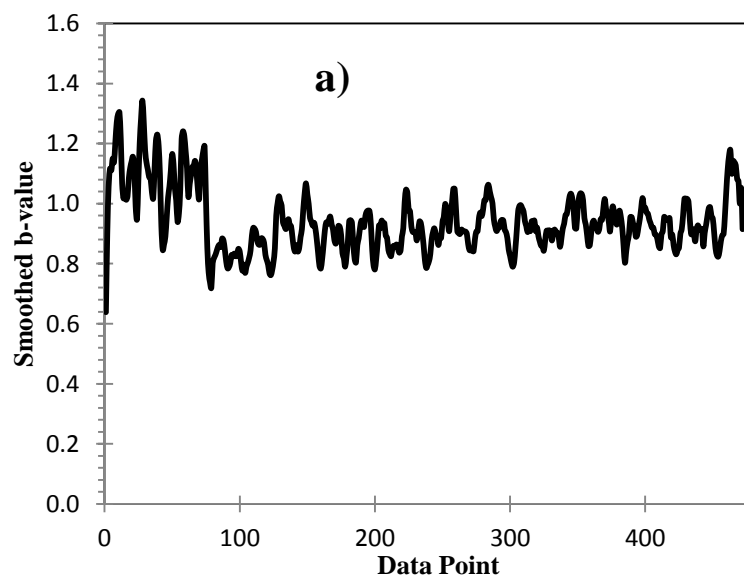


Figure 4.3: Smoothed b-value results for the entire dataset after filtering for #1

The fluctuation seen in stage II could be associated with formation of a few micro-cracks while the dominant fracture was identified as macro-cracking. Moreover, this b-value trend represented the entire data set recorded for all six AE sensors. Considering each individual channel dataset may result in a more evident or conversely less evident trend. For instance from Figures 4.4a-d, it is obvious that the above aforementioned trend is more evident in cases for sensors S2 and S6 which were placed closer to the path of occurrence of the main crack and S1 was close to the edge of left side of beam which was farther from the crack propagation region. From Figures 4.4b and 4.4d it can be inferred that in macro-crack opening stage when the crack width is widening, S2 and S6 which are positioned closer to the crack were affected significantly.

Therefore, a decrease in b-value trend of these sensors can be observed due to an increase in the severity of damage.

Interestingly, increasing the crack width in regions proximate to sensors S2 and S6 coincides with approaching crack tip to sensor S4 whereby a decrease in b-value trend of S4 was also recorded.



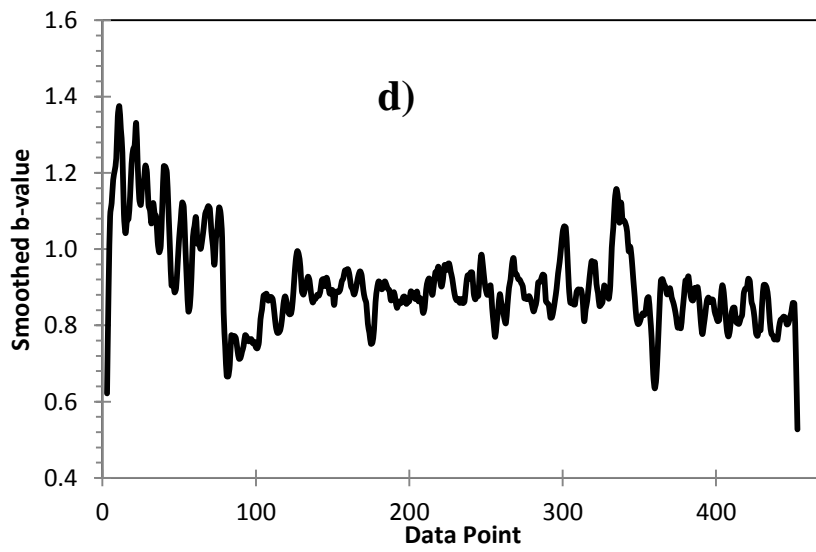
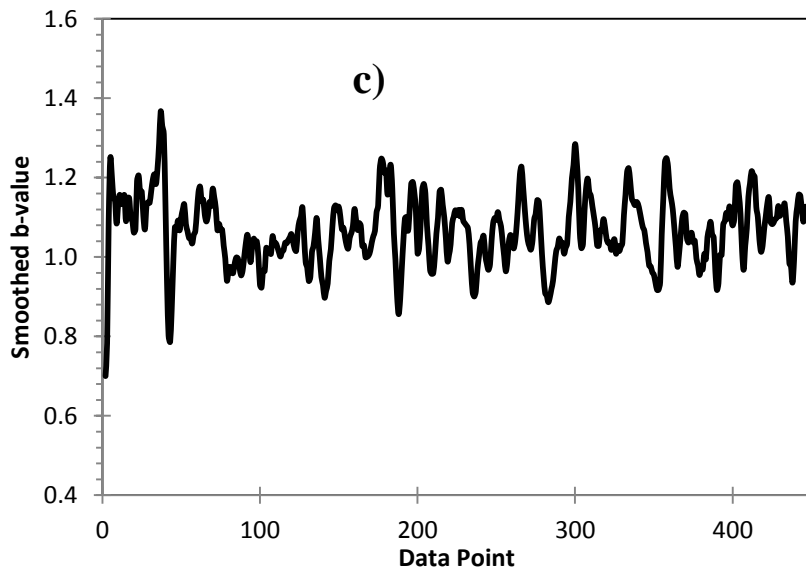
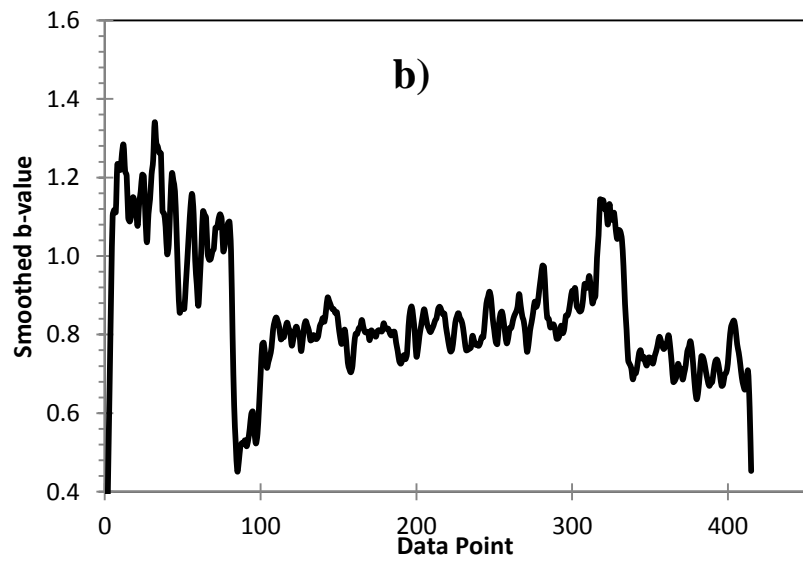
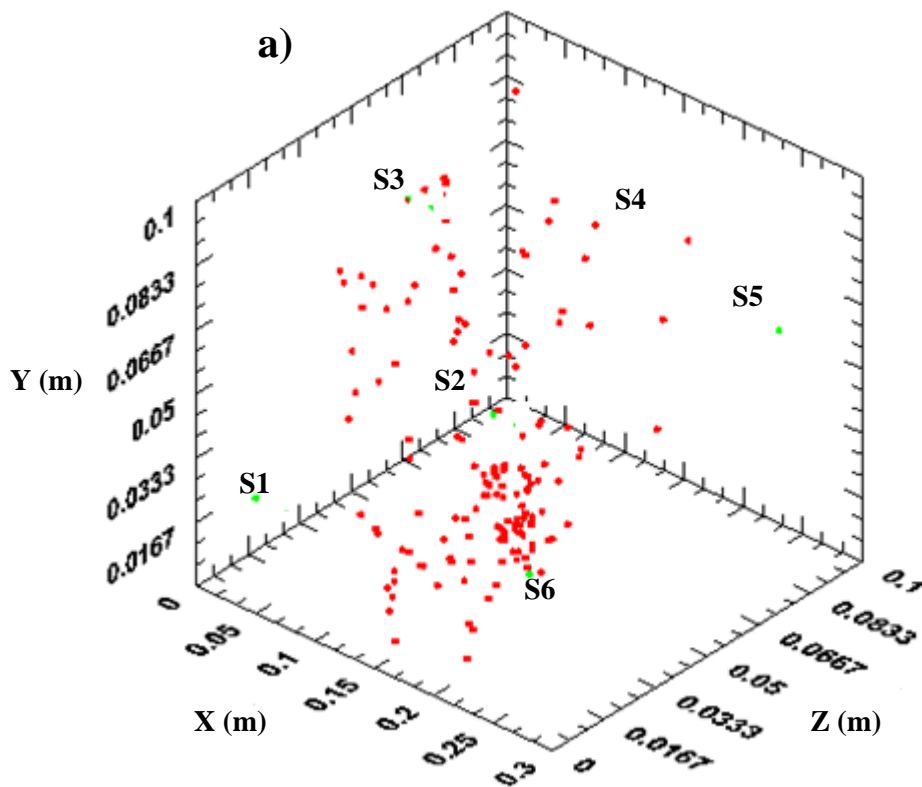


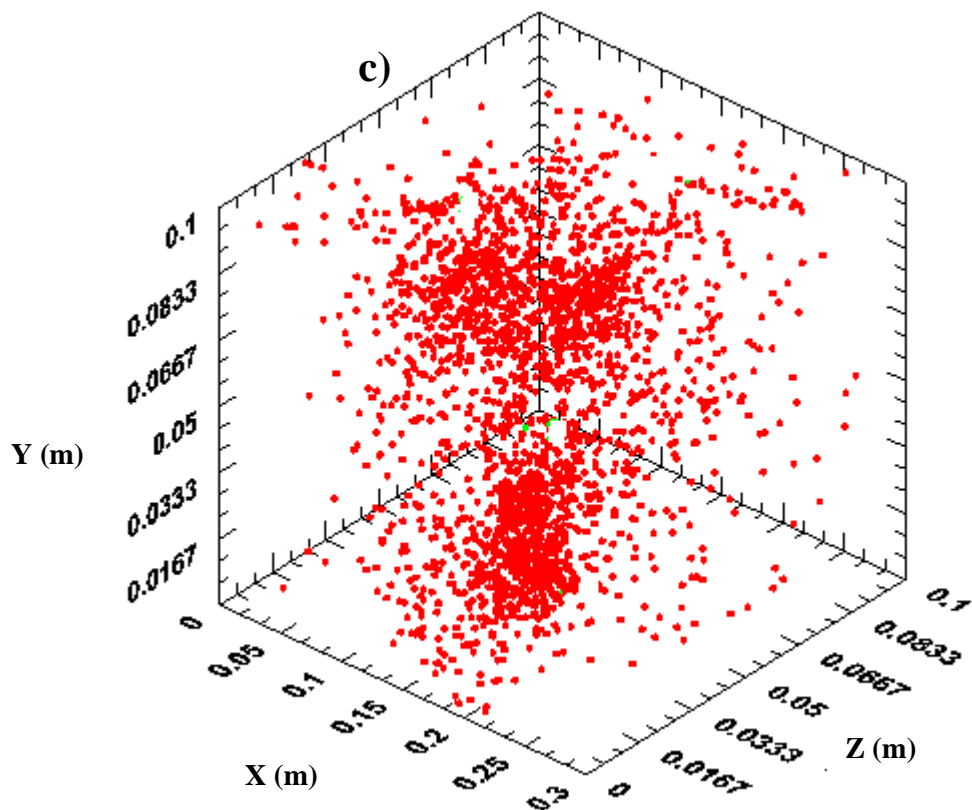
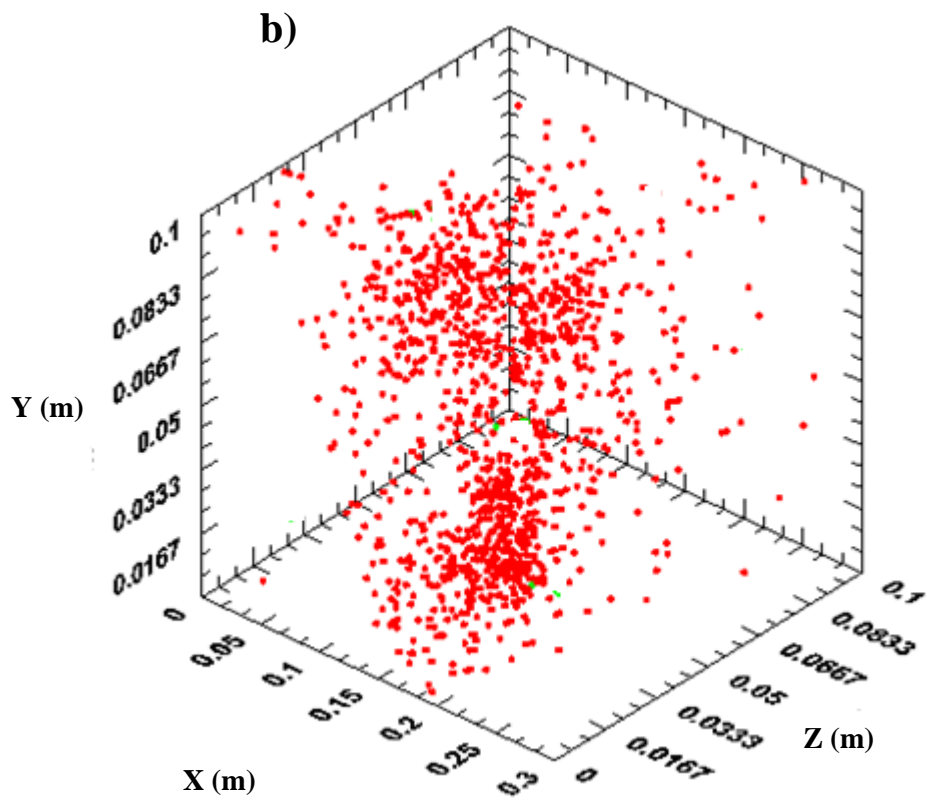
Figure 4.4: b-value variation trend based on smoothed curve for different sensors mounted on specimens #1: a) S1, b) S2, c) S5, d) S6

To verify this presumption a 3D localization analysis during the damage progress was carried out and the results are plotted in Figures 4.5a-c. As can be seen in Figure 4.5a, in the early stage of damage, a few events have occurred in the area proximate to sensors S2 and S6. The pattern of occurrence of events due to progress of damage in macro-crack stage followed the same pattern of events in early stage.

This pattern also conforms to the pattern of occurrence of the crack which was propagated in a spiral direction throughout the beam. However, in general, when the specimens reached their peak loads due to transition from linear state to nonlinear state a significant drop occurs in b-value either for the entire data set or individual channels.

For more precise analysis, an individual sensor tracking analysis scheme is considered essential to yield more reliable results. To this end, a PCA analysis was performed to track the individual sensor record during the monitoring.





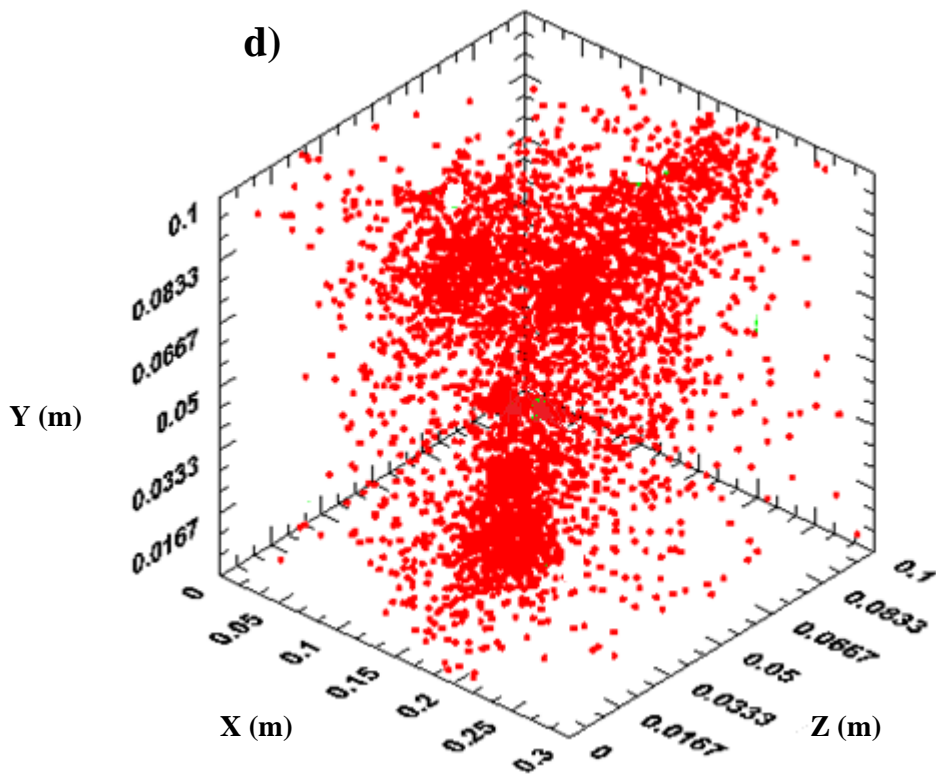


Figure 4.5: 3D event localization of damage progress with respect to progressive damage evolution for #1 (a: $t_1 = 0-1000$ sec, b: $t_2 = 1001-2000$ sec, $t_3 = 2001-3000$ sec, $t_4 = 3001-4700$ sec)

4.2.4.3. Principal component analysis (PCA)

As mentioned earlier, PCA is known as a mathematical method that transforms a number of possibly correlated variables into a smaller number of linearly uncorrelated variables which are called principal components. In this study a PCA method was performed on specimen #1 and results for sensors S1 and S2 are presented to highlight the effect of each individual channel data on the entire data set. Therefore, AE features from the time domain analysis (AE amplitudes, energy, counts, duration, and rise time) were taken. Prior to transformation to the principal components, the data were standardized by dividing the normalized data for each parameter by its respective standard deviation.

Each principal component will be represented using a single axis in the form of a new coordinate space. It should be noted that this new axis is a linear combination of the original variables.

Figure 4.6 shows the PCA visualization of the AE data for specimen #1. It can be noted that the dimensions from five AE parameters through PCA were reduced to two principal components. No normal conditions for AE data pertinent to onset of damage or damage propagation were identified. (0,0) is the origin where all insignificant AE events have been clustered. The obtained plot from PCA indicates that results from origin (0, 0) were moving away for both principal components. For the first principal component, the data shifted away toward the negative values while for the second principal the data moved slightly away from origin toward the positive values. It is noted that the data at the time of failure was found located away from the main cluster. As such, the data was associated with sensor S2 which was positioned close to the region of main macro-crack occurrence. It is showing that as crack starts to propagate toward S2 the more amounts of data are recorded by S2. Therefore, individual S2 b-value analysis presented in previous section gives better results due since it is less affected by signal attenuation problem at the time of failure due to close location to macro-cracks.

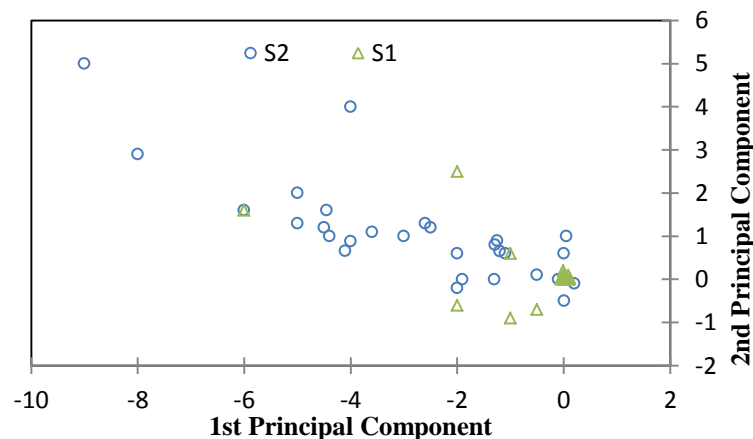


Figure 4.6: Principal components visualization AE data considering S1 and S2 for #1

4.2.4.4. Fracture Process Analysis by b-value

As can be seen from Equation 4.2, the b-value could be correlated to the value of the exponent of the power-law distribution of the crack size in a damaged medium. In addition, this interpretation is based on the assumption of a dislocation model for seismic source where the fractal dimension requires that $2 \leq D \leq 3$. In other words, the cracks which are distributed in fractal domain embrace a region between surface and volume of the analysed region (Carpinteri et al, 2013). Therefore, in case of diffused damage, the fractal dimension ($D=3$) corresponds to $b = 1.5$, whereas two-dimensional cracks lead to the separation of structural element then $D = 2$ which corresponds to $b = 1$.

In order to investigate the efficiency of the aforementioned fractal dimension method for the case under torsion loading, a b-value analysis in conjunction with fractal dimension analysis was performed. The torque moment versus time and event rate for specimen #2 is plotted in Figure4.7.

The torque-time graph is divided into three different stages. The first stage suggests the period from initial time of loading to peak torque (t_0, t_1); the second stage expanded from peak load to the main shock (t_1, t_2).

It is noted that the main shock is a point at which AE activity rate reaches its maximum value; the third and final stage expanded from t_2 to t_f , addressing the period from main shock to the end of fracture/loading process. The average b-values calculated for stage one to three are 1.25, 1.15, and 0.93, respectively. It is noted that at the onset of the loading process, the energy release was caused mostly by micro-crack nucleation which are scattered throughout the volume of the medium.

In this case $b = 1.25$ and consequently $D = 2.5$ ($D = 2b$) which estimates crack locations mainly distributed in the volume ($D \rightarrow 3$).

On the other hand, in final stage of fracture where scattered micro-cracks in volume have transitioned into a two dimensional macro-crack on concrete surface, $b = 0.93$ and then $D = 1.86$ which corresponds to the time of specimen separation $D \rightarrow 2$. Similar results were obtained for the other specimens and due to the space limitation only the final results are presented in Table 4.2. However, in particular, the results for concrete beams subjected to pure torsion test at the laboratory scale are in fairly good agreement with the previous studies for bending test carried out by Carpinteri et al. (2009). In general, it is noticed that in the final stage the lowest b-value was obtained which was associated with the softening/pull out branch of fracture. At this moment the b-value was close to 1 and the specimen was about to separate. Aside from the aforementioned explanation, b-value can be correlated to the changes of toughness in concrete specimens. Considering the correlation between fractal dimension and toughness specimen (Issa Mohsen et al., 2003), the correlation between mechanical properties and b-value could be established. However, Table 4.2 may justify correlation between mechanical properties with fractal dimension and b-value.

For example, the maximum fractal dimension and b-value belong to #7 which possesses the highest toughness, whereas #3 suggests the minimum fractal dimension and b-value when the minimum toughness also belonged to this specimen.

Interestingly, the maximum b-value drop belongs to specimen #1 with 33.78% total drop, whereas the minimum drop occurred in specimen #4. Comparing the initial stage, the b-value results for specimens #1 and #4 revealed that b-value in the first stage is higher for specimen #1 than specimen #4, while in the last stage b-value for specimen #1 is considerably smaller than specimen #4. This might explain the higher initial strength of specimen #1 prior to peak load due to lower water/cement ratio and ductile behavior of specimen #4 in the post peak stage since specimen #4 is SRFC and specimen #1 is a plain concrete.

Moreover, it is noteworthy that in all cases b-value drop could be used as an indication of serious damage. As can be seen, an average 26.34% drop of b-value can be a sign of serious damage in a concrete specimen subjected to torsion loading. It should be noted that although the minimum b-value belongs to the last stage, the maximum drop took place after the peak load in second stage (t_1 , t_2).

Table 4.2: b-value and fractal dimension results

Specimen	b_1	b_2	b_3	D_{max}	D_{min}	*Maximum drop (%)
#1	1.48	1.18	0.98	2.96	1.96	66.22
#2	1.25	1.15	0.93	2.5	1.86	74.40
#3	1.18	1.05	0.89	2.36	1.78	75.42
#4	1.32	1.26	1.02	2.64	2.04	77.27
#5	1.52	1.3	1.1	3.04	2.2	72.37
#6	1.42	1.28	1.1	2.84	2.2	77.46
#7	1.60	1.32	1.16	3.24	2.32	72.5

* This value presents the b-value in last stage as a percentage of b-value in the first stage.

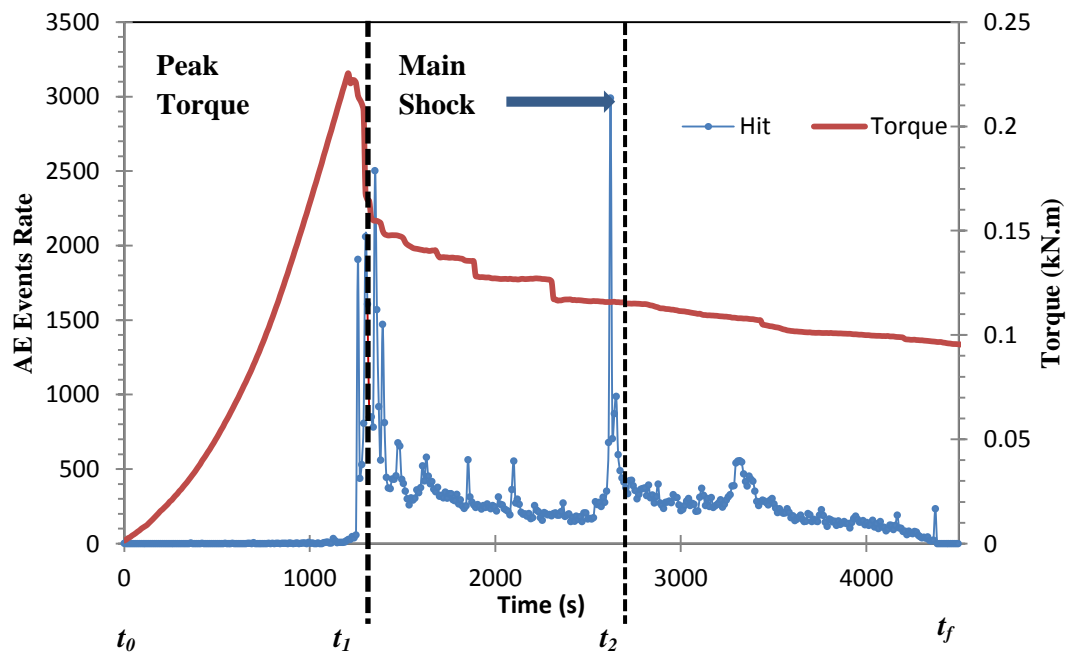


Figure 4.7: Torque moments versus time and event rate for #2

4.2.4.5. Weibull Damage Function and Mechanical Loading Correlation to AE

Data

The torque moment and AE hits data of #2 was correlated as depicted in Figure 4.8. It can be seen that there was no significant AE activity prior to the occurrence of macro cracks (main cracks), which coincides with ultimate torque moment capacity.

Torque moment imposed on the specimens has caused rotation and micro crack nucleation, resulting in the release of strain energy. This energy can trigger AE hits. A considerable increase in the AE hits can be observed at the point near maximum torque capacity.

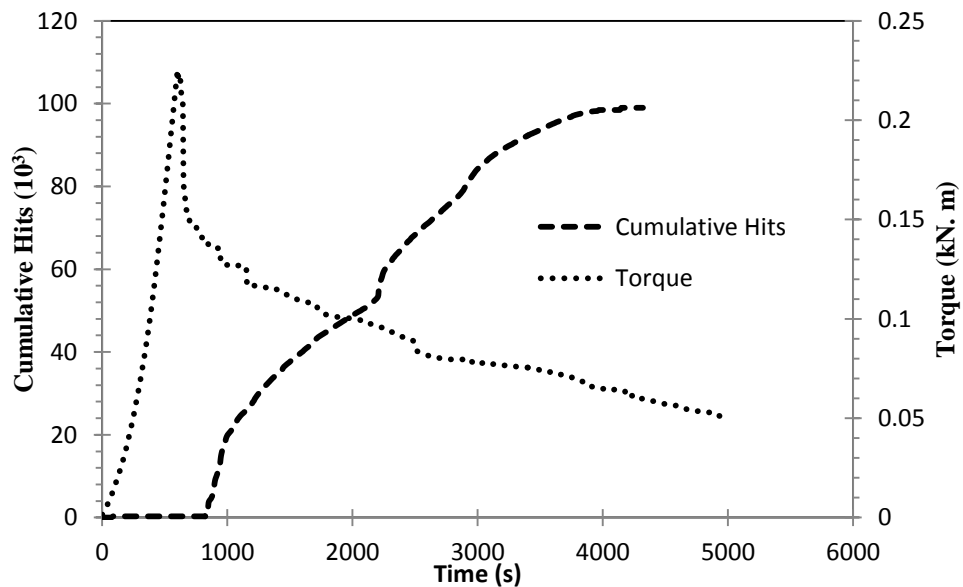


Figure 4.8: Correlation between mechanical response and AE accumulative hits for #2

Adopting statistical regression analysis procedures, the Weibull damage function was calibrated with AE cumulative hits measured at a range of twisting angle of specimen #2. All recorded data obtained from mechanical torsion tests were used to achieve the Weibull damage function calibration with the detected AE events. The Weibull damage function parameters have been calculated by implementing linear regression analysis (Equations (4.11) and (4.12)) with logarithmic values of $\ln [-\ln (1-N_{\theta}/N_{tot})]$ and $\ln (\theta-\theta_0)$.

A fitted trend line is performed to facilitate regression which is shown in the logarithmic chart in the top left corner of Figure 4.9a. The parameters m , n , R^2 , and θ_0 were calibrated as 2.04, 1.105, 0.9557 and 0.0966, respectively. The Weibull damage function parameters obtained in Equations 4.11 and 4.12 were inserted into Equation 4.10 to acquire the estimated AE cumulative hits.

As illustrated in Figure 4.9a, the average absolute relative difference between cumulative AE hits and Weibull damage distribution curve for specimen #2 is about 4.443%. The comparison made in this study demonstrated that the Weibull damage function associated with the acquired AE data can explain the damage response of specimen #2 in pure torsion test.

To demonstrate the efficiency of this method to predict AE hits trend and calibrate Weibull damage function, in the following the Weibull damage function for specimens #2 and #6 subjected to torsion are presented (Figures 4.9a-b).

As shown in Figures 4.9a-b, the Weibull damage distribution is capable of indicating the cumulative AE event trends in the pure torsion test as a function of the twisting angle, while torsion is known as an indirect tensile stress. However, from the results, it seems that the Weibull damage function may describe the damage distribution for SFRC beams and plain concrete while the results express a better estimation for SFRC beam which are more ductile. In the initial stage of the beam torsion test, the cumulative AE event is low as the specimen is still in a stable state.

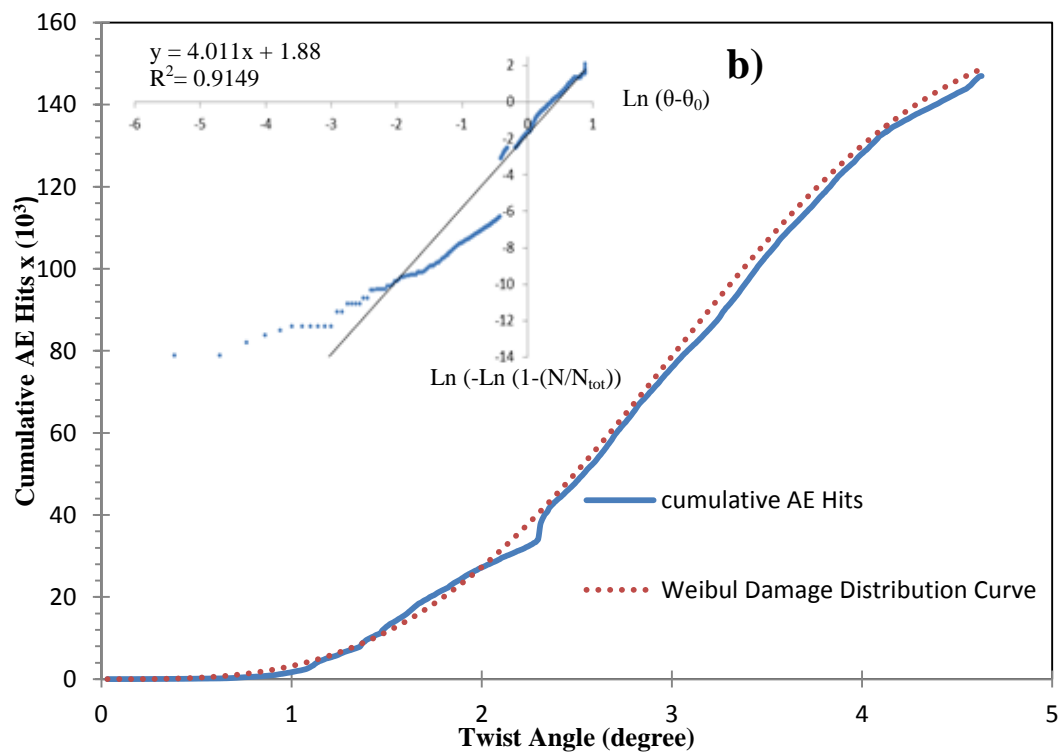
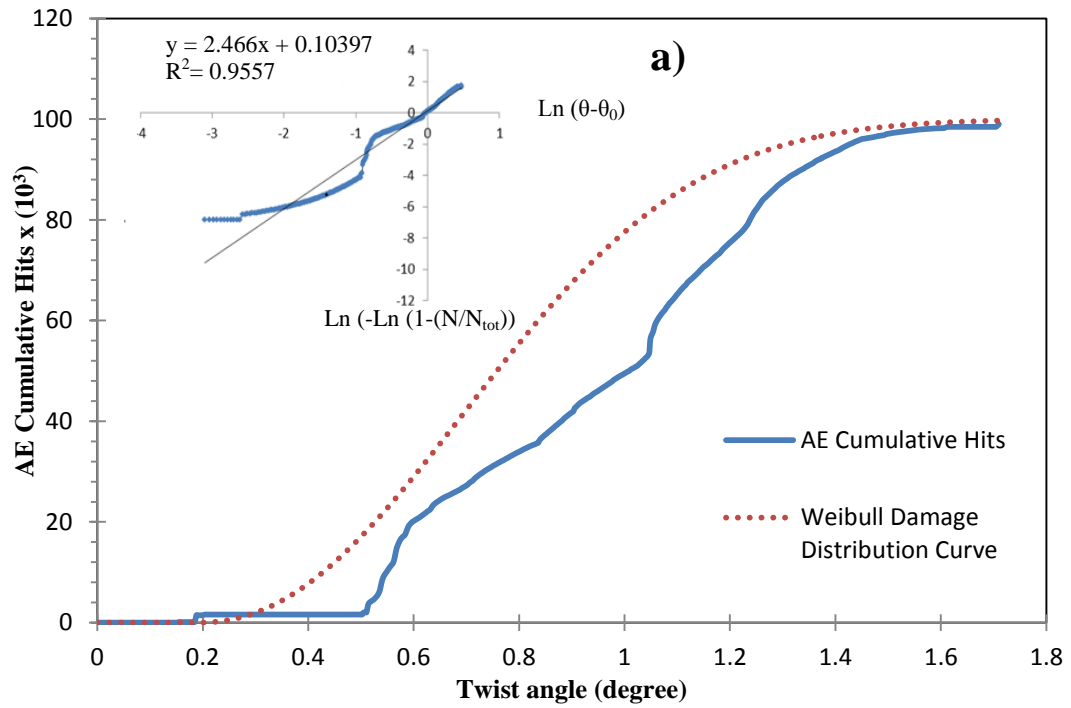


Figure 4.9: Description of mechanical damage behavior with acquired AE data for the #2 Specimen with comparison between cumulative AE hits and the Weibull distribution function curve based on rotation measurement, with Weibull distribution function parameters

When the load approached peak load, the AE hits increased substantially. The increase of AE hits was mainly caused by the fracture energy released from micro-crack growth. As soon as the peak load was achieved, the load decreased exponentially followed by a softening curve. In the softening stage, more micro-cracks were formed and propagated to form macro-cracks, thus leading to higher numbers of cumulative AE events. In the case of specimen #2, the micro crack starts at a twisting angle of 0.0996 degrees after 31 seconds of loading (triggering point) and there is no serious AE activity till peak load where we can observe a sudden increment in AE hits. Thereafter, although loading decreases, the rate of cumulated AE hits is increasing as the damage continues to progress until final stages. While damage is already localized and is merely continuing, new sources are not created. Registered AE activity will then be reduced. Subsequently, for other specimens the similar trend was consistent as observed.

On the other hand, with the aid of AE activities it became possible to calibrate Weibull damage function and obtain Weibull parameters through which the fracture process of the specimens could be reproduced. Table 4.3 displays the obtained Weibull distribution parameters, m and n which reflect the mechanical properties of concrete specimens. It is noted that variation of n ranged from 0.016 to 1.105 and there is no specific order relative to the type of specimen. In fact, these values are considerably small. Moreover, compared to other studies (Chen & Liu, 2004) the differences between values are quite negligible so that we can count them as an unchanged parameter. This phenomenon might be related to the size of specimen where all specimens possess equal dimensions. Therefore, n can be known as the scale size parameter in Weibull damage function. Conversely, m is found to be changed with respect to the change of type of material. It can be found that m is also in straight correlation with fractal dimension parameters.

Table 4.3: Parameters for Weibull damage functions

Specimen	m	n	R^2	Error %
#1	4.19	0.026	0.8862	11.38
#2	2.04	1.105	0.95557	4.443
#3	1.89	0.46	0.935	6.5
#4	3.06	0.069	0.9629	3.71
#5	4.66	0.16	0.916	8.4
#6	4.011	0.016	0.9149	8.51
#7	5.16	0.039	0.9336	6.64

Toward this end, Figure 4.10 depicts that m may suggest the lumped degree of macroscopic statistical strength. Larger degree of m offers higher torque strength and twist angle of failure. For example, from Figure 4.10 it is clear that damage state will be reached easier for specimen #3 than others since it has the lowest m . Therefore, m could be known as deformation properties of the specimens.

However, the fracture properties and brittleness of concrete can be related to two main aspects: geometry of the specimen and intrinsic brittleness of material. Through the experimental results which were correlated to the Weibull parameters, it was demonstrated that the brittleness of material can be quantified by implementing AE technique during the loading process.

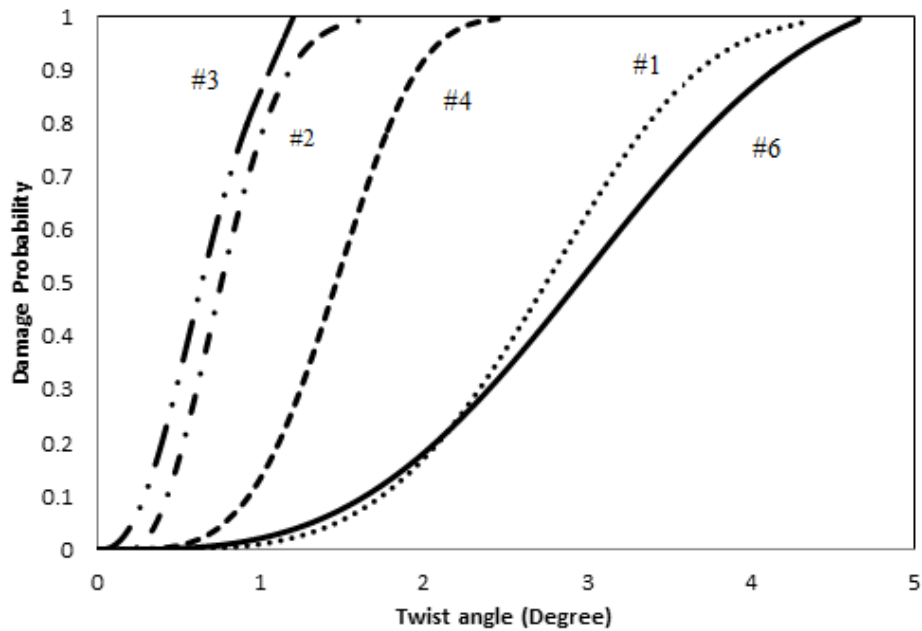


Figure 4.10: Influence of Weibull parameters on damage evolution

4.2.4.6. AE Parameters and Activity Correlation to Structural Behaviour

Observation of AE occurrence in torsion testing for both plain and SFRC concrete beams can be divided into three different phases. As a typical graph, Figure 4.11 displays the aforementioned discrimination from which the recognition of AE activity in each particular fracture phase for SFRC and plain concrete specimens is noticeable. The first stage, where AE activity was triggered, is the initial micro-cracking stage (I), where torque moment was constantly growing. It might be characterized by moderate or low portion AE events due to minor cracks in the concrete matrix.

Thereafter, the macro-cracking stage (II) would be recognized where the torque moment would drop and a macro-crack would progress from the support at grips towards another specimen face in spiral form. In this stage the AE activity rate was considerable because of intense cracking with the presence of steel fiber to bridge the crack. Stage (II) is known as the shortest stage.

The final stage, which was dominated by the gradual pull out of fibers (III) (for SFRC beams), would cause a decrease in AE activity rate to almost constant since the remaining portion of steel fiber which could be subjected to pull out phenomena was reduced continuously while cracking of the matrix continued.

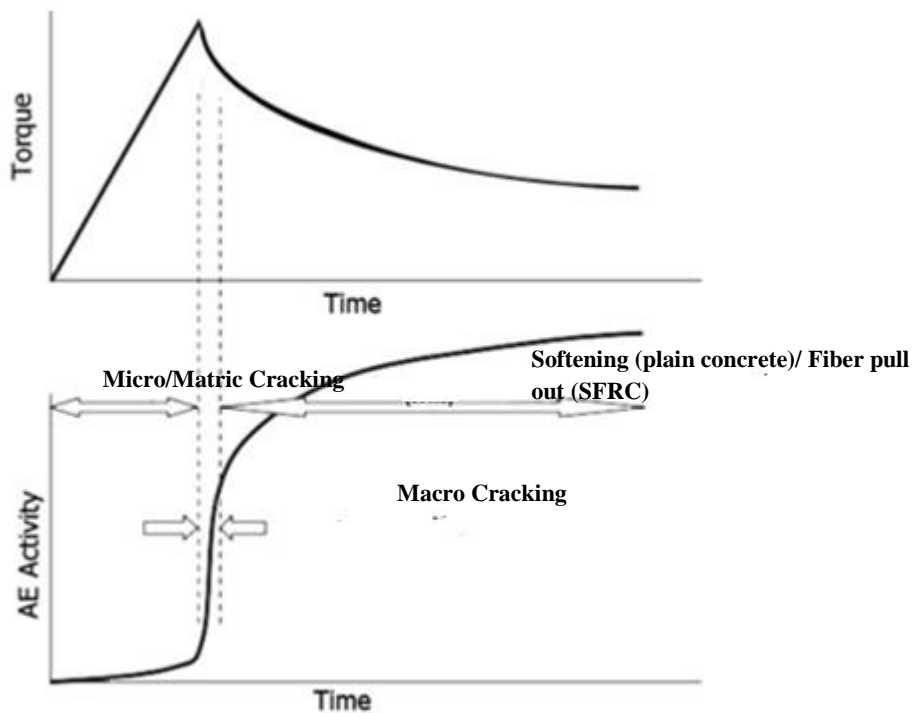


Figure 4.11: Mechanical description of SFRC and plain concrete specimens correlated to AE activity

4.2.4.7. AE Average Frequency and RA Variation in Fracture Process

Average frequency (AF) could be calculated from the number of threshold crossings of the waveform divided by its duration. This feature might be applicable to correlate the AE parameters to failure mode in fracture analysis.

In the current study, for the sake of clarity, it should be mentioned that the moving average is chosen as 70 points. AF started at an average of 100-120 kHz and 60-80 kHz for plain (#2) and SFRC specimens (#7), respectively.

These event activities were due to micro-cracking (matrix cracking) occurring on the specimen matrix, as there was no apparent drop of torque moment or occurrence of macro-cracking.

At the time of main fracture, a sudden drop was found in AF for plain concrete. Similar drop, albeit less significant, for SFRC specimen (#7) was seen at the time of main fracture. As can be observed in Figure4.12a, the AF after main fracture decreased considerably for plain concrete (specimen #2), but for the SFRC specimen (#7) after a drop in main crack, the decrease was much more gradual and smooth.

Since the trend of specimen #7 variation is not transparent enough, Gaussian filtering could be a proper approach to observe clearer trend of variation of AF. Therefore, Figure4.12b indicates smoothed AF value for specimen #7 which is in good agreement with the above statements.

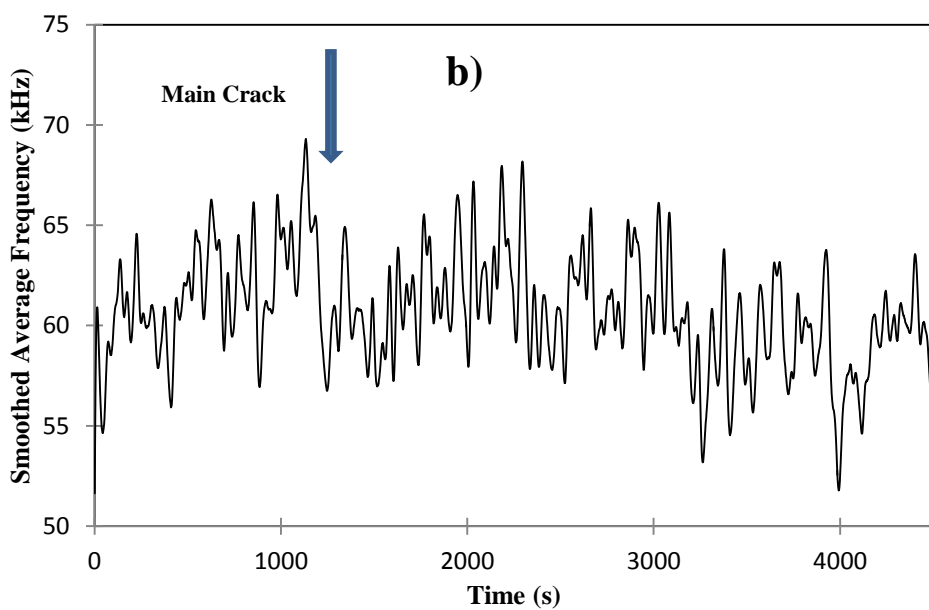
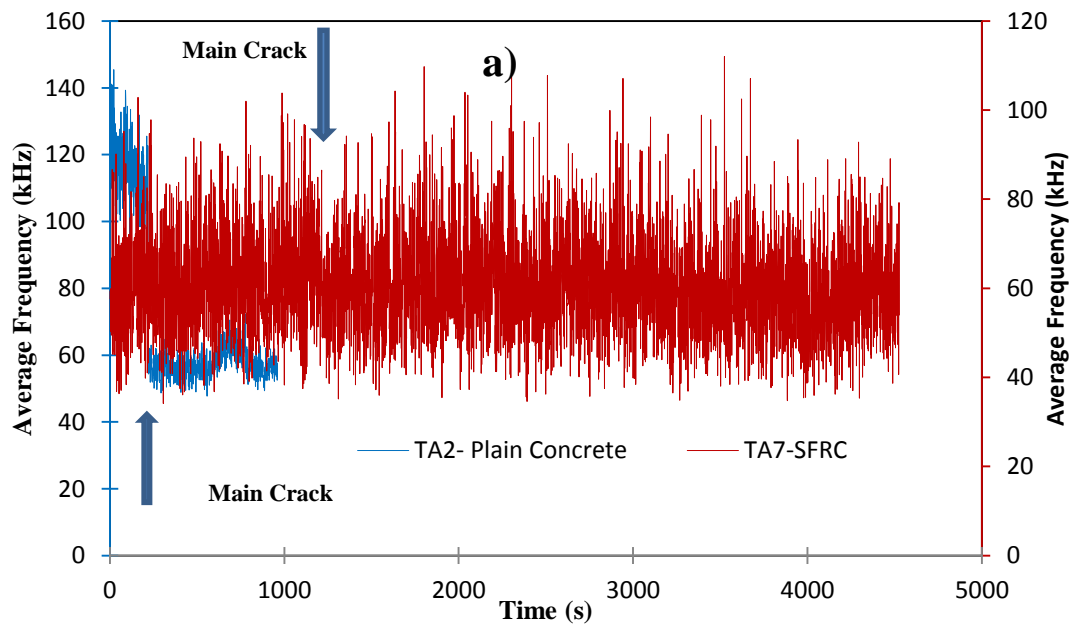


Figure 4.12: a) Average frequency variation versus data set in fracture process, b) Smoothed average frequency for specimen #7 versus data

The RA value is another AE parameter which was being used to describe the type of damage. It is defined as the ratio of the waveform Rise Time to Amplitude in $\mu\text{s}/\text{V}$. Generally, RA is considered to be related to the waveform shape which varies significantly as damage progresses. RA value was used to discriminate the changes in fracture modes (flexural to shear) in bending loading (Soulioti et al., 2012).

However, in the present study RA value could successfully highlight the damage stages in pure torsion loading systems, even though there were no changes in fracture mode as damage progressed.

Figure 4.13a shows examples of trend variations in RA for both the plain (#2) and SFRC (#7) specimens. Gaussian filtering was applied to the data of specimen #7 for increased clarity, as in Figure 4.13b. From the figures, short declines in RA value were observed during the initial stage of loading for both specimens. At the time of main fracture occurrence, apparent increase of RA value was obtained for specimen #2 and the increment was rather consistent throughout loading. On the other hand, a critical increase of RA value was found for specimen #7 at the time of main fracture. The RA value continued to increase in general until the end of loading. Interestingly, there is a relation between strength/toughness of specimens and signal parameters (RA & AF). As noted in Figure 4.13a, the variations in RA range from 0.57-1.88 and 0.21-4.42 for #2 and #7, respectively. Therefore, it can be inferred that #7 shows considerably higher range of RA while it has higher strength/toughness compared to #2. Conversely, it is found that #2 suggests higher range AF (47-145.45) kHz compared to #7 with average frequency ranging from 34 to 112 kHz. Therefore, lower strength/toughness may exhibit higher range of average frequency. To summarize, it is noteworthy that the variations in AF and RA for plain concrete specimen were greater during and after the occurrence of main fracture, whereas the variation seems less significant for SFRC specimen.

The phenomena mentioned above might be attributed to the difference in matrix macro-cracking mechanism of the two different concrete specimens. In pre-main crack stage, namely the micro-cracking stage, the trend of AE activity seemed to be similar in both types of specimens. For plain concrete specimen, at the moment of main fracture, there was a sudden release of energy which results in a sudden drop or rise in AF and RA, respectively.

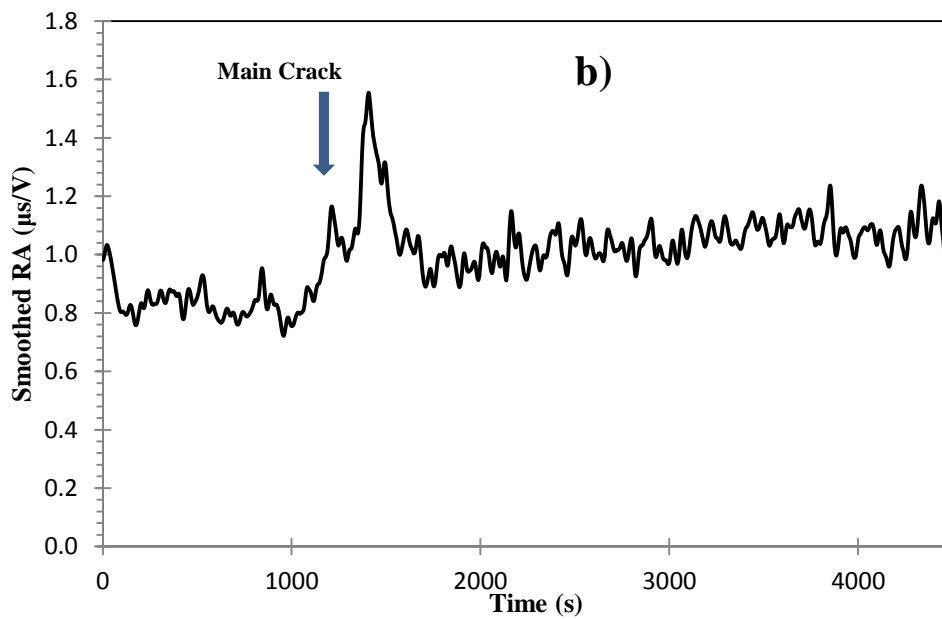
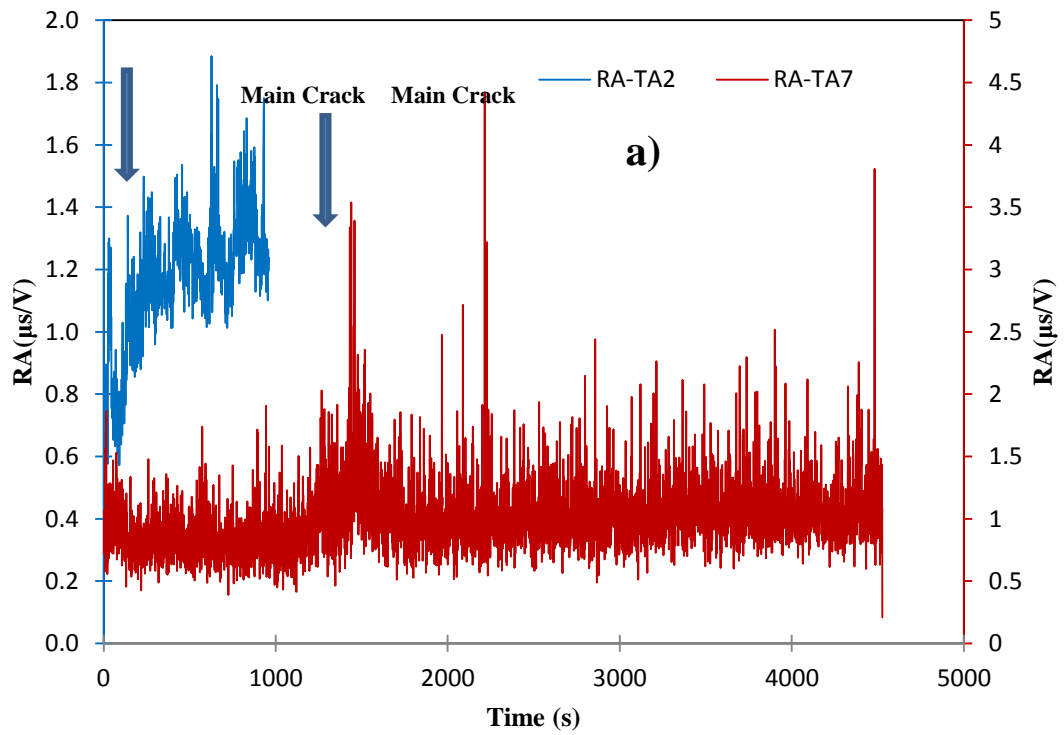


Figure 4.13: a) RA variation versus data set in fracture process, b) Smoothed RA for specimen #7 versus data

For the SFRC specimen, however, slightly lower energy was released at the main fracture point and the fracture energy was found to have been released gradually. Hence, the stress wave produced during this type of fracture might not cause sudden increases or reductions in AE occurrence. It should be noted that in the post crack stage, the failure was accompanied by fiber pull out phenomena. As failure progressed, the portion of fibers which were experiencing pull out decreased. Thus, it can be inferred that the matrix cracking and fiber pull out process may present distinct differences in AE occurrence, especially AF and RA parameters.

Also, higher frequency AE may always be related to matrix cracking (micro- cracking) but not fiber pull out or macro- cracking.

In general, it might be inferred from Figure 4.12 and 4.13 that RA may decrease in the first stage of fracture (micro-crack development), experience a peak in main crack occurrence and continue to increase until the end of the second stage (macro-crack localization). In the last stage of fracture (macro-crack width opening) a decreasing trend can again be observed. Conversely, to some extent an opposite trend can be found for average frequency.

4.2.4.8. AE Signal Amplitude Variation in Fracture Process

In order to comprehend the AE generated during fracture process, AE amplitude distribution analysis was carried out. Figure 4.14 shows the distribution of peak amplitude occurrence for specimens #2 and #7. Although the frequency of AE occurrence (number of occurrence) was considerably higher in the SFRC specimen (#7), its recorded maximum peak amplitude was slightly lower than that of the plain concrete specimen (#2) (90 dB compared to 93 dB).

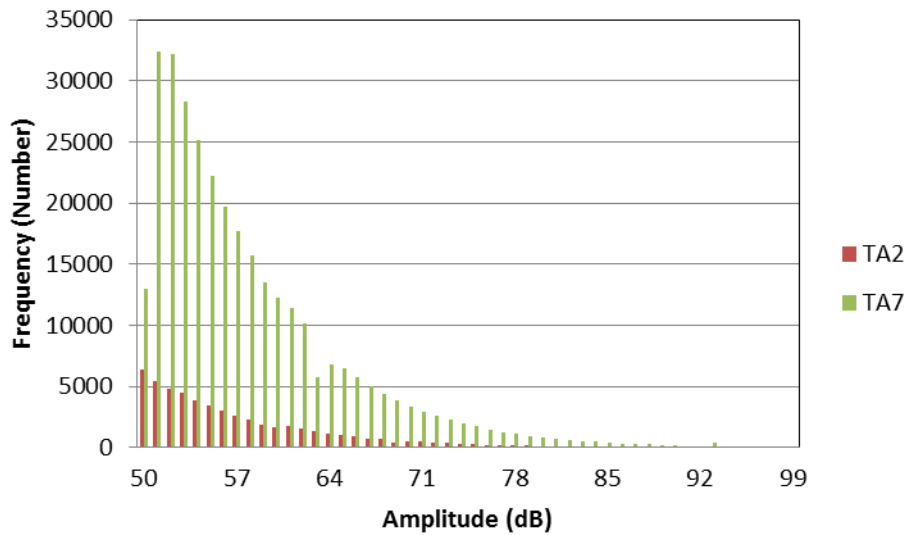


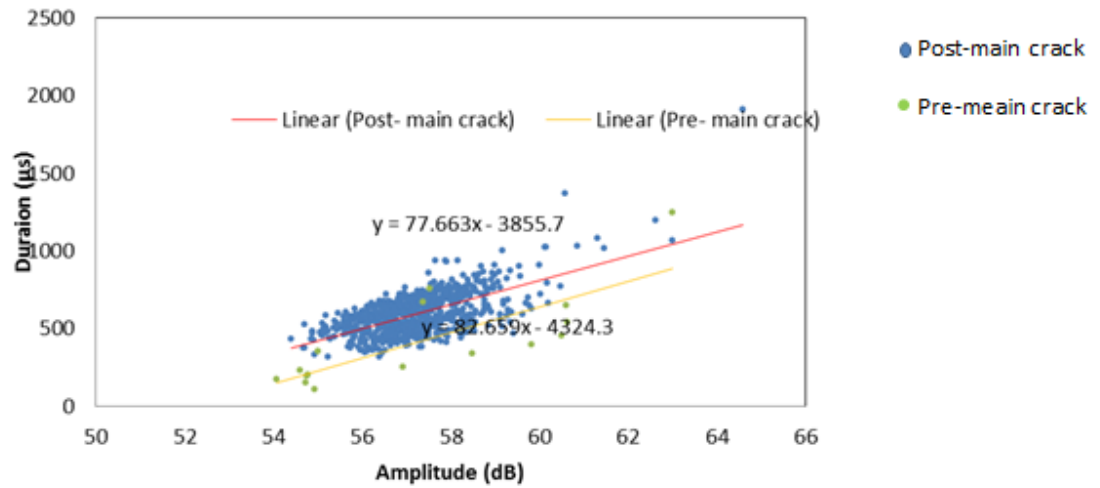
Figure 4.14: Amplitude distribution for plain and SFRC beams (TA2 or #2 and TA7 or #7)

Based on the findings given in Figure 4.15 the AE activities for the plain concrete specimen (#2) in the pre- main cracking stage (micro- cracking stage) were far lesser compared to the SFRC specimens (#6 and #7).

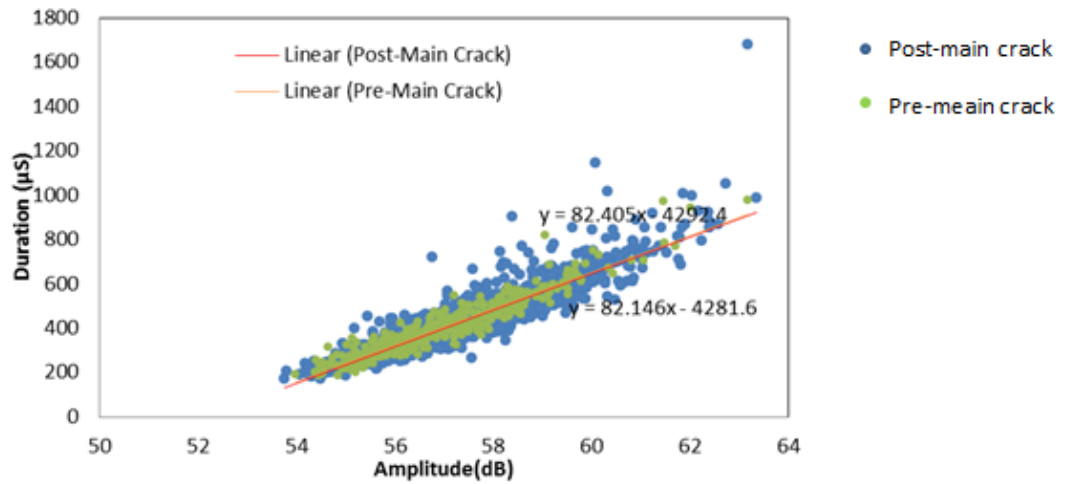
This might be due to concrete fracture behavior for plain concrete since plain concrete causes significant level of energy emission at the time of macro fracture which is attributed to its brittle nature. In addition, the released energy for plain concrete was slightly higher than to the SFRC specimen (Figure 4.14) as result of abrupt failure. On the other hand, the steel fibers have given rise to plastic deformation behavior that contributed to retaining a substantial portion of the energy before fracture. This behavior increased the energy absorbed by SFRC specimens, resulting in a more ductile beam, but at the same time decreased the peak amplitude and energy of AE signals.

Figure 4.15 shows duration versus amplitude data for specimens #2, #6, and #7. The signal duration for specimen #2 ranged between 200 μ s to 600 μ s while the range was between 200 μ s to 1000 μ s for the SFRC specimens. The longer range of signal duration could be used as an indicator to identify the presence of steel fibers in concrete beam.

a)



b)



c)

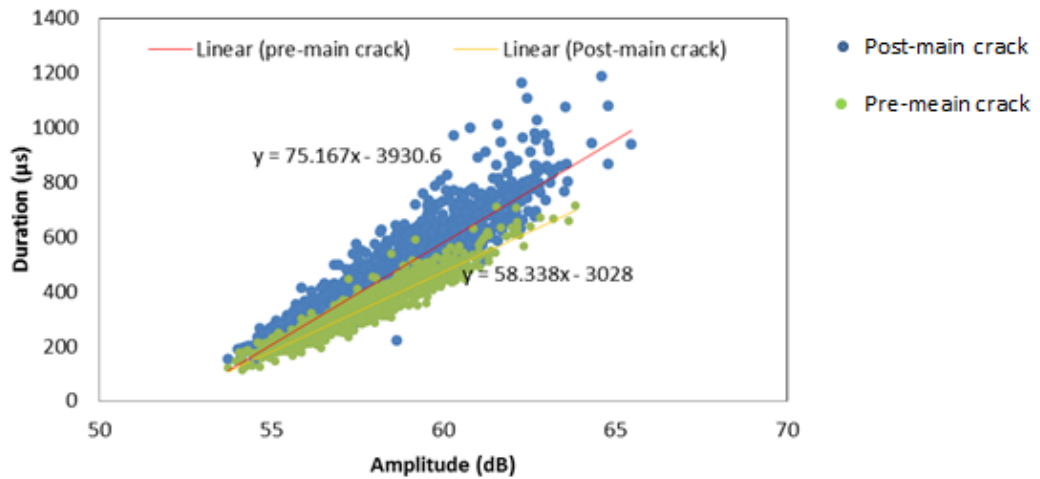


Figure 4.15: Typical AE amplitude distribution versus duration, a) specimen #2, b) Specimen #6, c) specimen #7

4.2.5. Conclusion

This study explored the application of acoustic emission technique in conjunction with Weibull statistical analysis for concrete specimens under torsional loading. A comprehensive study on b-value analysis demonstrated the capability of b-value results for the purpose of quantitative damage condition assessment and fracture process analysis in the case of torsional loading. In addition, Bi-logarithmic regression analysis was performed to determine the Weibull damage function parameters. The obtained parameters were implemented to create a Weibull damage distribution curve which was compared to the cumulative AE curve. The results suggested that the calibrated AE data can properly predict the fracture behavior on plain and SFRC beam specimens.

The plots obtained through the test also demonstrated that the cumulative AE events can be correlated to the mechanical loading–rotation curve (Torque-twisting angle) since the cumulative AE events increased significantly while load was approaching the maximum peak load due to the fracture energy released from micro-crack initiation.

Moreover, AE parameters such as AF, RA and amplitude are able to properly describe the progress of damage associated with torsional load.

4.3. Acoustic Emission Monitoring of Multi-Cell Reinforced Concrete Box Girders Subjected to Torsion

In the following the theories, analysis, results and conclusions is given for this article. The related experimental set up is presented in section 3.4.

4.3.1. Cumulative Signal Strength (CSS)

An increase in rate of recorded AE indicates an increase in the rate of crack propagation. Therefore the total number of AE hits as function of time is an important test parameter. However there are more valuable parameters such as cumulative signal strength. Signal strength is defined as the integral of the rectified voltage signal over the duration of the AE waveform packet. It is sometimes referred to as relative energy which relates to the energy amount released by the material or structure. Signal strength is independent of gain and calculated over the whole AE signal dynamic range. Thus, signal strength could be one of the more reliable parameters to evaluate the damage level quantitatively compared to other primary parameters such as hit. In fact, AE hit or count cannot provide information about the intensity and strength of signal. Signal strength itself is a function of both the amplitude and duration of the signal. In addition, the total number of hits may be affected by duration of loading and unloading.

Hence, the cumulative signal strength (CSS) is considered a feasible parameter to be used for assessing damage evolution in a material.

4.3.2. Intensity Analysis (IA)

IA evaluates the structural significance of an AE event as well as the level of deterioration of a structure by calculating two values called the historic index (HI) and severity (Sr) (Gostautas et al., 2005). The HI compares the signal strength of the most recent emissions to the signal strength of all emissions.

This requires estimating the slope changes of the cumulative signal strength (CSS) plotted as a function of time. The presence of one or more peaks may reveal the occurrence of new damage or the propagation of damage, respectively.

Severity is the average of J , the largest signal strength emissions received at a sensor. As the severity is a measure of structural damage, an increase in severity often corresponds to new structural damage. Analytically, the HI and the S_r are defined as

$$HI = \frac{N}{N-K} \left(\frac{\sum_{i=k+1}^N S_{oi}}{\sum_{i=1}^N S_{oi}} \right) \quad (4.13)$$

$$S_r = \frac{1}{J} \left(\sum_{m=1}^J S_{om} \right) \quad (4.14)$$

Where N is number of AE emissions (referred to as ‘hits’) up to time t ; S_{oi} is the signal strength of the i th event; K and J are empirical constants based on the material under investigation (Fowler and Blessing, 1992). In the present study the following values for K and J are used: for $N \leq 100$, K is not applicable; for $101 < N < 500$, $K = 0.8N$; and for $N > 500$, $K = N - 100$; for $N \leq 20$, J is not applicable whereas for $N > 20$, $J = 20$.

This technique is assessed based on the AE signal strength data collected from each sensor. The maximum values for S_r and HI are normally plotted as intensity chart zones, which indicate the structural significance of the emission.

4.3.3. b-value Analysis

The b-value is a parameter defined originally by Gutenberg and Richter for estimating the likelihood of occurrence of earthquakes above a specified magnitude M (Rao & Lakshmi, 2005; Ohstu, 1996). The equation is as follows:

$$\log_{10} N = a - bM \quad (4.15)$$

Where M is the Richter magnitude of earthquakes, N the incremental frequency (i.e., the number of earthquakes with magnitude greater than M), a is an empirical constant and b is (which is called b -value) is the slope, and A_{dB} is the peak amplitude of the AE signal in decibels.

For the application in AE technique, the Gutenberg-Richter formula, therefore, is modified as follows:

$$\log N = a - b(A_{dB}/20) \quad (4.16)$$

where N is the incremental frequency (i.e., the number of AE hits or events with amplitude greater than the threshold A_T), a is an empirical constant and b is the b -value (Colombo et al., 2003)

Although significant research has presented the applications of b -value, few if any such approaches have been applied for torsion damage quantification. In this study, a b -value analysis has been conducted to quantify damage process in large scale RC beams subjected to pure torsion loading.

In addition, a Gaussian Smoothing filter was implemented to deal with un-smoothed large data sets of the b -value which had caused an unclear trend in raw b -value preliminary results.

4.3.4. Test Result and Discussion

The results and discussions pertaining to the experimental program of this study by using introduced methodology will be presented in the following sections.

4.3.4.1. Crack development

Based on the visual observation on the mechanical fracture behavior, the propagation of crack could be classified into four different stages, namely: micro cracking, first visible crack initiation, crack distribution and damage localization.

Figure 4.16 shows the relationship between torque and angle of twist of all specimens. It could be observed that in general the twist developed linearly with torque at initial stage of loading.

In SC specimen, the first visible crack was observed at 4kN (Point A in Figure 4.16a), while for DC and TC specimens, it was observed at 14.2kN and 20kN (Figures 4.16b and 4.16c), respectively.

Prior to this micro cracking was considered to have taken place within the specimens, which occurrence could be detected with the aid of AE monitoring. It was also observed that the location of the first visible crack was near to the mid-span of specimen. As the loading was increased, the crack further propagated to cross the side face of the specimen and continued to the top face while there were some new cracks developing simultaneously. This stage, known as the crack distribution stage, was detected when load reached approximately 50% of its ultimate load (point B) as depicted in Figures 4.16a-c. As the increase in loading persisted, cracks propagated in a spiral pattern on the four faces of specimens. This process was observed till the torsional moment reached approximately 70% of the ultimate load, i.e. 16.2 kN, 38.5 kN and 72 kN for SC, DC and TC specimens respectively (point C in Figure 4.16a-c). During this stage, the width of the cracks expanded and no new crack initiation was observed, signifying the development of localized fracture by the existing cracks.

By considering the definition of stiffness, Figure 4.16 shows that as load increases the slope of torque-twist curve decreased which implies that the torsional stiffness of the specimens decrease with the widening of the cracks at mid span. The failure mode for all specimens was crushing of concrete.

The ultimate torque and angle of twist of the specimens at failure (point D) are tabulated in Table 4.4. The ultimate load for DC and TC specimen is 2.7 times and 4.5 times higher than ultimate load of SC specimen, respectively. It can be concluded that the torque angle for the single cell girder 25% higher than the total torque in case of the double cell based. For triple cells, the torque for a single cell is 33% higher than the total torque for multi cell girders.

Apparently, SC specimen has more ductility than the other two specimens DC and TC after reaching peak point at 15.40 degree. The angle of twist for single cell is 1.7 times and 1.3 times higher than that for double and triple cells, respectively.

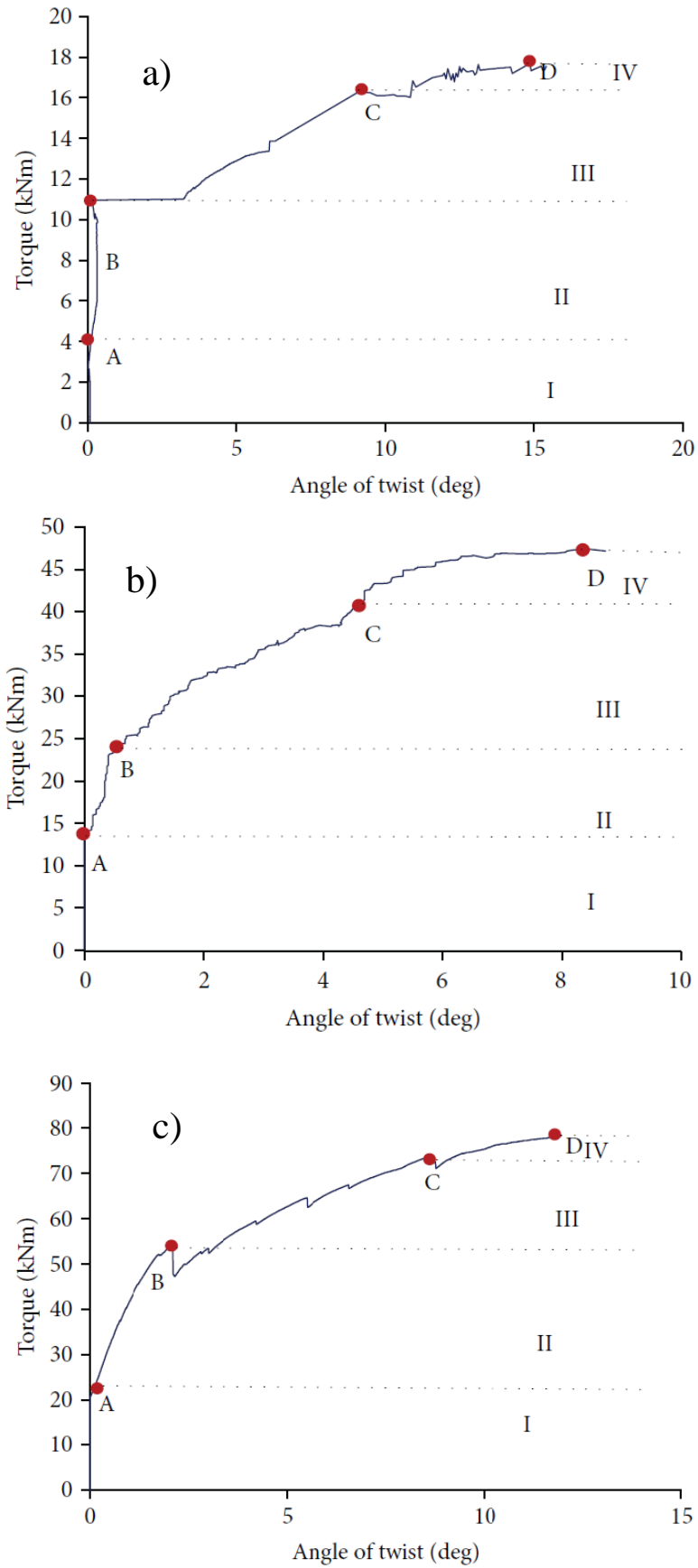


Figure 4.16: Torque-Angle of twist: a) Single cell section girder, b) Double cell section girder, c) Triple cell section girder

Table 4.4: Ultimate Torque and corresponding twist angle of specimens

Specimens	Ultimate Torque, (kNm)	Twist at Ultimate Torque, (degree)
SC	17.5	15.4
DC	47.13	8.9
TC	78.3	11.9

4.3.4.2. Damage localization process

Localization technique is required for quantitative methods in acoustic emission analysis in order to accurately obtain the source coordinates of the AE events. In practice, there is a variety of ways for AE localization to obtain the required resolution in one, two, or three dimensions. The principal of Acoustic emission source localization arose from modified earthquake source localization. A detailed description of earthquake localization methods can be found in (Behnia et al, 2014a). To determine the source location, the differences in the arrival times of recorded elastic waves emitted by the fracture at each sensor should be inversely calculated. The source location of acoustic emission is defined by the origin time (start of the rupture) and the source position in Cartesian coordinates (x_0, y_0, z_0). The onset time of the compression wave (P-wave) is the first arrival time of the elastic wave at each sensor (Behnia et al, 2014b). In this study a 3D localization system has been conducted where the principal is quite similar to the determination of earthquake hypocentres in seismology and uses the recorded arrival waves of an earthquake at multiple seismometers.

These algorithms can be modified to fit material testing requirements, and affords the possibility to study different specimen geometries in addition to considering the number of transducers and their arrangement around the object. Figure4.17 shows the crack and damage progress in the specimens under pure torsion loading.

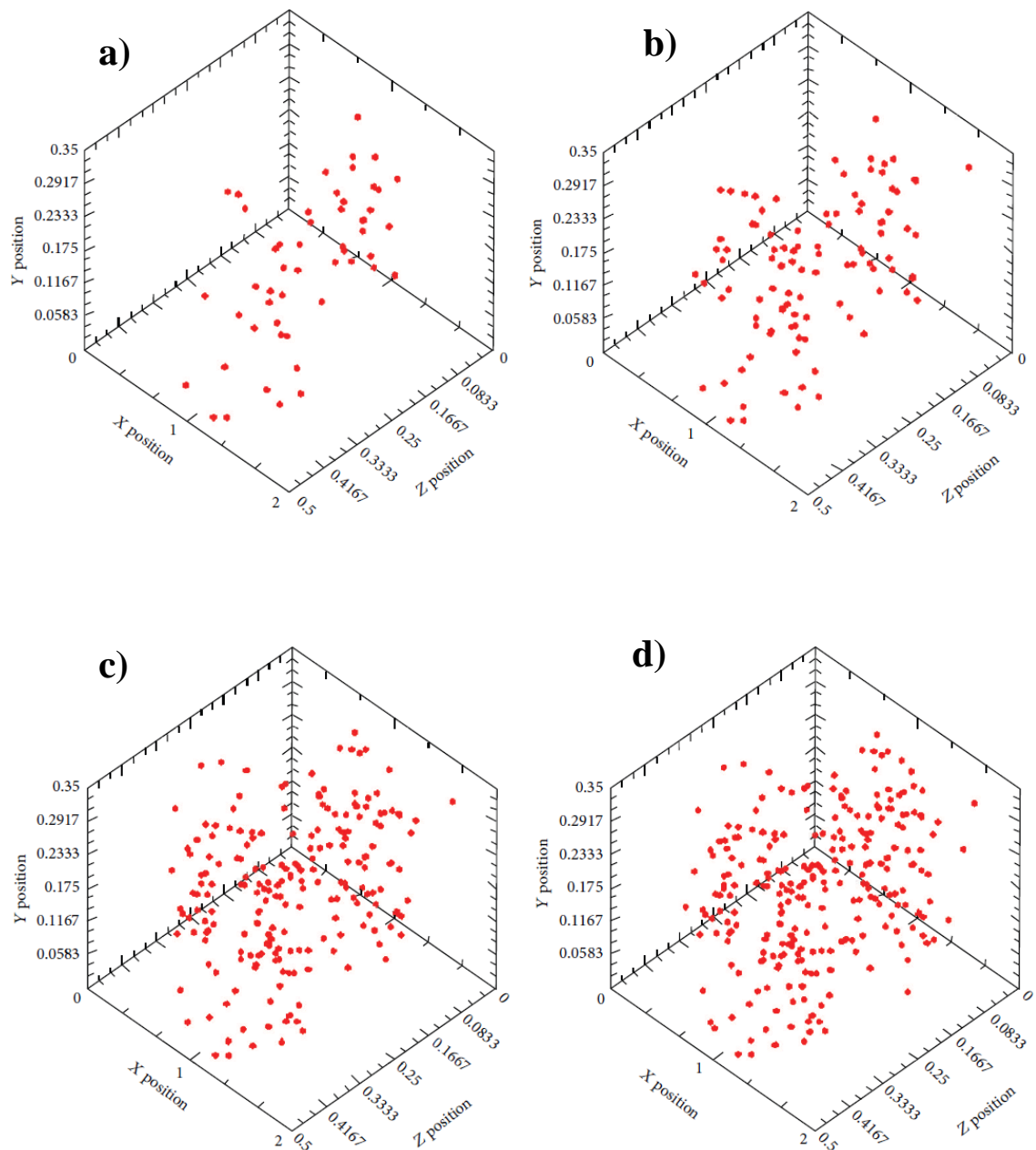


Figure 4.17: 3D even localization of damage progress with respect to progressive damage evolution. a) Stage I, b) Stage II, c) Stage III, d) Stage IV, (unit is based on meter)

It can be conferred from the figures that, although, there are only four sensors mounted on the specimens, there was still a possibility to monitor the active damage under the loading condition. First, it can be observed that in early stage of damage, there are a few events which have occurred in the area nearby position of S1 and S4. The pattern of the occurrence of the event due to progress of damage from early stage (micro-crack) to macro-crack stage tracks the pattern of events in early stage.

This pattern also adapts the pattern of occurrence of the crack which was propagated in a spiral direction throughout the beam. It is demonstrated that the specimens under the pure torsion will undergo the inclined cracks which propagate in spiral direction.

As it was observed in the early stage there were a few events while the rate of occurrence of AE signals rose in the second and third stage of damage, especially in the transition of first visible crack to the stage of crack localization. On the other hand, in the last stage while the cracks are being widened rather than being propagated, again the rate of occurrence of AE events dropped. This phenomenon also conforms to the b-value results in another way, i.e. when in the early stages the number of occurrence of AE events are high the amplitude of AE signals are lower, where as in the last stage while there are fewer numbers of AE event but with higher amplitudes.

4.3.4.3. Qualitative AE Analysis by AE Hit

The relation between torque time of loading and AE hits data of the specimens are given in Figure 4.18. The torque moment applied on specimens has caused rotation and micro crack initiation. The transient release of strain energy as a result of micro cracking was detected by AE sensors and identified as an AE hit. During the initial stage of loading, the cumulative AE hit was low until occurrence of micro-cracks. As damage in the specimens intensified, macro cracking took place and by the time the first visible crack was found the cumulative AE hit increased significantly. In the case of TC specimen, the micro cracking started 10 seconds into the test (triggering point) and there was no significant increase in AE hit till the first visible cracking. Thereafter, the rate of cumulated AE hits increased as the damage continued to progress until ultimate failure.

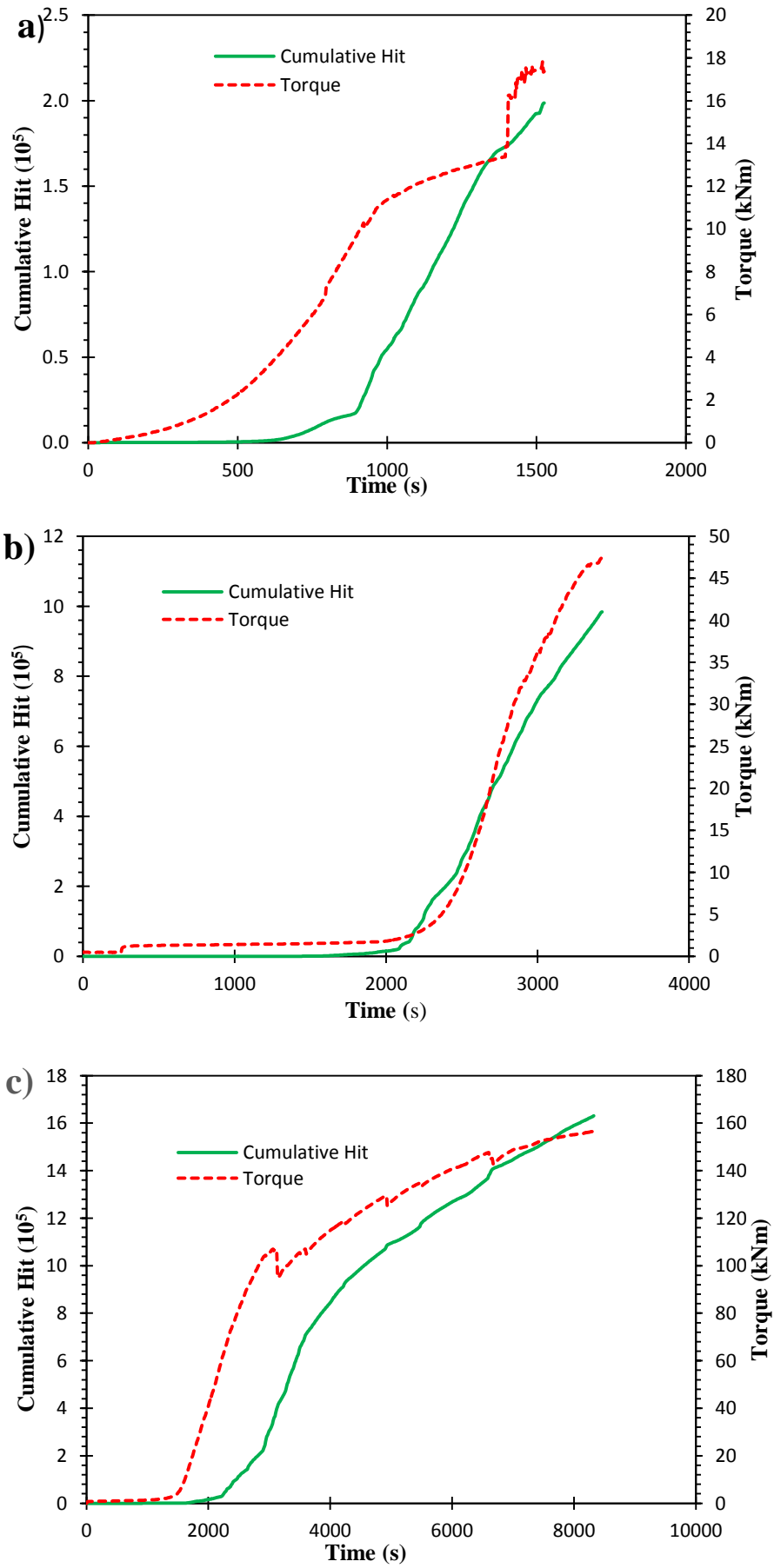
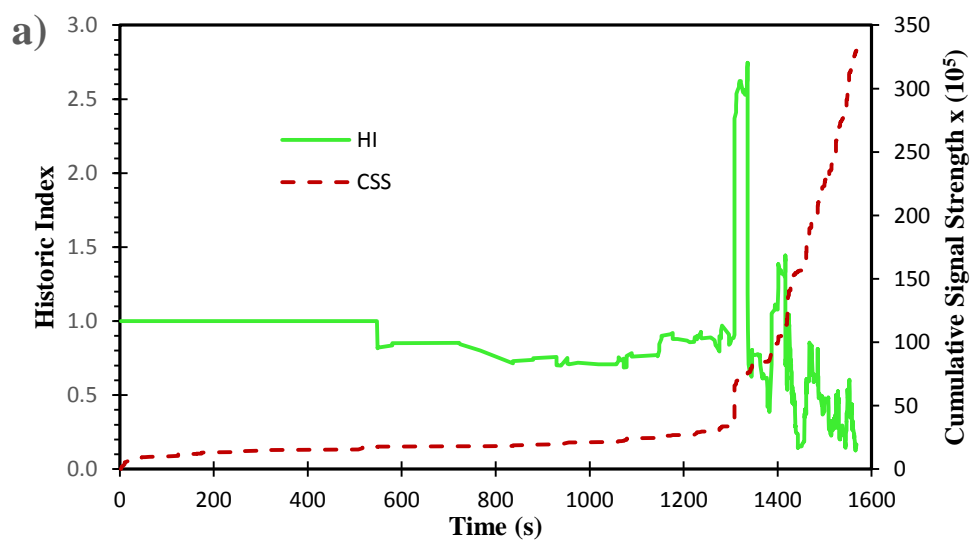


Figure 4.18: Cumulative Hits versus torque moment. a) Single cell section girder, b) Double cell section girder c) Triple cell section girder

4.3.4.4. Qualitative Analysis by AE Signal Strength

Signal strength is a function of both the amplitude and duration of signal. The relationship between cumulative signal strength and historic index could be utilized as a reliable parameter for evaluating damage in structures qualitatively. The condition of specimen can be assessed with data given in Figure 4.19, in which the historic index (HI) and cumulative signal strength (CSS) were plotted shown as functions of time. For clarity, a magnified portion of Figure 4.19a is depicted in Figure 4.24b. The presence of an AE 'knee' defined as a point of significant change in the slope of the CSS, was highlighted in the Figure 4.19. The AE knee may be used to identify possible damage mechanisms and to locate the onset of failure (Gostautas et al., 2005). At loading time of 1200-1260 s, AE knee was obtained for DC specimen. The time interval was in correspond to the occurrence of the first visual crack, signifying the change from micro to macro cracking. Concurrently, high density peaks were observed in the data curve of HI. With increase of torque, the CSS data curve increased gradually as a sign of stage crack propagation. The second AE knee was noticed on CSS data curve at time between 1440 s to 1500 s, which was related to the yielding of stirrups in the mid span of DC specimen. Prior to the initiation of the first visible crack, some HI peaks were observed on data curve. The values of these peaks were not substantial and were corresponding to initiation of micro cracks within the specimen. Figure 4.20 shows the severity (S_r), as a function of time with a plot of SCC superimposed. Both plots were qualitatively very similar. Distinct changes could be observed in both the S_r and CSS curve at almost the same time as indication to the apparent increase of damage in the specimen under loading. It has been demonstrate that signal strength as a conventional AE parameter, either in the form of cumulated or un-cumulated values, can be taken as an indication of damage state in specimen.

As can be seen in Figure 4.20 signal strength variation (either SCC or Sr) was negligible upon visible cracking point at which sudden increase occurred in signal strength. This incremental trend might indicate changes in damage state from stage II to stage III. A second incremental change was in corresponding to yielding of stirrup. Thereafter, a gradual increasing trend implies macro crack opening width which is a progressing damage till final failure. This should be highlighted that events like first macro crack occurrence or yielding or reinforcement could increase the signal strength and consequently increase in historic index and severity index can be recorded. However, although, the considerable increase is recorded for both, macro-crack and yielding occurrence, the amount of increase of Historic index at the time of micro-cracking trigger is higher than yielding time. This might be attributed to the number of emitted signals at the time of macro-crack happening. Moreover, at the macro-cracking stage the all four sensors are capturing somewhat same amount of data because of spiral direction of crack propagation, whereas at the time of yielding some of sensors might be affected by attenuation and therefore, the Historic index for group of sensors might be affected by energy attenuation.



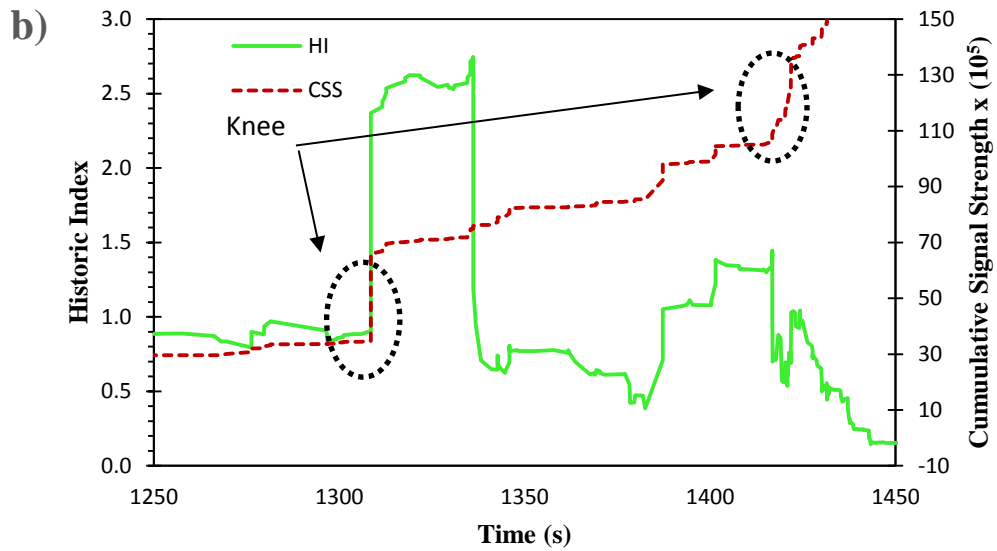


Figure 4.19: AE signal strength analysis for DC specimen. a) Historic index as a function of time. The plot of the cumulative signal is superimposed. b) Magnified portion of plot

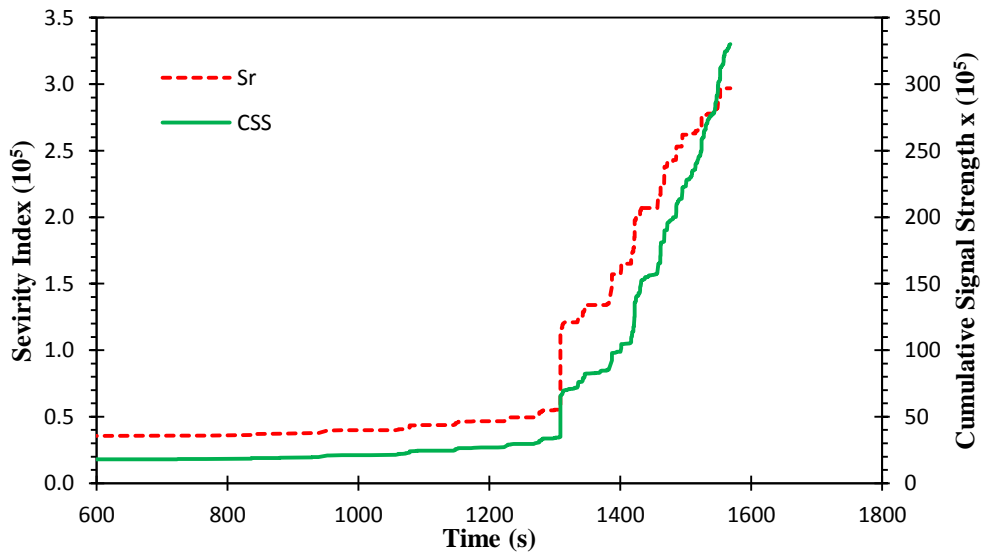


Figure 4.20: Severity index as a function of time for DC specimen. The plot of the cumulative signal is superimposed

4.3.4.5. Quantitative AE Analysis by Intensity Analysis (IA)

By adopting IA technique, the acquired AE data was used to obtain the indices from Equations 4.13 and 4.14. The intensity chart was prepared by plotting the maximum of the average values of HI and Sr for each stage of damage. Figure 4.21 shows the intensity charts for double cell specimen.

The maximum values of HI and Sr from each channel obtained for each stage of damage in the current experiment are plotted in Figure 4.21. In general, intensity values that are clustered toward the top are associated with the phenomena of high structural significance events, whereas less structurally significance events could be found concentrating near the bottom of the chart. Figure 4.21a shows the intensity chart for DC specimen at first stage of damage (stage I). From the start of loading and prior to initiation of the first surface crack, no significant AE activity was recorded with all channels. Therefore based on the IA, the specimen condition could be considered to be in stage, recognized as the micro-cracking stage.

As load was increased and the first visible crack was detected on the face of specimen, significant increase in severity index value was observed at channel 1 which was closer to the area of first visible cracking. The damage condition shifted to stage II, which represented the minor surface cracking. After occurrence of the first visible crack, the transverse strain of stirrups was found to increase dramatically. Crack propagation and distribution was observed more at left side of the specimen where sensors 2 and 4 were mounted. The higher Sr values were obtained at channels 2 and 4, which confirm that the greater amount of damage occurred in the area of channels 2 and 4. In stage III of damage elaboration of the defects is required. As load was increased until the maximum, cracks started to localize to form major cracks, with the width of cracks increasing considerably.

The value of severity index from all channels was increased considerably. The damage severity stage was identified to be in stage (IV) which was known as serious fracture that required detailed inspection.

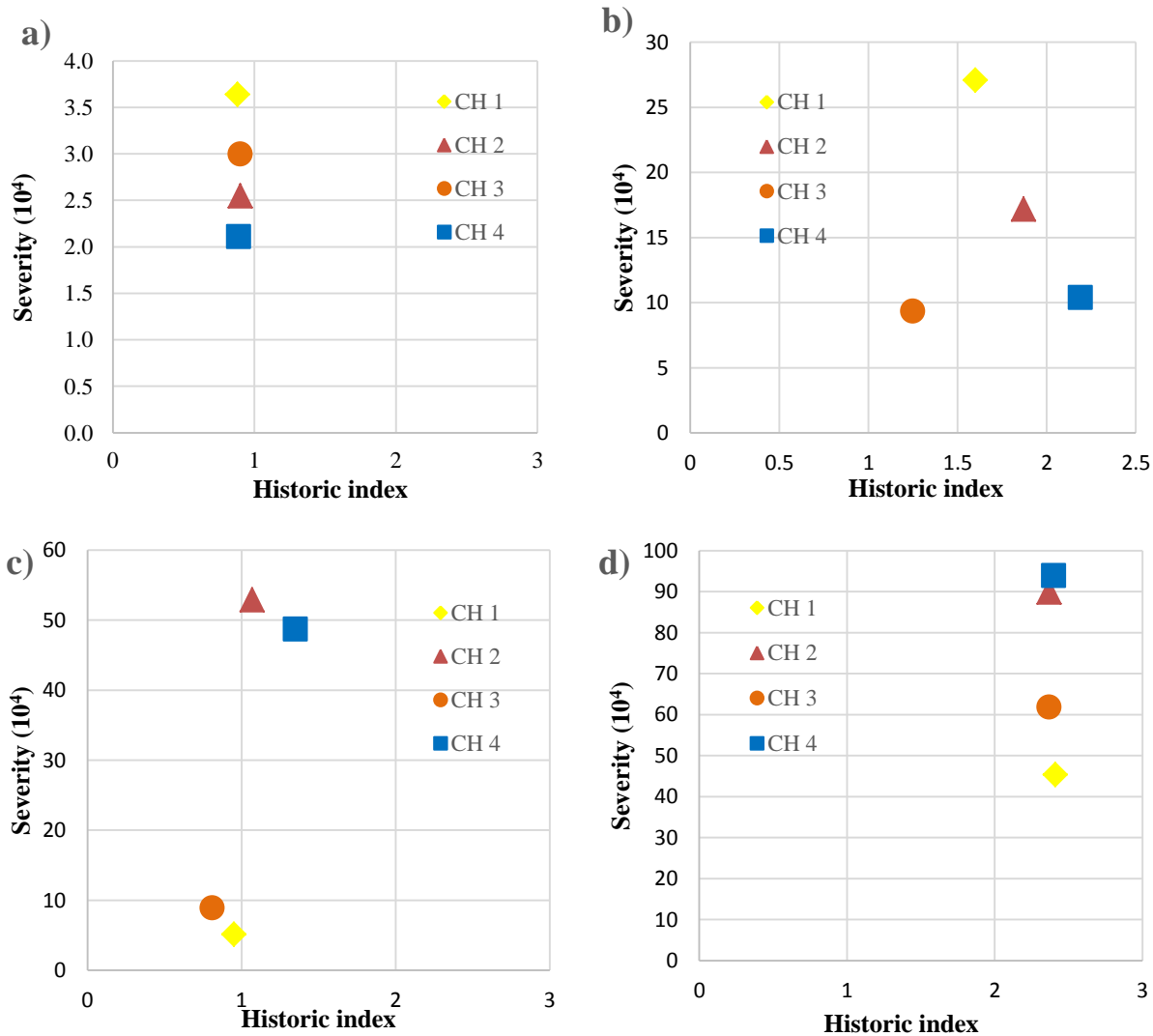


Figure 4.21: Intensity chart for double cell specimen at each stage of damage. a) Stage I, b) stage II, c) stage III, d) stage IV

4.3.4.6. Damage Quantification by b-value Analysis

A b -value analysis was performed to quantify torsion damage of specimens in a different way. The b -value was computed based on using groups of $n = 100$ AE signals. Figure 4.22 illustrates the b -value obtained taking into account AE signals recorded from the whole monitoring period for TC specimen. The estimated probability density function is placed in the top side of Figure 4.22.

It is interesting to find that a Gaussian distribution could be fitted reasonably well with the mean and the standard deviation calculated from the b -values.

As can be seen for the Figure4.22, although the general decreasing trend of the b -value was indicative of the evolution and progress of damage in the specimen, it became challenging to identify a definite trend for the b -value in each particular stage of damage. The discrepancy that occurred most likely attributed to the large amount of AE activities generated during the process concrete fracturing during torsion loading. In the case for the other specimens, similar results were obtained for the DC specimen but not for the SC specimen because of the insufficient data for analysis. It is reckoned that the difficulty in identifying a proper b -value trend for each stage of damage could be a drawback in real time monitoring of structures. Therefore, to provide a reliable elaboration for b -value trends associated with the progress of damage, the Gaussian filtering was introduced to analysis. The window span selected was 5% of the data vector length. In addition, the standard deviation was set as a quarter of the window span. Figure4.23 shows the smoothed b -value data after application of Gaussian filtering method. The corresponding damage level is indicated in the graph. As can be seen, from the Figure4.23, after filtering the raw data, the trend of b -value variation corresponding to each stage of damage could be distinguished more confidently.

Three distinct stages of damage were recognized to have influenced the trend of b -value. In general, the b -value exhibited during stage I damage was pertinent to initiation and accumulation of microcracks. As fracture in concrete shifted to stage II, which was associated with the formation of the first visible crack followed by macro-cracking, slight fluctuation in b -values results was registered that was accompanied by a drop in magnitude. Finally, in stage III of damage, which is also called macro-crack, a significant drop occurred, while thereafter general decrease is imposed on b -value.

It should be noted that the fluctuation seen in stage II could be associated with formation of a few microcracks that happened in this stage, while the dominant cracks are macro-cracks. The b -value could be regarded as a useful indicator to the stage of damage. Table 4.5 gives the b -value results for all specimens during the different levels of fracture under torsion. It was found that the evolution of damage in RC box girder specimens due to torsional loading could cause significant drop in the b -value. The maximum drop for as acquired from the current analysis ranged between 70% and 75%. It could thus be inferred that the drop in b -value within this range was an indication of critical fracture developed in girders under torsion. A gradual decrease for b -value from stage I to stage III of damage was noteworthy as well, with the b -value decreasing to approximately 1.00 before ultimate failure.

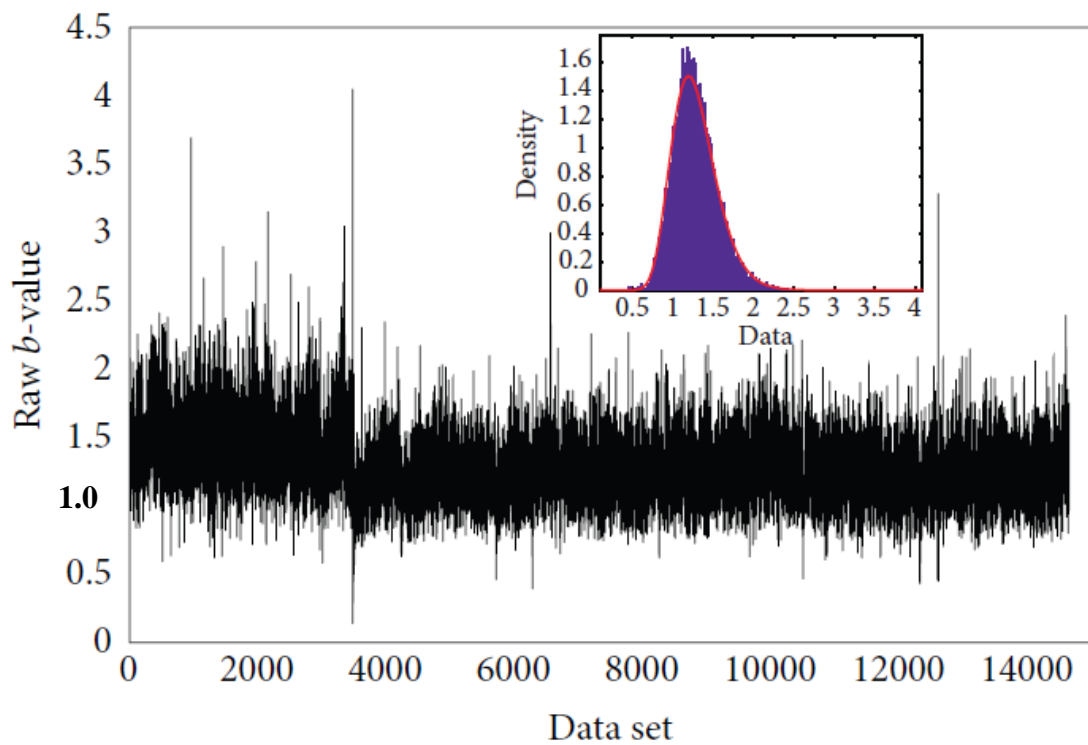


Figure 4.22: Values results for the entire data set before smoothing process for TC specimen

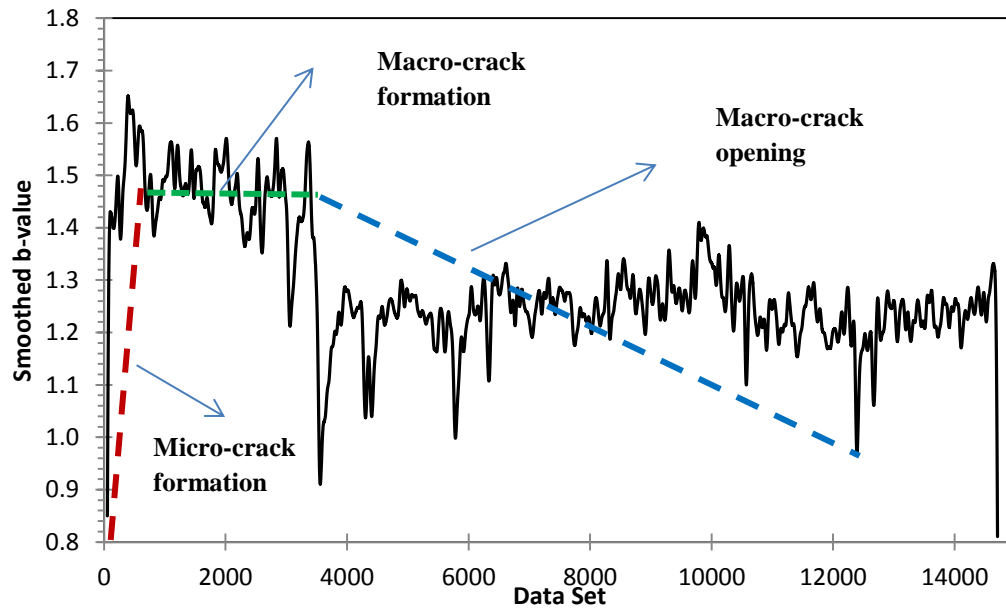


Figure 4.23: Smoothed b-values results for entire data set of TC specimen

Table 4.5: The average b-values for each stage of damage

Specimen	$b1$	$b2$	$b3$	*Maximum drop (%)
SC	1.44	1.30	1.05	73
DC	1.50	1.32	1.12	75
TC	1.68	1.41	1.16	70

*This value presents drop of b-value in last stage relative to the first stage.

4.3.5. Conclusion

Results of AE monitoring of reinforced multi-cell hollow girder specimens are presented in this paper. The AE technique was implemented to characterize torsional failure of girder specimens. AE analysis were carried out in order to provide fundamental information for damage assessment of girder specimens, both qualitative and quantitatively. Hits and signal strength were obtained to provide qualitative evaluation of damage process of girders under monotonic load. Correlation between torque curves and AE cumulative hits for specimens was in good agreement. Analysis of CSS slopes demonstrated that when significant structural events such as macro-cracking and rebar yielding occur, CSS experiences significant changes in the form of a knee in its curve. This study indicates that cumulative hits and signal strength correlate well with the degree of damage of specimens. Furthermore intensity chart was generated for the DC specimen up to the failure point. The results obtained from intensity chart demonstrate the efficiency of this analysis to provide quantitative information on the level of damage severity. In addition, b -values results can be used as a useful quantitative indication of damage. In general, b -value may increase in the early stage of fracture where microcracks are forming and decreases when macro-cracks are being localized.

It can be concluded that when the average of b -values results are approaching unity that might be an indication of serious damage or final failure of the structure subjected to torsion loading. To sum up, both qualitative and quantitative methods might be required to assess the level of damage and register the true pattern of the structure failure.

4.4. Unsupervised Acoustic Emission Damage Detection Technique Incorporating Kernel Fuzzy C-Mean for Structural Concrete Subjected to Pure Torsion

In the following the theories, analysis, results and conclusions is given for this article. The related experimental references are presented in section 3.3.

4.4.1. Theory and Procedure of Application of Pattern Recognition in AE

Application of AE to differentiate mode of fracture in FRC beams by means of moment tensor analysis has been demonstrated in some studies (Reinhardt, Grosse & Weiler, 2001). Consequently, crack classification may enable prediction of the final fracture mode through which required action can be taken in necessary conditions (Aggelis et al., 2012). It should be mentioned that for such materials, application of AE involves serious difficulties. The main concern is the accuracy of the interpretation of the results as there are different stages contributing to fiber reinforced concrete fracture (FRC).

It is noteworthy, while loading concrete structures until failure, matrix cracking develops at moderate loading level and rapid expansion of cracks develop at high loading level. Therefore, it can be useful to monitor and differentiate stages of damage progress to evaluate structural damage state. Although AE conventional parameters have been using to characterize and quantify the damage state for concrete structure, conventional AE analysis are mostly inadequate for real time monitoring and warning systems. This is because conventional AE analysis does not consider the uncertainties predominant in the structural characterization problem. It should be noted that uncertainty is an imperative challenge for damage analysis in practical health monitoring cases. Several factors such as geometry of structure, environmental noise, material properties, sensor properties, temperature, and measurement inaccuracy are among significant sources of uncertainty.

The above mentioned uncertainty might be added to the random nature of fracture process which increases the inherent variability of AE measurements. Actually, fracture process in terms of crack propagation trend is a unique event in which different fractured areas or released energy from one event to another can be observed. The above stated facts reveal that there are several external sources of error or variability which might mask the accurate classification of AE features. To this end with the aid of the ever progressing field of computer science, probabilistic and pattern recognition approaches are pervasively being utilized in the field of structural health monitoring. Consequently, the field of acoustic emission (AE) is gaining popularity to enhance pattern recognition techniques in order to understand the underlying source of mechanism or to define criteria for probabilistic decision making (Godin, 2004; Sause et al., 2012; De Oliveira and Marques, 2008; Sause and Horn, 2013; Kahirdeh and Khonsari, 2013).

However, thus far conventional AE parameters such as counts, amplitude, and energy were used in most studies to discriminate between different AE events and their relationship to the progress of failure mechanisms. Moreover, each signal might be associated with a pattern formed of multiple relevant descriptors. The simultaneous study of various AE parameters may result into more consistent information to obtain better comprehension of AE source mechanisms, particularly when associated with pattern recognition algorithms (Bar et al., 2004). Since it may not be possible to distinguish the origin of an AE event precisely to provide a training set of patterns belonging to various combined damage mechanisms, unsupervised pattern recognition can be utilized to solve the problem of cluster labelling (Moëvus, 2008).

Numerous studies were put forward to improve multi-variable clustering of AE data to enhance accuracy of classification (Pappas et al., 1998; Huguet et al., 2002; Godin et al., 2005; Chandrashekar et al., 2003; Johnson, 2002; De Oliveira and Marques, 2008; Omkar et al., 2002; Omkar and Karanth, 2008). Although there are several studies were dedicated, most of them were in supervised method and they are not practical for concrete structure application. Furthermore, there is a technique called Fuzzy c-mean performs that was demonstrated as a great tools for unsupervised monitoring in composite material. FCM performs well fairly well in cases where a high level of overlapping of data (acoustic emission has many overlapping data) may cause confusion. However, in noisy condition like concrete structural loading there is a high level of noise. FCM seems to be sensitive in noisy environment because of their non-linear clustering approach (spherical), the main drawback for FCM algorithm is the sensitivity to noise or outlier.

To this end, in this study a kernel trick was added to FCM kernel fuzzy c-means (KFCM), to overcome existing drawbacks in FCM for fracture process classification in concrete structures.

Therefore, in this study small-scale concrete samples were tested under the pure torsion loading. AE raw data were taken to classify different stages of fracture mechanism.

First, the relevance of AE parameters were found by principal component analysis (PCA) and after reduction of input parameters, kernel fuzzy c-means (KFCM) was adopted to classify each particular stage of fracture process by using unlabelled AE data. It should be noted that KFCM compared to the other classical methods such as FCM which has been recently applied to AE data, is capable to map nonlinearity of the input data space into a high dimensional feature space. Fuzzy c-means clustering method will be largely limited to spherical clusters only.

By applying kernel fuzzy c-means algorithm attempts to solve this problem by mapping data with nonlinear relationships to appropriate feature spaces Principles of PCA and KFCM descriptions are discussed briefly as below.

4.4.2. Principal Component Analysis (PCA)

PCA is known as a mathematical algorithm that might be implemented to decrease the dimensionality of a data set for compression, pattern recognition and data interpretation.

PCA description is given earlier in section 4.2.3.1.

4.4.3. Kernel Fuzzy C-mean (KFCM)

For determination of the structure in data, fuzzy clustering provides an imperative insight by generating gradual degrees of membership to individual patterns within clusters. The technique of the fuzzy c-means (FCM) (Bezdek, 1981) is a well-known approach of data classification thereby a set of data will be clustered by making use of mutual distance between a pair of objects. Indeed, the clustering is called unsupervised classification since the clustering will be accomplished without utilizing any standards from outside (Duda et al., 2001). The FCM take advantages of the probabilistic limitation that the memberships of a data point across classes are equal to one.

This constraint is considered to create the membership update equations for an iterative algorithm. Nevertheless, in case of noisy or distorted data the FCM technique may lead to wrong clusters of the data due to its abnormal feature data which may be the main limitation of FCM. On the other hand, the kernel trick was a well-known method as a general approach to achieve the nonlinear classification boundaries. Kernel-based clustering algorithms will provide mapped features from the feature space to a higher dimensional kernel space and accomplish classification in the kernel space. There are two key variations of kernel-based fuzzy clustering.

One generates prototypes in the feature space (input space) while the other generates prototypes in the higher dimensional kernel space and finalizes an inverse mapping of prototypes from kernel space back to the feature space. They are given the acronyms kernel fuzzy c-mean (KFCM) and multiple kernel fuzzy c-mean (MKFCM), respectively. Kernel based fuzzy c-mean was effectively applied to overcome FCM drawback (Wu et al., 2003). It builds the nonlinear version of FCM and makes a kernel-based fuzzy C-means clustering algorithm.

The fundamental concept of KFCM is twofold: first is to map the input data into a feature space with higher dimension via a nonlinear transform and second is to perform FCM in that feature space. Therefore, the original complexity and nonlinearity existing in data structure in input space may turn out to be simple and linearly separable in the feature space after the nonlinear transform.

KFCM takes some non-linear mapping function $H: \varphi: x \rightarrow \varphi(x) \in \mathbb{R}^{D_K}$, where D_K is the dimensionality of the transformed feature vector x . Most, if not all, kernel-based techniques do not explicitly transform x and then operate in the higher-dimensional space of $\varphi(x)$; instead, they utilize a kernel function k that represents the inner product of the transformed feature vectors, and H can be presented by a kernel function $k(x_i, x_j) = (\varphi(x_i) \cdot \varphi(x_j))$ and then $K_{ij} = k(x_i, x_j)$.

This kernel function can take many forms, with the polynomial ($k(x_i, x_j) = (\sigma x_i^T x_j + r)^d$), and radial-basis-function (RBF), $k(x_i, x_j) = \exp(-\|x_i - x_j\|/\sigma^2)$, being two of the most popular forms. It should be noted that r , d , and σ are kernel parameters. Since,

$$d_H(x, y) = \sqrt{\|\varphi(x) - \varphi(y)\|^2} = \sqrt{k(x, x) - 2k(x, y) + k(y, y)} \quad (4.17)$$

When the kernel function is taken as radial basis function (RBF) then: $K(x_n, x_n) = 1$, $K(v_k, v_k) = 1$, therefore:

$$\|\varphi(x_n) - \varphi(v_k)\|^2 = 2(1 - K(x_n, v_k)) \quad (4.18)$$

The KFCM algorithm can be generally defined as modification of the objective function of FCM

$$J_m(U;V)=\sum_{k=1}^c \sum_{n=1}^N u_{kn}^m \|\varphi(x_n) - \varphi(v_k)\|^2 = \sum_{k=1}^c \sum_{n=1}^N 2u_{ij}^m (1 - K(x_n, v_k)) \quad (4.19)$$

The parameters of KFCM were computed according to the below equations:

$$u_{kn} = \frac{(1-K(x_n, v_n))^{\frac{1}{m-1}}}{\sum_{k=1}^c (1-K(x_n, v_n))^{\frac{1}{m-1}}} \quad (4.20)$$

$$v_k = \frac{\sum_{n=1}^N u_{kn}^m K(x_n, v_n) x_n}{\sum_{n=1}^N u_{kn}^m K(x_n, v_n)} \quad (4.21)$$

$$\text{If } \|J^{(l)}(U, V) - J^{(l+1)}(U, V)\| \leq \varepsilon, \quad (4.22)$$

Then the iteration would be ceased and final matrix U and V are acquired.

In using the pattern recognition technique, classification of AE waveforms has been difficult due to the complexity of the nature of signals. Therefore, reliable descriptors have to be chosen noting that the number of descriptors should be sufficient to perform accurate pattern recognition based on multi-parameter statistical analysis. Most of the studies in AE clustering have used three and up to six descriptors.

In fact, in these studies time domain (e.g. rise time) or frequency domain (e.g. average frequency) descriptors were used separately in order to reduce dimension of clustering space. In this study, eight descriptors have been taken into account by considering the significant diversity of AE waveforms: amplitude, duration, rise time, energy, counts, average frequency, and peak frequency. In order to reduce the dimension of AE data, a PCA algorithm was implemented.

This technique projects data into visible subspace, e.g. two or three dimensions, which is of low dimension space. The PCA was applied on a matrix with $n \times m$ dimension, where m was time and frequency parameters based AE descriptors registered from n AE waveforms. The PCA projection into lower dimension subspaces reveal the similarity and correlation between parameters. If descriptors and data do not overlap with each other, then accurate discrimination between damage or fracture stages can be achieved. Therefore, the relevant features and the their effects in PCA variance have to be validated to derive an accurate pattern of damage or fracture stages. However, after dimensional reduction of AE decriptors, a k-means algorithm was used to determine the sufficient number of clusters. A brief flow chart of the k-means application to reveal the number of clusters is plotted in Figure 4.24.

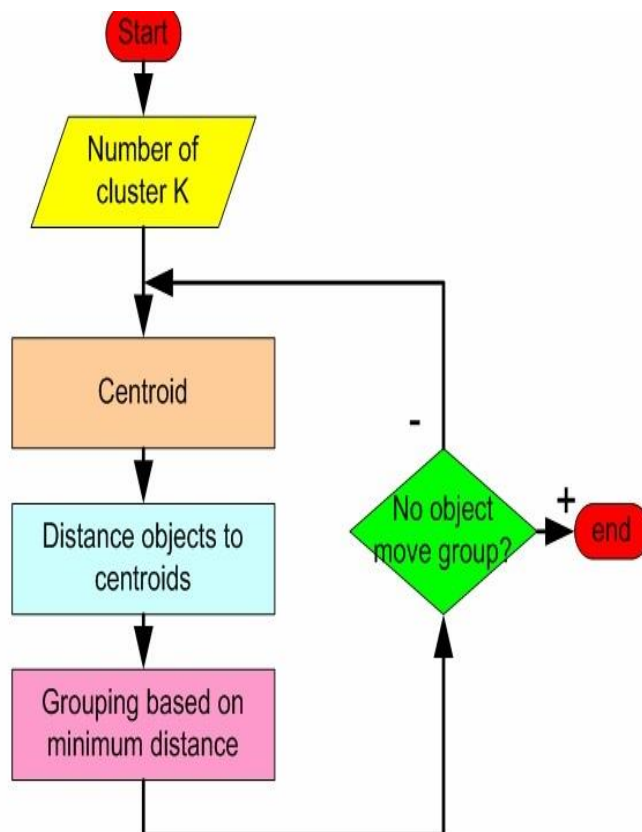


Figure 4.24: Flowchart of determination of number of required clusters by application of k-means

In the last stage the most effective principal components were inserted into the unsupervised KFCM algorithm. Finally, in a low dimensional feature space each cluster is plotted in a particular colour to differentiate the different stages of fracture process.

4.4.4. Spatial Intelligent b-value (SIb) analysis

In the preceding study (Bagherifaez et al., 2014), it was concluded that the classical b-value due to high range of fluctuation might not provide conclusive results. Therefore, a Gaussian filtering was introduced to reveal conclusive trend of b-value variation.

In addition to the above mentioned drawback, outliers and overlapping data in the boundary of each particular stage of fracture may cause difficulty to achieve accurate b-value pertinent to each stage of fracture and point out the damage condition. Therefore, in order to monitor damage condition for each particular stage of fracture process, a novel algorithm called “spatial intelligent b-value (SIb)” is presented in this study. Figure 4.25 illustrates the flow of general SIb-value analysis. The proposed algorithm correlates b-value and cluster analysis to offer more accurate information about the high level of confidence of structural integrity can be obtained in real time monitoring of structures.

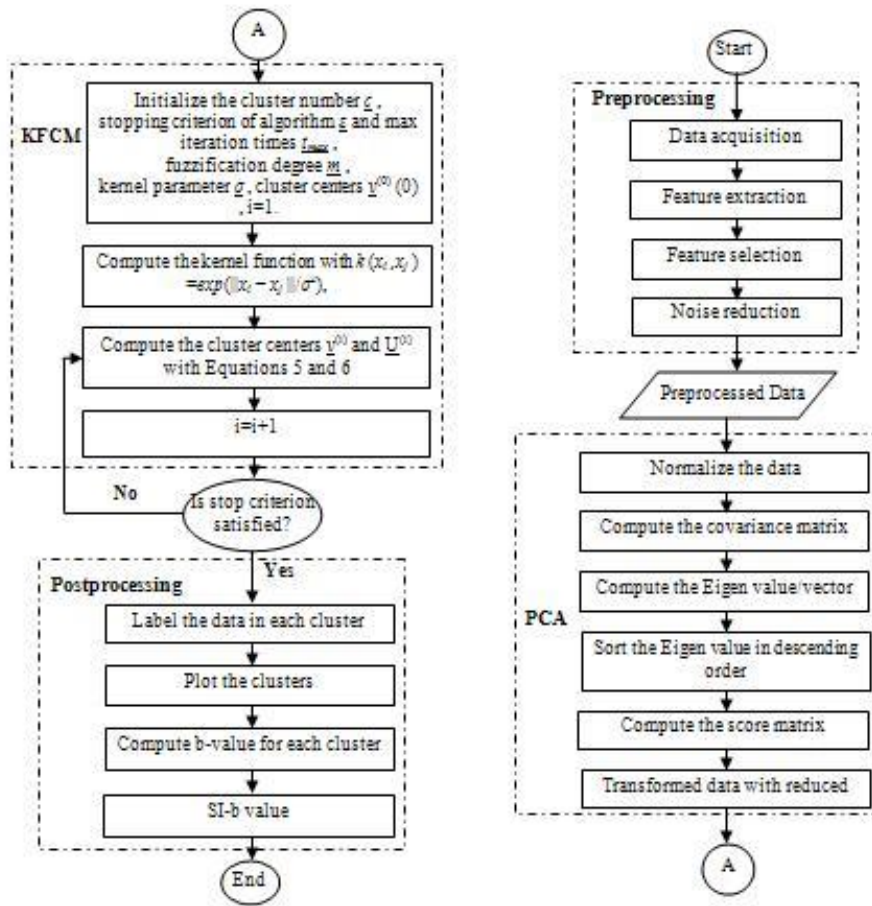


Figure 4.25: Flow chart of SIb analysis

4.4.5. Results and discussion

In the following the related results, discussion and conclusions will be presented.

4.4.5.1. Mechanical Behavior Correlation with AE Activity

Physical and mechanical characteristics of the investigated specimens have experimentally been determined and presented in section 4.2.2.1. The details of structural behavior are given in section 4.2.2.1.

On the other hand, observation of AE occurrence in torsion testing for both plain and SFRC concrete beams can be divided into three different phases. As a typical graph, Figure 4.11 presented in section 4.2.4.6 displays the aforementioned discrimination through which the definition of AE activity in each particular phase for SFRC and plain concrete specimens is noticeable. There are three different stages: 1. stage(I) is micro-cracking in the concrete matrix, 2. macro-cracking stage (II), 3. stage (III) is dominated by softening in plain concrete or gradual pull out of fibers (III) (for SFRC beams). The details were discussed earlier in section 4.2.4.6.

4.4.6. Unsupervised Acoustic Emission Data Clustering

Cluster data of AE analysis will be used in two different approaches, qualitative and quantitative manners.

4.4.6.1. Qualitative Damage Analysis

Different damage mechanisms were registered for plain and SFRC specimens according to the experimental results and AE monitoring. The fracture process in SFRC may start by matrix cracking leading to the failure of different interfaces i.e. between cement paste, sand, aggregates and fiber. Aggregate crushing and fiber rupture occur due to final failure (Aggelis et al., 2012).

In general it is acknowledged that in the fracture process of fiber reinforced concrete (FRC) three different stages might occur: stable micro-cracks, growth of micro-cracks and appearance of visible macro-crack, and rapid expansion of micro-cracks which lead to macroscopic fracture and fiber pull-out. It should be noted that the growth of micro-cracks continues up to a saturation level depending on the fiber volume content whereas in plain concrete for the last stage instead of fiber pull-out phenomenon, the tension softening behavior can be observed.

However, in the present study by aid of k-means algorithm addressed in Figure 4.24 the number of clusters obtained were in good agreement with general behavior of concrete specimens. Therefore, the classification created a three-cluster problem. Multivariate analysis was implemented to discriminate between the damage mechanisms considering AE data. To keep higher level of accuracy, eight descriptors registered from AE parameters were taken into account: amplitude, duration, rise time, energy, counts, average frequency, and peak frequency. The descriptors were then normalized between [-1.5, 1.5] in order to have a comparable set of values between all the descriptors. Therefore, KFCM was then applied with three clusters according to the algorithm described in Figure 4.25. A PCA technique was utilized to reduce the space dimension and to determine the certain required number of dimensions to visualize the results in a two or three dimensional subspace. Figure 4.26 illustrates the percent of the total variability by each principal component.

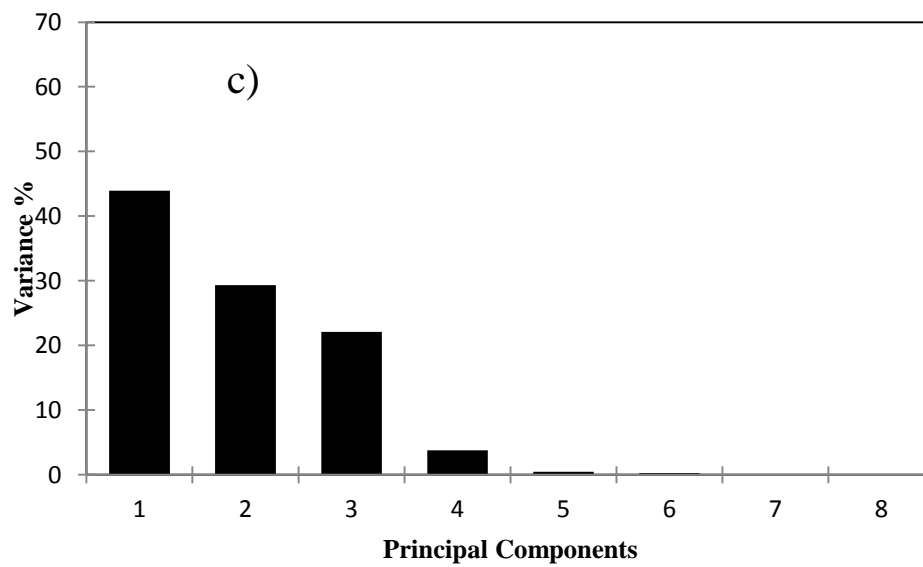
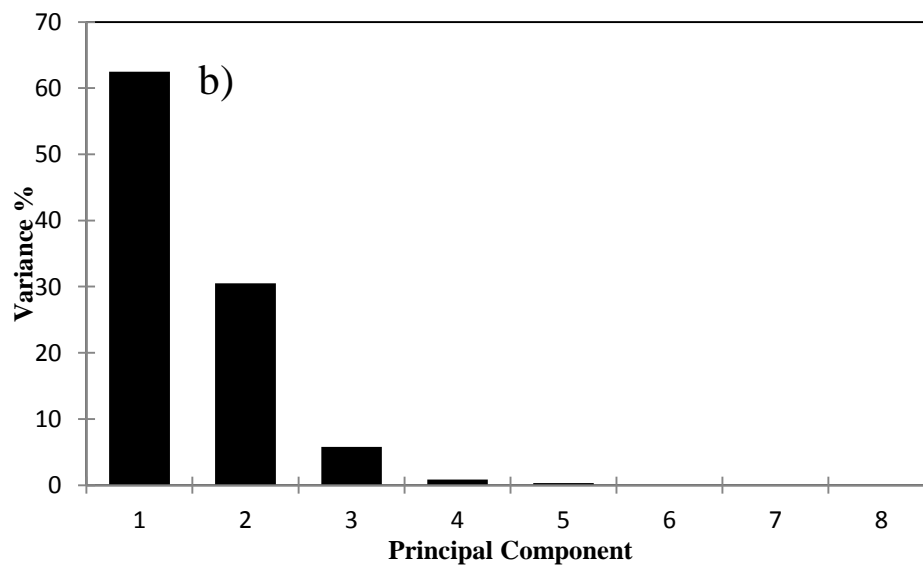
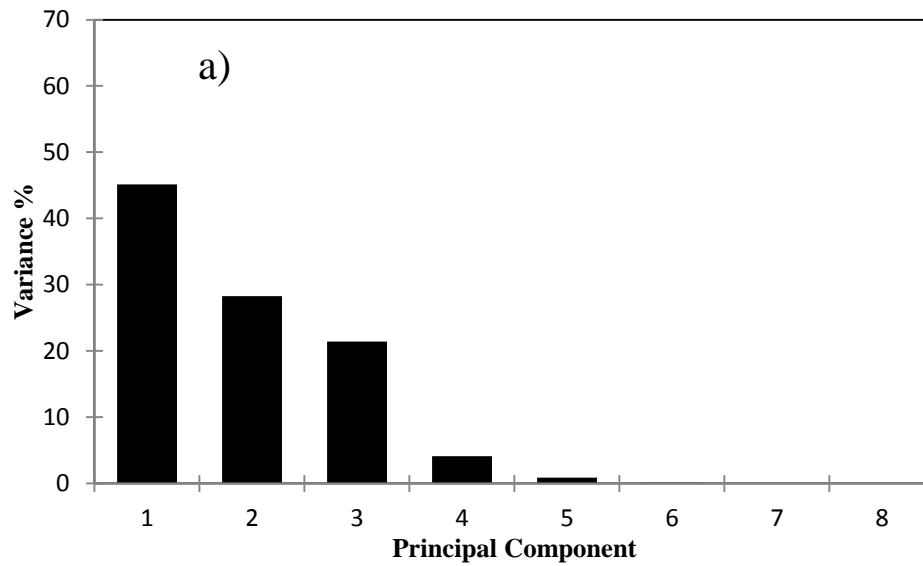


Figure 4.26: The percent of the total variability explained by each principal component for specimen: a) #2, b) #4, and c) #7

It can be realized from Figure 4.26 that the first two components, except case #4, were not merely adequate to explain the total variability in the signal space of three concrete specimens. It might be due to the high number of descriptors. In fact, the combination of time and frequency domains of AE data might be the main reason of this since this combination has less correlation between descriptors. On the other hand, it is noted that the first three principal components can address more than 90% of the total variability in AE data descriptors.

The above statement implies that the first three principal components possess a 3D projection which includes more than 90% of the variance of 8D-data. As noted, this result may refer to successful implementation of PCA technique to reduce the dimension size of space and required computational time for the analysis. Nevertheless, KFCM is able to visualize clustering data in a 3D space. Therefore, by processing signal data projected onto the first three principal components, a 3D plot of signal classifications could be obtained as in Figure 4.27.

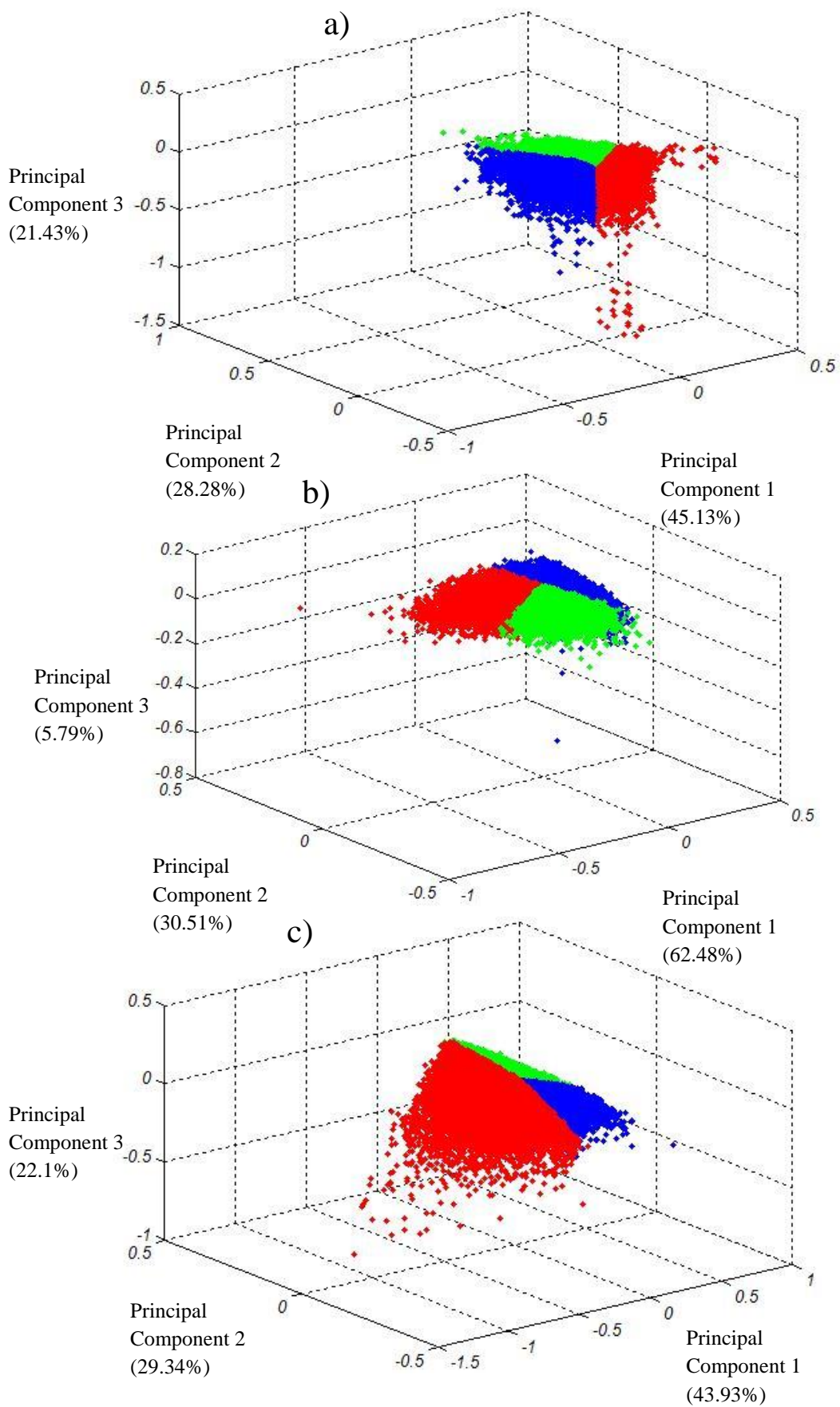


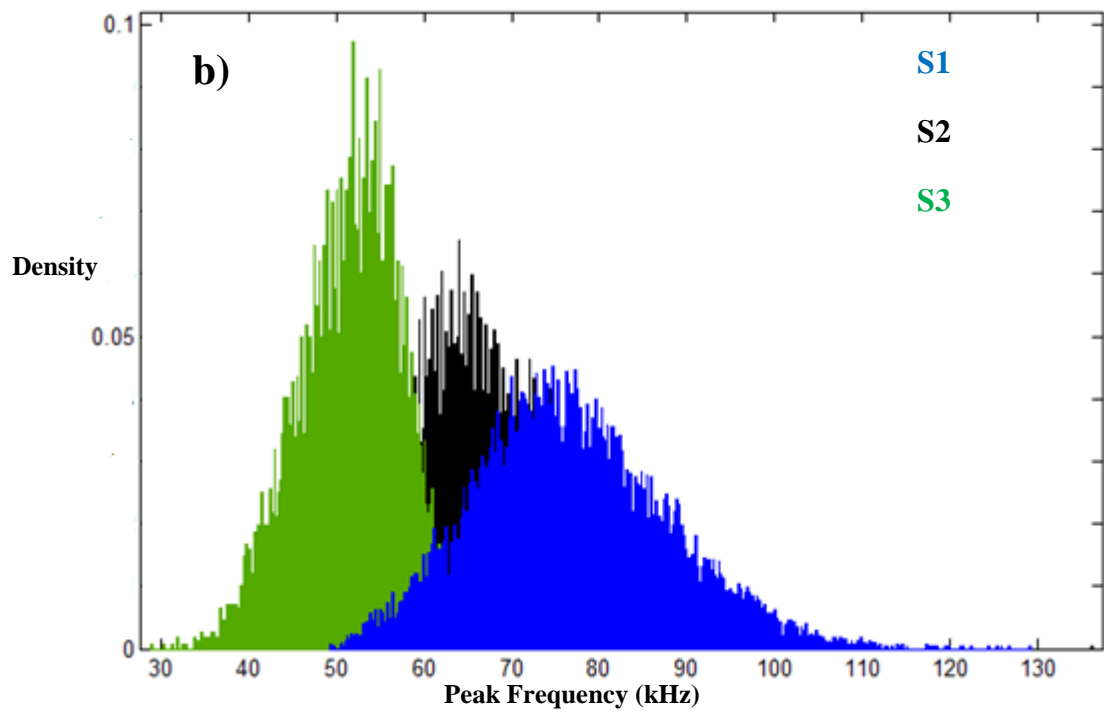
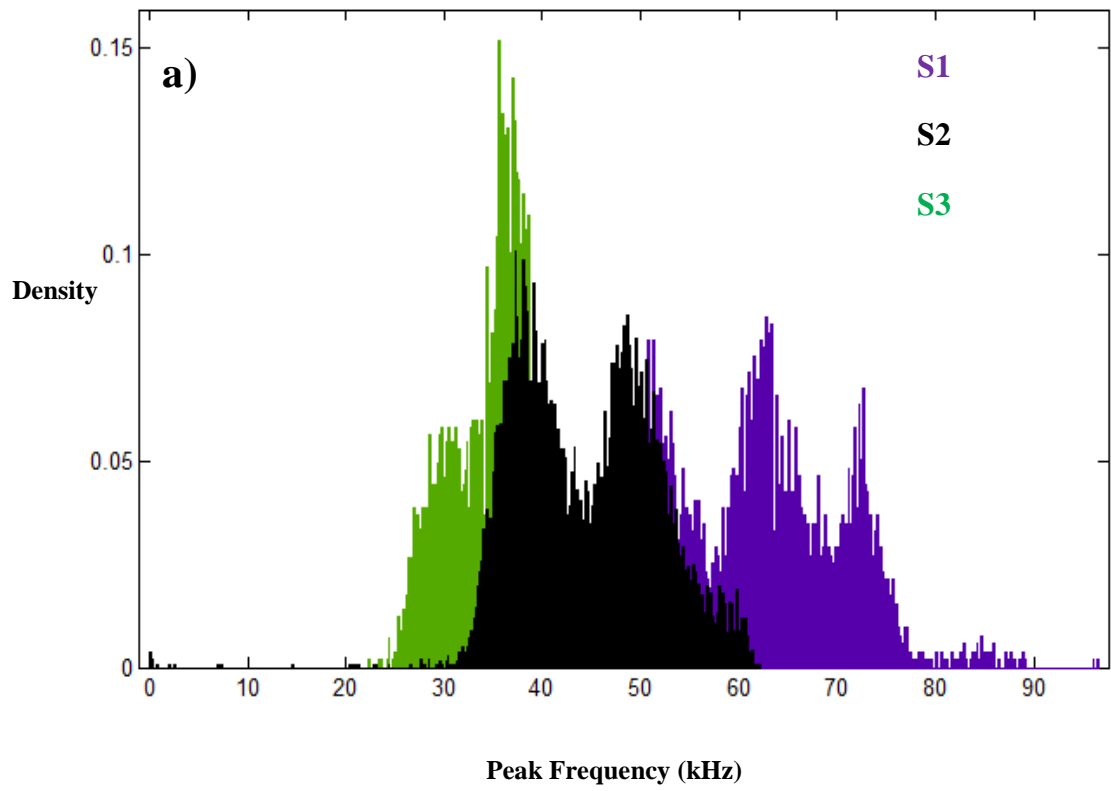
Figure 4.27: PCA visualization of the kernel fuzzy c-means clustering: a) #2, b) #4, and c) #7

The AE signals are classified in three different clusters by utilizing KFCM. Moreover, this clustering in PCA projection implies that the distribution of data did not overlap. Hence, AE data classification and consequently damage mechanism discrimination became easier, as indicated in Figure 4.27 in which PCA visualization of the kernel fuzzy c-mean was presented. It is noteworthy that the dissemination between three classes made by KFCM was consistent with localization of pattern. This is approved by comparison made after clustering. It should be noted that clustering process was validated by using another set of concrete samples which were classified through manual labelling in the process of experiment.

The three clusters obtained in the clustering process have to be related to damage mechanisms of the concrete specimens. To achieve this, AE signal labels that were obtained in clustering process should be matched to corresponding damage stage.

Thus, the peak frequency distribution of the patterns belonging to each cluster corresponding to each stage of damage was plotted in Figure 4.28.

The peak frequency range for each cluster representing each damage stage was obtained by the proposed method (KFCM clustering).



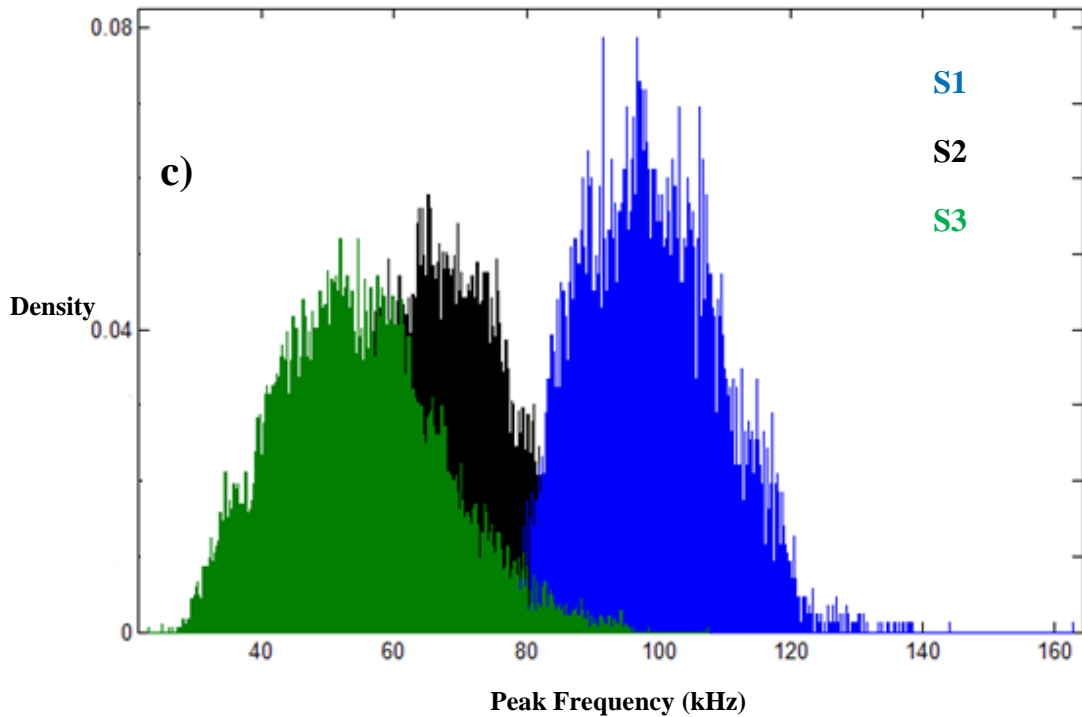


Figure 4.28: Peak Frequency distribution of the patterns belonging to each cluster at different stages for specimen: a) #2, b) #4, and c) #7. S1: matrix micro cracking, S2: visible macro cracking, S3: fiber pull-out/tension softening (plain concrete)

Although peak frequencies pertinent to each damage stage overlap slightly with those of other stage peak frequencies, the centroid of the distribution is still representative of the particular damage stage. Therefore, the AE signal frequency could be deemed as a feasible parameter for monitoring and evaluating damage qualitatively. As can be seen in Figure 4.28, the increase in the damage severity from micro cracking to tension softening has resulted in a decrease in AE signal frequency content. The peak frequency drop was associated with the change of signal shape as damage in the specimen developed. In other words, the increase of damage severity has caused expansion in the signal length as well as wavelength increase and frequency decrease. The AE signal frequency could have shifted due to damage and it could be justified by a fundamental concept of physics which is known as the pendulum principle. It is given that the frequency of pendulum f and its length l are in inverse relation:

$$\left(\frac{1}{f}\right) = 2\pi \left(\frac{l}{g}\right)^{\frac{1}{2}} \quad (4.23)$$

When there was increase in the crack size, either attributed to the enlargement of one previous crack or the coalescence of several previous smaller cracks, or both, the AE signal correspondingly turned out to be of progressively lower frequency, until leaving the ultrasonic range and attaining the sonic range to be identified as the well-known seismic roar. It is also noteworthy that by inclusion steel fibers as well as increasing fiber volume fraction the centroid and density of distribution of peak frequency in each particular damage stage was shifted to a higher range compared to the plain concrete.

4.4.6.2. Quantitative damage analysis by Spatial Intelligent b-value

To monitor the fracture process of all specimens under torsion, the b-value analysis was conducted using groups of 100 AE signals ($n = 100$). Figure 4.2 presented in earlier gives the b-values obtained considering AE signals recorded for the entire data set of specimen #2. The related detailed discussion on b-value trend is given in section 4.2.4.2. It should be mentioned that the discrepancy found in the b-value most likely arose because of the large amount of AE activity generated under torsion loadings. However, the difficulty in identifying b-value trend in each stage of damage might appear as a drawback in real time monitoring of structures while determining the more confident average of b-value pertinent to each damage stage might be another challenge. To this end, in order to provide a precise elaboration of variation in b-value trend which is associated with the progress of damage, Gaussian filtering was introduced to the b-value results. It should be noted that the window span selected was about 5% of the length of the data vector. The resulted graph was presented and discussed in Figure 4.3 (section 4.2.4.2) through which the smoothed b-value data after being processed by Gaussian filtering method was displayed.

As can be seen, after filtering the raw b-value data, the trend of variation of b-value corresponding to each level of damage is fairly well distinguished. But it is only a qualitative trend with trade of in value of b-value.

With reference to Figure 4.3, it can be realized that there are three distinct stages of damage which can impact the trend of b-value. The b-value is stage I (micro-cracking), stage (II) macro-crack formation and localization and stage (III) which is called macro-crack opening (softening branch for plain concrete or fiber pull out branch for SFRC). By implementing the Gaussian filtering, a visible trend of b-value variation was obtained. On the other hand, it is considered that the utilization of Gaussian filtering is a trade-off between trend visualization and real values.

Moreover, manual discretion of b-values related to each damage stage would be a challenge, particularly at boundary of damage stages owing to occurrence of numerous events. For example, it would be quite difficult to separate precisely the data corresponding to micro cracking damage stage in the time of transition to macro cracking damage stage. Therefore, in order to track and separate the micro-to-macro crack transition stages, the KFCM unsupervised method was utilized to cluster different damage stages. Data related to each particular stage were processed to compute the corresponding b-values, known as Sib-values. It is found that the KFCM is able to detect outliers besides clustering data.

Therefore, considering this characteristic of the KFCM technique, b-values outliers were detected while data related to each clusters were classified. Spatial intelligence b-value results and ordinary b-value results are presented in Table 4.6.

Table 4.6: SIb-value and b-value related to each stage of damage

Specimen	b_1	b_2	b_3	$SIb1$ $SIb2$	SIb3	*Max drop b-value (%)	*Max drop SIb-value (%)
#1	1.25	1.15	0.93	1.29 1.16	0.92	74.40	71.3
#2	1.32	1.26	1.02	1.41 1.24	1.00	77.27	71.2
#3	1.60	1.32	1.16	1.62 1.28	1.06	72.5	65.4

* This value presents the b-value in last stage as percentage of b-value in the first stage.

It can be observed from the results presented in Table 2 that SIb-values are in fairly good agreement with b-value results. In addition, a slight increase in SIb-value results for the first stage of damage is visible while in last stage of damage there can be found lower values. Interestingly, SIb-value results might be indicating a SIb-value of 1 which can be indicative of the approach of final damage failure.

4.4.7. Conclusion

This study explores the application of acoustic emission monitoring in conjunction with unsupervised pattern recognition technique (KFCM) for plain concrete and steel fiber reinforced concrete in different fiber volume fractions on the torsional behavior of concrete beams. Pure torsion testing machine (GT-704-C) and AE sensor system were utilized simultaneously to record desired data, such as loading, torque moment, twisting angle, and cumulative AE hits. To diagnose ambient noise and to discriminate this noise from AE signals, a low amplitude- high duration filtering which resembles swansong filtering is performed. Multivariable analysis was utilized to discriminate the damage mechanisms in terms of their AE patterns. Eight AE descriptors including time and frequency domain data were chosen to improve the characterization and the discrimination of the damage process in concrete specimens. A PCA projection was adopted to visualize the clustering results in a three dimensional space. It was concluded that the first three principal components describe fairly well more than 95% of the total variability of AE signals for three concrete specimens. Prior to the classification process a k-means algorithm was used to determine the required number of clusters. Consequently, the AE signals by means of KFCM method were clustered in three distinguished classes based on k-means results which are corresponding to their damage mechanism: (micro-cracking, macro-cracking, and fiber pullout/or tension softening). The peak frequency range corresponding to each damage stage was determined considering obtained clusters to track the damage progress qualitatively. Finally, a novel method called spatial intelligent b-value analysis (SIb-value) was proposed to quantify damage level for each stage of damage. This analysis by aid of KFCM method uses amplitudes located in each stage of damage to compute b-values while boundary lines between damage stages were determined automatically by KFCM pattern recognition when incorporating outlier detection analysis as its inherent characteristic.

4.5. Acoustic Emission Fracture Monitoring of Multi-Layered Wire Mesh-Reinforced Cementitious Composite Slabs

In the following the theories, analysis, results and conclusion are given for this article. The related experimental references are presented in section 3.5.

4.5.1. Introduction and Theory

Ferrocement Structures are gaining ever-increasing attention because of their cost effectiveness, raw material availability, easily fabrication and installation where shapes and forms are complex (Ibrahim, 2011; Hago et al., 2005). Inherent physical properties of ferrocement provide a refined material which shows proper resistance against shrinkage, cracking, and usually possesses high level of ductility (Paul and Rama, 1978, ACI 549-IR-88 and IR 93, 1993; Cheah and Ramli, 2012; Yerramala et al., 2013). These qualities enable successful applications of ferrocement composites in different industries, such as ship hulls, building construction and rehabilitation, sewerage pipelines, domes, and water tanks (Naaman, 2000).

The close spaced reinforcement confines the cementitious matrix and leads to enhanced material response and structural uniformity (ACI549- R97, 1997). However, it has been shown that the minimization of crack-width and subsequent performance enhancement in the reinforced concrete and ferrocement structures can be achieved by reducing the thickness of concrete or mortar cover of reinforced concrete and ferrocement structural elements (Kubaisy and Jumaat, 2005). Therefore, the resulted ferrocement slab could be a thin shell with refined mesh; as a result, its vibration process to produce a homogenous material could pose a problem. Hence, to avoid difficulties of the matrix vibration, self-compacting concrete (SCM) which possesses much higher fluidity without segregation and bleeding can be a suitable alternative in ferrocement production (Svec et al., 2014; Salehian and Baros, 2015).

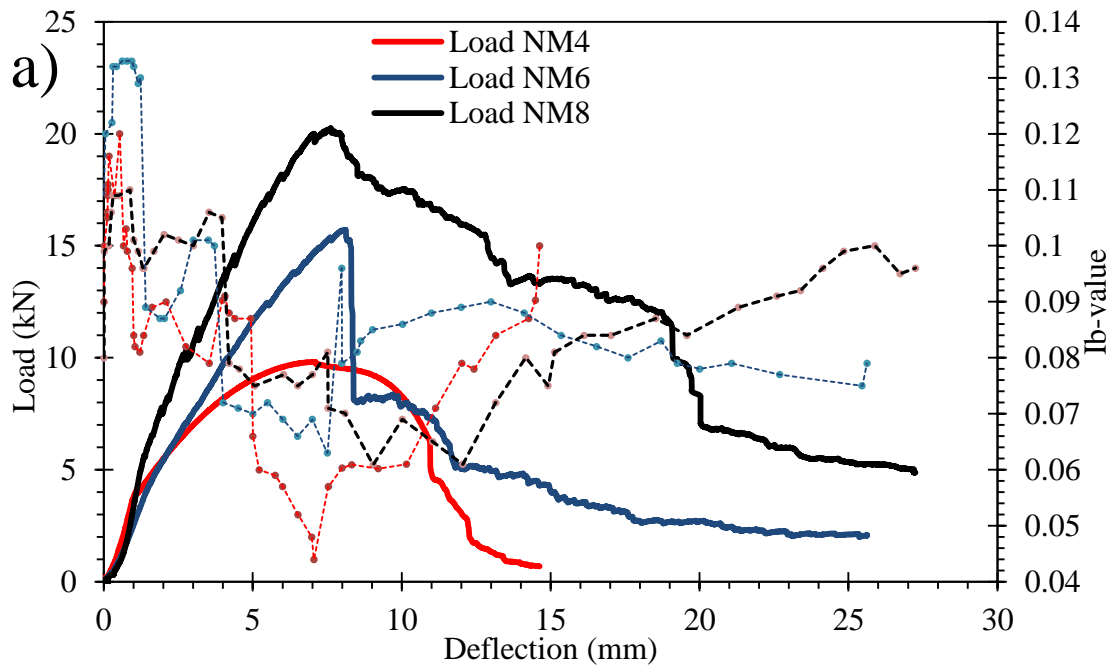
To increase the toughness of cementitious matrix and the mode of failure, replacement of aggregates by materials with a high degree of energy absorption such as rubber was researched by AiÈtcin (AiÈtcin, 2000) Increasing disposal rate of used tires is emerging as an important environmental threat worldwide (Oikonomou and Mavridou, 2009).

Waste or by-product usage in ordinary or special concretes as filler materials, aggregates, mineral admixtures, etc. also enables the production of durable, affordable and environmental friendly concrete (Ossola and Wojcik, 2014; Topçu and Bilir, 2009).

Incorporation of waste tire products in concretes lead to more plastic deformation and much higher fracture energy (Grinys et al., 2012; Benazzouk et al., 2007; Ganesan et al., 2013; Liu et al., 2012; Oikonomou and Mavridou, 2009). Thus, inclusion of this waste in constructional industries is a promising solution. To this end, considering the aforementioned applications of ferrocement creates a need to provide a ductile material while preserving adequate strength. Since the inclusion of tire rubber in plain concrete gave rise to a higher strain rate resulting in further plastic deformation, this process may have great potential by replacing the fine aggregate of normal and self-compacting ferrocement slabs. To the best of the author's knowledge, little research about rubberized multi-layered ferrocement slabs built of normal and self-compacting concrete has been conducted. To date, fracture behaviour of normal concrete ferrocement slabs were extensively investigated by using experimental and analytical approaches. Nevertheless, considering the complexity of multi-layered composite ferrocement slabs, the sole implementation of conventional analysis methods might not suffice to fully comprehend the real behavior of multi-layered ferrocement slabs. Moreover, ferrocement slabs in some cases suffer from an abrupt punching failure. Therefore, utilizing a method like acoustic emission with the capability of online monitoring of material fractures may lead to better understanding of these ferrocement composite slabs.

4.5.2. Mechanical Behavior of Ferrocement Slabs

In the present study the load versus central deflection curves as well as crack and failure patterns for the ferrocement slabs have been used to analyse and classify the modes of fracture and types of failure. Figures 4.29 and 4.30 with Table 4.7 present the load-deflection curves, Ib-value results, and the summary of specimens' behaviour for the tested slab specimens. From Figures 4.29 and 4.30 with test observations, it can be found that normal mortar specimens of four mesh layers failed in the flexural mode, while increasing the mesh volume fraction (number of layers) changed the failure mode to punching failure. In general, as can be observed in Figures 4.29 and 4.30, the wire meshes acted in carrying tensile loading in the tension zone of the slab. When the number of mesh layers was increased from four to six and eight, the specific surface and mesh fraction volume increased, resulting in increased flexural strength.



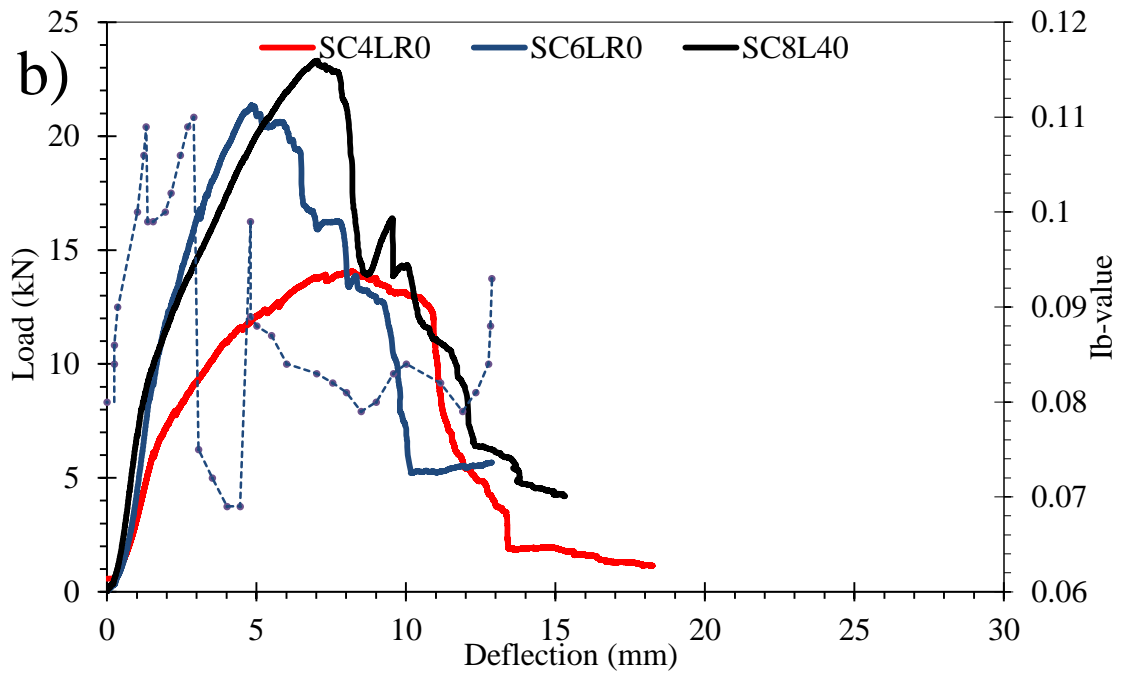
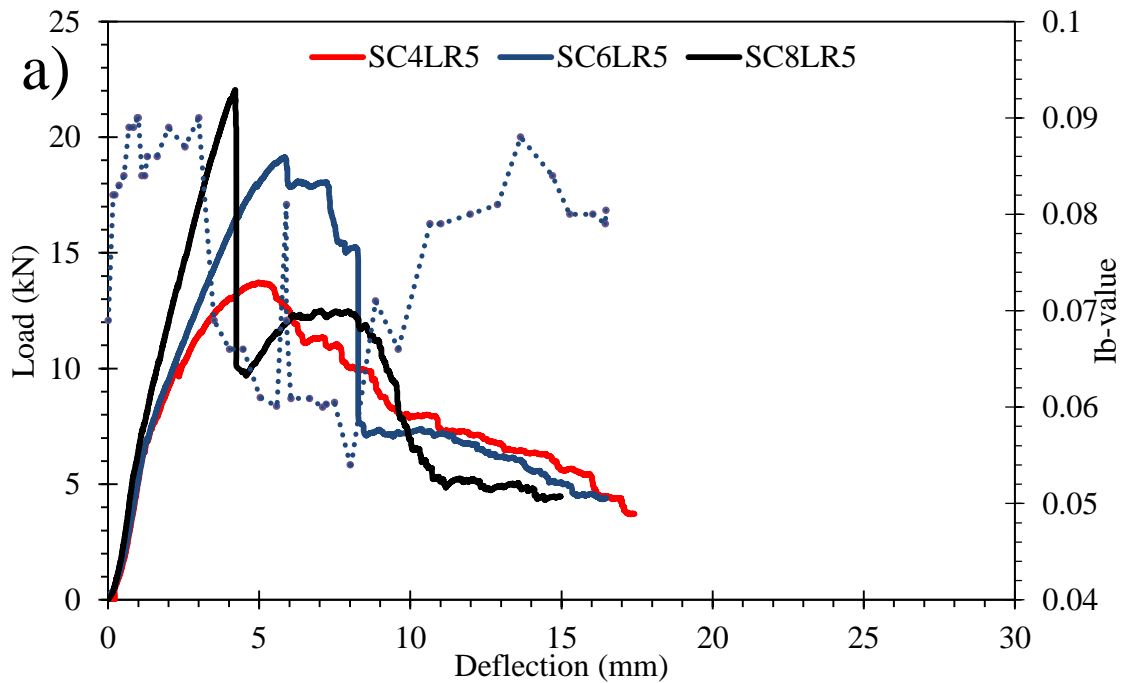


Figure 4.29: A) Load- deflection curves for ferrocement slab specimens: a) Normal mortar series (NM), b) Self-compacting mortar series (SCMR0), B) Ib-value



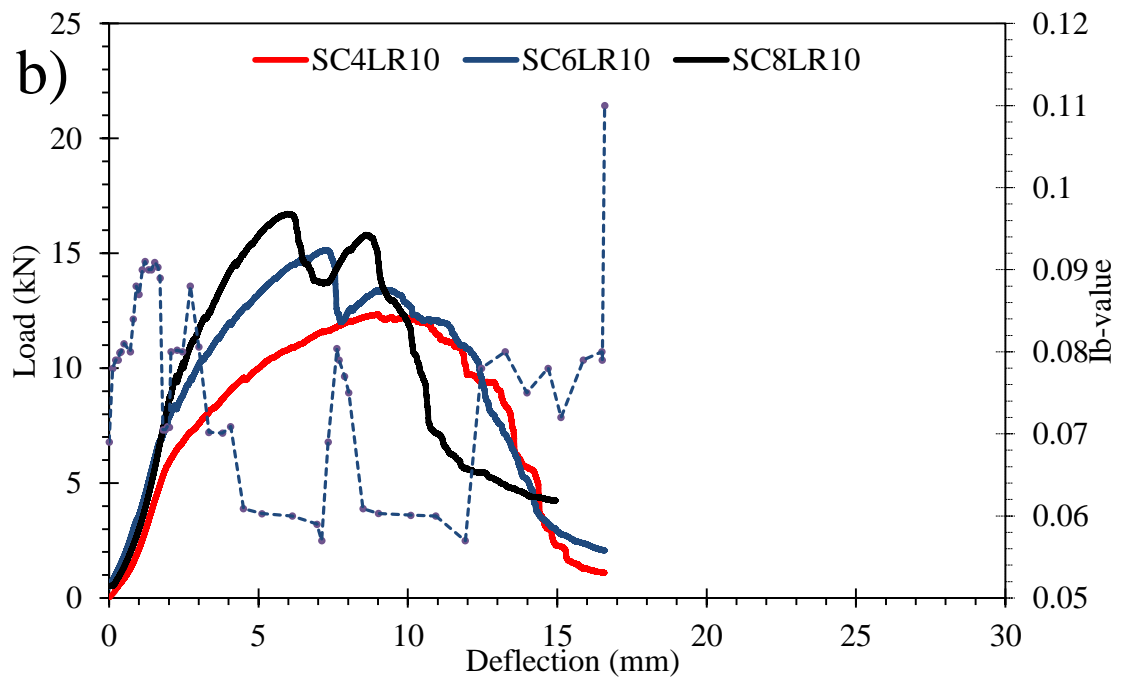


Figure 4.30: A) Load- deflection curves for ferrocement slab specimens: a) Self-compact 5% rubberized mortar series (SCMR5), b) Self-compact 10% rubberized mortar series (SCMR10), B) Ib-value

Table 4.7: Test results for ultimate load, flexural strength, ultimate deflection and fracture mod

Meshing layers	Slab	Load at failure (N)	Flexural strength (N/mm ²)	Deflection at failure (mm)	Energy absorption at failure (N.mm)	Ultimate Energy absorption (N.mm)	Ductility ratio (D _c)	Mode of fracture
4	NM4	9650.42	23.161008	6.89	52500	89625	3.56	Flexural failure
	SCL4R0	14067.5	33.762048	8.01	75600	133600	4.4	Flexural failure- rupture of mesh
	SCL4R5	13718.9	32.925456	5.01	55600	130400	4.65	Flexural failure/ Rupture of mesh (failure started by slight punching but followed but flexural)
	SCL4R10	12353.2	29.647728	10.07	141200	289000	5.92	Full flexural failure- starting from center at the bottom- fully two ways action- high ductility- yield of mesh- divided to four equal square- stress distributions was full event.
6	NM6	15732.4	37.757736	7.97	81000	144875	3.03	Punching failure/Fracture of mesh/ debonding between concrete and meshing
	SCL6R0	21394.3	51.3462	4.8	66800	154800	3.51	Flexural semi-Punching failure- Rupture of mesh
	SCL6R5	19147.8	45.954696	5.7	71200	159200	4.79	Punching - started by flexural failure but dominated by punching- nearly one way yield of mesh- top surface only faced a punch by load surface and cracks did not extend to the top surface, meaning punch dominated
	SCL6R10	15149.2	36.358184	9.5	80400	158400	5.3	Flexural failure/ fully two ways action/ high ductility/ yield of mesh/ Stress distribution was full (Bridging effect)
8	NL8	20254.97	48.611928	6.5	87500	183000	3.6	Punching started by flexural fracture/Fracture of mesh
	SCL8R0	23318.24	55.963776	6.8	101600	187200	5.5	Starting with flexural cracks but fails in punching mode/rupture of mesh
	SCL8R5	22045.64	52.909536	6.9	88800	209000	5.61	Punching- top surface not affected/ after punching on the bottom surface, wires started to deform by concrete till rupture
	SCL8R10	16722.74	40.13458594	8.5	176400	384400	5.71	Flexural failure/ fully two ways action/high ductility/ yield of mesh/ Stress distribution was full event (Bridging effect)

For example, from Figure 4.29a and Table 4.7 it can be observed that upon increasing the number of mesh layers from four to eight, the ultimate load and flexural strength were improved up to 63% and 109% for NM6 and NM8, respectively, relative to the NM4. However, with two additional layers of wire meshes included, it was observed that the mode of failure for normal mortars changed from flexural to punching shear manifested by abrupt formation of a hole on the top face and an outline of truncated failure cone on the bottom face which has larger perimeter than top face.

In addition, considering the toughness values (or energy absorption) presented in Table 4.7, it was found that toughness of failure until the end of fracture process have been considerably improved by increasing fraction volume of wire meshes. For the evaluation of ductility, the ductility ratio was introduced which was computed by dividing the ultimate deflection of a specimen by the deflection measured at the time of first visible crack. According to above description, it was found that NM4 was slightly more ductile than NM6 and NM8, although its total energy absorption was lower.

Replacing normal mortar with self-compacting mortar resulted in a considerable increase in the ultimate load and flexural strength. For example, for SC4LR0 the ultimate failure load and flexural strength were considerably increased to 45.77% and 43.45%, respectively, compared to NM4. It is noteworthy that by replacing normal cement mortar with self-compacting mortar, ferrocement slabs with four layers of wire mesh exhibited 45.71% and 49.1% increases in toughness (energy absorption) until failure and total toughness (total energy absorption), respectively. Interestingly, the ultimate deflection for SC4LR0 was increased up to 16.26% compared to NM4, whereas the ductility ratio declined by 31.68%. This phenomenon was associated with differences between the tensile strength of these two mortars. Although SC4LR0 displayed larger deflection than NM4, tensile strength (F_t) for normal cement mortar was about 47.43% lower than self-compacting mortar.

On the other hand, the first visible crack took place when the tensile strain in the extreme fibre of the slab exceeded the ultimate tensile strength of the mortar. Hence, self-compacting mortar with higher tensile strength and strain underwent the first crack later than normal cement mortar. As a result, there was a larger distance between ultimate deflection and first crack deflection for normal cement mortar which resulted in higher ductility ratio.

However, the replacement of normal mortar with self-compact concrete caused slight changes in mode of failure.

Although similar to normal cement slabs with six and eight layers, the dominant failure mode of SC6L0 and SC8L0 was in punching as there were flexural cracks prior to punching failure in these specimens.

In general, inclusion of rubber in self-compact mortars decreased ultimate load and flexural strength. However, inclusion of 5% and 10% of rubber in self-compacting mortars caused different effects in slabs' behaviour. Inclusion of 5% rubber resulted in slight decrease in flexural strength and energy absorption, whereas in all cases ductility ratio was increased relative to the self-compact mortar without rubber. In addition, there were no significant changes caused in modes of failure.

On the other hand, 10% rubber inclusion caused significant changes in flexural strength and slab behaviour. The addition of 10% of rubber could significantly decrease the ultimate load and flexural strength, causing higher energy absorption and ductility ratio compared to self-compact mortar without rubber. For example, flexural strength for SC4LR10 in comparison with SC4LR0 declined about 12.2%, whereas the failure deflection and ductility ratio were considerably increased to 26% and 36%, respectively. Moreover, inclusion of 10% rubber effectively changed the failure modes in all specimens so that all SCR10 composite slabs failed in the flexural mode.

The addition of 10% rubber efficiently reduced the flexural strength and increased tensile strain at ultimate failure as seen in SC8LR10. Therefore the rubber particles with high level of elasticity could perform like a barrier against crack growth, whereas the rubber content of SC8LR5 seems insufficient to significantly diminish the flexural strength and change the mode of failure.

Hence, in the experiment of SC8LR5 which considers the congested layers of meshes showed a high flexural strength, and the mortar failed in punching mode. The reason for this behaviour may be revealed by understanding the microstructure features of the rubberized material.

The poor adhesion between cement and rubber was observed in the Scanning Electron Microscope (SEM) image and illustrated schematically in Figure 4.31. Poor adhesion was associated with the existence of zinc stearate as a chemical composition in the rubber formula. This zinc stearate moved and spread toward the rubber surface through which a soap layer would be produced. This soap layer could repel the water in the mortar (Fernando et al., 2011). In addition to the aforementioned reasons, the rubber exhibited low hydraulic conductivity and a soft surface. Considering all the above mentioned descriptions, rubber created a weak bond with cement. That could be the main reason why when sufficient volume of rubber is added, it can result in the reduction of flexural and compressive strength of the rubberized mortars where the cracks were usually formed and generated from interfacial transition zone (ITZ) between rubber and cement. On the other hand, the rubber may cause the bridging effect because it had a much higher level of elasticity compared to the mortar; therefore, it could linger and suppress the initial crack growth in the matrix.

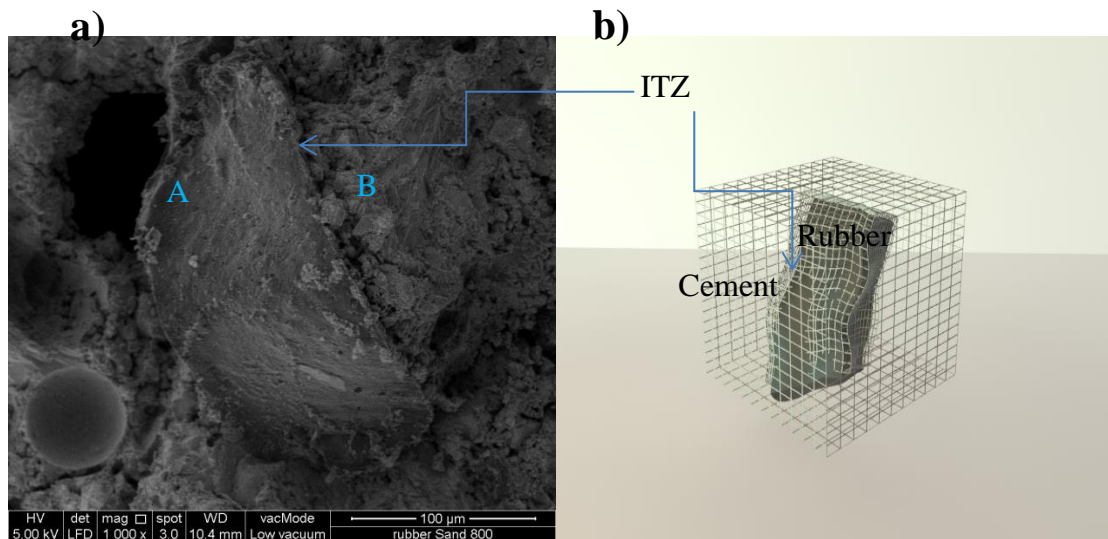


Figure 4.31: a) S.E.M. images of interface surface of rubber (10%) and cement paste (A) Rubber particle; (B) Cement paste, b) Schematic illustration of ITZ

4.5.3. Generalized Behaviour of Ferrocement Composite Slabs

Through test observations and analysis the behaviour of tested specimens can be generally divided in two principal failures as depicted in Figure 4.32: flexural and punching modes.

Shear failure as illustrated in Figure 4.32a was considered when a sudden drop occurred for the load capacity almost immediately post peak load, forming a vertical branch in the load-deflection curve. As a typical behaviour, there was a linear relationship between loading and deflection until flexural cracking, which occurred in the centre of the loading path. After cracking, a noticeable reduction in stiffness could be noted. As the load increased, new cracks were formed and existing cracks propagated slightly in the radial direction. The load-deflection curve slope (stiffness) was still decreasing until the final punching failure. Punching failure was highlighted by a sudden drop in the applied load.

At this moment, punching shear failure was completely obvious, indicated by the formation of a "hole" on the top face. On the bottom face, on the other hand, an outline of a truncated failure cone was merely noted which had a much larger perimeter than the hole which formed on the top face.

In some cases, the corners of slabs were also lifted. When most of the reinforcement yielded prior to failure and the slabs subsequently underwent large deflection, the dominant failure mode was flexural failure. The flexural failure as illustrated in Figure 4.32b could be characterized as a smooth decline of the carrying load with a progressing increase in deflection.

In general, when ferrocement slabs are subjected to flexural or tensile failure, the development of fracture behaviour can be attributed to three stages: 1. Ferrocement behaves like a homogenous elastic material until the first visible crack occurs, 2. Multiple cracking occurs after the first visible crack has developed until the onset of yielding of reinforcing meshes.

In this stage the length and number of cracks increase, and at the same time the crack-width increase becomes negligible, 3. The crack-widening phase starts in which the formation of new cracks ceases to occur. Yielding of reinforcement was triggered in this stage, which continued until ultimate failure. The aforementioned stages can be termed as: 1. Elastic stage/Pre-cracking stage, 2. Elasto-plastic stage/Multiple cracking stage, and 3. Plastic stage/Post-cracking stage.

In addition, in some cases where a second peak was usually observed from the load-deflection curve, flexural punching failure was found. In such case, the continuity between the punched area and either portion of the slab was maintained by the aid of wire mesh reinforcement, which was responsible for giving the second peak in the load-deflection curve after a drop by the punching shear.

The occurrence of the second peak could be explained by the development of tensile membrane action given by the wire mesh.

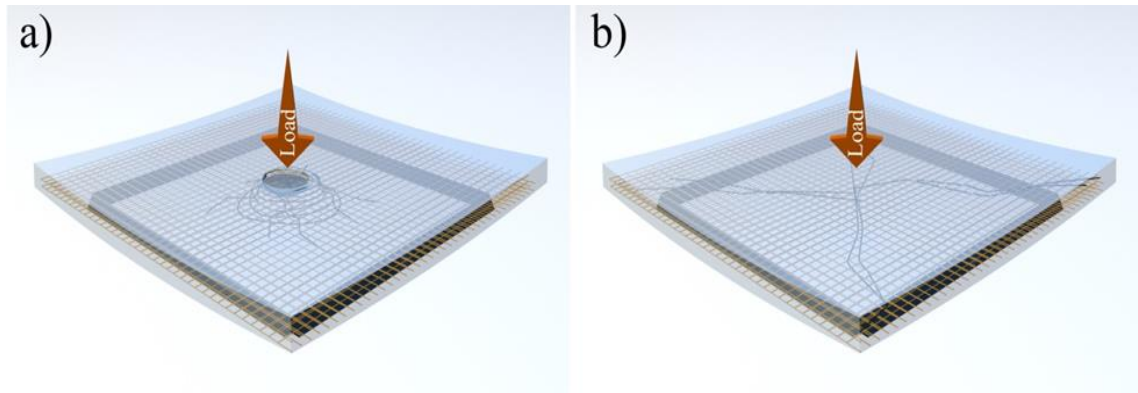
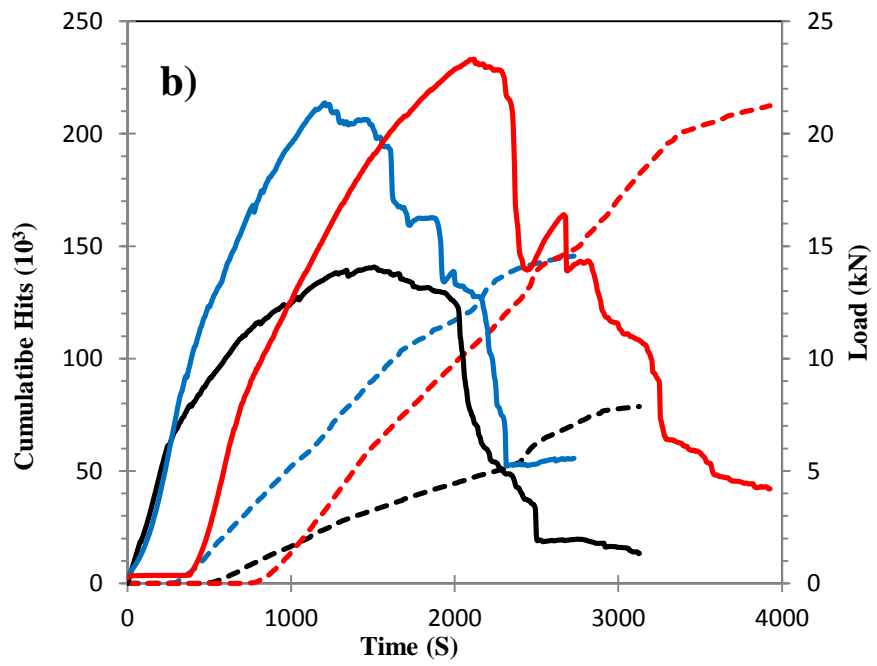
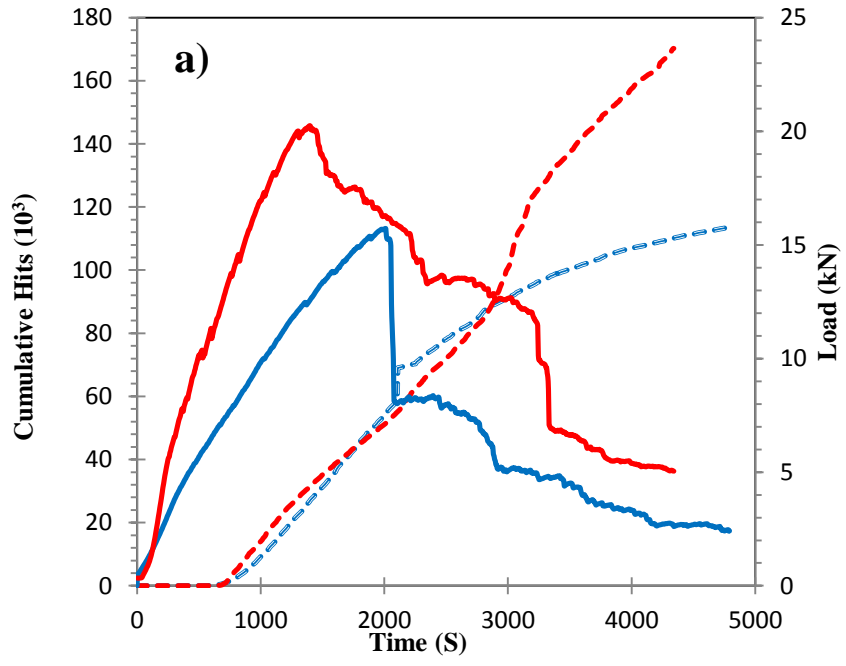


Figure 4.32: General types of failure modes: a) Punching failure, b) Flexural failure

4.5.4. AE parametric Analysis and Material Properties Correlation

Results of acoustic emission monitoring involve all AE activities and AE signal features. Figure 4.33 depicts the variation of cumulative AE hits along the loading subjected to the slabs. A typical trend for the variation of cumulative AE hits is distinguishable for all slabs. Not much AE activity is seen in the elastic region of the loading period prior to occurrence of the first visible crack. As a macro-crack appeared on the slab, a sudden increase in AE hits was noted. Thereafter, the rate of cumulative AE hits was progressively increased as the monotonic loading was approaching its ultimate value. At the moment of fracture when slabs reached their maximum load capacity, the cumulative AE hits kept increasing though by a lower rate than the previous stage.



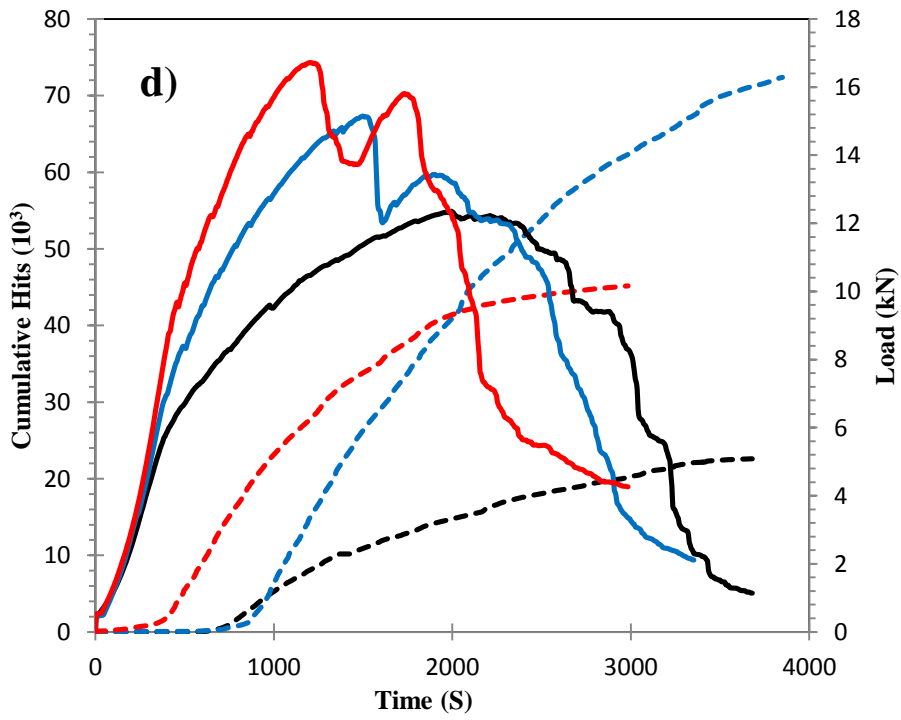
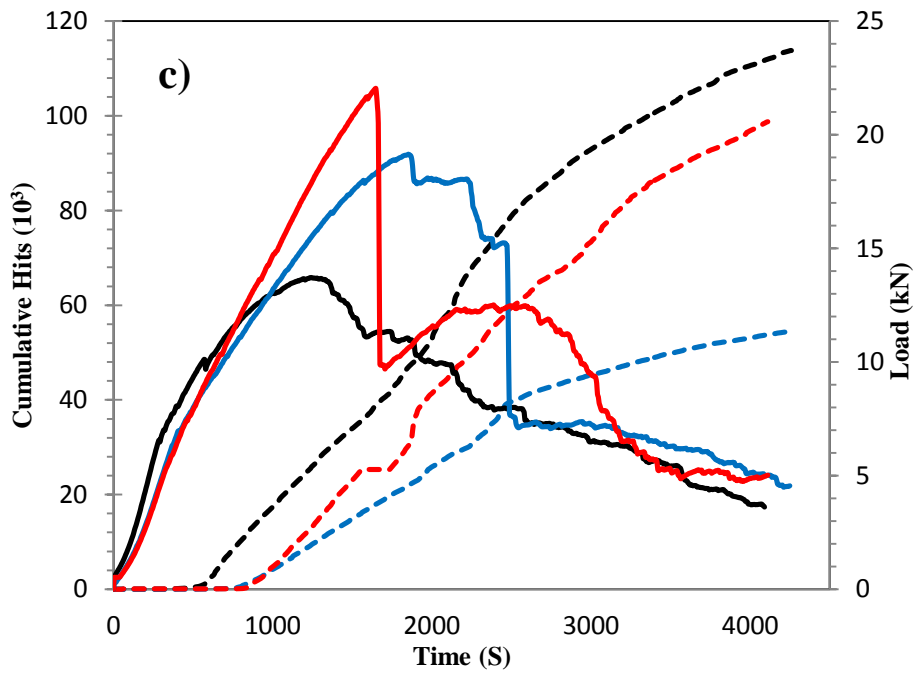
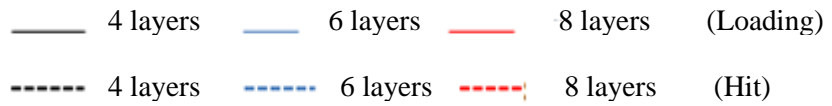


Figure 4.33: Cumulative AE hits along the loading, a) NM, b) SC, c) SCR5, d) SCR10



However, as noted, information obtained by cumulative AE hits analysis merely provides a general idea of the failure process of slabs, and it is difficult to make a distinction between different material properties and subsequent structural behaviour of each particular type of slab. Therefore, in order to characterize the material properties for different types of slab and the particular structural behaviour associated with fracture process, monitoring the real rate of AE hits may be used as an informative analysis.

To this end, Table 4.7 addresses two principal types of failure which were caused by the influence of material properties and reinforcement configuration. Figure 4.34 presents typical samples for each type of failure mode in terms of the rate of AE hits against loading. The first type of slab fails in a punching failure mode which shows membrane action.

For these types of slabs, the fracture process starts with micro-cracking stage (I) which is the so-called pre-cracking or elastic stage. As can be observed in Figure 4.34a, in this stage the AE activity level is considerably lower than the following stages. Upon the emergence of the first macro-crack/flexural crack in the centre on the bottom side of slab which is highlighted by the reduction in the slope of load-deflection curve, a sudden increase in the AE hit rate was registered. This stage (II) is called post-cracking/multiple cracking or Elasto-plastic cracking regarding the elastic behaviour of this stage after the first nonlinearity. The AE emission rate remained moderate due either to propagation of existing cracks or to the occurrence of new cracks until the peak load at which the punching failure was captured. Punching failure coincided with the main shock of the AE hits rate which is identified by the maximum rate of AE hits. Thereafter, in the post-punching stage (III), a considerable drop in AE hits rate was observed due to significant drop in the loading. In this stage, the tensile reinforcements started to yield.

Most AE hits in this stage can be attributed to the crack widening and yielding tensile reinforcement in the form of membrane action of the slab. Hence, yielding of reinforcement results in a low population of AE activity with a higher amplitude compared to the previous stages (Behnia et al., 2014). The second type of slabs exhibited flexural failure. The first and second stages of fracture process in this type of slab resemble the first and second stages of the first type of slab.

For this type of slab, at the end of Elasto-plastic stage, the slope of the load deflection-curve experiences another reduction which leads the Elasto-plastic stage to plastic or post-yielding stage (III) that continues until the peak load. As can be observed in Figure 4.47b, the AE hit rate in the post-yielding stage was characterized by a moderate decreasing trend until the peak load.

This phenomenon may be caused by the yielding of reinforcement that causes a reduction in AE signal emission (Behnia et al., 2014). In the post-peak stage, the tensile reinforcements tend to tear out of the concrete accompanied by bond failure which finally may result in the fracture of meshing in the truncated zone around the centre of loading. As depicted in Figure 4.34b, the main shock of AE occurred in this stage which is an indication of considerable increase in AE activity for the initial period of this stage. This phenomenon may be caused by the emission of AE signals resulted from bonding failure between reinforcement and concrete or reinforcement tearing. It is noteworthy that in some cases, especially in the case of self-compacting mortar without rubber (SC6LR0, SC8LR0), a dowel action of slab was observed, thereby slabs started failing in the flexural mode but the failure mode was dominated by punching. In the post-punching failure stage, a composite behaviour of the slabs could be observed. The trend of AE hit rates was more and less similar to those slabs with flexural behaviour.

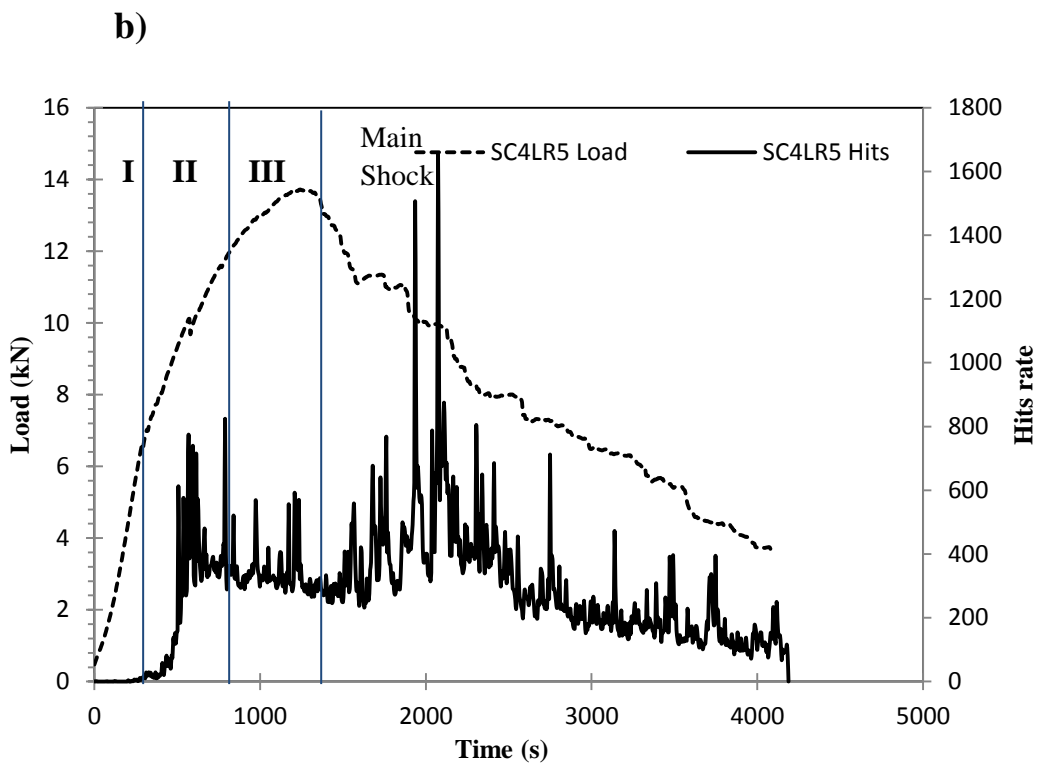
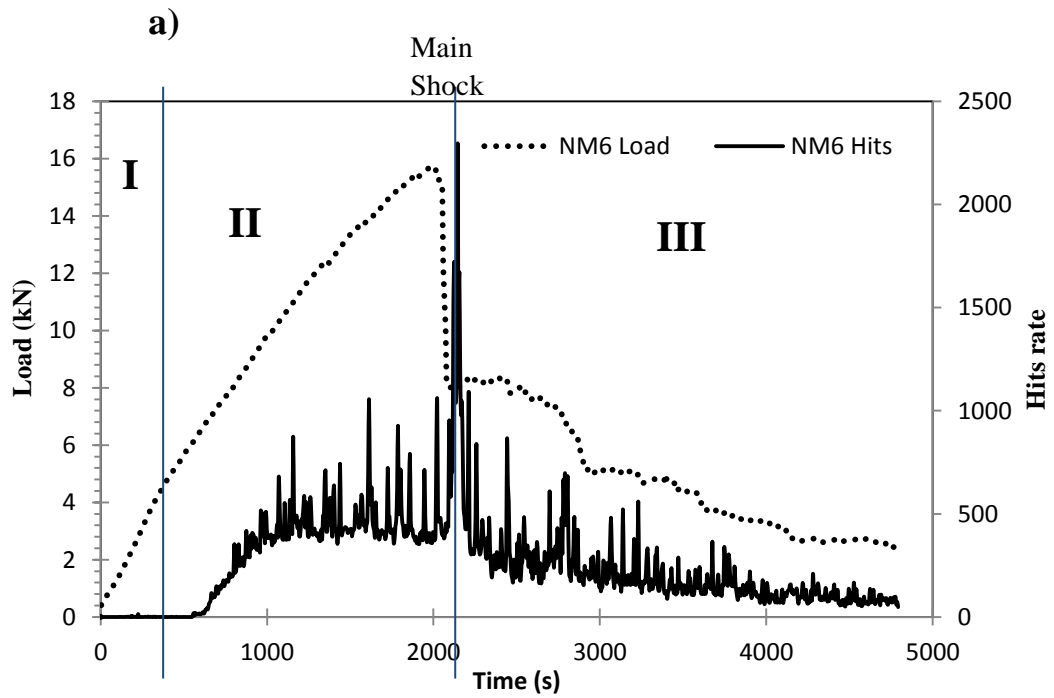


Figure 4.34: AE hits rate against loading: a) Punching failure, b) Flexural failure

It is also interesting to investigate the effect of the inclusion of rubbers on the variation of AE hit rates. As demonstrated in previous sections, inclusion of 10% rubber could completely change the material behaviour and shift the mode of slab failure in the case of punching failure to flexural failure. These changes imposed to material behaviour directly influence AE hit rates. For instance, Figure 4.35 illustrates the trend of AE hit rates for SC6LR10 and SC8LR10. For these cases the first stage still resembles the other types of slab. Low and moderate AE activity was registered in the pre-cracking stage, whereas the highest AE activity occurred in the second stage (multiple cracking/post cracking).

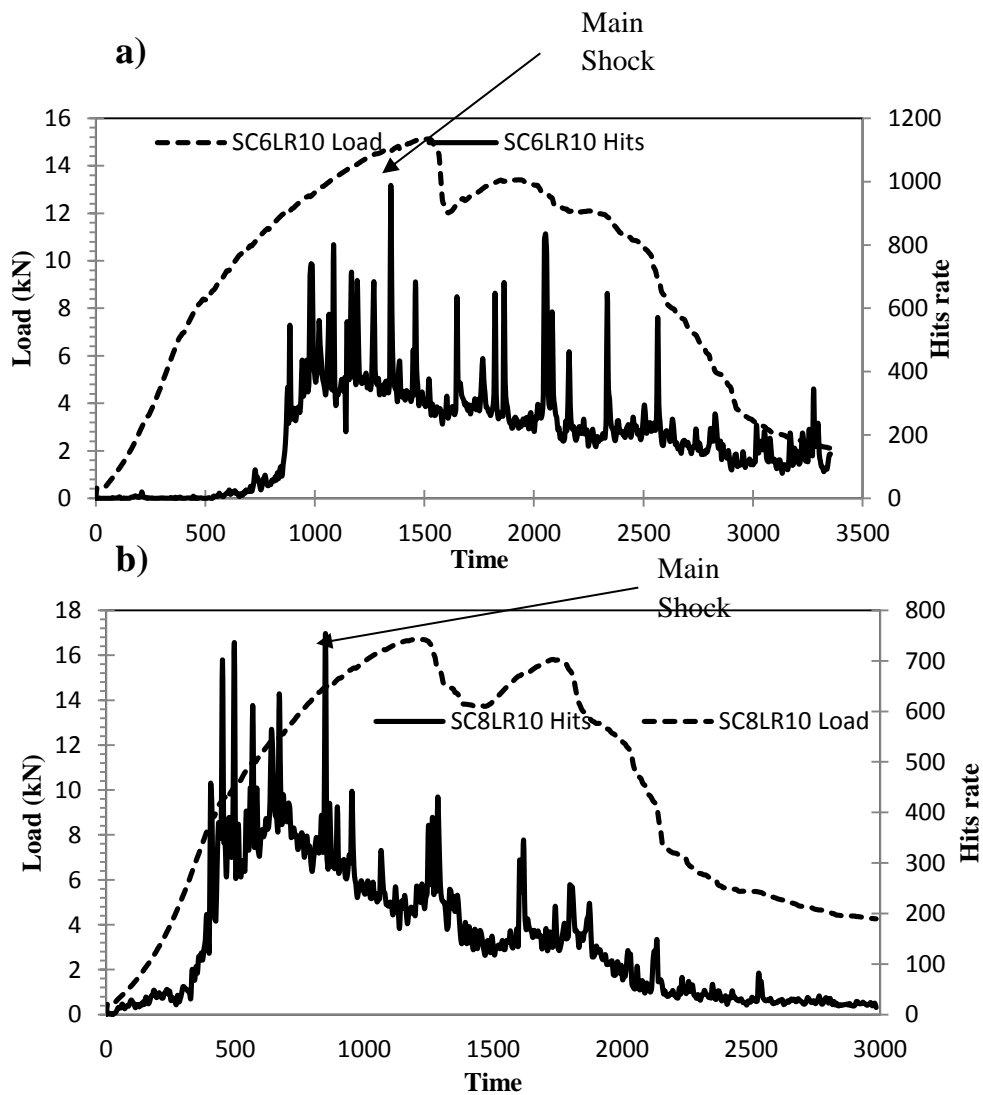


Figure 4.35: AE hit rates against loading: a) SC6LR10, b) SC8LR10

As depicted in Figure 4.35 by the occurrence of the first macro-crack, a significant increase was observed in the AE hits rate. It is interesting to note that the main shock of AE hits rate took place in the multiple cracking stage, which is placed before the peak load. However, the frequency of occurrence of AE hits in this stage is considerably higher than in other stages. The main reason for this phenomenon may be attributed to the properties of rubberized mortar. As discussed in previous sections, as the percentage of rubber increases, the tensile strength decreases while the tensile strain increases. In addition, as presented in Table 4.7, the stress distribution was even for these types of slabs while the bridging effect in crack propagation was observed. Therefore, the high tensile strain and bridging effect may result in even propagation of cracks.

Hence, in this stage the density of cracks and AE hits could be significantly increased. Starting from the yielding stage, the AE hits decreased until the peak load. After the peak load the main crack, which was distributed in entire length of slabs, started to widen until the end of the fracture process. Therefore, the number of generated AE hits continues to diminish with higher amplitude or energy.

To the best of the author's knowledge, thus far there is no information in the literature to utilize AE hits data as a quantitative analysis. To this end, in this study an attempt was made to correlate AE hits with slabs' stiffness variation. Stiffness is defined as the slope of load-deflection curve in each instant. Therefore, it is expected that as load increases, stiffness decreases, meanwhile AE hits are being accumulated. Hence, AE hits trend may convey the trend of stiffness variation.

As an example, Figure 4.36 shows the occurrence of AE events with increasing time of testing for NM6. It was observed that there is a prompt increase in the number of AE hits with a significant drop in the stiffness curve near the ultimate peak load. Therefore, the trend of AE hits variation may be a suitable indication of slab failure.

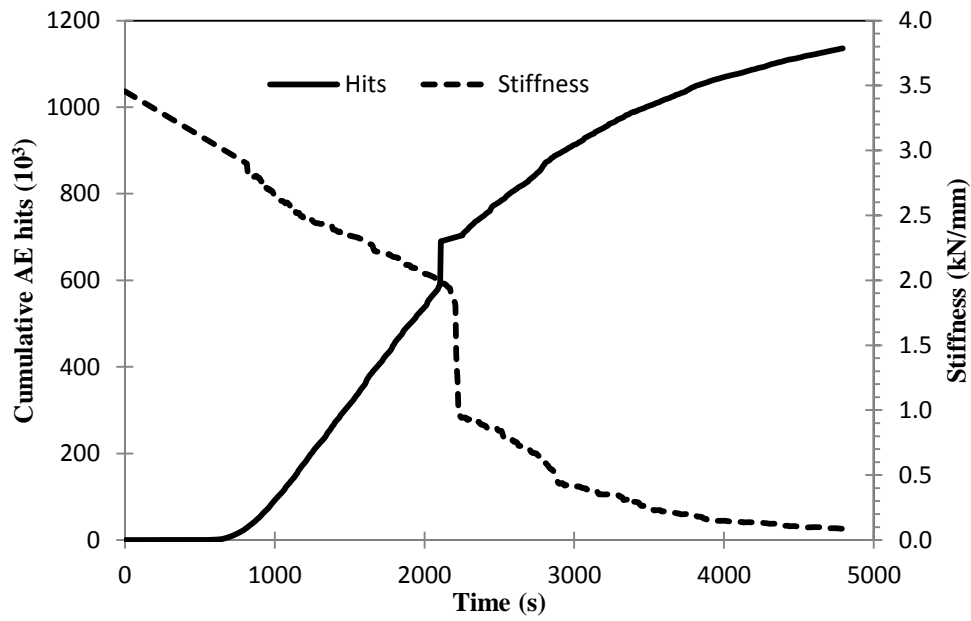


Figure 4.36: Cumulative AE hits and stiffness versus time for NM6

In order to attain quantitative information regarding failure process, normalized cumulated AE hits were plotted against the loss of slabs' stiffness during the loading period. For example, Figure4.50 shows the variation of loss of stiffness versus the normalized cumulated AE hits for NM6, SC4LR0, and SC8LR5.

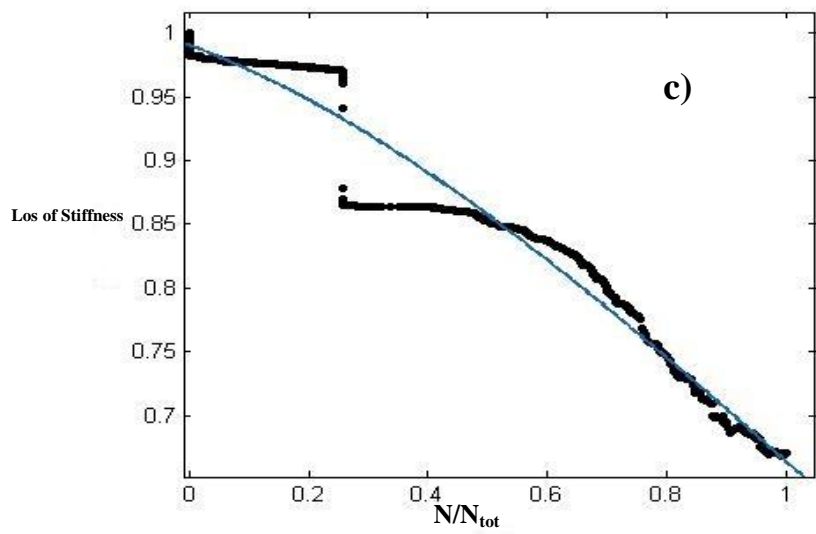
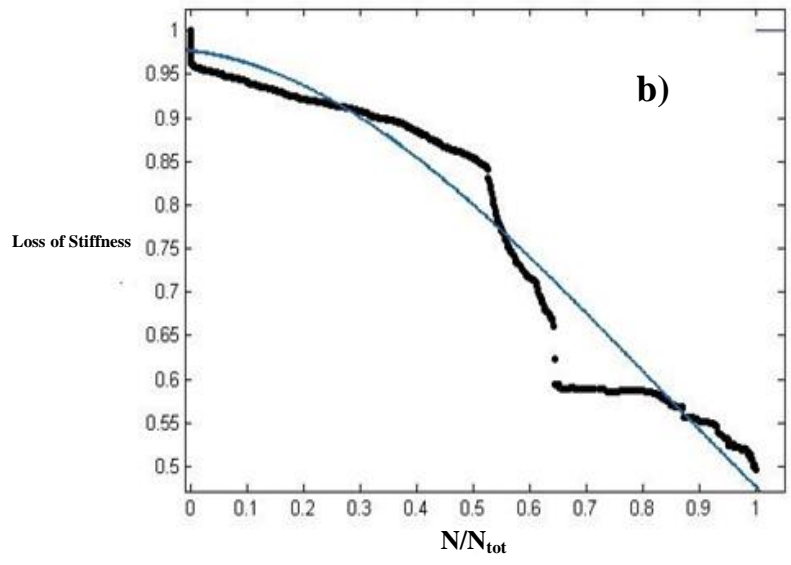
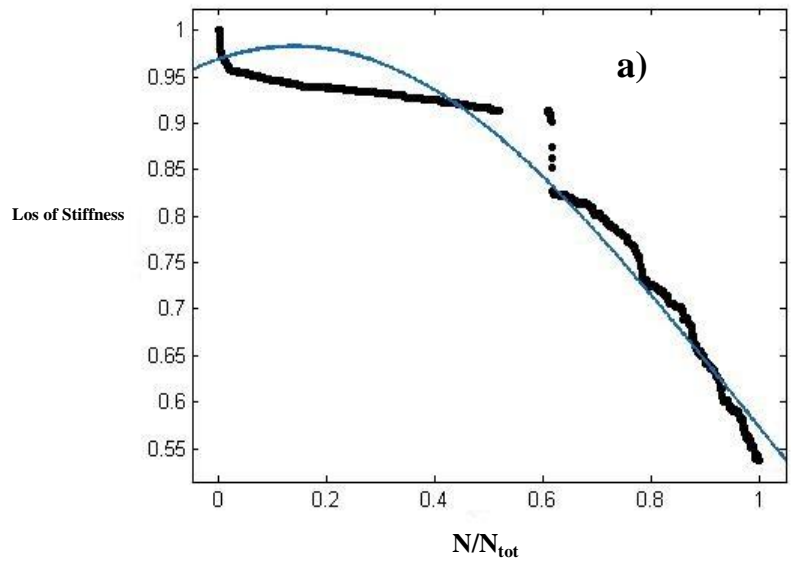


Figure 4.37: Loss of stiffness versus normalized cumulated AE hits, a) NM6, b) SC4LR0, c) SC8LR5

It can be inferred that the increase in number of AE hits was accompanied by the loss of stiffness. Interestingly, it was found that a general Gaussian model could be developed to estimate the loss of stiffness relative to the number of cumulated hits for all experimented slabs. Therefore, the following simple Gaussian model with merely one term is proposed to estimate the loss of stiffness in online AE monitoring:

$$F(x) = a_1 \cdot \exp(-((x-b_1)/c_1)^2) \quad (4.24)$$

It was demonstrated that the Gaussian model with almost 95% confidence was successfully applied. The detail of error and level of confidence is tabulated in Table 4.8.

Table4.8: Gaussian model confidence level and parameters

Sample	a_1	b_1	c_1	<i>R-square</i>	<i>SEE</i>	<i>RMSE</i>
NM4	0.98	0.14	1.17	0.9725	0.63225	0.02602
SC4LR0	0.98	0.06	1.2	0.9593	0.7044	0.03404
SC8LR5	1.02	0.04	2.1	0.9721	0.3007	0.01938

4.5.5. AE Technique for Structural Behavior Analysis

AE may facilitate the evaluation of the structure condition and the monitoring of active cracks using transducers mounted on the specimen through recording transient response induced by cracking events. Concerns such as event and damage location, nature of damage, and severity of damage can be addressed by AE analysis. The obtained information from sensors is associated with the effect of the fracture of material on the signal waveforms. Therefore, differences in emitted signals might be attributed to individual failure mechanisms. There are several AE parameters which have the potential to be used as a fracture process signature.

Thus far, average frequency and RA (Rise time/Amplitude) were used to discriminate tensile cracking from shear cracking during fracture process (Aggelis et al., 2013a; Aggelis et al., 2013; Shah and Li, 1994) Hence, in this study to examine the sensitivity of RA and AF in flexural and punching mechanism, NM6 slab was taken as a sample. Figure 4.38 shows the trend of variation in RA and AF, respectively. Interestingly distinct effects of the fracture progress on RA and AF could be observed.

At the moment of first visible crack on the surface which can be associated with flexural cracking of matrix, a visible surge occurred in the RA curve, while at the same time a significant drop took place for the AF curve. The increasing and decreasing trend remained consistent for both RA and AF, respectively, until the ultimate load capacity.

At the time of failure there is a paramount peak in RA, whereas considerable drop was registered for AF. Thus, RA and AF can be significantly affected by imposed damages in the structure. Therefore, it can be useful to utilize these features, RA and AF, for analysing the nature of source and damage. This is because of the way these features responded to the fracture process.

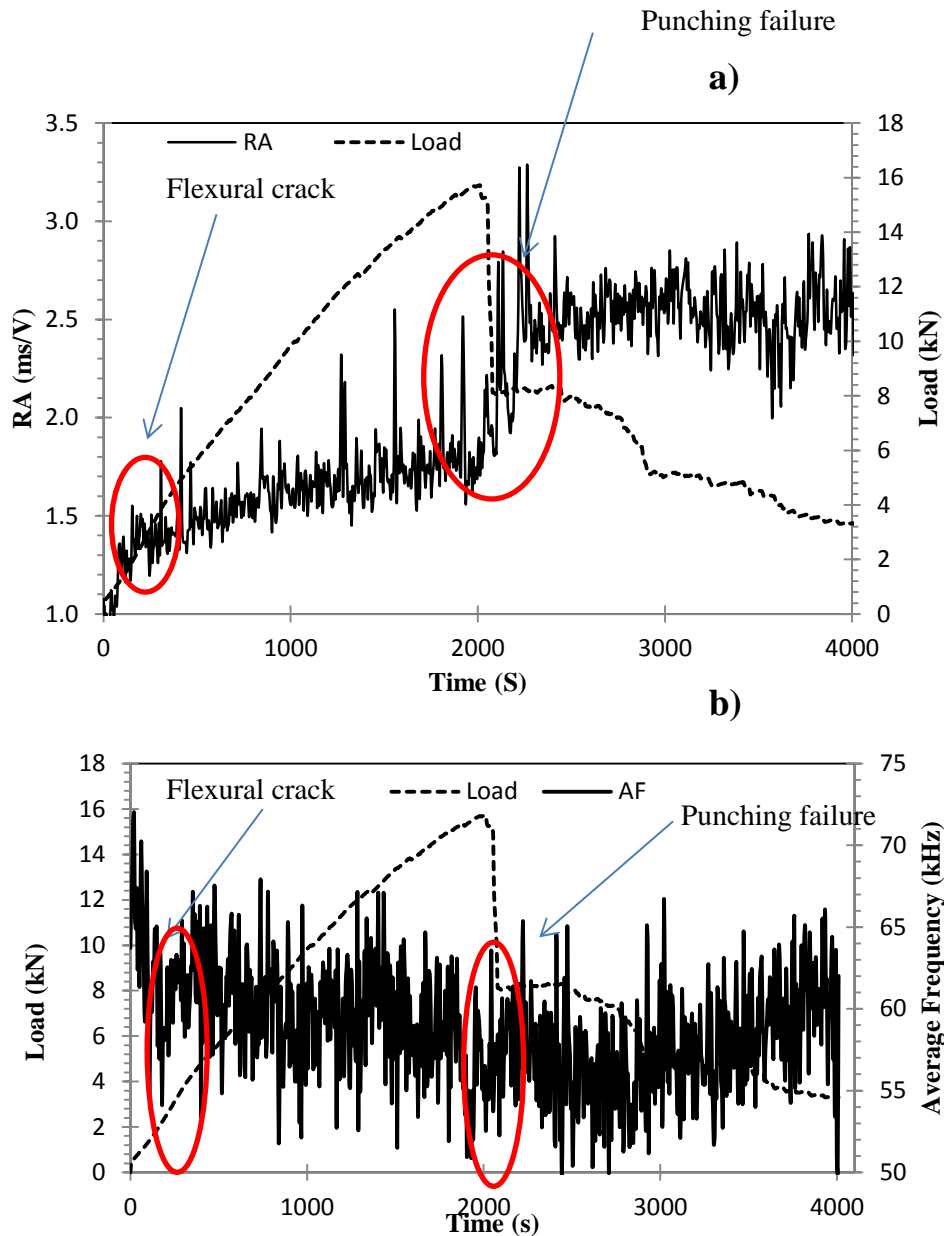


Figure 4.38: RA and Average frequency variation against loading for NM6

As recorded in Figure 4.39, punching could cause a higher level of increase and decrease in RA and AF, respectively, in comparison with flexural cracking. Figure 4.39a shows that the RA value which is related to the first part of waveform was shifted to a higher value as damage changed from flexural to punching. It can be seen that the average trend for SC4LR0 with flexural failure was lower than those relating to NM6 and NM8 with punching failure. This phenomenon can reasonably be attributed to the wave modes which would be excited by different type of cracks or damages.

Flexural failure might be accompanied by tensile cracks resulting in a transient or short-lived burst of volumetric change inside the material. This type of volumetric change converts the released energy to a longitudinal or dilatational (p-wave) wave. Therefore, most excited pulses consist of longitudinal waves with larger amplitude which are subsequently faster than any other excited types which produce shorter rise time signals. On the other hand, punching failure is principally accompanied by shear cracks through which most energy would be transmitted to shear distortional waves (s-wave), although there might be longitudinal waves which were still excited. However, it is known that a shear wave is the wave in which the oscillations are occurring perpendicular to the direction of the wave propagation, and consequently the wave velocity is slower than p-wave. Thus, the major portion of energy in the s-wave which contains maximum amplitude arrives later than the first p-wave arrivals leading to longer rise time. It should be also noted that the s-wave embraces a larger amount of energy than the P-wave (s-wave amplitude > p-wave amplitude). Consequently, considering the above explanations, punching failure shows a higher RA value than flexural failure. Figure 4.39b shows AF curves for flexural and punching failure samples. Generally, it was shown that AF was shifted to a lower value as damage was altered from flexural to punching.

This can be reasonable considering earlier work by Shah and Li (Shah and Li, 1994; Antonaci, et al., 2012) where they have shown that the p-wave has higher frequency than the s-wave. Therefore, flexural failure shows higher frequency than punching failure when flexural failure is dominant.

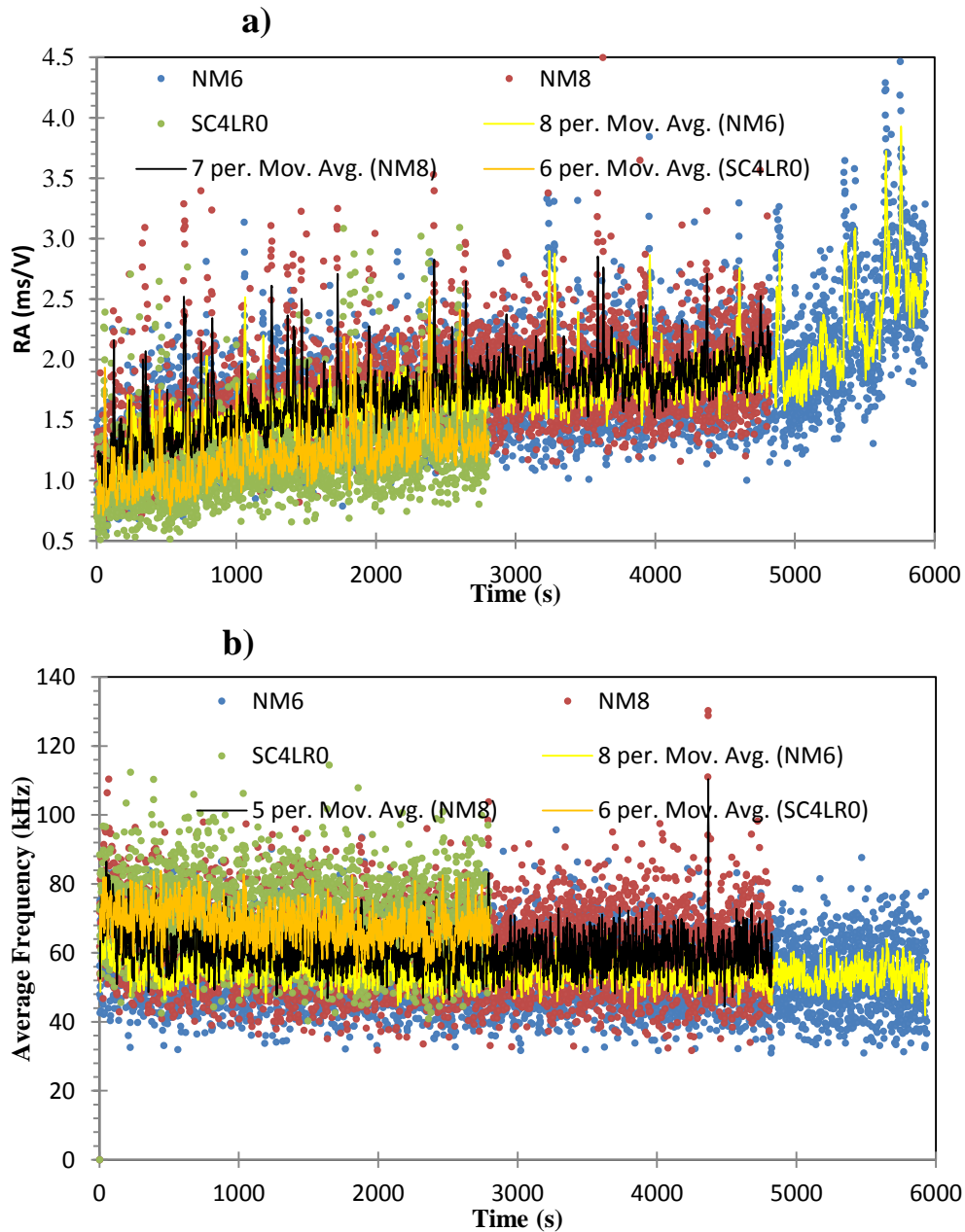


Figure 4.39: Trend of variation of AE features in different type of failures: a) RA, b) AF

To shed light on failure type identification, RA and AF were extensively investigated for different samples. Figure 4.40 for example is plotted to show the approach of AF and RA combined in a single graph to discriminate flexural failure from punching failure. The classification of failure types was performed successfully so that the results presented in the above figure are in agreement with failure types discussed earlier in Table 4.7. To separate flexural and punching failure, predefined diagonal lines in the figures were defined based on the results presented in JCMS for AE monitoring.

It should be noted that this predefined diagonal line might be a general separation line so that precise clustering can be obtained through classification methods. Therefore, it might be more precise to define this predefined diagonal line in each specific project by considering its material properties.

However, as depicted in Figure 4.40a for the flexural failure case (SC4LR0) data located above the diagonal line and punching failure cases, NM6 and NM8, some parts of data were positioned below the diagonal line. In another example, Figure 4.40b is comparing the failure behaviour for different types of ferrocement material with 8 layers of wire mesh. It was observed that the transition of punching failure for NM8, SC8LR5 to flexural in SC8LR10 was successfully captured. It is noteworthy that for those cases of punching failure there are some data placed above the diagonal line. It is justified simply by the concept of fracture process. Fracture process in this slab starts by micro-cracking and then continues by tensile macro-cracking of the matrix which generates tensile or flexural cracking signatures.

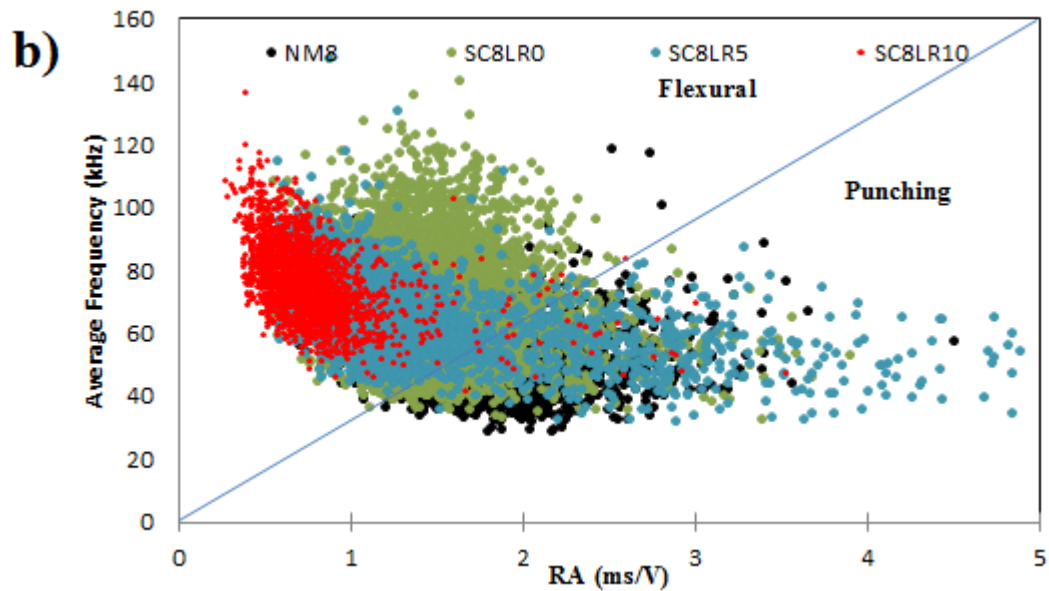
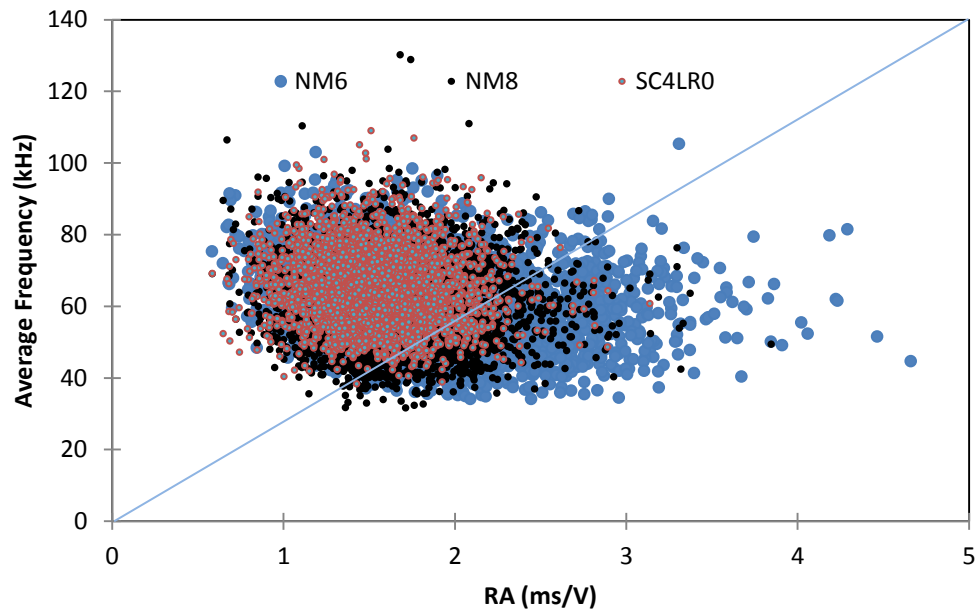


Figure 4.40: Failure type classification based on average frequency versus RA

4.5.6. Early warning failure system

Considering the overall behaviour of ferrocement slabs, it is noted that punching failure could happen in some cases which might be an abrupt failure. Thus, by using AE parameters there would be a possibility to have an early warning system. It is known that macro-cracks produce higher amplitude than micro-cracks (Aggelis et al., 2011).

Due to the occurrence of macro-cracking events, a high amount of the elastic energy can be released resulting in high amplitude events. Therefore, it is reasonable to use amplitude distribution during the fracture so that the damage progress can be predicted. Consequently, the “Ib-value” which represents the ratio of weak to strong events can be utilized (Shiotani et al., 1994). The formula of Ib-value can be calculated as below:

$$Ib = \frac{[\log N(\mu - \alpha_1 \sigma) - \log N(\mu + \alpha_2 \sigma)]}{(\alpha_1 + \alpha_2)} \quad (4.25)$$

With preceding explanations, micro-cracking causes a relatively high Ib-value, which is the absolute value of the slope of the cumulative amplitude distribution, whereas macro-cracking results in relatively low Ib-values. The detail of the above formula can be found in Reference (Shiotani, Fujii, Aoki & Amou, 1994). However, the average calculated Ib-value is superimposed in the load-deflection curve presented in Figures 4.29 and 4.30. In general, there were two considerable drops in Ib-value trends. The first drop occurred when the macro-cracks were going to form and the more significant second drop occurred much earlier than the peak load. However, although the main drop in Ib-value results took place much earlier than the peak load, the Ib-value decreased in specimens with punching failure earlier than specimens with flexural failure.

The main drop in Ib-value occurred at 85% of ultimate load for NM4, whereas this drop ranged from 65-73% of ultimate loading in specimens with punching failure. It was also noted that the Ib-value at the moment of fracture ranged from 0.06 to 0.09. However, this drop which can be attributed to the macro-crack formation and localization can be used as an early warning failure system.

4.5.7. Conclusion

Twelve ferrocement multi-layered composite slabs, including normal cement, self-compact, and rubberized self-compact mortars with varying mesh layers, were subjected to concentrated loading. Disposed rubber powder of tires was used a potential by-product replacement in self-compact mortars. An acoustic emission technique was incorporated into mechanical and micro-structure analysis to monitor the fracture behaviour of ferrocement composite slabs. The following conclusions were drawn.

It was demonstrated that rubber powder can be used in self-compact mortar as a partial replacement of cement while it may slightly decrease the ultimate load capacity of slabs. However, inclusion of 10% rubber powder can significantly change the type of slab failure, converting punching failure to a moderate flexural failure by higher ductility. In addition, an increase in number of wire meshes also increased the flexural strength of slabs resulting in punching failure.

The acoustic emission technique successfully characterized the fracture behaviour of slabs. AE hits rate variation could differentiate various stages of fracture. The structural behaviour of slabs and types of failure, punching and flexural, were characterized by the aid of AE parameters as a source discrimination system.

Finally, it was observed that AE hits can be correlated to stiffness reduction in structure through which an early warning indicator can be attained while AE hits amplitude distribution could provide an early warning failure system.

4.6. Damage Detection and Monitoring of Ferrocement Composite Slabs by Means of Acoustic Emission Technique

In the following the theories, analysis, results and conclusions are presented for this article. The related experimental references are presented in section 3.5.

4.6.1. Theory of Application of Damage Sensitive Feature and Control Charts in AE

It should be noted that because acoustic emission damage detection technique relies on experimental data with high level of uncertainty other than environmental effects on the AE results, utilization of statistical analysis procedures seems to be very efficient if quantification of damage from changes imposed to AE response is required. Moreover, the inherent complex nature of cementitious composite materials adds additional uncertainty for structural health monitoring purposes. Therefore, the concerns mentioned above can result into a comprehensive general damage detection scheme and reliability analysis with the aid of acoustic emission technique. The principal approach is based on: 1) introducing suitable damage-sensitive features and 2) providing a statistical framework to monitor any inconsistency and outlier data as an indication of damage other than quantification of damage.

To this end, an autoregressive (AR) model is integrated with exponentially weighted moving average (EWMA) and Shewhart control charts to present a damage detection scheme for multilayer ferrocement composite slabs.

Six samples composed of four and six-layer wire mesh composite slabs were prepared. The slabs were tested under concentrated loading, resulting in two types of failure, namely flexural and punching. AE sensors were used to acquire AE parameters. Initially, in order to obtain the framework of damage detection scheme, the efficiency of AE energy were investigated.

An autoregressive model was used to construct a damage-sensitive feature by using AE energy time history which allows one to identify different damage stages. In the first step an AR model of order 3 was examined to be used as a damage sensitive-feature. The constructed AR model was used as an input to plot control charts. Two types of control charts, Shewhart and Exponentially Weighted Moving Average (EWMA), were examined to determine the efficiency of both for AE monitoring purposes.

The variation in the number of outliers in control charts could be used as an indication of changes in damage state. In the next step, considering the high dimensionality of AR model of order 3, two projection techniques (Linear and Quadratic) were used to transform 3D space of AR model of 3 into one space which can maximize the damage stages discrimination. In the final step, by using AE signal strength and intensity analysis (IA) damage imposed to the composite slabs were quantified. Figure4.41 presents the pertinent flowchart.

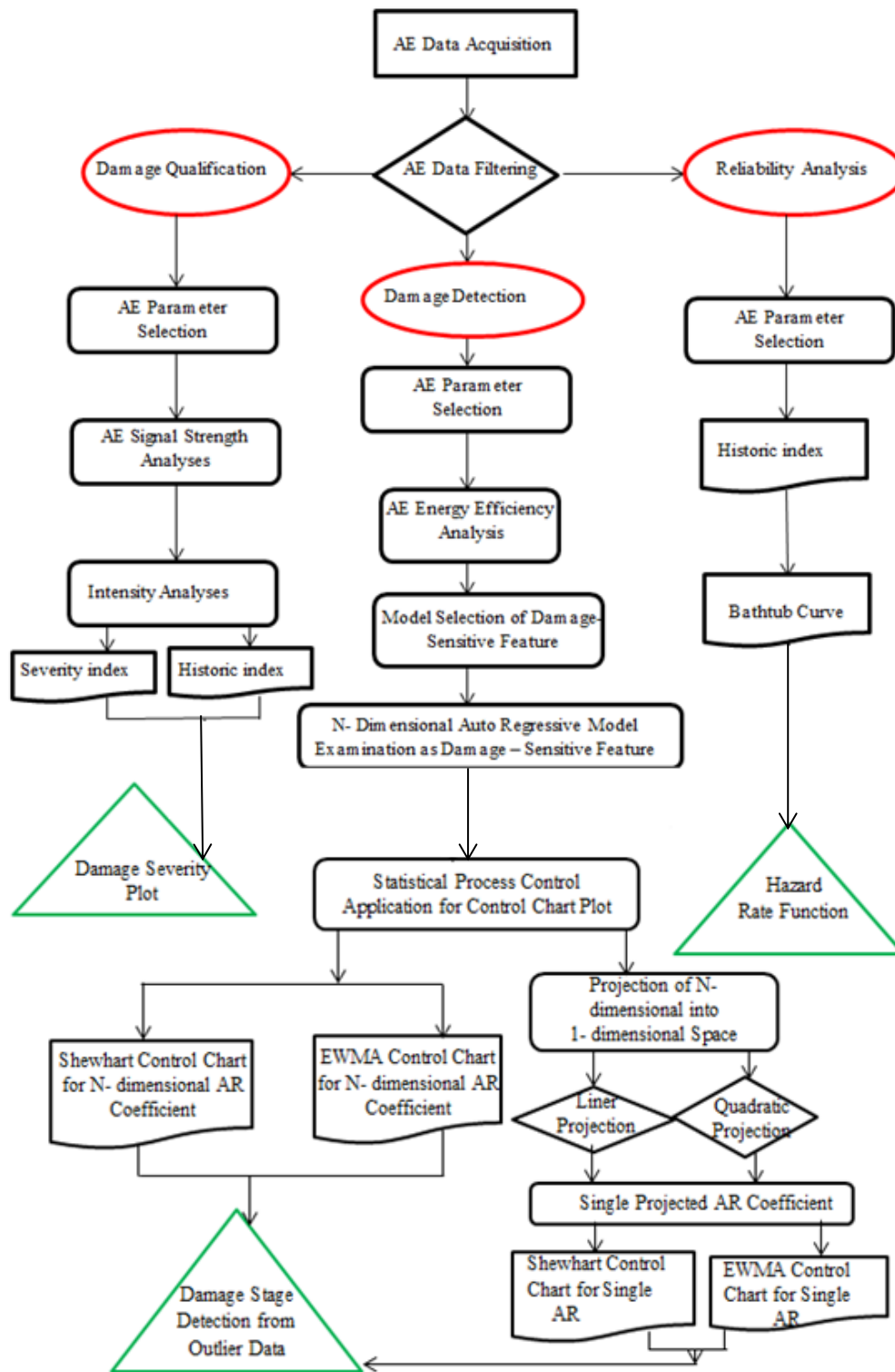


Figure 4.41: Proposed damage detection scheme flowchart

4.6.2. Statistical Process Controlling of AE Energy to Evaluate Damage State

The inherent AE features acquired in the experimental process, particularly for concrete structures, embrace a high level of uncertainty. Therefore, if one is to quantify changes in the AE responses and correlate them with damage state of structures, statistical analysis procedures seems to be necessary for facilitating related processes. The paradigm of SPC can be explained in four subsequent parts: 1. Operational assessment, 2. Data acquisition and de-noising, 3. Feature extraction and if needed reduction of dimension (Fanning and Carden, 2001), 4. Implementation of statistical model (Fugateet al., 2001). Therefore, a paradigm of data feature extraction, damage sensitive feature definition, and statistical model development will be processed in the following sections.

4.6.3. Damage-sensitive Feature Extraction With an AR Model

The process of damage-sensitive properties extraction from the measured AE data will be termed as feature extraction through which one would be able to distinguish different states of damage imposed to the structure. However, distinguishing systematic differences between different damage states by having a look into AE data is likely impossible. Therefore, forming a model of AE data for damage detection purpose would be quite helpful. Generally, two key procedures are required to proceed with SHM reference point state: 1. Representation of AE response time history, 2. Benchmark definition.

In this study for building a model to represent AE energy response time history, an auto regressive (AR) series was formed as damage-sensitive features (model). AR will provide a series of coefficients on which statistical procedures and analysis can be applied to establish the benchmark.

The AR model can be constructed from the time series of individual measurement point, or spatial compressed form of data after space reduction/projection. In the AR model of order p (AR(p)), the current point in the AE response time series will be modelled as linear combination of the previous p points. The equation below describes the essence of the AR model:

$$f(t) = \sum_{j=1}^p \phi_j f(t-j) + e(t) \quad (4.26)$$

where $f(t)$ is the time history at time t , ϕ_j is unknown AR coefficient, and $e(t)$ is the random error with zero mean and constant variance. Brockwell and Davis (1991) proposed a model so-called Yule-Walker to estimate AR coefficient (ϕ_j). For this current study, AE energy time history was adapted in the form of several smaller size windows by breaking the total time history into several windows. The AR coefficients will be computed for each time window. Consequently, a large set of AR coefficients will be resulted for which statistical procedures may be applied to achieve a damage diagnostic system.

4.6.4. EWMA and Shewhart Control Charts for Statistical Process Controlling (SPC) Model

Development of a proper statistical model concerns the implementation of an appropriate algorithm so that analysis of distributed extracted features (AR coefficients) may result in determination of damage stages in the structure. The algorithm development in SPC can be generally considered in three different categories as follows: 1. Classification of different groups, 2. Regression technique, and 3. Outlier detection. Proper algorithm selection is concerned with whether or not the method is to use a supervised or unsupervised approach.

It is noted that the supervised learning method addresses the technique where data of different damage states are known, whereas in unsupervised method data are available for benchmark or reference point. This study developed a SPC model for AE energy data through an unsupervised method. In this study, control chart analysis as one of the most well-known SPC technique was used because it is well suited for monitoring an automated continuous system. If the system or structure under investigation experiences an abnormality, the mean and variance of the extracted features will change.

Here two types of control charts, Shewhart (X-bar) and Exponentially Weighted Moving Average (EWMA) were examined to determine the efficacy of each method to monitor variation of the extracted feature means though which inconsistency in data can be detected.

In order to monitor the variation in the means of extracted features, the features (i.e. AR coefficients) were initially rearranged in subgroups of size n . Now, let the variable ψ_{ij} denote the j th feature from the i th subgroup. It is also noted that the subgroup size n is usually taken to be 4 or 5 as suggested by (Sohn, Czarnecki & Farrar, 2000). However, other than reduced data size, using subgroups offers a significant advantage as distribution of subgroups mean values often can be easier to approximate with a normal distribution owing to central limit theorem (Sohn, Czarnecki & Farrar, 2000). In the next step, \bar{X}_i means of subgroups and S_i standard deviations of the features were calculated in each subgroup. It should be noted that when the number of subgroups was denoted by q , $i = 1, \dots, q$.

$$\bar{X}_i = \text{mean}(\psi_{ij}); \quad S_i = \text{std}(\psi_{ij}) \quad (4.27)$$

Now the Shewhart X-bar control chart can be plotted through drawing a centre line (CL) at the subgroup mean while the plot was completed by adding two lines addressing upper and lower control limits (UCL and LCL). To define centre line and corresponding boundary limits the following equation can be applied:

$$UCL, LCL = CL \pm Z_{\alpha/2} \frac{S}{\sqrt{n}} \quad \text{and} \quad CL = \text{mean}(\bar{X}_i) \quad (4.28)$$

where $Z_{\alpha/2}$ is the percentage point in the normal distribution with zero mean and unit variance so that $P[z \geq Z_{\alpha/2}]$. It should be noted that by averaging all subgroup variance (S^2_i) the total variance can be obtained: $S^2 = \text{mean}(S^2_i)$. However, the control limits of above equation correspond to a $100(1-\alpha)$ % confidence interval if \bar{X}_i can be approximated by a normal distribution. Finally, any outliers' occurrence by crossing the boundary limit will be recorded.

The next type of X-bar control chart used in this study is Exponentially Weighted Moving Average (EWMA). EWMA is a statistic monitoring process in which the data averaging will be in a manner that offers less and less weight to data as they are further removed in time.

It is noteworthy that for the Shewhart chart control method, at any time t , the decision on the state of control of the process relies solely on the most recent measurement from the process and, of course, the degree of "trueness" of the estimates of the control limits from historical data. Conversely, for the EWMA control technique, the decision relies on the EWMA statistic. It means EWMA considers exponentially weighted average of all prior data. In general, if η denotes weighting factor, by choosing a proper η , EWMA control procedure can be built sensitive to gradual drift in the process of data.

It is noteworthy that Shewhart control chart only exhibits reaction against outlier data for the last data point. The EWMA can be defined as follows (Sohn et al., 2000):

$$EWMA_t = \eta Y_t + (1-\eta) EWMA_{t-1} \quad \text{for } t=1, 2, \dots, n. \quad (4.29)$$

where

- $EWMA_0$ is the mean of historical data (target)
- Y_t is the observation at time t
- n is the number of observations to be monitored including $EWMA_0$

- $0 < \eta \leq 1$ is a constant that determines the depth of memory of the EWMA.

The parameter η controls the rate at which "older" data come into the calculation of the EWMA statistic. A value of $\eta=1$ suggests that only the most recent measurements impact the EWMA. Thus, a large value of η (closer to 1) attributes more weight to recent data and less weight to older data; a small value of η (closer to 0) results in more weight to older data. The value of η is usually taken between 0.2 and 0.3 (Hunter) although this is a somewhat arbitrary choice. Lucas and Saccucci (1990) suggested tables that facilitate choosing η . In addition, the variance of EWMA can be estimated as follows:

$$s_{ewma}^2 = \frac{\eta}{2-\eta} s^2 \quad (4.30)$$

when t is not small and where s is the standard deviation calculated from the historical data. The center line would be target value or $EWMA_0$ and the boundary limits can be defined as follows:

$$UCL = EWMA_0 + k s_{ewma} \quad \text{and} \quad LCL = EWMA_0 - k s_{ewma} \quad (4.31)$$

In the above equation k can be either chosen 3 or taken from table proposed by Lucas and Saccucci (1990).

4.6.5. Data Compression on AR Model by Means of Linear and Quadratic

Projection

The previous section explained how to plot control charts for extracted features (i.e. AR coefficients). As explained in section 4.6.4 a p -dimensional AR model can be used as a damage-sensitive feature. Therefore, for such multidimensional feature vectors, Shewhart and EWMA monitoring control chart procedures were used to discriminate feature vector. In other words, AR coefficients were monitored individually by employing above mentioned statistical procedures.

Alternatively, AR coefficients as damage-sensitive features can be monitored in simultaneous monitoring of all AR coefficients through either multivariate feature vectors or transformed one-dimensional (1D space) AR coefficient.

Nevertheless, individual monitoring of multivariate feature vectors with high dimensionality might result in a huge amount of data for which data visualization can be extremely difficult. Therefore, the multidimensional feature vectors will be projected onto 1D space for which SPC (control charts) can be applied readily.

In the present study, in order to optimize damage states separation, feature vector transformation procedure includes linear and quadratic projection. AR coefficients will be subjected to linear and quadratic projection techniques resulting in a one-dimensional AR coefficient which will be then monitored by means of Shewhart and EWMA control charts.

For instance, assume there are two classes (A and B) and multidimensional feature vector x is resulted. Based on Bayes' theorem a decision boundary $D(x)$ was proposed through which the probability of the error can be minimized (Fugate et al., 2001). In other words, the probability of misclassification refers to the reduced probability of assigning a vector to class A when it belongs to class B.

The Bayes 'decision rule $D(x)$ can be presented in a quadratic format when both classes, A and B, have normal distribution (Fugate et al., 2001).

$$D(x) = x^T Q x + V x \quad (4.32)$$

in which Q and V are quadratic and linear projection matrices, respectively. Furthermore, Fukunaga showed that if both A and B classes have identical covariance matrices, further simplification can be applied which results in a linear form.

$$D(x) = F^T x \quad (4.33)$$

The above decision approach can also be taken into account as a sort of projection that is able to map multidimensional space x to reduce 1D space $D(x)$. Therefore a transformed feature $\psi = D(x)$ will be defined in which the means of two classes would be as far as possible while their variances are small after linear or quadratic projection. To provide this projection in an optimized manner Fisher criterion (Bishop, 1995) can be utilized as follows:

$$f = ((\mathbf{m}_a - \mathbf{m}_b)^2 / (\sigma_a^2 - \sigma_b^2)) = ((\mathbf{F}^T(\mathbf{m}_a - \mathbf{m}_b) (\mathbf{m}_a - \mathbf{m}_b)^T) \mathbf{F}) / (\mathbf{F}^T(\boldsymbol{\Sigma}_A + \boldsymbol{\Sigma}_B) \mathbf{F}) \quad (4.34)$$

where \mathbf{m}_a and \mathbf{m}_b are the mean vectors of class A and class B distributions and $\boldsymbol{\Sigma}_A$, $\boldsymbol{\Sigma}_B$ are covariance matrices of class A and class B, respectively. In addition, m_a and m_b are the means of projected features in both classes while σ_a and σ_b are the standard deviations of transformed features of class A and class B, respectively. Next, the multidimensional feature of vector x will be correlated to the moments of projected features as follows:

$$m_i = \mathbf{F}^T \mathbf{m}_i \quad \text{and} \quad \sigma_i^2 = \mathbf{F}^T \boldsymbol{\Sigma} \mathbf{F} \quad \text{for } I = A \text{ or } B \quad (4.35)$$

Linear projection can be resulted from derivation of f with respect to \mathbf{F} that is set to zero (Bishop, 1995):

$$\mathbf{F} = 2 (\boldsymbol{\Sigma}_A + \boldsymbol{\Sigma}_B)^{-1} (\mathbf{m}_a - \mathbf{m}_b) \quad (4.36)$$

It should be noted that if distribution of class A and B have similar covariance matrices ($\boldsymbol{\Sigma}_A$ and $\boldsymbol{\Sigma}_B$), the linear projection will be optimized. For the current test data acquired from AE responses, AE energy time history exhibited different covariance matrices in different damage states. Since in the general condition, the Bayesian decision boundary is quadratic with unequal covariance matrices, the optimized transformation might be quadratic. However, the computation of terms presented in Equation 4.32 (Q and V) seems more intensive rather than linear projection.

Nevertheless, Sohn et al. (2000) proposed to introduce a new variable y_i which is representative of products of two x_i s. Therefore, Equation 4.32 can be rewritten in linearized form as follows:

$$D(x) = \sum_{i=1}^p \sum_{j=1}^p q_{ij} x_i x_j + \sum_{i=1}^p v_i x_i = \sum_{i=1}^p a_i y_i + \sum_{i=1}^p v_i x_i \quad (4.37)$$

in which q_{ij} and v_i are components of quadratic and linear forms (Q and V). Moreover, y_i denotes the product of x_i s, while corresponding entry in matrix Q is denoted by a_i . As stated before, p is either the order of AR model or dimension of AR coefficients.

Assume C and D represent the column vector of y_i s and x_i s, respectively. Then, by introducing a new variable $W = [C^T D^T]^T$ and taking E and S as the expected vector and covariance matrix of W, respectively, the following equation similar to linear form can be written for A and V:

$$[a_1 \dots a_{n(n+1)/2} V_1 \dots V_n]^T = 2 [S_A + S_B]^{-1} (E_A - E_B) \quad (4.38)$$

Thereafter, by rearranging a_i s and v_j s matrix Q and vector V will be obtained. It is noteworthy that aim of using the above explained projection technique was twofold: 1. Dimension reduction, 2. Providing a discriminant function. In a general manner, n -dimension of AR model was projected to a single space through which mean differences between damage states were maximized. Damage diagnosis technique was constructed by using SPC model applied on the transformed features.

4.6.6. Results and Discussion

In the following the pertaining results and discussions will be presented.

4.6.6.1. Mechanical Behaviour of Composite Slabs

Two types of composite slabs presented in section 4.5.2 were taken for this study. Specimens NM4 and NM6 with flexural failure and punching failure modes, respectively, were taken. The structural behaviour and analysis is presented in section 4.5.2.

4.6.6.2. AE Signal Strength Analysis

From the AE measurement and analysis performed on the AE data, the trend of variation of AE energy with respect to the evolution of damage was investigated. Toward this purpose, the largest AE energy was chosen. According to the energy level of AE hit, all AE hits were categorized into four groups (Classes). There are three selected energy levels through which subsequent classes were formed. The energy levels and associated classes are listed below:

Level 1= $10000 \text{ V}^2\mu\text{s}$, Level 2= $100000 \text{ V}^2\mu\text{s}$, Level 3 = $1000000\text{V}^2\mu\text{s}$

Class A = under level 1, Class B= above level 1, Class C= above level 2, Class D = above level 3

The number and percentages of AE events and corresponding AE energy released during the damage process of composite slabs relative to the associated total values are presented in Table 4.9 and Figure4.42. As presented in Table 4.9 results for both composite slabs (NM4 and NM6) show that while the number of occurrences of AE events in class A was considerably high, the AE energy released during these AE events were significantly low. Consequently, it might be inferred that the level of damage pertinent to these AE activities is significantly low. It was observed that in terms of energy level, most AE events belonged to class B.

It means that most of the signals which were emitted during the damage process had energy level greater than $100000 \text{ V}^2\mu\text{s}$ (Level 2).

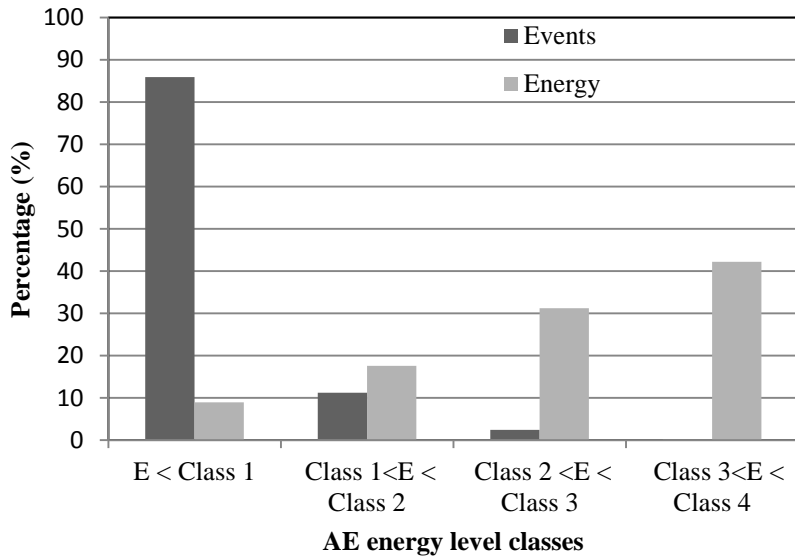


Figure 4.42: AE energy level distribution against AE events distribution for NM6

Table 4.9: Acoustic emissions events and the recorded AE energy

AE Energy V^2 us		AE Events		AE Energy	
		Number	Percentage %	Total AE Energy	Percentage %
S6	Total	21007	100.00	5663318794	100.00
	class A	18042	85.89	509046273	8.99
	class B	2965	14.11	5154272521	91.01
	class C	556	2.65	4159084183	73.43
	class D	47	0.22	2392668000	42.24
S4	Total	6935	100.00	36829054849	100.00
	class A	4817	69.46	259394399.2	0.70
	class B	2118	30.54	36569660450	99.30
	class C	200	2.88	36056950447	97.90
	class D	67	0.97	35212307000	95.61

Figure 4.43 presents the AE events source localization for NM6 during damage process considering different classes of AE energy levels. As indicated in Figure 4.43, AE energy level of class C contributed significantly to the fracture process zone while AE energy above Class C (Class D) possessed fairly high acoustic emission energy per unit area of fracture process zone. These observations indicate that AE events with higher energy level than $100000 \text{ V}^2\mu\text{s}$ predominantly contributed to the fracture process zone because of their high energy level, whereas the total numbers of AE activities were quite low.

In general for all composite slabs, the intensity of AE event for class A and B was considerably high while these AE events possessed low energy. Conversely, AE events intensity for class C and D were lower while associated AE energies were considerably high especially these events located in fracture zone (punching area). Therefore, in general, it was found that AE energy has great potential trace changes imposed to the structure during the fracture process. In this line, a damage index by using AE energy time history of NM6 was extended.

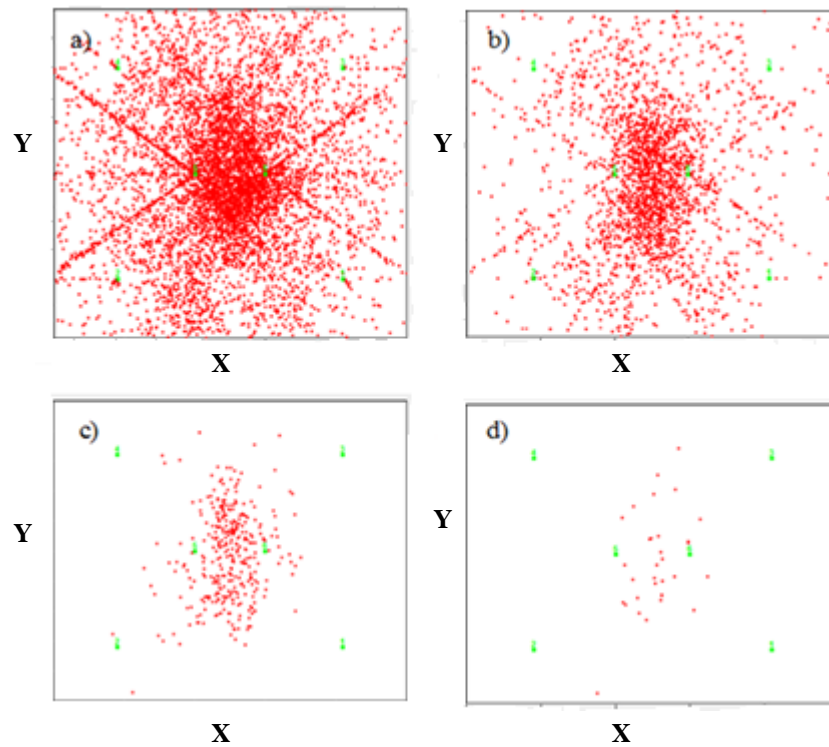


Figure 4.43: Acoustic emission event source localization with respect to different energy classes: a) Class A, b) Class B, c) Class C, d) Class D, $X = Y = 0.5$ m

4.6.6.3. Feature extraction and damage detection analysis

In the first step the SPC as a damage diagnosis technique is applied on the damage sensitive features (AR coefficients) and subsequently control charts will be constructed for each individual AR coefficient by means of Shewhart X-bar control chart and EWMA control chart. In the next step, the application of projection technique is sought. In order to map multi-dimensional AR coefficients into 1D space, the linear and quadratic projection are utilized through which the mean differences between data set acquired from different damage states will be maximized. Thereafter, SPC technique will be introduced to the transformed 1D scale feature. The 20001-point measured AE energy time series were first divided into 1000 20-point time windows (eliminating one-point). Then AR model of order three (AR (3)) was fit to an individual window resulting in 1000 set of AR coefficients.

Thereafter, as stated earlier, subgroups of size 4 were built resulting in 250 subgroups ($1000/4 = 250$) for each of which the means of data set were calculated.

For instance, damage diagnosis results in the form of a Shewhart control chart for the first AR coefficient were shown in Figure 4.44. By setting $\alpha = 0.01$ in Equation 4.28 the corresponding upper and lower limits by 99% confidence interval level were obtained.

Moreover results indicating different damage states obtained by EWMA and Shewhart X-bar control chart were presented in Table 4.10. Note that for computing outliers in EWMA control chart related parameters k and λ were set 3 and 0.3, respectively. Thereafter, subsequent damage states were plotted by means of constructed UCL, LCL, and CL. It should be noted that prior to plotting the control charts the extracted features (e.g. in Figures 4.44 and 4.45 the first AR coefficient) were first standardized by subtracting the features from the mean and normalizing the features by standard deviation. In the next step, features were plotted in each damage state with respect to corresponding control limits. It is noteworthy that the mean and standard deviation of first damage state were used to standardize the other damage states features.

The diagnosis results obtained by other AR coefficients were also presented in Table 4.10. As found in this case study, the third AR coefficient is the most sensitive and indicative damage indicator, whereas the first AR coefficient showed less sensitivity to the damage progress. For damage level I the total number of outliers are 2 out of 750 samples and 7 out of 750 samples resulting in 0.27% and 0.93% outliers for Shewhart and EWMA control charts, respectively. However, it should be noted that the plotted control chart was constructed considering 99% of confidence interval which means features extracted from the control charts can still generate 1% outliers without indication of damage.

As a result, it is not clearly certain if the system has experienced any damage at this level considering results obtained by individual AR X-bar control chart, especially Shewhart method.

As could be observed in Table 4.10 some AR coefficients are more sensitive than others in some levels of damage and vice versa. In addition, calculating and constructing X-bar control charts for individual AR coefficients can be a long process.

To this end, the procedure of constructing X-bar control charts for individual AR coefficients was simplified into a single X-bar control chart of 1D space. Therefore, the projection techniques presented in previous sections were introduced to multiple space AR coefficients to transmit into 1D AR space.

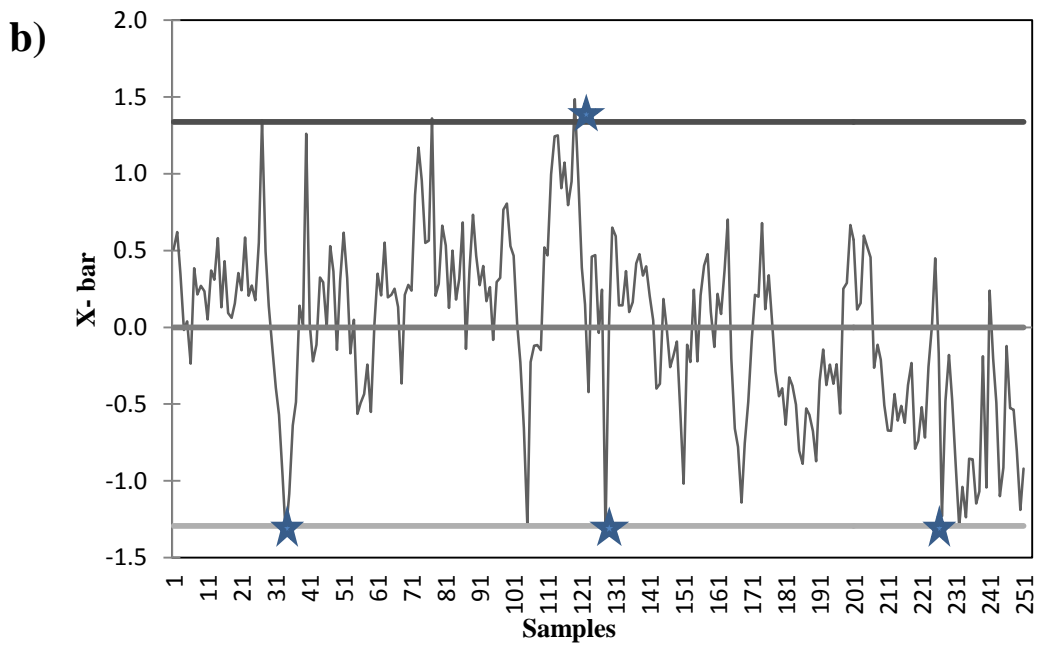
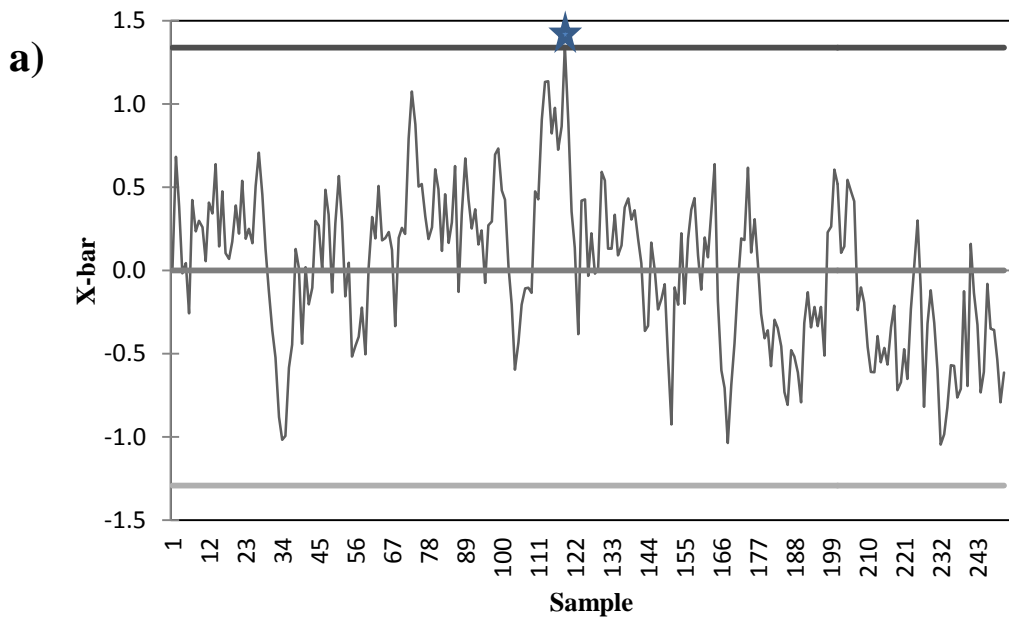


Figure 4.44: X-bar control chart using the first AR coefficient, a) Damage level I (25%), b) Damage level II (50%)

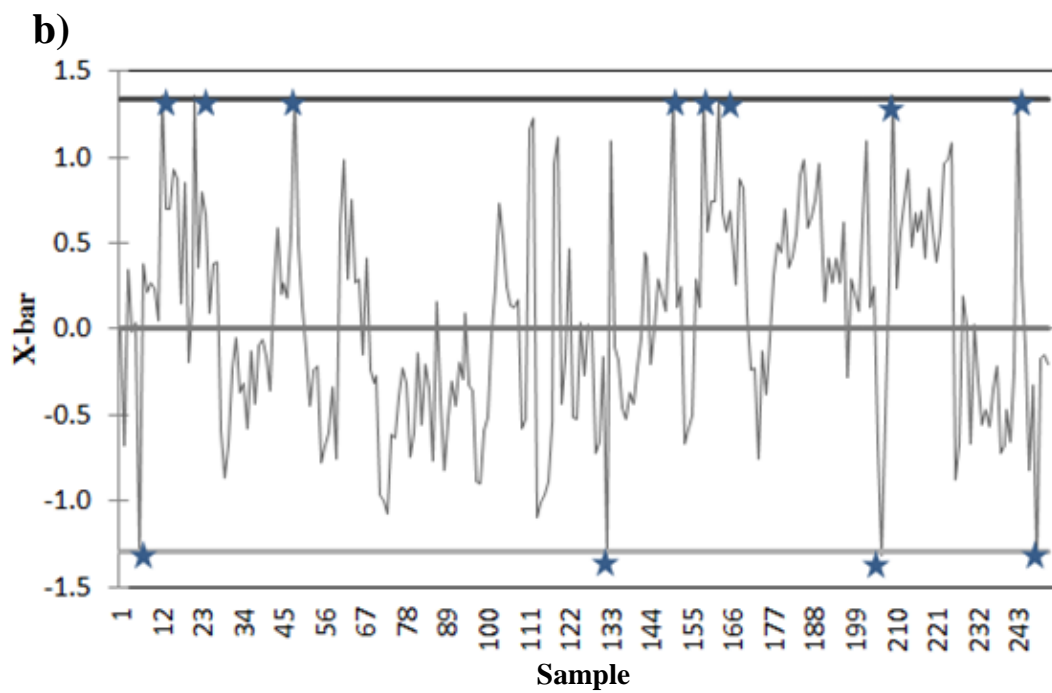
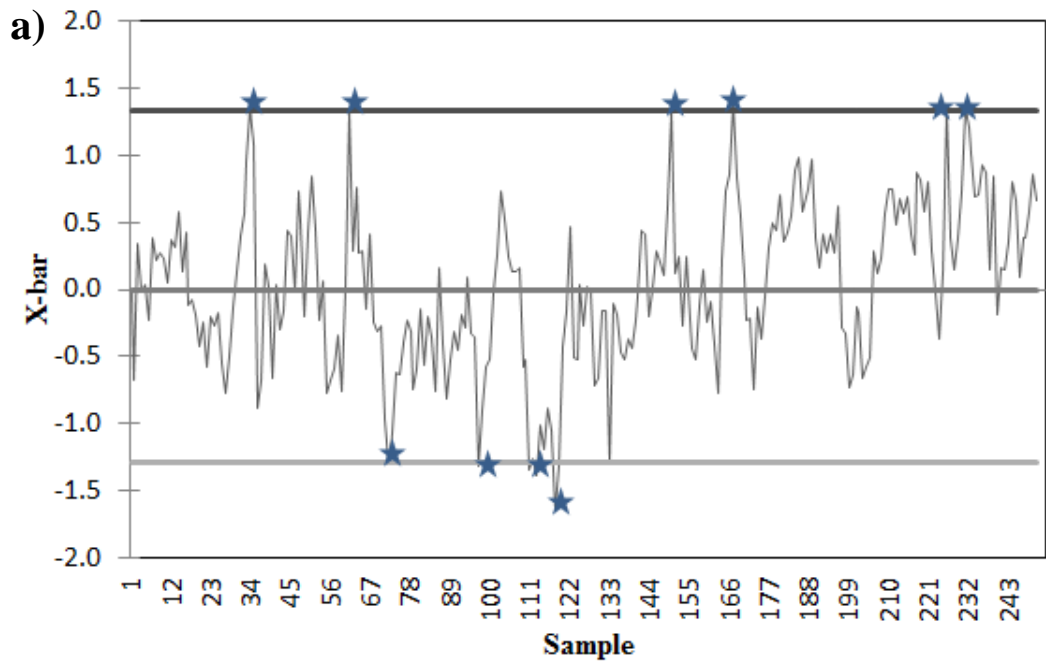


Figure 4.45: X-bar control chart using the first AR coefficient, a) Damage level III (75%), b) Damage level IV (100%)

Table 4.10: Outlier of X-bar control charts by using different AR coefficients

Damage level								
AR coefficient	Shewhart X-bar control chart				EWMA			
	Level 1	Level 2	Level 3	Level 4	Level 1	Level 2	Level 3	Level 4
α_1	1/250	5/250	10/250	12/250	0/250	5/250	35/250	53/250
α_2	0/250	7/250	12/250	22/250	4/250	25/250	97/250	155/250
α_3	1/250	16/250	55/250	53/250	3/250	36/250	106/250	196/250
Total outliers	2/750	28/750	77/750	87/750	7/750	66/750	238/750	404/750
Percentage %	0.27	3.7	10.27	11.6	0.93	8.8	31.7	53.87

In this particular example, 3D AR coefficients are initially projected into 1D space. Next the transmitted features were used to plot X-bar control charts. It is noteworthy that, in general, projection and transmission features from higher space to lower space may result in loss of information. Therefore, to overcome this problem Fisher criterion presented in Equation 4.34 was implemented. By Fisher criterion the projection is led to maximize the class separation.

Table 4.11 presents the results of monitoring process after a Linear and Quadratic projection. By comparing results obtained for multiple AR coefficient presented in Table 4.10 with results obtained in Table 4.11, the improvement in diagnosis performance can be clearly found. The diagnosis measurements for the other specimens resulted in a similar performance improvement by using projection technique. It is noteworthy that, in general, the linear projection might not be the optimized projection since the order of different class covariance matrices (different damage states) is different. In view of theory, Quadratic projection minimizes the misclassification error. In this particular case study, linear projection still shows acceptable performance while presenting results close to EWMA method.

Table 4.11: Outlier of Shewhart X-bar control chart by Linear and Quadratic projection

Damage level								
Linear projection					Quadratic projection			
AR coefficient	Level 1	Level 2	Level 3	Level 4	Level 1	Level 2	Level 3	Level 4
α	2/250	21/250	99/250	165/250	3/250	26/250	112/250	216/250
Percentage%	0.8	8.4	39.6	66	1.2	10.4	44.8	86.4

It is quite visible from Figure 4.46 that the quadratic technique had considerably better performance compared to other techniques. However, EWMA monitoring performance showed acceptable performance especially for those damage states of level 1, 2, and 3. Results obtained in EWMA are somewhat close to those for linear projection especially for damage state level 1, 2, and 3. However, for the first two damage levels, somewhat similar performances were observed for all presented methods, whereas quadratic technique was the only reliable scheme for damage level 1 with higher outlier percentages than interval error.

Relative increment in damage indicator for each stage of damage is presented in Figure 4.46b. Interestingly, Shewhart and linear project schemes showed lower level of increment in damage indicator for the last damage level, whereas quadratic projection kept steady incremental trend in each subsequent damage level. The increment rate for the last level of damage in EWMA scheme was similar to its damage level 3.

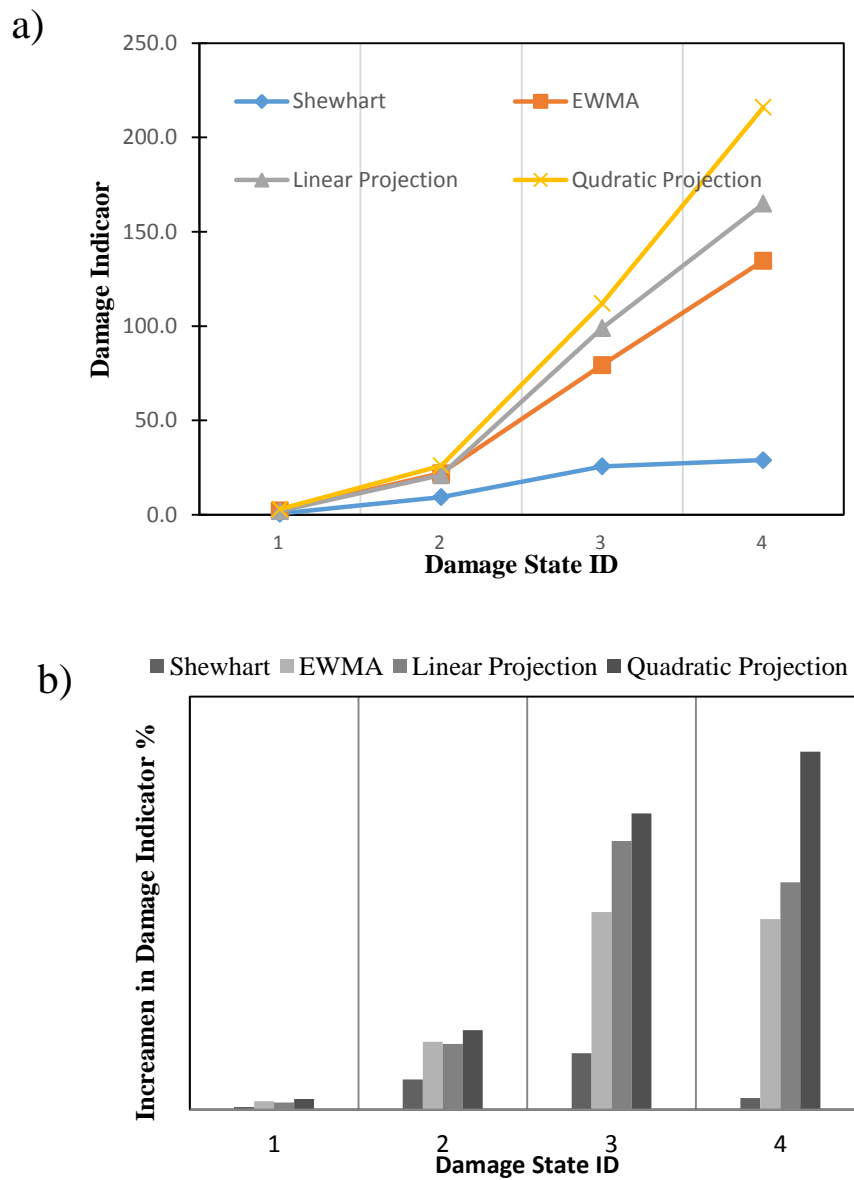


Figure 4.46 Comparisons of structural damage detection schemes: a) Damage sensitivity of different schemes, b) Increment in damage indicator in different schemes

In order to study the effect of AR model order for Shewhart and EWMA damage monitoring schemes, three different AR orders were examined and results were presented in Figure 4.47. Figure 4.47 presented the effect of AR models order of 3, 5, and 7 on the damage indicator values for Shewhart and EWMA control charts.

It can be observed that structural damage was successfully detected in all of the damaged states. The clear increase in damage indicators corresponding to the increase in damage severity was captured for all the damage schemes with different AR model order. For the data and results obtained for this particular case, the monitoring scheme using AR model order of 7 is less sensitive especially for Shewhart model in the last states of damage. It is because showing smaller increments in damage indicator result in less sensitivity to structural damage. Results for AR model order of 3 and 5 were quite similar which resulted in either the same damage indicator values or increment rate of damage indicators. Therefore, AR model order of 3 could be preferable for this case when producing less volume of data in monitoring process.

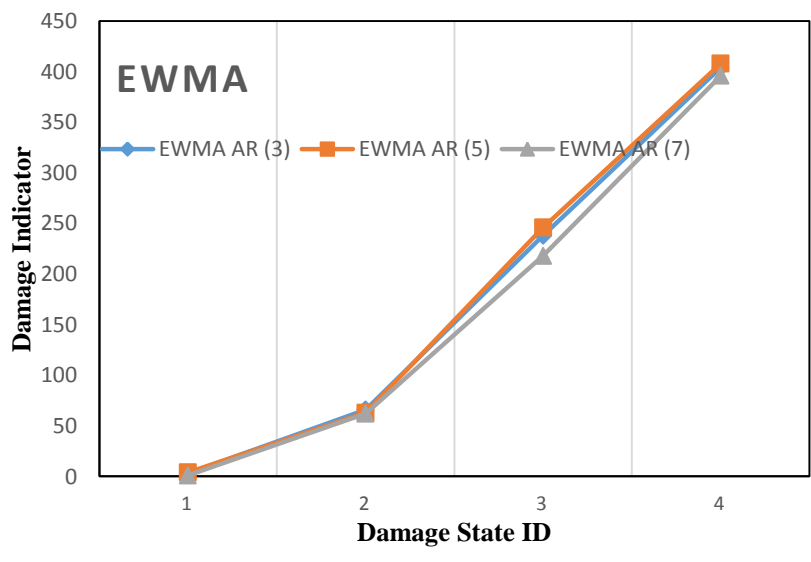
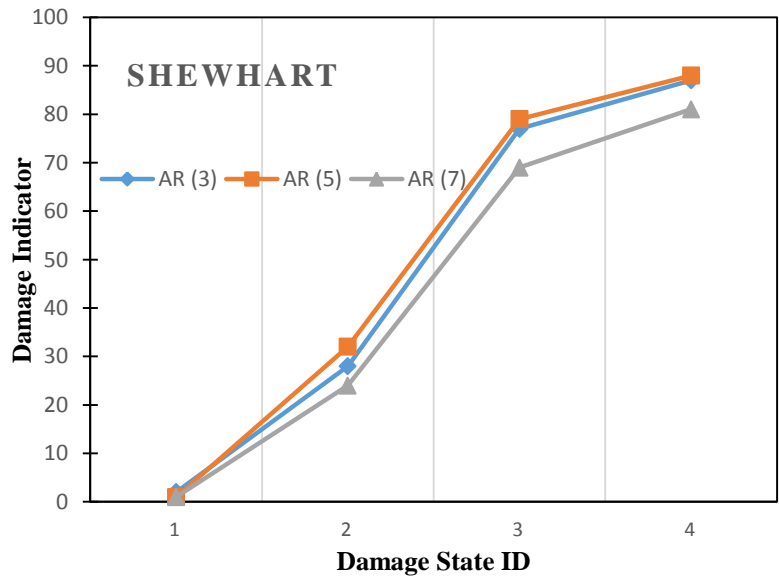


Figure 4.47: Effect of AR model order on damage indicator sensitivity

In general, although the proposed control chart could successfully highlight the inconsistency and subsequent outliers that was in good agreement with the damage states imposed to the slabs, the observation of outliers does not quantify the damage level imposed to the structure. Hence, a quantitative approach with the aid of AE signal strengths known as intensity analysis can be incorporated to the preceding proposed scheme at any instance of monitoring stage.

4.6.6.4. Intensity Analysis (IA)

Intensity analysis evaluates the structural significance of an AE event as well as the level of deterioration of a structure by calculating two values called the historic index (HI) and severity (Sr) (Bagherifaez et al., 2014). The HI compares the signal strength of the most recent emissions to the signal strength of all emissions. This requires estimating the slope changes of the cumulative signal strength plotted as a function of time. The presence of one or more peaks may reveal the occurrence of new damage or the propagation of damage, respectively. As the severity is a measure of structural damage, an increase in severity often corresponds to new structural damage.

Analytically, the HI and the Sr are defined as

$$HI = \frac{N}{N-K} \left(\frac{\sum_{i=k+1}^N S_{oi}}{\sum_{i=1}^N S_{oi}} \right) (4.39)$$

$$S_r = \frac{1}{J} (\sum_{m=1}^J S_{om}) (4.40)$$

where N is number of AE emissions (referred to as ‘hits’) up to time t ; S_{oi} is the signal strength of the i th event; K and J are empirical constants based on the material under investigation. Figures 4.48a and 4.48b present intensity chart and historic index profile for composite slabs, respectively. Results for all composite slabs affirmatively showed that state of damage can be quantitatively presented by intensity chart with some modifications applied in previous studies.

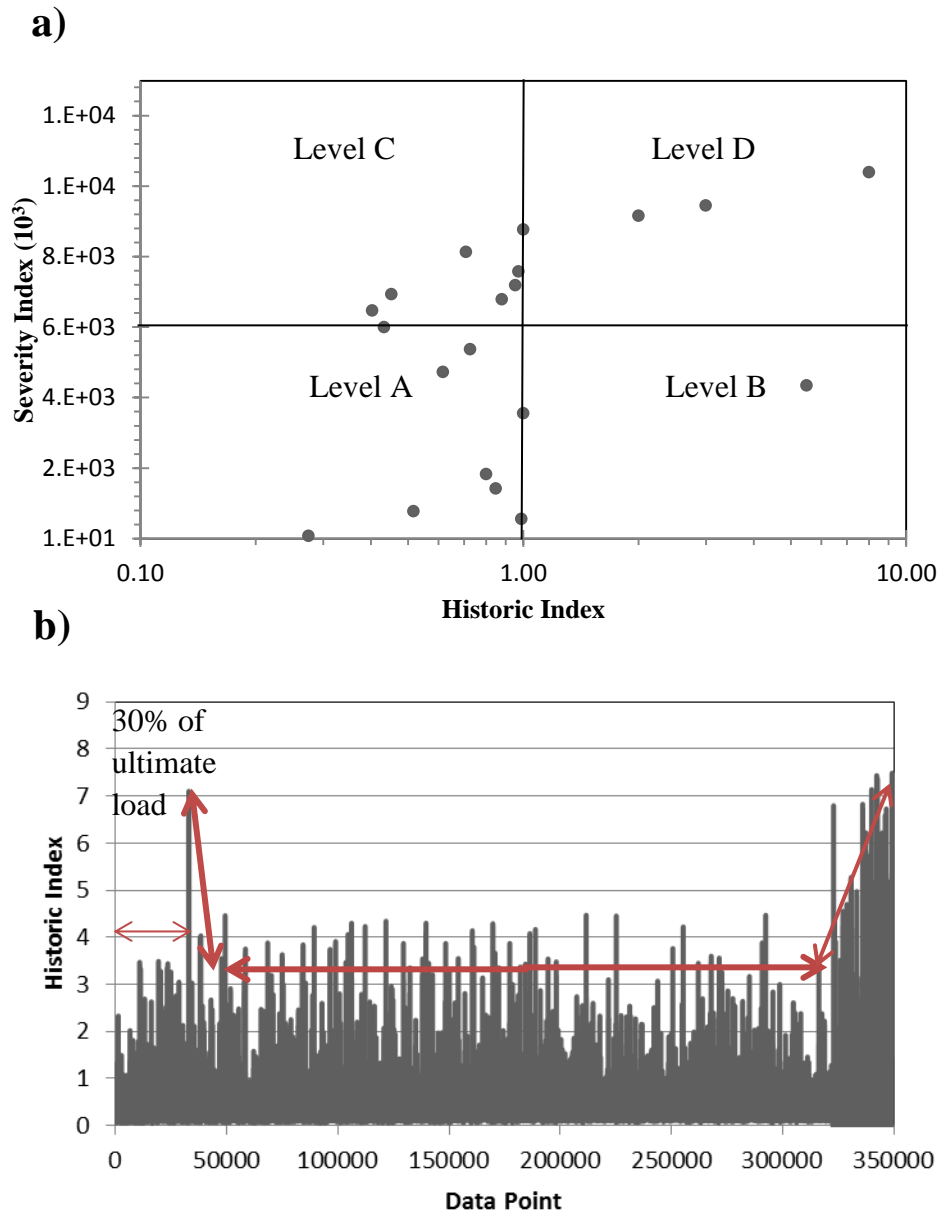


Figure 4.48: Intensity analysis for composite slabs: a) Severity versus Historic index, b) Historic index profile

The damage states in Figure 4.48a are categorized in four classes according to the relation between AE signal strength and loading percentile. Level A represents the stage prior to macro-crack occurrence from 0 to 30% of loading (low damage). Level B indicates the stage after macro-crack occurrence from 30% to 50% of loading strength (low intermediate damage). Level C implies higher level intermediate damage from 50% to 80% of ultimate strength (high intermediate damage).

Level D belongs to severe damage relating final stage of loading strength of composite slabs prior to punching failure. It should be noted that historic index graph has been highlighted with two knees which are indicative of two imperative changes in the composite slabs damage state. The first knee happened in the macro-crack occurrence stage (30% of ultimate loading) and the second one occurred prior to punching failure of composite slabs which are highlighted in Figure 4.48b. This can be related to the large amount of energy released from high energy events resulting in a significant rise in the slope of the historic index.

On the other hand, the graph presented in Figure 4.48b shows a great potential to be used as a hazard rate function for reliability analysis.

The historic index curve is used to develop hazard rate function and consequently a method of reliability analysis and evaluation of current condition of a structure. The three distinguishable stages in historic index curve resemble bathtub curve stages. This curve has three distinct stages. The first stage presents a decreasing failure rate which denotes the infantile or early-life failures, where the system is adopting to the new situation. The second stage exhibits a constant hazard function, whereas the third stage is displaying a rising failure rate which is called wear-out stage. It is noted that the hazard function can be explained by a Weibull function as follows.

$$f(t) = \frac{\beta}{\eta} \left(\frac{t - \lambda}{\lambda} \right)^{\beta - 1} \left(e^{-\left(\frac{t - \lambda}{\eta} \right)^\beta} \right) \quad (4.41)$$

where β is the shape parameter; η the scale parameter; λ the location parameter. The shape parameter, β , also known as the Weibull slope parameter from which the slope of the Weibull probability density function (pdf) can be obtained and the three stages of the bathtub curve is discriminated.

In Figure 4.49 the three stages are defined as below:

$\beta < 1$ infantile failure

$\beta = 1$ constant failure

$\beta > 1$ wear-out failure

However, the hazard function can be obtained from Equation (4.41) as follows.

$$f(t) = \frac{\beta}{\eta} \left(\frac{t - \lambda^{\beta-1}}{\lambda} \right) \quad (4.42)$$

In order to plot the bathtub curve and hazard rate function of composite slabs failure, historic index was used as a frequency or failure rate to obtain Weibull parameters pertinent to each stage of failure. The results of Weibull analysis and failure function plot is presented in Figure 4.49.

It can be realized that in the first stage, infant mortality, the composite slab damage severity was high because of first breakage of slabs at the time of first macro crack emergence. In the infant mortality stage, the initial failure rate is high which can be an indication of sudden release of energy at time of macro-crack occurrence for a short period. In the second stage, steady state, the rate of failure in slabs was constant at a very low failure rate. It can be inferred that, after macro-cracks occurrence, wire meshes in tension parts started to carry tensile load resulting in propagating cracks. The third stage, wear out, is the sudden increase of damage in composite slabs and local damages combined to form material or component damage with a very high rate of punching failure known as a sudden failure. In the third stage the failure rate takes place in a very short time due to the inherent characteristics of punching failure.

In general, the failure can be considered as a local phenomenon rather than failure of a structural element. Local damages are occurring inside the composite slabs when signal strengths are increasing which finally resulted in composite slabs failure.

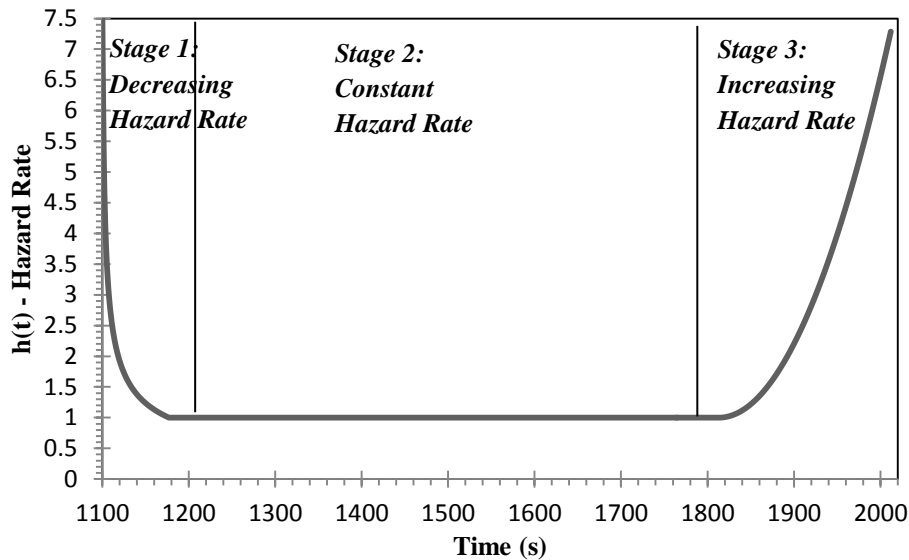


Figure 4.49: Bathtub curve for hazard rate function

4.6.6.5. Conclusion

In the present study, six samples of two types of multi-layer composite slabs with four and six layer meshes were prepared and examined until the final failure load. The slabs were tested under concentrated loads resulting in two types of failure, flexural and punching. Six R6I AE sensors were mounted on the slabs to monitor the failure of composite slabs during the loading process. Acoustic emission parameters such as AE energy and signal strength were investigated to find out the appropriate damage indication parameters. AE energy time history was used as input data for an auto regressive model of order 3 to present damage-sensitive features. Obtained damage sensitive features were used to plot different control charts to find out the relation between the variation of number of outliers and damage state in the composite slabs. In addition, using AE signal strength the highlighted damage in each stage was quantified.

The following main conclusions were drawn from the results.

- AE events with high energy contributed in fracture process zone, therefore, AE signal energy could be used as a proper damage index parameter to present the loss of stiffness in composite slabs.
- A novel structural damage detection scheme based on AE energy using autoregressive-model-incorporating exponentially weighted moving average (EWMA) and Shewhart control chart was presented. It was realized that EWMA was more sensitive damage scheme compared to Shewhart control charts.
- Damage diagnosis results were significantly improved by using either a linear or quadratic projection technique from a 3D space into 1D space.
- AE signal strength showed a great potential to classify the level of damage in composite slabs and to be used for failure reliability analysis.
- The proposed bathtub curve utilizing historic index divided the composite slabs failure in three distinctive stages which could enable one to predict punching failure as an abrupt failure.

4.7. Integrated non-destructive assessment of concrete structures under flexure by acoustic emission and travel time tomography

In the following the theories, analysis, results and conclusions are presented for this article. The related experimental references are presented in section 3.3.

4.7.1. Theory of Global and Local Monitoring

One of the proper approaches for real-time monitoring is the acoustic emission (AE) technique. This non-destructive evaluation (NDE) technique detects signals resulting from irreversible cracking process (Aggelis et al., 2011). On the other hand, owing largely to advancement in computer and sensor technologies, the travel time tomography (TTT) utilizing transient elastic wave propagation has emerged as one of the modern NDE techniques for assessing large-scale structures. The unique feature of TTT lies in its capability to provide visualization of the measured object interior that facilitates better identification of anomalous regions or estimation of physical properties (Momoki et al., 2013). Therefore, considering the essence of AE and TTT, there can be a potential to form a global and local monitoring system. The detailed AE literature and AE parameters have been discussed in previous sections.

4.7.1.2. Theory of Travel Time Tomography (TTT)

Travel time tomography (TTT) is recognized as an NDT method in which the change of propagation time of elastic waves is utilized to evaluate concrete interior by providing velocity distribution map of the measured target. The velocity gradient indicated in the distribution is usually attributed to the presence of anomaly in concrete, which could be, but not necessarily, in the form of a defect such as crack and void.

Because of the different acoustic properties that these anomalies possess, interference to waves occurs, in single or combined forms of diffraction, reflection and refraction (Chai et al., 2012; Chai et al., 2010).

The gradient or difference in travel time would be recorded by a low velocity area on the tomogram demonstrating the location encompasses irregularities, usually in the form of a defect such as a void or crack. In other researches, it is shown that P-wave attenuation (amplitude gradient) present better resolution of mapping due to higher sensitivity of attenuation parameter (Niak et al., 2004; Kobayashi et al., 2007).

The travel time tomography (TTT) method usually includes implementing a multiple source and receiver approach to directly acquire travel time difference, which are resulted from localized physical conditions of the measured structure. The velocity distributions obtained from the inversion procedure provides an essence for leading more accurate tests to acquire information about the measured object interior such as precise characterization of defect. This technique might be straightforward in implementation, but exposes several limitations. For instance, it necessitates that the receivers be located on a side or surface different from that of the source. Although some recent systems like MIRA can capture reflection for this purpose, they are not well known and the another type of recording system should be provided. In addition, the variation in travel time of waves is sometimes less noticeable towards defects of relatively small scale, such that the accuracy of evaluation could pose as a reliability issue. However, it is widely acknowledged that the tomography technique should be positioned as an approximate local method alongside one global method during monitoring process. However, global method such as AE technique has added advantages because of its capability in local analysis other than global monitoring. Travel time tomography essence can be briefed as follow.

Once stress waves propagate in an inhomogeneous medium, refraction and reflection usually happen, causing in variations of velocity and ray path.

The changes are always accompanied with variations in travel time of wave, which is registered in source-receiver measurement as the principal observed data.

To estimate or calculate the travel paths of waves, a method generally recognized as the ray tracing approach is implemented, which occur prior to the inversion computation for “mapping” each of the cells involved with a characteristic slowness value. The methodology utilizes a three dimensional model meshed into hexahedral cells.

A ray is projected from a dispatch point in the model to all available directions for reaching the destination points (nodes). The ray travels in straight path from one node to another and the length of ray-path in each cell is gained by computing the distance between two-intersections. By taking the straight ray approximation, the travel time from the first (dispatching or source) to the second (receiving) would be calculated. The ray will be dispatched again from each of the nodes that were previously reached to new destinations. Another set of travel time data can then be calculated from the new projection-receiving configuration. Through repeating of this process, the direction of projection as registered on each node is used to compute the length of ray path between two scan lines in a subsequent manner. The restoration of velocity profile is performed through inversion procedure of the travel time data. The inverse problem could be expressed by the following governing equation:

$$\int_L \frac{1}{v} dl = \int_L s dl = t \quad (4.43)$$

Where L is the ray path, v is the velocity, s is the slowness (reciprocal of velocity), dl is the length of cell and t is the travel time.

The simultaneous iterative reconstruction technique (SIRT) was performed to solve this highly non-linear problem.

This technique simplifies distributions of the difference between theoretical and observed travel times to the elements which were intercepted by the ray. The distribution is expressed numerically as follows (Kobayashi et al., 2007; Shiotani et al., 2012):

$$S_i = \sum_j \Delta S_{ij} L_{ij} / \sum_j L_{ij} \quad , \quad \Delta S_{ij} = \left(\sum_j \Delta t_i L_{ij} \right) / \left(\sum_j L_{ij} \right)^2 \quad (4.44)$$

In which Δt_i is the difference of travel time between theoretical and observed value. The distributed value for each relevant cell is repetitively amended so that the difference between collective slowness value of the ray and the observed data falls within a standard error range. The three-dimensional map drawing needs isoparametric coordinate projections of ray using hexahedral cells. The cells are transformed into first-order isoparametric elements in this process. The intersection point of the ray on the element would be achieved using the isoparametric coordinate and by conversion to the global coordinate, the length of the ray (travel path) in any particular element can be computed.

4.7.2. Results and Discussion

The pertinent results and discussion will be presented in the following sections.

4.7.4.1. Damage mapping by TTT

Figure 4.50 shows the load–displacement curves of the specimens tested in flexure. The SFRC specimen achieved the highest maximum load among the three, registering differences of approximately 5 kN and 10 kN compared to the PFRC and the RC specimens, respectively.

Also, the SFRC specimen seemed to recorded displacement equivalent to the RC specimen before the ultimate failure, which was approximately 4 mm greater than the PFRC specimen.

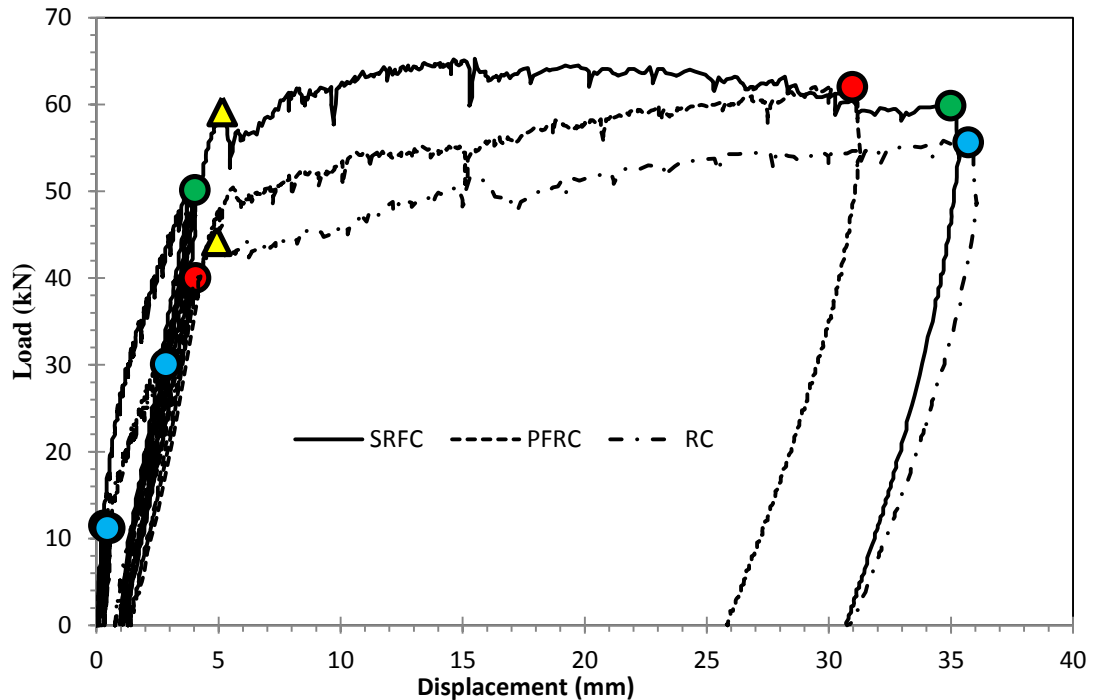


Figure 4.50: Load-displacement curves of beam specimens

As shown in Figure 4.51, the failure was manifested by propagation of flexural cracks and development of critical shear cracks at the later step of loading. Slight fracture due to compression on the top side of specimen in the vicinity of loading points was also observed. The mechanical test results revealed in general that by incorporating 1% polypropylene fibers into concrete, the flexural capacity of specimen can be improved, although no significant improvement in ductility could be suggested due to the low fiber volume fraction. In the case for SFRC specimen, despite the steel fibers being able to offer a more superior performance in enhancing flexural capacity of concrete beams as compared to the polypropylene fibers, the steel fibers would potentially pose issues related to corrosion, especially when the usage volume is high and the corroded fibers no longer provide the desired property for enhancement.



Figure 4.51: Failure pattern of PFRC specimen at ultimate load

The average computed velocity values for all three specimens are given in Figure 4.52 with respect to mode of excitation. The average velocity obtained from steel ball hammer impact, which excitation has a dominant frequency of approximately 20 kHz, was found to give lower discrepancies between data obtained before loading and after failure when compared to pulser excitations that have a dominant frequency of approximately 100 kHz.

It is inferred that the lesser sensitivity of steel ball hammer impact is for mapping of damage, as confirmed by the velocity distribution results of tomographic reconstruction in Figure 4.53. It was also observed from results in Figure 4.52 that the computed velocities for PFRC specimen before the start of test were in general slightly lower than those of the steel ball hammer excitations. This suggests the inhomogeneity introduced by polypropylene fibers, which also have a lower wave velocity compared to concrete and steel, has instigated a more pronounced effect in slowing down waves propagating in the specimen due to interferences such as diffraction and reflection.

On the other hand, waves with higher frequency (pulsar excitations) could be perceived to be more sensitive towards the development of fracture, resulting in higher contrast between velocity distributions obtained before loading and after failure for better visualization effect and more convincing assessment (It should be noted that it is combined effect of frequency and amplitude). The observation was in agreement with previous research findings on pulse velocity tomography (Aggelis and Shiotani, 2007), in which it was indicated that ultrasonic pulse velocity in general reduced with frequency of excitation in damaged concrete.

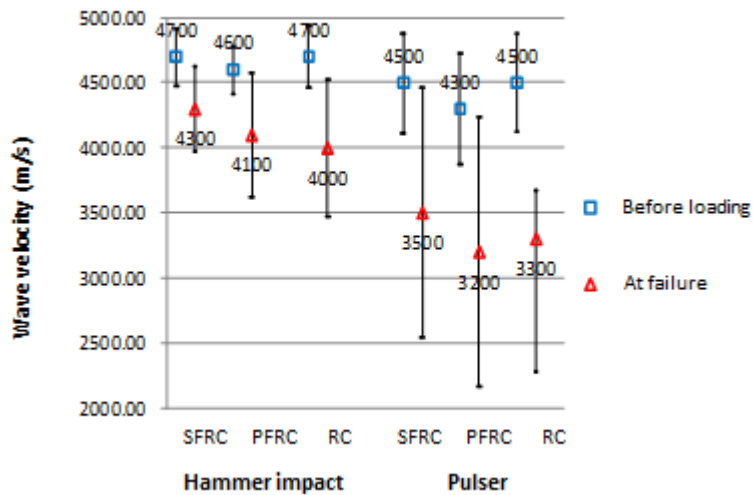


Figure 4.52: Variations of measured velocity in accordance to specimen type

A three-dimensional velocity distribution by pulser excitation is presented in Figure 4.54 for showing the transition of damage mapping as result of continuous loading. Before loading, all the specimens were intact because all the velocities as measured were higher than 4000 m/s, a rough benchmark value for sound concrete. The distribution showed declined in values as damage accumulated, with the final one obtained after specimen failure giving velocity values below 2500 m/s, in particular at the inner section of specimen near the mid-span, where critical cracks were observed.

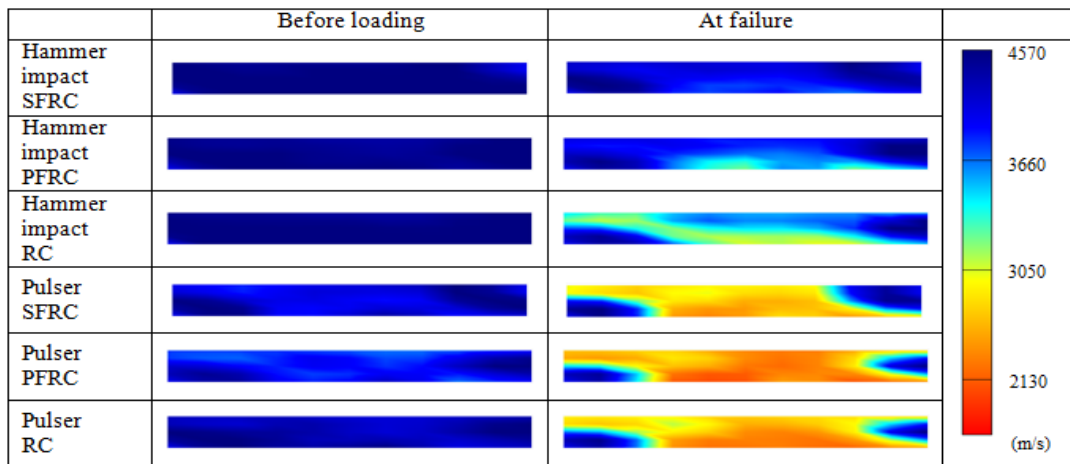


Figure 4.53: Velocity distribution results of the beam center cross sections, perpendicular to transverse direction

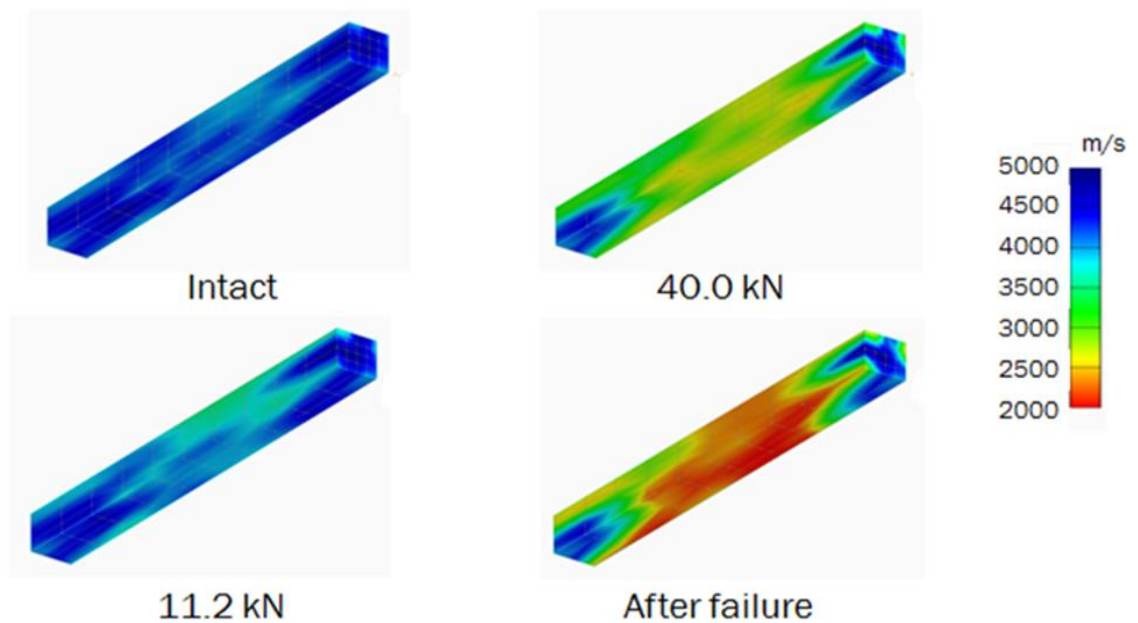


Figure 4.54: 3D wave velocity mapping in different damage level for the PFRC specimen

Figure 4.55 shows the relation between wave propagation distance and attenuation given as the energy ratio. The energy ratio was taken as the ratio between P-wave amplitude of data obtained after failure and that measured at before the start of loading. As compared to waves generated with hammer impact that possessed lower frequency, the high frequency waves generated using pulser were more sensitive towards the presence of defects in the form of cracking.

The energy of waves from electrical source such as a pulser, however, are generally weak, making it slightly more difficult to identify the arrival for picking up the correct arrival time as result of poor signal-to-noise ratio, particularly for long propagations in medium highly inhomogeneous or porous. On the other hand, waves generated using mechanical impact such as by steel ball hammer gave significantly higher wave energy, which enabled the waves to propagate longer distance without compensating the signal-to-noise ratio. These waves, nevertheless, are less sensitive to be interfered by damage in concrete mainly because of the longer wavelengths that are greater than the size of crack, as discussed herein earlier based on the results of velocity distribution. Hence in the utilization of tomography for evaluating concrete structures, it is vital to understand the scale of damage of interest as well the size and geometry of measured object, so that strategic instrumentation and signal processing methodology can be adopted to ensure effectiveness of measurement.

However, the effect of distance on the longitudinal velocity (Aggelis et al., 2009) is crucial and should be considered in condition assessment, particularly if the structure is of large size. In an independent research (Aggelis et al., 2009) it was demonstrated that there might be two main reasons for decreasing trend of velocity. One reason for the decaying trend of velocity with distance could be related to the length of distance where short distances are more likely to be crack-free than long ones and, therefore, show higher velocity.

In addition, the decreasing signal-to-noise ratio that seems to be an important drawback for correct identification of the waveform's leading edge for signals collected at large distances. This can be considered as an indirect effect of damage on the velocity, through the attenuation it imposes.

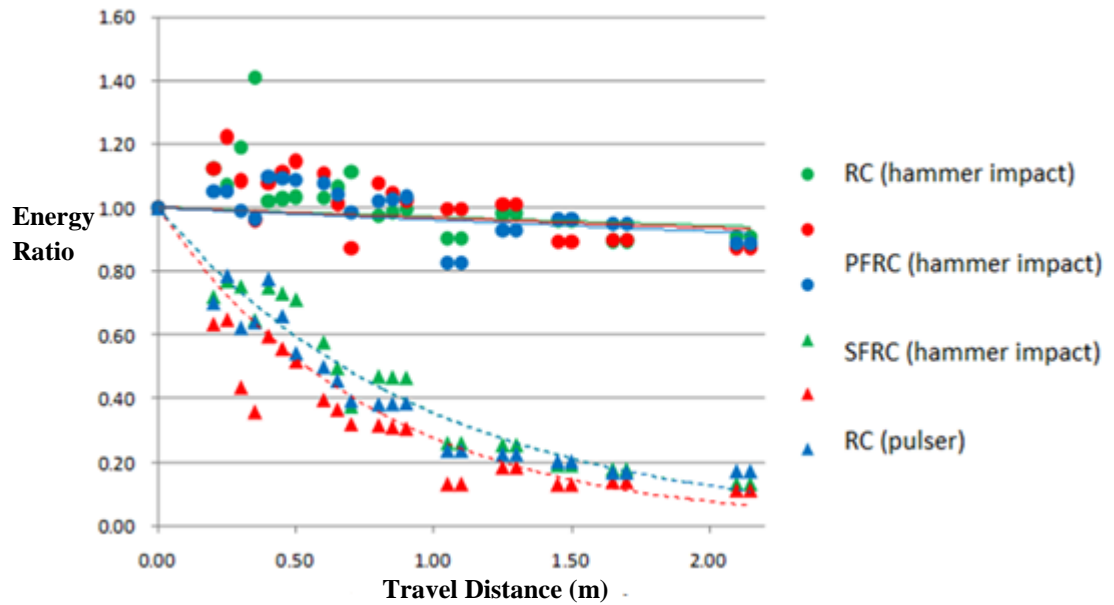


Figure 4.55: Relation between wave attenuation and travel distance

4.7.4.2. AE Evaluation and Crack Propagation

An example of the above load classification scheme is illustrated in Figure 4.56 for RC specimen. Four levels of damage under different load steps were classified for the specimens, in which significant AE activities were recorded between damage level I and damage level II. It was observed as well that at the transition between these two steps, while micro-cracking continued to develop, macro-cracking has started to occur. By analysing the AE data, evaluation of damage for different steps of loading was carried out, specifically. Loading type and its configurations influence to a great extent crack formation and propagation pattern. In the typical case of a flexurally-loaded reinforced concrete structures till failure, formation of tensile crack was first observed, followed by shear cracks that dominated the final failure mechanism (Aggelis, 2011a; Aggelis, 2011b). In this current study, it was manifested that all the beam specimens cracked in flexural mode initially and when approaching the ultimate failure, a combination of shear and flexural cracking became apparent.

As was expected, major cracking was found initiated from area around the middle bottom of the specimen which was under maximum tension. The crack initiation was justified through AE monitoring. It was observed that the macro-cracking locations coincided with the initial micro-cracking ones. This could be inferred from Figure 4.57 in which two dimensional localization of AE occurrence for the PFRC specimen in three different steps of damage development was depicted.

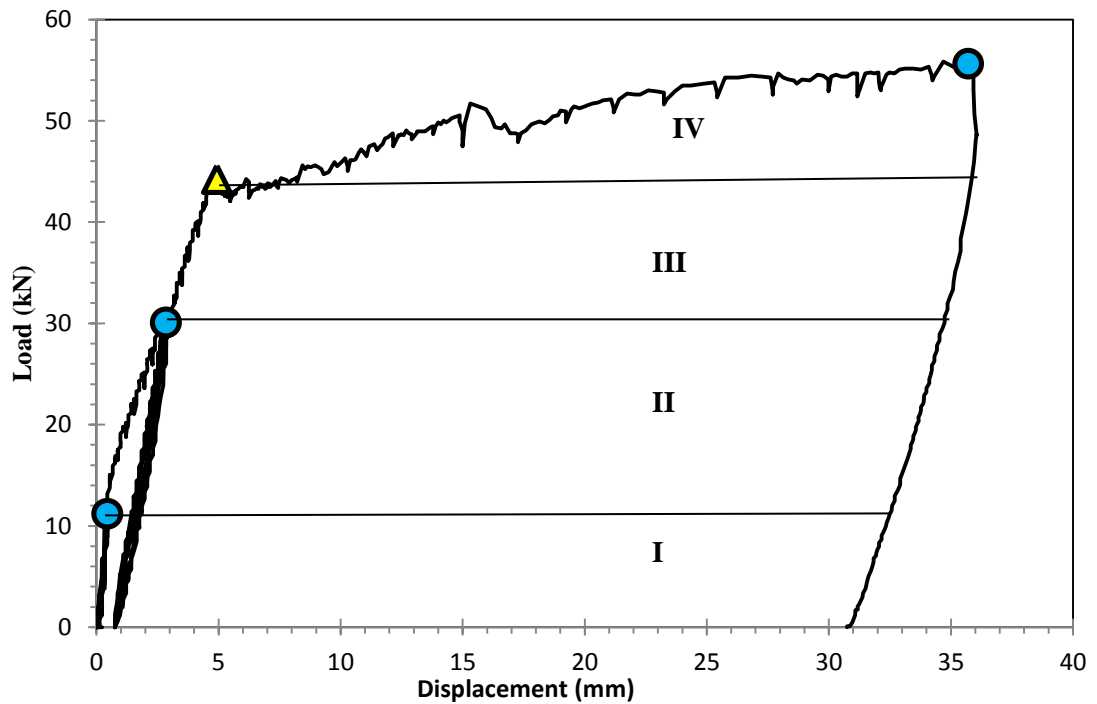


Figure 4.56: Load- displacement of RC beam specimen: damage categories

In the early step of loading, although there was no visible crack on concrete surface, occurrences of AE event were registered, implying that micro-cracking has already initiated at the tensile zone of the specimen because the centroid of the “group mass” of AE events was close to the bottom of the specimen. With increase in the load value followed by formations of visible cracks in the tensile zone, the aforementioned centroid seemed to be shifted upward and eventually to the upper part of specimen in the compression zones at failure.

The other two specimens, namely the RC and SFRC specimens were found to exhibit similar behavior in load-displacement, suggesting the uniformity for damage level classification. The different levels of damage were identified as: (I) micro-cracking or elastic damage, (II) first visible cracking (starting at point A), (III) flexural crack distribution (starting at point B), and (IV) localized damage where major cracks have developed (starting at point C).

Formation of first micro-cracking in the RC specimen was marked by occurrences of AE activity at proximity of the tension side of mid-span after 7.79 seconds of loading, which was at 6.9 kN. On the other hand, the PFRC specimen also registered micro-crack formation at 7.56 kN after 12 seconds of loading with AE activities detected near to the mid-span of specimen at the tensile side. Similarly, the same phenomenon was indicated by the SFRC specimen after 5.9 second of loading at a lower load of 3.73 kN. The lower trigger load as observed in the SFRC specimen could be due to the lower rate of loading process. However, all three specimens showed similar responses against loading till the formation of the first visible crack, namely the macro-crack. Similar load value was registered for all three specimens at this point, i.e. 11.2 kN, which also represented the change of structural behavior to become an inelastic one.

From this onward, the steel reinforcements would be stressed further under loading and ductile deflection was yielded. It was confirmed that the macro-cracks occurred in regions where micro-cracks had formed earlier.

The propagation of macro-cracks persisted until the maximum load. Based on the results, the SFRC specimen has achieved the highest load, at 65 kN before failure, followed by PFRC and RC specimens at 60 kN and 55 kN, respectively.

In the two specimens reinforced with fibers, when the loading reached 80% of the ultimate failure load in final step of loading, steel reinforcement started to yield and the effect of fibers toward ductility improvement became more pronounced. For SFRC specimen, after yielding of steel reinforcements, most part of post-peak branch was associated with softening behavior. In PFRC and RC specimens however, the hardening behavior was dominant from after steel yielding till final failure. The in post-peak behavior of specimen affected the magnitudes of AE parameters including signal strength and the number of events or hits.

For all three specimens, after yielding of steel reinforcements has occurred, the amount of AE activity dropped especially in the unloading step of the last loading step as compared to that recorded during the loading steps. This was the implication of the process of damage accumulation and its increased severity when loading and unloading were in process. However, after yielding of steel reinforcements, which resulted in the loss of ductility and the specimens were unable to return fully to original shape during unloading, friction and movement between cracks was lesser to produce AE activity.

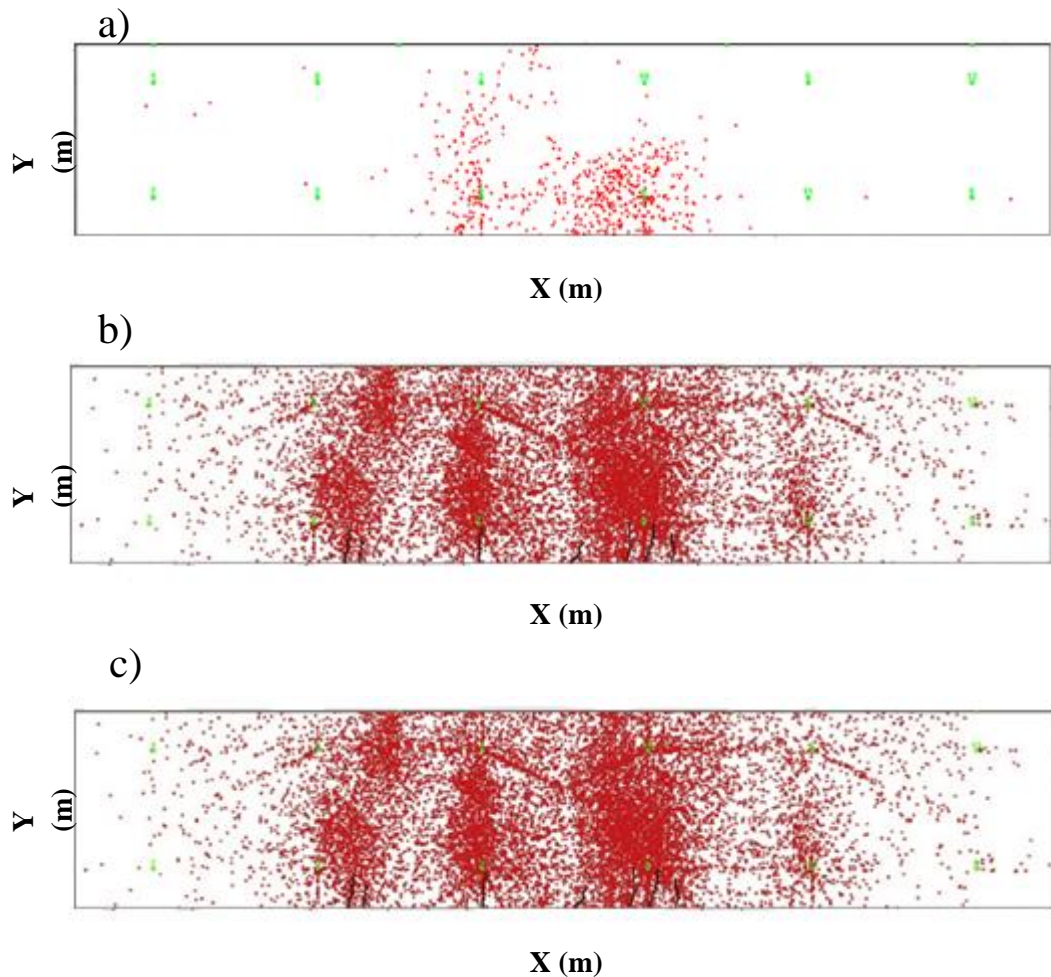


Figure 4.57: 2D localization by acoustic emission events activity in: a) micro-elastic crack formation, b) macro crack formation stage, c) crack localization stage, $X=2.5$ m, $Y=0.25$ m

4.7.4.3. AE Count Rate Analysis

Figure 4.58 illustrates AE count activity versus strain of steel reinforcements for all the three specimens during the incremental cyclic loading process. From the graphs it could be inferred that the strain varied cyclically with load. Prior to the occurrence of the first macro-crack, no considerable AE activity was observed in the unloading steps except those from the initial loading in which micro-cracking occurred. At this instance AE activities dominantly occurred at the loading step which was an indication of stable micro-cracking.

In the seventh step of loading, the increase in the steel strain gave rise to a peak for AE count activity and this was when the first visible crack (macro-crack) was observed. Thereafter, more AE activities were detected even in the exclusive unloading step, justifying the events associated with macro-crack propagations.

The specimens sustained severe damage in the final load cycle where the unloading step continued to instigate increase in the amount of AE activity count. It could be noted that prior to the seventh loading step (fourth load cycle) the specimens were experiencing elastic micro-cracking where the difference of steel strain was less than 10%. From the seventh load step (fourth load cycle) until the end of the twelfth load step (the sixth load cycle), strains in steel reinforcements were found to range between 60% and 64% of the yielding strain.

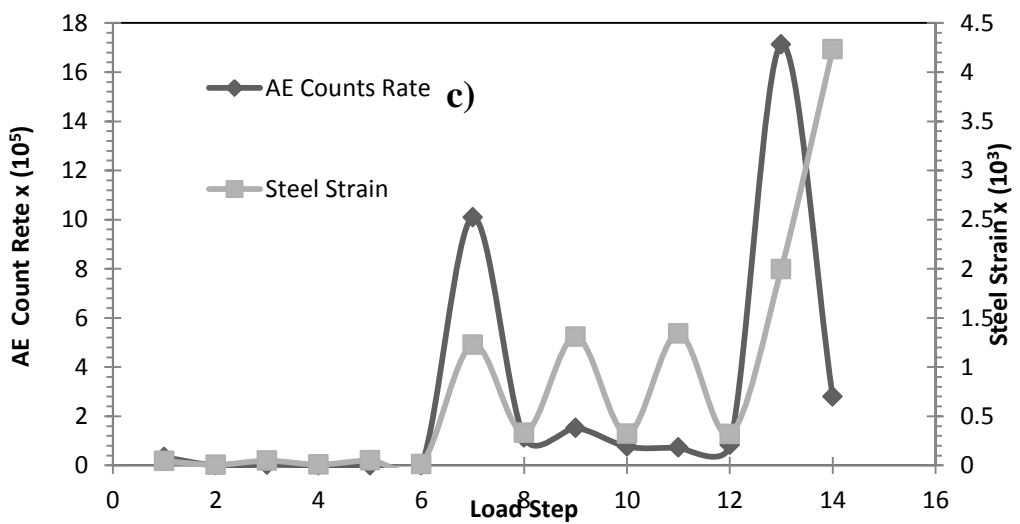
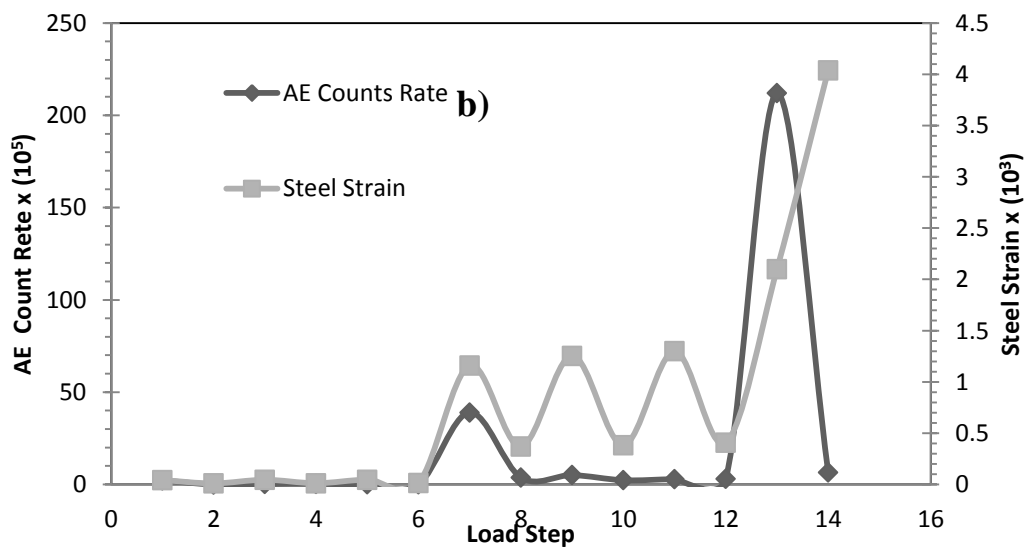
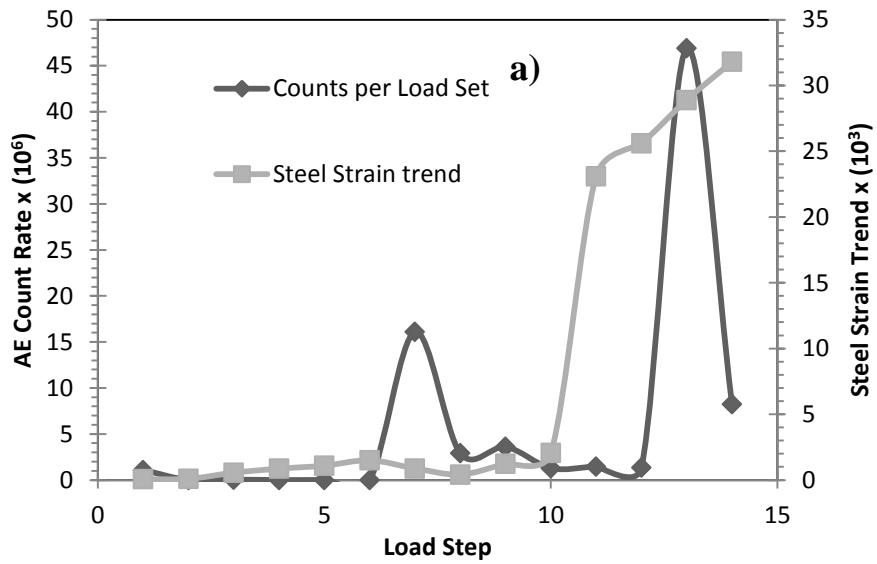


Figure 4.58: AE activity (count) versus strain in steel; a) PFRC, b) SFRC, and c) RC

4.7.4.4. AE Signal Strength Analysis

Signal strength is defined as the integral of the rectified voltage signal over the duration of the AE waveform packet. It is sometimes referred to as relative energy which relates to the energy amount released by the material or structure. Signal strength is independent of gain and calculated over the whole AE signal dynamic range. Thus, signal strength could be one of the more reliable parameters to evaluate the damage level quantitatively compared to other primary parameters such as hit.

In fact, AE hit or count cannot provide information about the intensity and strength of signal. Signal strength itself is a function of both the amplitude and duration of the signal. In addition, the total number of hits may be affected by duration of loading and unloading. Hence, the cumulative signal strength (CSS) is considered a more feasible parameter to be used for assessing damage evolution in a material. The CSS data obtained from the specimens tested in this study are plotted in Figure4.59. It was clear that due to the formation of micro-cracks in the early loading steps, the CSS was found to increase. However, since there was no visible and major cracking at this period of test, there was almost no increment in CSS during the unloading step in the first three cycles. In the unloading step of the fourth cycle, although the load was decreasing, the CSS was found increasing, which manifested the initiation of macro-cracking. Thereafter, the incremental trend in CSS plot persisted till the collapse point, indicating the accumulation of damage in the specimens. For further clarification of the use of signal strength, in Figure4.60 the signal strength for each individual loading step was plotted for the PFRC specimen. The signal strength dropped during unloading steps for the first three cycles, justifying the specimens' elasticity against load.

In the unloading step of the fourth cycle, although the unloading step caused insignificant drop in signal strength, it was a slight decrease and it happened as a sign of formation of macro-cracks.

The fifth and sixth loading cycles have instigated more damage to the specimen, as suggested by the increase in signal strength in the unloading step obtained. In the last cycle of loading, a slight drop in signal strength was visible at unloading step despite the fact that damage was still developing. This could be due to yielding of steel reinforcement which caused significant loss in specimens' ductility.

This drop in ductility caused lesser friction between crack surfaces and thereby AE activity reduced considerably.

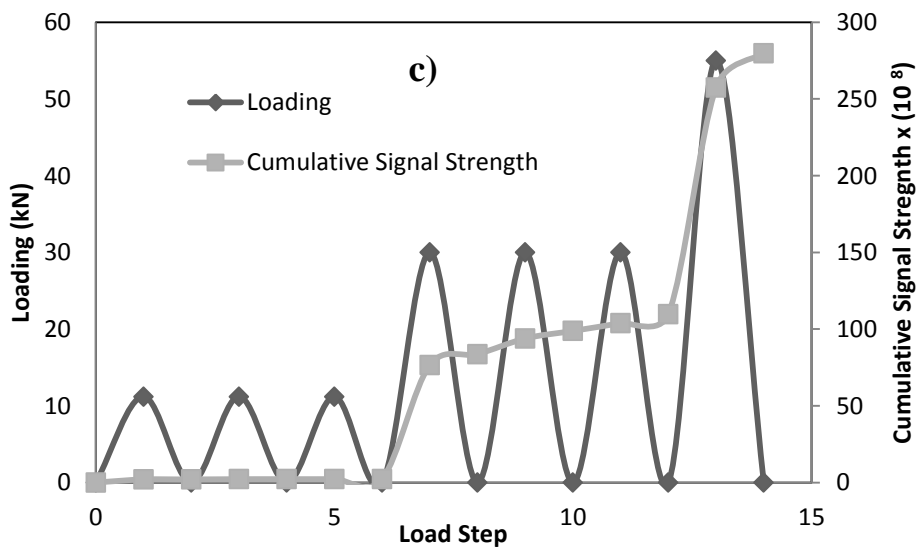
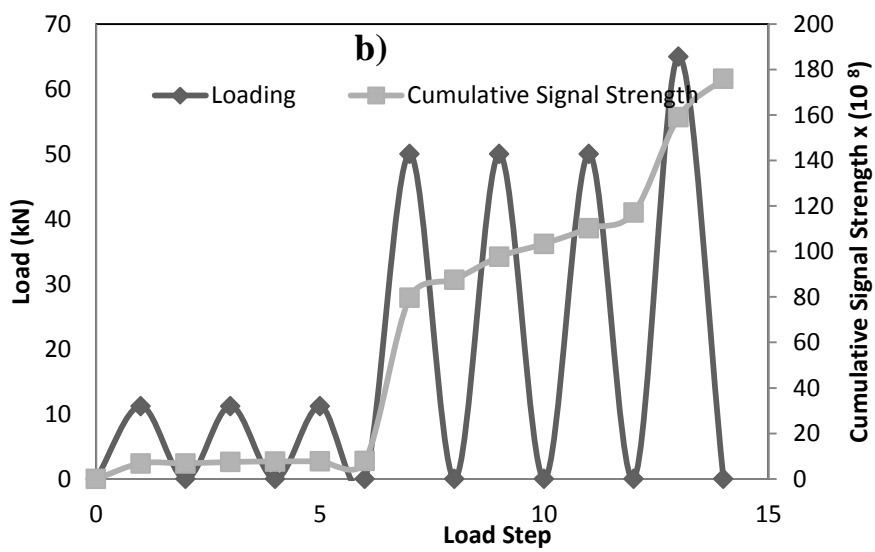
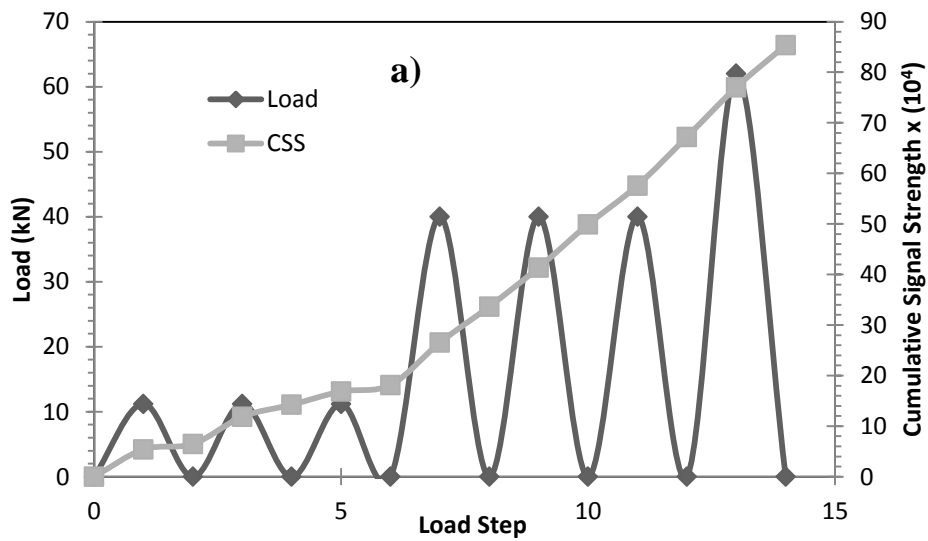


Figure 4.59: Cumulative signal strength versus loading in: a) PFRC; b) SFRC; and c) RC

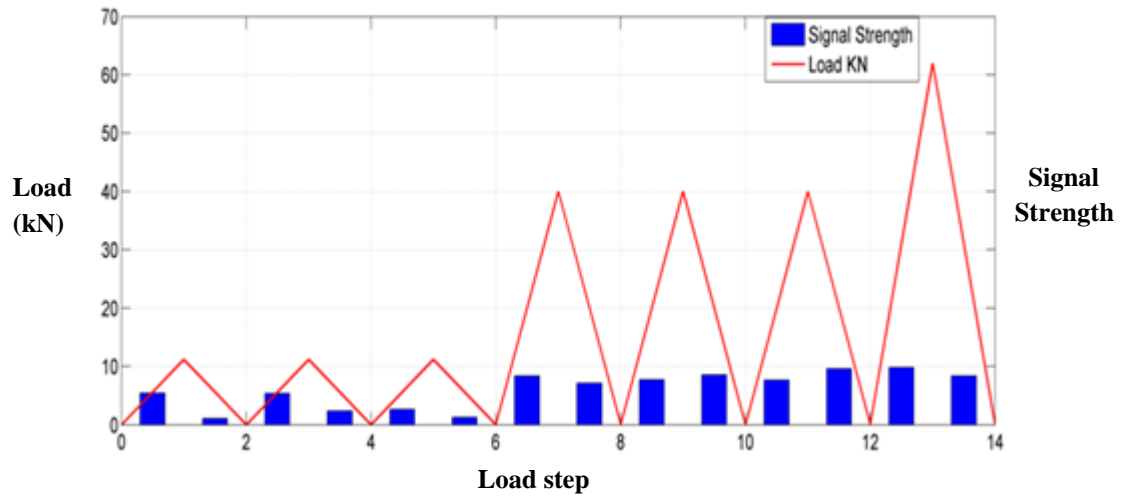


Figure 4.60: Signal strength versus loading in PFRC beam

4.7.4.5. AE Frequency Analysis

The AE signal frequency is another feasible parameter for monitoring and evaluating damage. The average values of peak frequency and centroid frequency for the three specimens were obtained during the test period. The results are given in Figure 4.61. As can be seen from the Figures, the increase in the damage severity has resulted in decrease in AE signal frequency content.

The frequency drop was associated with the change of signal shape as damage in the specimen developed. In other words, the increase of damage severity has caused contraction in the signal length and caused amplitude dilation and frequency decrease.

The AE signal frequency could be shifted due to damage and it could be justified by a fundamental concept of physics which was discussed in earlier sections of this thesis. As stated before this is known as the pendulum principle. It is given that the frequency of pendulum (f) and its length (l) are in inverse relation.

When there was increase in the crack size, either attributed to the enlargement of one previous crack or the coalescence of several previous smaller cracks, or both, the AE signal correspondingly turned out to be of progressively lower frequency, until leaving the ultrasonic range and attaining the sonic range to be identified as the well-known seismic roar. This fact was the matching of the seismic phenomenon. On another note, while the specimens were loaded flexurally, the majority of AE signals were originated from the captured longitudinal waves (P-waves). When approaching the final failure and shear cracks were propagated, the AE sensors started to receive transverse waves (S-waves) as the dominant wave component. In fact the evolution of the frequency parameters reflect different failure mechanism. As demonstrated earlier by Shah and Li in their study (Shah and Li, 1994), P-waves possessed higher range of frequency compared to S-waves.

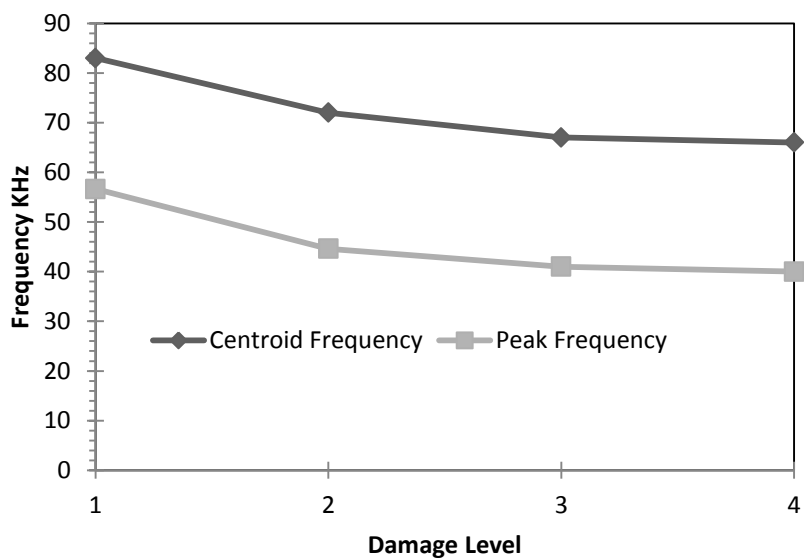
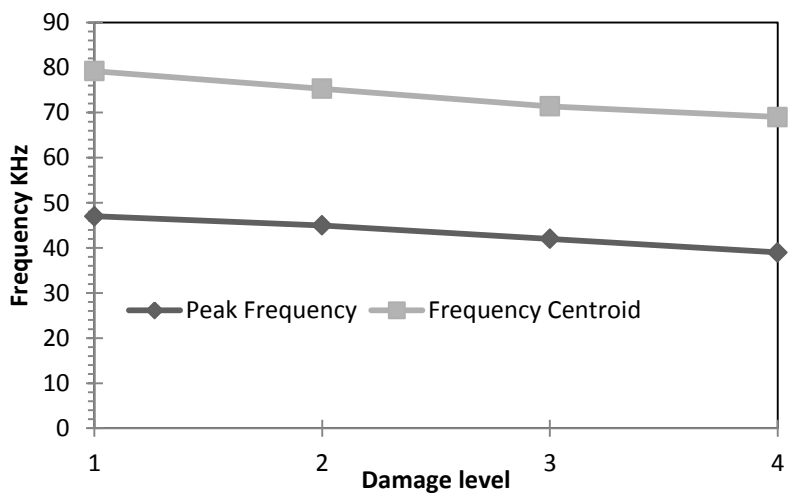
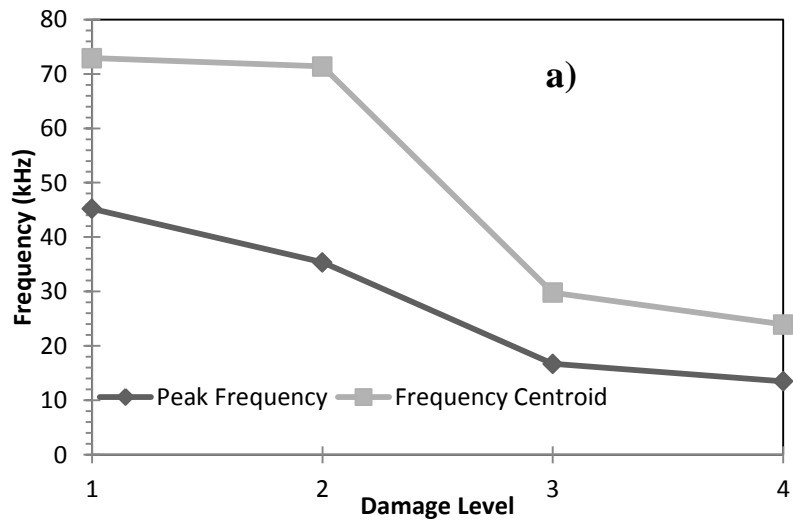


Figure 4.61: Trend of variation of frequency versus damage level; a) PFRC, b) SFRC, and c) RC

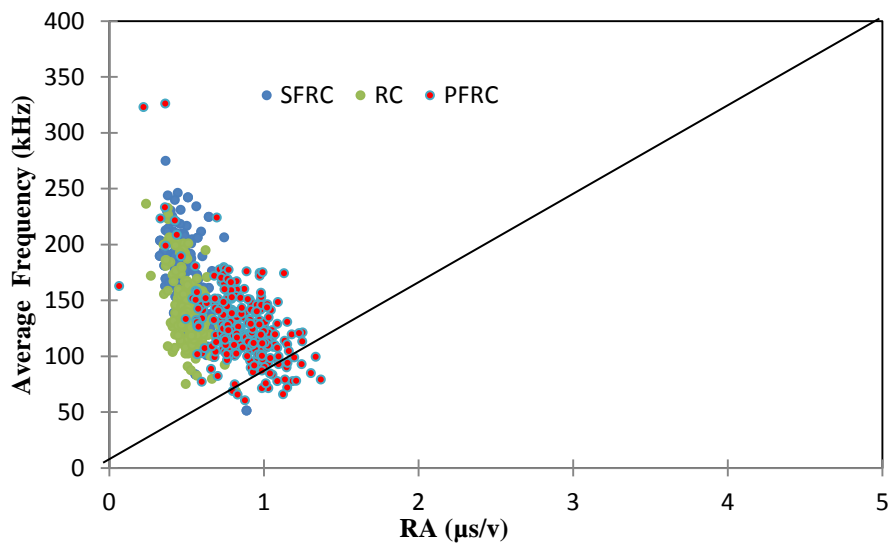
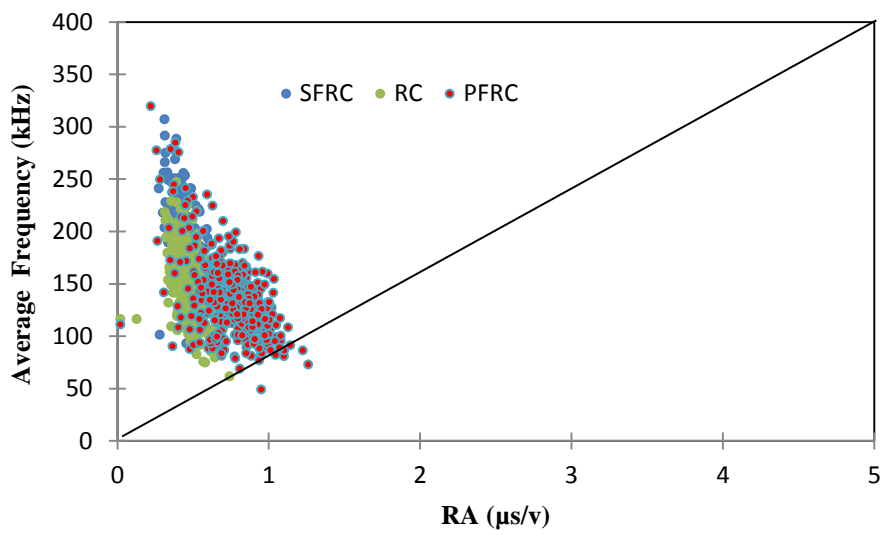
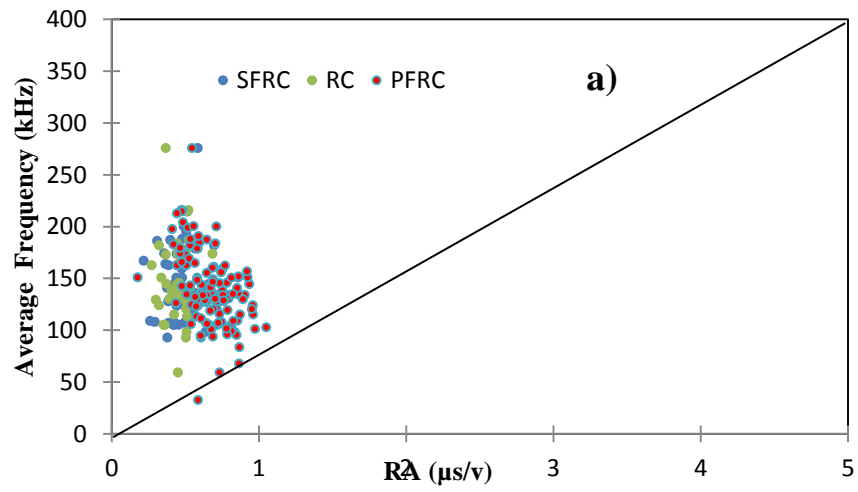
4.7.4.6. Damage Classification Based on AE Parameters

The AE parameters that are linked to the mode of fracture, namely the average frequency (A-FRQ) and RA value were used to classify cracking in the specimens. The A-FRQ is derived from AE counts and duration, while the RA value is the ratio of rise time (RT), which is defined as the delay between the onset and the maximum amplitude, over the maximum amplitude (A).

The behavior and properties of AE signal features during fracture process of specimens can be classified into two classes according to the failure modes.

An analysis of AE parameters was performed to classify the types of distributed cracks. The results were presented in Figure 4.62. The diagonal threshold line in the figures were included in the Figures, which was based on the result of AE monitoring in flexural, tensile and direct shear test (JCMS, 2003) to enable classification of crack type. However, it should be kept in mind that this predefined diagonal line in each specific case would be variable considering the type of media, sensor position, and etc. Therefore this predefined longitudinal should be obtained in each specific case. Nevertheless, in this study we assume it as a general indication for crack type. The results showed the existence of lower severity of tensile cracks at the beginning load steps, which further developed by increased loading. Fracture in shear then occurred at increasing rate as the specimen underwent the final step of loading, before ultimate failure took place.

As damage were developing, Slight shifts of the centroid of data group for the respective specimens to lower average frequency and higher RA value region were found. This was indication of progressive damage, especially from damage level 3 to damage level 4.



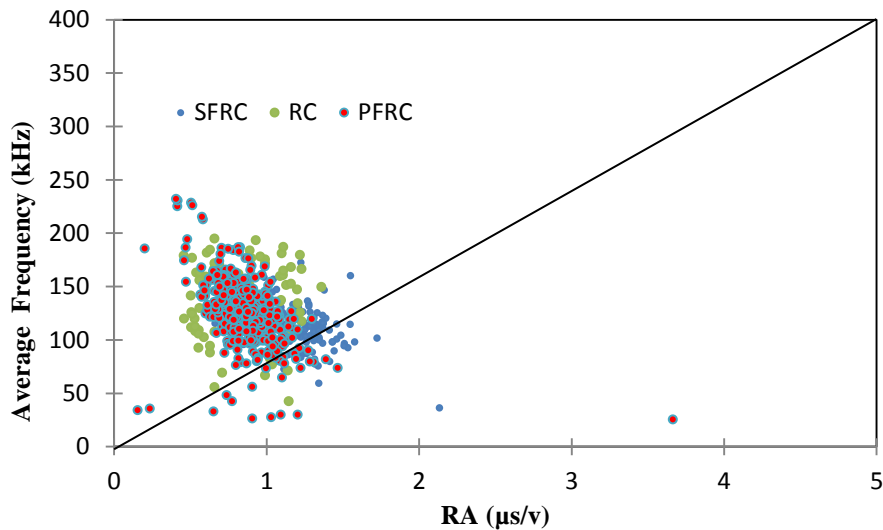


Figure 4.62: Crack type classification in different Damage Level based on average frequency versus RA; a) damage level I, b) damage level II, c) damage level III, d) damage level IV

4.7.4.7. ISA Evaluation and Elastic Wave Velocity Tomography

The intensity signal analysis (ISA) is a technique with which the structural implication of damage could be identified. This analysis method utilizes signal strength of AE. Theoretically, signal strength can be correlated to the integral of rectified voltage signal over the AE signal duration. The premise of this analysis which tackles the application of two parameters named history index (HI) and severity index (Sr) were discussed in earlier sections.

The damage state of a structure can be evaluated by application of ISA in conjunction with elastic wave velocity computed in the tomography measurements. There were two possible approaches with which integrity of the specimens tested in this study could be evaluated. The first one was global assessment of stability and integrity of the structure in which ISA analysis was accompanied by evaluation of average wave velocity for the entire of the structure. This approach was demonstrated for the PFRC specimen as given in Figure 4.63. The graph in this figure was partitioned into five zones, each zone representing a particular level of damage as stated in Table 4.12 (A to E).

Figure 4.63 indicated the results of ISA during loading. The graph has S_r as the left vertical axis. For the right vertical axis, average measured elastic wave velocity was used. From the start of loading till 18% of failure load, no significant AE signal emission was noticed. Based on the ISA, the specimen condition could be considered to be in Region A. On the other hand, the average computed wave velocity obtained during this period of loading conformed to the interpretation. Upon reaching 50% of the failure load, the condition of specimen shifted to Level C, with average wave velocity of approximately 3700 m/s. The dropped in velocity value was a good indication to the reduced integrity, although it could not be representative of local damage development but only as approximate indicator.

It should be noted that although the damage in specimen has in general increased, the HI index became lower compared to that from the preceding.

This finding was possibly attributed to the consequence of taking into account the signal strength data for all channels during calculation of HI.

When the failure load of the PFRC specimen was reached, damage level based on ISA moved drastically to Level E with the average wave velocity of 3000 m/s.

In light of addressing problems in association with accuracy and reliability of damage assessment using the average wave velocity, the beam structure could be sectioned into different zones based on the computed wave velocity in each element. This can be realized by considering Table 4.13 whereby maximum, minimum, and average wave velocities have been shown. As indicated in Table 4.13 the range of variation of wave velocities was quite pivotal. Thus, zonal approach could be a potential alternative to have more accurate evaluation process in wave velocity tomography technique. As explained above, Figure 4.64 illustrated the zonal evaluation approach.

In this method the specimen was divided to smaller elements and wave velocity in each element (meshing) could be calculated. The specimen has been partitioned to three different zones where each zone possessed several elements itself. Calculating wave velocity for each element and taking an average for each zone will delivered more accurate results based on zonal approach. At the same time, in each zone there were some AE sensors which could be provide zonal AE based analysis. For example, this was addressed in Figure4.65 where ISA has been examined for zone C by aid of related sensors and average wave velocity for elements in this zone. As Figures 4.64 and 4.65 illustrated, computed average wave velocities for the first two damage levels were lower compared to the global measurements while in the last two measurements could be seen the damage level in zone C was more severe than the global condition of the beam. Thus, it was shown that the regional wave velocities were better indicative for condition assessment.

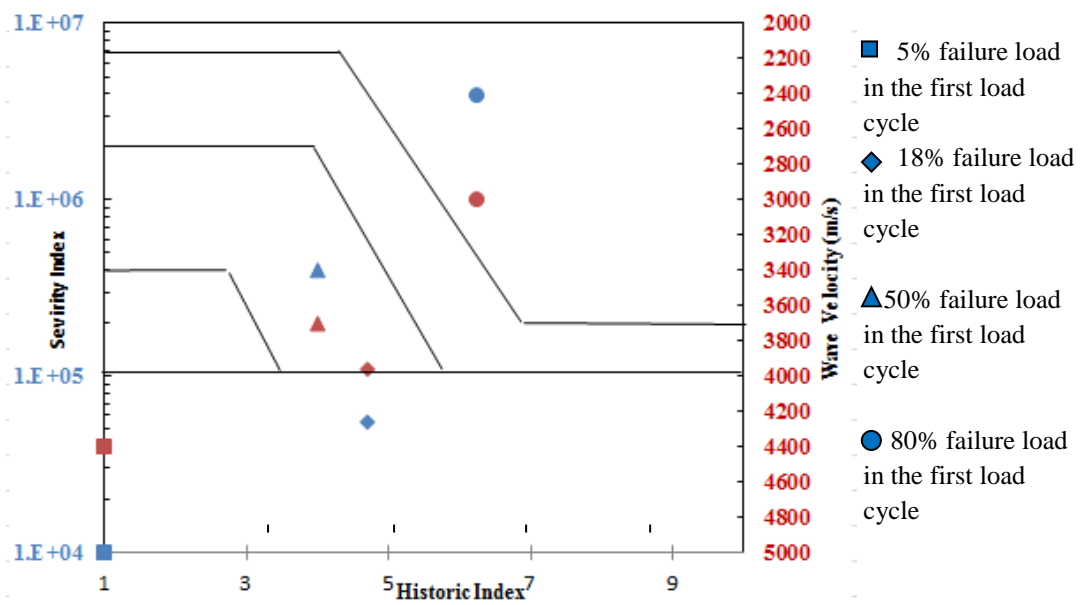


Figure 4.63: Intensity signal analysis versus elastic wave velocity for the entire length of PFRC beam specimen

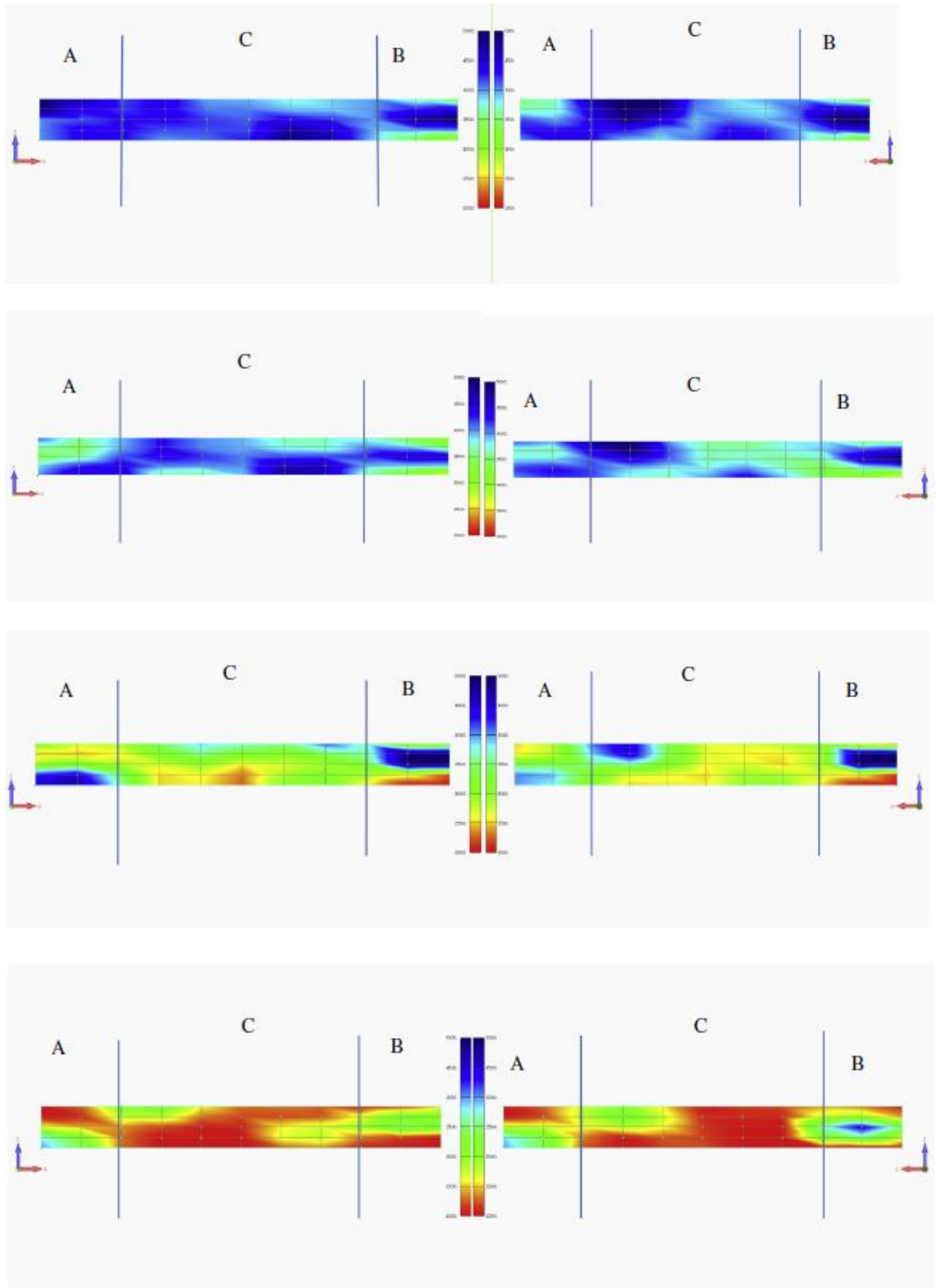


Figure 4.64: Zonal based damage severity assessment based on elastic wave velocity distribution map

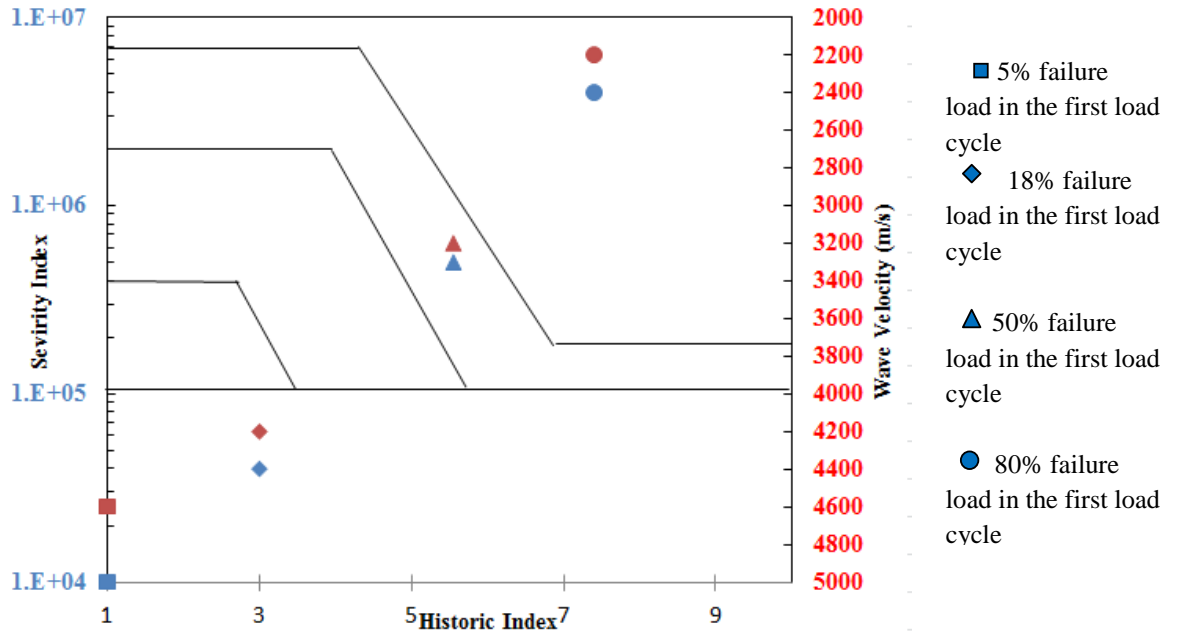


Figure 4.65: Intensity signal analysis versus elastic wave velocity for PFRC beam specimen at region C

Table 4.12: Intensity Analysis Description

Zone intensity	Recommended action
A	Insignificant acoustic emission
B	Note for reference in future tests. Typically minor surface defects
C	Defects require follow-up evaluation. Evaluation may be based on further data analysis or complementary destructive examination
D	Significant defect requires follow-up inspection
E	Major defect requires immediate shut-down and follow-up inspection

Table 4.13: Elastic Wave Velocity Distribution for PFRC beam (m/s)

Loading Level	Minimum	Average	Maximum
Starting point of test	3600	4200	6010
20%	2616	4036	5749
50%	1829	3700	4404
100%	1405	3000	5596

4.7.5. Conclusion

This study examined the feasibility of adopting travel time tomography measurements for mapping damage integrated to acoustic emission technique in fiber-reinforced concrete beams subject to flexure to characterize and evaluate different damage level criteria. Conclusions can be drawn as follows:

1. At 1% cement volume replacement, the inclusion of either steel fibers or polypropylene fibers did not marked apparent change in the wave velocity measured when concrete was intact, regardless of the means of wave generation.
2. In the case where concrete beams have accumulated damage due to flexure loading, waves generated using electric pulser provided velocity distribution with higher contrast because of the higher sensitivity of the high-frequency waves towards inhomogeneity introduced by cracking.
3. Waves generated using mechanical impacts from steel ball hammer have higher energy compared to those by electric pulser. This characteristic facilitated identification of wave-front for accurate picking-up of arrival time. On the other hand however, the low frequency waves from hammer impact have resulted damage mapping that has low contrast and could become inaccurate, owing mainly to the long wavelengths that were less sensitive towards the introduction of local inhomogeneity by cracks that were relatively small in dimensions and sizes.
4. AE was demonstrated to be a powerful tool for real time monitoring and flaw and crack pattern recognition. Through AE technique damage could be readily localized and micro- elastic crack or minor damages could be detected precisely whereas wave velocity tomography may not be able to provide these data comprehensively.

5. Through AE analysis different level of damage based on average frequency and RA parameter could be classified and distinguish the type of failure.

6. While integrating ISA (AE based analysis) and tomography analysis could be taken as a global method for damage level evaluation, the zonal approach based on combination of these two methods may provide more accurate and useful results for different parts of structure. This may enable practitioners to take required remedial action for a specific region in a structure.

To stress out the main innovative aspect of this work, it should be mentioned that these two methods are perfectly complementary. First the online monitoring of crack propagation can be carried out with AE and then in an offline mode, TTT can be implemented as an off line technique and the map of distribution velocity of signals can provide a great visual insight of interior condition qualitatively in local defected area. In the case of any possible damage found by TTT in a qualitative manner, AE can be utilized to quantify the level of damage by either primary or secondary AE analysis through which global stability and condition of structure can be inspected. In addition, AE will provide information on the type of possible existing damage within structure and this can be also identified if this is an active or passive damage. In addition, using tomography velocity technique can provide an insight of critical zone suspected to damage. Then as performed in this study, AE sensors can quantify damage level in each specific zone while the effect of distance will be eliminated. This confirms to finding of section 4.2 conclusion where individual b-value could provide very better results.

In general, utilizing same instrumentation, integration of both techniques is advantageous for complementary purpose to increase reliability of assessment thereby engineers and practitioners might be reinforced with a power tool to monitor infrastructures carefully, locally and globally.

CHAPTER 5

CONCLUSION

5.1. Conclusions and Recommendations

Civil concrete structures can be known as of the key components of a sustainable society. The safety and durability of concrete structures holds a crucial role in ensuring economic and industrial prosperity. Thus, it is necessary to plan for reliable assessment schemes that evaluate the operational condition of structures. The primary objective of this research is to provide integrated Structural Health Monitoring (SHM) scheme for the non-destructive evaluation (NDE) of civil concrete structures by using acoustic emission. In this line, experimental measurements were armed with different types of analysis in each specific section such as statistical fracture modelling, advanced data processing tools such as pattern recognition, and automated monitoring systems for reinforced concrete composite structures. These systems were validated through experimental studies.

However, concrete structures structural health monitoring involves two imperative factors: 1.Characterization of fracture of material, 2. Assessment of overall performance of structures.

Therefore, in this study, four experiment programs were designed to answer the objectives of this research so that by using acoustic emission (AE) technique we could characterize fracture behavior and establish reliable approaches for concrete structures condition monitoring. AE technique was comprehensively utilized for different types of structures, loading and failure modes. To sum up, AE was successfully showed a great potential to characterize torsional fracture behavior by predicting fracture parameters.

Moreover, quantitative and qualitative analysis by using AE waveforms parameters resulted in a robust damage detection method which could provide damage localization, severity of damage, and type of failure. The important specific conclusions can be listed as below:

- Torsional fracture process was characterized by AE parameters so that each stage of damage can be differentiated by changes imposed to AE signal waveform.
- Weibull damage distribution parameters were calibrated by AE hit data so that the probability damage function was obtained.
- Unsupervised damage detection algorithm by using kernel fuzzy c-mean was developed to cluster damage stages and quantify damage level.
- Mode of failure could be separated by examining different types of slabs so that punching and flexural failure was distinguished by using acoustic emission parameters.
- A damage indicator parameter was proposed by using an auto regressive model as a feature extraction model.
- Statistical process control (SPC) was successfully provided a general structural health monitoring scheme.
- Failure reliability analysis by using AE signal parameters could be interceded in bathtub curve model.
- A global and local monitoring system was proposed by integration of acoustic emission and travel time tomography data.

To this end, it can be observed that despite existing problems, the direction of current effort and AE applications in concrete structure monitoring reveals the potential of this versatile technique and its promising future. The technological advances made in recent years have made the method more suitable for on-site monitoring situations.

Although more research may be required to fully exploit the current methods and devices, the future of AE seems promising for the application of this technology in efficient continuous concrete monitoring scenarios.

However, there are still some significant drawbacks in utilization of AE technique for which extensive researches could be recommended. The following concerns can be considered as future studies which are highly required to be answered.

- AE signal attenuation level, denosing process are crucial concerns which should be studied comprehensively. To this end, application of Q-value for including attenuation level
- AE parametric analysis may not reveal the whole details of fracture. To this end, application of wavelets in denosing process and analysing waveforms energy rather than converted signals parameters can be priority of future studies.
- In addition to the above methods, statistical process control (SPC) incorporated with AR model which was firstly introduced for AE application in this research, showed a high potential to be used as an online sensor selection tool so that effects of distance between sensors and source location can be eliminated.
- For an example, an online sensor network can be constructed so that at each specific time interval an individual sensor can be selected as a damage indicator which possesses higher level of outliers.
- To address a possible method we can look for tools such as an artificial intelligence device, ANN. Establishing a comprehensive and general flowchart would enable an understanding of consistent trends to assess the current state of concrete structures.
- It is also noteworthy that the development of clustering and filtering method could be very helpful in parametric assessment.

- The effect of shape of structures, types of sensors, distribution of aggregate and aggregate properties in signal attenuation should be investigated in detail.

REFERENCES

- Abdelrahman, M., ElBatanouny, M.K., Ziehl, P.H. (2014). Acoustic emission based damage assessment method for prestressed concrete structures: Modified index of damage. *Engineering Structure*, 60, 258-264.
- ACI Committee 549.(1997). *State-of-the-art report on ferrocement*.ACI549-R97, in Manual of Concrete Practice, ACI, Detroit, 22.
- ACI.ACI 549-IR-88 and IR 93. (1993). *Guide for the design, construction and repair of ferrocement*. *Manual of Concrete Practice*. Farmington Hills, Michigan: American Concrete Institute.
- Aggelis, D.G. Soulioti, D., Sapouridis, N., Barkoula, N., Paipetis, A., & Matikas, T. (2011).Acoustic emission characterization of the fracture process in fibre reinforced concrete. *Construction and Building Material*,25, 4126-4131.
- Aggelis, D.G, Matikas, T., & Shiotani, T. (2012a). Advanced acoustic techniques of health monitoring of concrete structures. In S. Kim & K. Ann (Eds.), *The Song's Handbook of concrete Durability*. London: Middleton Publishing.
- Aggelis, D.G. (2011b). Classification of cracking mode in concrete by acoustic emission parameters. *Mechanics Research Communications*,38(3), 153-157.
- Aggelis, D.G. (2011c). Classification of cracking mode in concrete by acoustic emission parameters.*Mechanics Research Communications*, 8 (3): 153–7.
- Aggelis, D.G., Kordatos, E.Z., Strantza, M., Soulioti, D.V., & Matikas, T. (2014). NDT approaches for characterization of subsurface cracks in concrete,” *Construction and Building Material*, 25(7), 3089-3097.
- Aggelis, D.G., & Shiotani, T. (2007). Repair evaluation of concrete cracks using surface and through-transmission wave measurements, *Cement Concrete Composite*, 29, 700-711.
- Aggelis, D.G., Barloulou, N., Matikas, T., & Paipetis, A. (2010). Acoustic emission monitoring of degradation of cross ply laminates. *Journal of the Acoustical Society of America*,127(6), 246-251.
- Aggelis, D.G., Kleitsa, D., & Matikas, T. (2013a). Ultrasonic Characterization of the Fiber-Matrix Interfacial Bond in Aerospace Composites. *The Scintific World Journal*, DOI 10.1155/2013/154984; 8.
- Aggelis, D.G., Momoki, S., & Chai, H.K. (2009). Surface wave dispersion in large concrete structures. *NDT&E International*, 42, 304-307.
- Aggelis, D.G., Shiotani, T., Papacharalampopoulos, A., & Polyzos., D. (2012b). The influence of propagation path on acoustic emission monitoring of concrete. *Structural Health Monitoring*,11(3), 359-366.

Aggelis, D.G., Solouti, D., Barkoula, N., Paipetis, A., & Matikas, T. (2012c). Influence of fiber chemical coating on the acoustic emission behavior of steel fiber reinforced concrete. *Cement and Concrete Composite*, 34, 62-67.

Aggelis, D.G., Solouti, D., Barkoula, N., Paipetis, A., Matikas, T., & Shiotani, T. (2008). Acoustic emission monitoring of steel-fiber reinforced concrete beams under bending. *Journal Acoustic Emission*, 14, 287-294.

Aggelis, D.G., Soulioti, D., Gatselou, E., Barkoula, N., & Matikas, T. (2012d). Monitoring of the mechanical behavior of concrete with chemically treated steel fibers by acoustic emission. *Construction and Building Material*, 48, 1255-1260.

Aggelis, D.G., Verbruggen, S., Tsangouri, E., Tysmans, T., & Van Hemelrijck, D. (2013b). Characterization of mechanical performance of concrete beams with external reinforcement by acoustic emission and digital image correlation. *Construction Building Material*, 47, 1037-1045.

Aid, K., & Richards, P. (1980). *Quantitative seismology: Theory and methods*. San Francisco.

AiÈtcin, P.C.(2000). Cements of yesterday and today concrete of tomorrow. *Cement Concrete Research*, 30, 1349-1359.

Aldahdooh, M., Bunnori, N., & Johari, M. (2012). Damage evaluation of reinforced concrete beams with varying thickness using the acoustic emission technique. *Construction and Building Material*, 44, 812-821.

Antonaci, P., Bocca, P., & Masera, D. (2011). Fatigue crack propagation monitoring by Acoustic Emission signal analysis. *Key Engineering Materials*, 465, 370-373.

Antonaci, P., Bocca, P., & Masera, D. (2012). Fatigue crack propagation monitoring by Acoustic Emission signal analysis. *Engineering Fracture Mechanics*, 81, 26-32.

Bagherifaez, M., Behnia, A., Majeed, A.A., Chai, H.K. (2013). Acoustic Emission Monitoring of Multicell Reinforced Concrete Box Girders Subjected to Torsion. *The Scientific World Journal*, <http://dx.doi.org/10.1155/2014/567619>.

Bar, H.N., Bhat, M.R., & Murthy, C.R.L. (2004). Identification of failure modes in GFRP using PVDF sensors: ANN approach. *Composite Structures*, 65, 231-237.

Beck, P., Lark, R., & Holford, M. (2003). Moment tensor analysis of acoustic emission in concrete specimens failed in four bending. *Key Engineering Materials*, 245, 443-450.

Benavent, A., Castro, E., & Gallego, A. (2009). AE monitoring for damage assessment of RC exterior beam-column subassemblages subjected to cyclic loading. *Structural Health Monitoring*, 8, 175-189.

Benavent, A., Castro, E., & Gallego, A. (2010). Evaluation of low-cycle fatigue damage in RC exterior beam-column subassemblages by acoustic emission. *Construction and Building Material*, 24, 1830-42.

Benazzouk, A., Douzane, O., Langlet, T., Mezreb, K., Roucoult, J.M., & Queneudec M. (2007). Physicomechanical properties and water absorption of cement composite containing shredded rubber wastes, *Cement and Concrete Composite*, 29(10), 732-740.

Bezdek, J.C. (1981). *Pattern recognition with fuzzy objective function algorithms*. New York: Plenum Press.

Bishop, C. M. (1995). *Neural networks for pattern recognition*, Oxford University Press, Oxford, U.K.

Brockwell, P. J., & Davis, R. A. (1991). *Time series: Theory and methods*, Springer, New York.

BSI.BS 882.(1992). *Specification for aggregates from natural sources for concrete*. London: British Standards Institution.

Calabrese, L., Campanella, G., & Proverbio, E. (2013a). Use of Acoustic Emission Data Clustering to Identify Damage Mode in Concrete Structures. *Nondestructive Testing of Materials and Structures*, 6, 329-34.

Calabrese, L., Campanella, G., & Proverbio, E. (2013b). Identification of corrosion mechanisms by univariate and multivariate statistical analysis during long term acoustic emission monitoring on a pre-stressed concrete beam. *Corrosion Science*, 73, 161-171.

Calabrese, L., Campanella, G., & Proverbio, E. (2012). Noise removal by cluster analysis after long time AE corrosion monitoring of steel reinforcement in concrete. *Construction and Building Material*, 34, 362-371.

Carpinteri A., Lacidogna, G., & Puzzi, S. (2009). From criticality to final collapse: Evolution of the b-value from 1.5 to 1.0. *Chaos, Solitons & Fractals*, 41, 843-853.

Carpinteri, A., & Lacidogna, G. (2007). Damage evaluation of three masonry towers by acoustic emission. *Engineering Structures*, 29, 1569-1579.

Carpinteri, A., Grazzini, A., Lacidogna, G., & Manuello, A. (2013). Durability evaluation of reinforced masonry by fatigue tests and acoustic emission technique. *Structural Control and Health Monitoring*, DOI: 10.1002/stc.1623.

Carpinteri, A., Lacidogna, G., & Niccolini, G. (2006). Critical behaviour in concrete structures and damage localization by acoustic emission. *Key Engineering Materials*, 312, 305-310.

Carpinteri, A., Lacidogna, G., & Niccolini, G. (2011). Damage analysis of reinforced concrete building by the acoustic emission Technique. *Structural Control Health Monitoring*, 18, 660-673.

Carpinteri, A., Lacidogna, G., & Paggi, M. (2007a). Acoustic emission monitoring and numerical modeling of FRP delamination in RC beams with non-rectangular cross-section. *Materials Structures*, 40, 553-566.

Carpinteri, A., Lacidogna, G., & Pugno, N. (2007b). Structural damage diagnosis and life-time assessment by acoustic emission monitoring. *Engineering Fracture Mechanics*, 74, 273-89.

Carpinteri, A., Lacidogna, G., & Puzzi, S. (2008). Prediction of cracking evolution in full scale structures by the b-value analysis and Yule statistics. *Physical Mesomechanics*, 11, 260–271.

Carpinteri, A., Lacidogna, G., Niccolini, G., & Puzzi, S. (2007c). “Critical defect size distributions in concrete structures detected by the acoustic emission technique. *Meccanica*, 43(3), 349-363.

Chai, H.K., Aggelis, D.G., Momoki, S., Kobayashi, Y., & Shiotani, T. (2010). Recent development in tomography techniques for non-destructive evaluation of concrete, *Proceedings of the 2nd Asia-Pacific Young Researchers and Graduates Symposium: Advance in Structural Engineering*, Hangzhou, 10-18.

Chai, H.K., Momoki, S., Aggelis, D.G., Kobayashi, Y., & Shiotani, T. (2011). Tomographic reconstruction for concrete utilizing attenuation of ultrasound, *NDT&E International*, 44 (2), 206-215.

Chai, H.K., Yorikawa, M., Momoki, S., & Terazawa, M. (2012). Damage assessment of fiber-reinforced concrete beams by stress wave velocity distribution, *Proceedings of the 4th Asia-Pacific Young Researchers and Graduates Symposium*, Hong Kong, 60-5.

Chandrashekhar, B., Bhat, M.R., & Murthy, C.R.L. (2003). Acoustic emission characterization of failure modes in composites with ANN. *Composite Structures*, 61, 213–220.

Chang, P.C., & Liu, S.C. (2003). Recent research in nondestructive evaluation of civil infrastructures. *Journal of Materials in Civil Engineering*; 15, 298-304.

Cheah, C.B., & Ramli, M. (2012). Load capacity and crack development characteristics of HCWA–DSF high strength mortar ferrocement panels in flexure. *Construction and Building Material*, 36, 348-357.

Chen, B., & Liu, J. (2007). Investigation of effects of aggregate size on the fracture behavior of high performance concrete by acoustic emission. *Construction and Building Material*, 21, 1696-701.

Chen, B., & Liu, J. (2004). Experimental study on AE characteristics of three-point-bending concrete beams. *Cement and Concrete Research*, 34, 391–397.

Chen, B., & Liu, J. (2008). Damage in carbon fiber-reinforced concrete, monitored by both electrical resistance measurement and acoustic emission analysis. *Construction and Building Material*, 22(11), 2196-201.

Colombo, I.S., Main, I., & Forde M. (2003). Assessing damage of reinforced concrete beam using “bvalue” analysis of acoustic emission signals. *Journal of Materials in Civil Engineering*, 15, 280-286.

Colombo, S., Forde, M., Main, I., & Shigeishi, M. (2005). Predicting the ultimate bending capacity of concrete beams from the “relaxation ratio” analysis of AE signals. *Construction and Building Material*, 19, 746-754.

Dai, Q., Ng, K., Zhou, J., Kreiger, E.L., & Ahlborn, T.M. (2012). Damage investigation of single-edge notched beam tests with normal strength concrete and ultra-high performance concrete specimens using acoustic emission techniques. *Construction and Building Material*, 31, 231-242.

De Oliveira, R., & Marques, A. T. (2008). Health monitoring of FRP using acoustic emission and artificial neural networks. *Computer & Structures*, 86, 367–373.

Degala, S. (2008). *Acoustic emission monitoring of reinforced concrete systems retrofitted with CFRP* [master’s thesis]. University of Pittsburgh.

Degala, S., Rizzo, P., Ramanathan, K., & Harries, KA. (2009). Acoustic emission monitoring of CFRP reinforced concrete slabs. *Construction and Building Material*, 23, 2016-2026.

Drouillard, T. (1990). *Anecdotal history of acoustic emission from wood*. Colorado (USA), Rocky Flats Plant: EG and G Rocky Flats.

Duda, R.O., Hart, P.E., Stork, D.G. (2001). *Pattern Classification*, 2nd Ed., New York: Wiley.

ElBatanouny, M., Larosche, A., Mazzoleni, P., Ziehl, P., Matta, F., & Zappa, E. (2014). Identification of Cracking Mechanisms in Scaled FRP Reinforced Concrete Beams using Acoustic Emission. *Experimental Mechanics*, 54, 69-82.

Elfergani, H.A., Pullin, R., & Holford, KM. (2013). Damage assessment of corrosion in prestressed concrete by acoustic emission. *Construction and Building Material*, 40, 925-933.

Ester, M., Kriegel, H., Sander, J., & Xu, X., (1996) A density-based algorithm for discovering clusters in large spatial databases with noise. *Proceedings of 2nd International Conference on Knowledge Discovery and Data Mining (KDD-96)*, 226–231.

Fanning, P., & Carden, E.P. (2001). Auto-regression and statistical process control techniques applied to damage indication in telecommunication masts. *Key Engineering Material*, 204 (5), 251-260.

Farhidzadeh, A., Dehghan-Niri, E., Salamone, S., Luna, B., & Whittaker A. (2012). Monitoring Crack Propagation in Reinforced Concrete Shear Walls by Acoustic Emission. *Journal Structural Engineering*, 139 (12), 04013010.

Farhidzadeh, A., Salamone, S., & Singla, P. A. (2013a). Probabilistic Approach for Damage Identification and Crack Mode Classification in Reinforced Concrete Structures. *Journal of Intelligent Materials Systems and Structures*, 24 (14), 1722-1735.

Farhidzadeh, A., Salamone, S., Luna, B., & Whittaker, B. (2013b) Acoustic Emission Monitoring of a Reinforced Concrete Shear Wall by b- value based Outlier Analysis. *Structural Health Monitoring*, 12 (1), 3-13.

Fernando, P., Nilomar, Z., Tiago, L., Adriano, B. (2011). Concrete made with recycled tire rubber effect: Effect of alkaline activation and silica fume addition. *Journal of Cleaner Production*, 19, 757-763.

FIB, (2001). Externally Bonded FRP Reinforcement for RC Structures. *FIB Bulletin 14. FIB-International Federation for Structural Concrete*, Lausanne, 59-68.

Finck F. (2002). Acoustic emission analysis of SFRC beams under cyclic bending loads. *Otto Graf Journal*, 13, 83-92.

Finck, F., & Manthei, G. (2004). On near-field effects in signal based acoustic emission analysis. *Otto Graf Journal*, 15, 121-134.

Fowler, T.J, Blessing, J., & Conlisk, P. (1989). New directions in testing. *AECM-3: International Symposium on Acoustic Emission from Composite Materials*, 3rd Paris, France, 16-27.

Fowler, T.J. (1986). Experience with acoustic emission monitoring of chemical process industry vessels. In: *Progress in Acoustic Emission, III, Proceeding 8th International Acoustic Emission Symposium, Tokyo, Japan*, 150-62.

Fowler, T.J., & Blessing, J.A. (1992). Strauser FE. Intensity analysis. In: *Proceedings of fourth international symposium on acoustic emission from composite materials. Columbus (OH): American Society for Nondestructive Testing*, 16-27.

Fugate, M.L., Sohn, H., & Farrar, C.R. (2001). Vibration-based damage detection using statistical process control. *Mechanical Systems and Signal Processing*, 15 (4), 707-721.

Ganesan, N., Raj, B.J., & Shashikala, A.P. (2013). Flexural fatigue behavior of self-compacting rubberized concrete. *Construction and Building Material*, 44, 7-14.

Godin, N. (2004). Clustering of acoustic emission signals collected during tensile tests on unidirectional glass/polyester composite using supervised and unsupervised classifiers. *NDT & E International*, 37, 253-264.

Godin, N., Huguet, S., & Gaertner, R. (2005). Integration of the Kohonen's self-organising map and k-means algorithm for the segmentation of the AE data collected during tensile tests on cross-ply composites. *NDT & E International*, 38, 299-309.

Godin, N., Huguet, S., Gaertner, R., & Salmon, L. (2004). Clustering of acoustic emission signals collected during tensile tests on unidirectional glass/polyester composite using supervised and unsupervised classifiers. *NDT & E International*, 37, 253-64.

Golaski, L., Gebiski, P., & Ono, K. (2002). Diagnostic of reinforced concrete bridges by acoustic emission, *Journal of Acoustic Emission*, 20: 83-98.

Gostautas, R.S. Ramirez, g., Peterman, R.J., & Meggers.D. (2005). Acoustic emission monitoring and analysis of glass fiber-reinforced composites bridge decks. *ASCE Journal of Bridge Engineering*, 10(6), 713-721.

Grinys, A., Sivilevicius, H., & Dauksys, M. (2012). Tyre rubber additives effect on concrete mixture strength, *Journal of Civil Engineering and Management*, 18(3), 393-401.

Grosse, C., & Ohtsu, M. (2008). *Acoustic emission testing*. Berlin: Springer.

Grosse, C., Reinhardt, H., & Dahm, T. (1997). Localization and Classification of Fracture Types in Concrete with Quantitative Acoustic Emission Measurement Techniques, *NDT&E International*, 30 (4), 223-230.

Grosse, C.U., & Finck, F. (2006). Quantitative evaluation of fracture processes in concrete using signal-based acoustic emission techniques. *Cement Concrete Composite*, 28, 330-6.

Haneef, T., Kumari, K., Mukhopadhyay, C., Rao, B.P., & Jayakumar, T. (2013). Influence of fly ash and curing on cracking behavior of concrete by acoustic emission technique. *Construction and Building Material*, 44, 342-350.

Holford, K., Carter, D., Pullin, R., & Davies, A. (1999). Bridge Integrity Assessment by Acoustic Emission—Global Monitoring. *2 nd International Conference on Identification in Engineering Systems*, 392-400.

Huguet S, Godin N, Gaertner R, Salmon L, & Villard D. (2002). Use of acoustic emission to identify damage modes in glass fibre reinforced polyester. *Composites Science and Technology*, 62, 1433–1444.

Ibrahim, H.M. (2011). Experimental investigation of ultimate capacity of wired mesh-reinforced cementitious slabs. *Construction and Building Material*, 25, 251–259.

Issa Mohsen, A., Issa Mahmud, A., & Islam M.S. (2003). Chudnovsky A. Fractal dimension—a measure of fracture roughness and toughness of concrete. *Engineering Fracture Mechanics*, 70, 125–137.

Bezdek, J.C. (1981). *Pattern Recognition with Fuzzy Objective Function Algorithms*, Plenum, New York.

JCMS-IIIB5706.(2003). *Japan Construction Material Standards. Monitoring Method for Active Cracks in Concrete by Acoustic Emission*. Japan: The Federation of Construction Material Industries.

Johnson, M. (2002). Waveform based clustering and classification of AE transients in composite laminates using principal component analysis. *NDT&E International*, 35, 367–376.

Jolliffe, IT.(2002). *Principal component analysis*. Berlin: Springer.

Kahirdeh, A., & Khonsari, M.M. (2013). Criticality of degradation in composite materials subjected to cyclic loading. *Composite Part B*, 61, 375-382

Kaiser, J. (1953). Knowledge and research on noise measurements during the tensile stressing of metals.*ArCh Eisenhüttenwes*, 24, 43-44.

Kawasaki, Y., Wakuda, T., Kobarai, T., & Ohtsu, M. (2013).Corrosion mechanisms in reinforced concrete by acoustic emission. *Construction and Building Material*, 48, 1240–1247.

Kobayashi, Y., Shiotani, T., Aggelis, D.G., & Shiojiri, H. (2007). Three dimensional seismic tomography for existing concrete structures, *Proceedings of second international operational modal analysis conference*, Copenhagen, 2, 595-600.

Kohonen, T. (1990).The self-organizing map.*Proceeding IEEE*, 78, 1464-1480.

Köppel, S., & Grosse, C. (2000).Advanced acoustic emission techniques for failure analysis in concrete. *Proceeding of 15th World Conference on Nondestructive Testing Roma October*, Roma- Italy.

Kubaisy, A.M., & Jumaat, M.Z. (2005). Crack control of reinforced concrete members using ferrocement tension zone cover. *Journal of Ferrocement*, 35(1), 490–499.

Labuz, J. F., Chang, H.S, Dowding, C.H., & Shah, S.P. (1998).Parametric study of acoustic emission location using only four sensors. *Rock Mechanics and Rock Engineering*, 31(2), 139-148.

Labuz, J.F., Cattaneo, S., & Chen. L-H.(2001). Acoustic emission at failure in quasi-brittle materials.*Constrtion and Building Material*, 15, 225-233.

Likas, A., Vlassis, N. J., & Verbeek, J. (2003).The global k-means clustering algorithm. *Pattern Recognition*, 36, 451-461.

Liu, F., Chen, G., Li, L., & Guo, Y.(2012). Study impact performance of rubber reinforced concrete, *Construction and Building Material*, 36, 604-616.

Lovejoy, S.C. (2006). *Development of acoustic emission testing procedures applicable to convetionally reinforced concrete deck girder bridges subjected to diagonal tension cracking*. PhD Dissertation. Oregon State University.

Lovejoy, S.C. (2008). Acoustic emission testing of beams to simulate SHM of vintage reinforced concrete deck girder highway bridges. *Structural Health Monitoring*, 7(4), 329-346.

Lucas, J.M., & Saccucci, M.S. (1990). Exponentially weighted moving average control schemes: properties and enhancements, *Technometrics*, 32, 1-12.

Luo, X., Haya, H., Inaba, T., Shiotani, T., & Nakanishi, Y. (2002). Experimental study on evaluation of breakage in foundations using train-induced acoustic emission. *Proceeding Structural Engineering World Congress*, T9-1.

MacGregor, J.M., & Ghoneim, M.G. (1995). Design for Torsion. *Structural Journal American Concrete Institute*, 92(2), 211-218.

Mangual, J., ElBatanouny, M.K., Ziehl, P., & Matta, F. (2013). Acoustic-Emission-Based Characterization of Corrosion Damage in Cracked Concrete with Prestressing Strand. *ACI Material Journal*, 110, 89-98.

Manson, G., Worden, K., Holford, K., & Pullin, R. (2001). Visualisation and dimension reduction of acoustic emission data for damage detection. *Journal of Intelligent Material Systems and Structures*, 12, 529-536.

McDad, P., Medlock, R., Fowler, T., & Ziehl, P. (2004). Structural health monitoring of an efficient hybrid FRP/reinforced concrete bridge system. *Proceeding 2nd International Workshop on Structural Health Monitoring of Innovative Civil Engineering Structures*.

Miller, R., & McIntire, P. (1987). *Nondestructive Testing Handbook* (Vol.5). Acoustic Emission Testing 2nd American Society for Nondestructive Testing.

Minemura, O., Sakata, N., Yuyama, S., Okamoto, T., & Maruyama K. (1998). Acoustic emission evaluation of an arch dam during construction cooling and grouting. *Construction and Building Material*, 12, 385-392.

Moevus, M., Godin, N., R'Mili, M., Rouby, D., Reynaud, P., & Fantozzi, G. (2008). Analysis of damage mechanisms and associated acoustic emission in two SiCf/[Si-B-C] composites exhibiting different tensile behaviours. Part II: Unsupervised acoustic emission data clustering. *Composites Science and Technology*, 68, 1258-1265.

Mogi, K. (1963). Magnitude-frequency relation for elastic shocks accompanying fractures of various materials and some related problems in earthquakes (2nd paper). *Earthquake Research Institut*, 40, 831-854.

Momoki, S., Chai, H., Aggelis, D.G., Hiram, A., & Shiotani, T. (2009). Acoustic emission for characterizing behavior of composite concrete elements under flexure. *Journal of Acoustic Emission*, 27, 186-193.

Momoki, S., Shiotani, T., Chai, H. K., Aggelis, D. G. & Kobayashi, Y. (2013). Large-scale evaluation of concrete repair by three-dimensional elastic-wave based visualization technique, *Structural Health and Monitoring*, 12(3), 241-252.

Mustapha, F., Manson, G., Pierce, S., & Worden, K. (2005). Structural health monitoring of an annular component using a statistical approach. *Strain*, 41, 117-27.

Naaman, A.E. (2000). *Ferrocement and laminated cementitious composites*. Ann Arbor, Michigan: Techno press 3000.

Nair, A., & Cai, C. (2010). Acoustic emission monitoring of bridges: Review and case studies. *Engineering Structures*, 32, 1704-1714.

Obert, L. (1977). The microseismic method: discovery and early history. *First conference on acoustic emission/microseismic activity in geologic structures and materials*, 11-12.

Obert, L., & Duvall, W. (1945). *Microseismic method of predicting rock failure in underground mining. Part II. Laboratory experiments*. Bureau of Mines, Washington, DC (USA).

Ohno, K., & Ohtsu, M. (2010). Crack classification in concrete based on acoustic emission. *Construction and Building Material*, 24, 2339-2346.

Ohtsu, M. (1989). A review of acoustic emission in civil engineering with emphasis on concrete. *Journal of Acoustic Emission*, 8, 93-8.

Ohtsu, M. (1991). Simplified moment tensor analysis and unified decomposition of acoustic emission source: Application to in situ hydro fracturing test. *Journal of Geophysical Research: Solid Earth*, 96, 6211-6221.

Ohtsu, M. (1996). The history and development of acoustic. *Magazine of Concrete Research*, 48, 321-330.

Ohtsu, M. (2010). Recommendations of RILEM Technical Committee 212-ACD: acoustic emission and related NDE techniques for crack detection and damage evaluation in concrete: Test method for classification of active cracks in concrete structures by acoustic emission. *Materials and Structures*, 43(9), 1187-1189.

Ohtsu, M., & Watanabe, H. (2001). Quantitative damage estimation of concrete by acoustic emission. *Construction and Building Material*, 15, 217-224.

Ohtsu, M., & Yuyama, S. (2000). Recommended practice for in situ monitoring of concrete structures by acoustic emission. *15th International Acoustic Emission Symposium*, 63-68.

Ohtsu, M., Kaminaga, Y., & Munwam, M.C. (1999). Experimental and numerical crack analysis of mixed-mode failure in concrete by acoustic emission and boundary element method. *Construction and Building Material*, 13, 57-64.

Ohtsu, M., Mori, K., & Kawasaki, Y. (2010). Corrosion Process and Mechanisms of Corrosion-Induced Cracks in Reinforced Concrete identified by AE Analysis. *Strain*, 47(2), 179-186.

Ohtsu, M., Okamoto, T., & Yuyama, S. (1998). Moment tensor analysis of acoustic emission for cracking mechanisms in concrete. *ACI Structural Journal*, 95(2), 87-95.

Ohtsu, M., Uchida, M., Okamoto, T., & Yuyama, S. (2002). Damage assessment of reinforced concrete beams qualified by acoustic emission. *ACI Structural Journal*, 99, 411-417.

Oikonomou, N., & Mavridou, S. (2009). Improvement of chloride ion penetration resistance in cement mortars modified with rubber from worn automobile tires. *Cement and Concrete Composite*, 31(6), 403-407.

Omkar, S.N., & Karanth, R. (2008). Rule extraction for classification of acoustic emission signals using ant colony optimisation. *Engineering Applications of Artificial Intelligence*, 21, 1381-1388.

Omkar, S.N., Suresh, S., Raghavendra, & T.R., Mani, V. (2002). Acoustic emission signal classification using fuzzy C-means clustering. In: *Proceedings of the 9th international conference on neural information processing (ICONIP02)*, (vol. 4). Singapore; IEEE, 1827-1831.

Ossola, G., & Wojcik, A. (2014). UV modification of tire rubber for use in cementitious composites. *Cement and Concrete Composite*, 52, 34-41.

Ozawa, M., Uchida, S., Kamada, T., & Morimoto, H. (2012). Study of mechanisms of explosive spalling in high-strength concrete at high temperatures using acoustic emission. *Construction and Building Material*, 37, 621-628.

Pappas, Y.Z., Markopoulos, Y.P., & Kostopoulos, V. (1998). Failure mechanisms analysis of 2D carbon/carbon using acoustic emission monitoring. *NDT&E International*, 31, 157-63.

Paul, B.K., & Rama, R.P. (1978). Ferrocement. Bangkok: *International Ferrocement Information Center*.

Philippidis, T.P., Nikolaidis, V.N., & Anastassopoulos, A.A. (1998). Damage characterization of carbon/ carbon laminates using neural network techniques on AE signals. *NDT&E International*, 31(5), 329-340.

Pollock, A. (1981). Acoustic emission amplitude distributions. *International Advances in Nondestructive Testing*, 7, 215-239.

Pullin, R., Carter, D., Holford, K., & Davies, A. (1999). Bridge Integrity Assessment by Acoustic Emission-Local Monitoring. *Proceeding 2nd International Conference on Identification on Engineering Systems*, Swansea, 401-409.

Pullin, R., Holford, K.M., Lark, R.J., & Eaton, M.J. (2008). Acoustic emission monitoring of bridge structures in the field and laboratory. *Journal of Acoustic Emission*, 26, 172-181.

Rao, M., & Lakshmi, K.P. (2005). Analysis of b-value and improved b-value of acoustic emissions accompanying rock fracture. *Current Science*, 89(9), 1577-1582.

Rao, M., Prasanna, L. K., Nagaraja, R. G., Vijaya, K. K., & Udaykumar, S. (2009). Pre-failure damage caused by micro cracks in rock: A laboratory study using acoustic emission. *Proceedings of the National Seminar and Exhibition on Non-Destructive Evaluation, NDE*, 323-327.

Reinhardt, H., Grosse, C., & Weiler, B. (2001, May). Material characterization of steel fibre reinforced concrete using neutron CT, ultrasound and quantitative acoustic emission techniques. From <http://www.ndt.net/article/v06n05/grosse/grosse.htm>.

Ridge, A.R., & Ziehl, P.H. (2006). Evaluation of strengthened reinforced concrete beams: cyclic load test and acoustic emission methods. *ACI Structural Journal*, 103, 832-841.

Rippengill, S., Worden, K., Holford, K.M., & Pullin, R. (2003). Automatic classification of AE patterns. *Strain*, 39, 31-41.

Rossi, P., Robert, J., Gervais, J., & Bruhat, D. (1990). The use of acoustic emission in fracture mechanics applied to concrete. *Engineering Fracture Mechanics*, 35, 751-763.

Rossi, P., Tailhan, J.L., Le Maou, F., Gaillet, L., & Martin, E. (2012). Basic creep behavior of concretes investigation of the physical mechanisms by using acoustic emission. *Cement Concrete Research*, 42, 61-73.

Saeedifar, M., Fotouhi, M., Najafabadi, M.A., Toudeshky, H.H., (2015). Prediction of delamination growth in laminated composites using acoustic emission and cohesive zone modelling techniques. *Composite Structures*, 124, 120-127.

Sagar, R.V. (2011). Damage assessment reinforced concrete beams using acoustic emission technique. *Proceedings of the National Seminar & Exhibition on Non-Destructive Evaluation NDE*, 128-132.

Salehian, H., & Baros, J.A. (2015). Assessment of the performance of steel fibre reinforced self-compacting concrete in elevated slabs. *Cement and Concrete Composite*, 55: 268-280.

Salinas, V., Vargas, Y., Ruzzante, J., & Gaete, L. (2010). Localization algorithm for acoustic emission. *Physic Procedia*, 3, 863-871.

Sause, M.G.R., & Horn, S. (2013). Quantification of the Uncertainty of Pattern Recognition Approaches Applied to Acoustic Emission Signals. *Journal of Nondestructive Evaluation*, 32(3), 242-255.

Sause, M.G.R., Gribov, a., Unwin, A. R, & Horn S. (2012). Pattern recognition approach to identify natural clusters of acoustic emission signals. *Pattern Recognition Letters*, 33, 17–23.

Schofield, B. (1963). *Acoustic emission under applied stress*. Defence Technical Information Center Document.

Scholz, C. (1968). The frequency-magnitude relation of microfracturing in rock and its relation to earthquakes. *Bulletin of the Seismological Society of America*, 58, 399-415.

Schumacher, T., Higgins, C.C., & Lovejoy, S.C. (2011). Estimating operating load conditions on reinforced concrete highway bridges with b-value analysis from acoustic emission monitoring. *Structural Health Monitoring*, 10, 17-32.

Schweitzer, J., Fyen, J., Mykkeltveit, S., & Kværna, T. (2002). Seismic Arrays. In *New Manual of Seismological Observatory Practice* (Vol. 5, pp. 368-412). Beijing: State Seismological Bureau, Seismological Press.

Shah SG, & Chandra Kishen J. (2012). Use of acoustic emissions in flexural fatigue crack growth studies on concrete. *Engineering Fracture Mechanics*; 87:36-47.

Shah, S.G., & Chandra, K.J. (2010). Fracture behavior of concrete–concrete interface using acoustic emission technique. *Engineering Fracture Mechanics*, 77, 908-924.

Shah, S.P., & Li, Z. (1994). Localization of micro cracking in concrete under uniaxial tension. *ACI Material Journal*, 91(4), 372–81.

Shahidan, S., Pulin, R., Bunnori, N.M., & Holford, K.M. (2013). Damage classification in reinforced concrete beam by acoustic emission signal analysis. *Construction and Building Material*, 45, 78-86.

Sharma, S. (1995). *Applied multivariate techniques*: John Wiley & Sons, Inc.

Shearer, P.M. (1999). *Introduction to seismology*. Cambridge University Press.

Shigeishi, M., & Ohtsu, M. (2001). Acoustic emission moment tensor analysis: development for crack identification in concrete materials. *Construction and Building Material*, 15, 311-319.

Shiotani T, Ohtsu M, & Ikeda K. (2001). Detection and evaluation of AE waves due to rock deformation. *Construction and Building Material*, 15, 235-246.

Shiotani, T, Bisschop, J., & Van Mier, J. (2003). Temporal and spatial development of drying shrinkage cracking in cement-based materials. *Engineering Fracture Mechanics*, 70, 1509-1525.

Shiotani, T. (2006a). Evaluation of long-term stability for rock slope by means of acoustic emission technique. *NDT & E International*, 39, 217-228.

Shiotani, T. (2006b). Evaluation of repair effect for deteriorated concrete piers of intake dam using AE activity. *Advanced Materials Research*, 13, 175-180.

Shiotani, T. (2012). Recent Advances of AE technology for Damage Assessment of Infrastructures. *30th European Conference on Acoustic Emission Testing & 7th International Conference on Acoustic Emission*, University of Granada, 12-15 September.

Shiotani, T., & Aggelis, D.G. (2009). Wave propagation in cementitious material containing artificial distributed damage. *Materials and Structures*, 42, 377-384.

Shiotani, T., & Ohtsu, M. (1999). Prediction of slope failure based on AE activity. *ASTM Special Technical Publication*, 1353, 156-174.

Shiotani, T., Aggelis, D.G, & Makishima, O. (2009). Global monitoring of large concrete structures using acoustic emission and ultrasonic techniques: Case study. *Journal Bridge Engineering.-ASCE*, 14(3), 188-192.

Shiotani, T., Bisschop, J., & Van Mier, J. (2003). Temporal and spatial development of drying shrinkage cracking in cement-based materials. *Engineering Fracture Mechanics*, 70, 1509-1525.

Shiotani, T., Fujii, K., Aoki, T., Amou, K.(1994). Evaluation of progressive failure using AE sources and improved B-value on slope model tests. *Progress in Acoustic Emission*, 7, 529-34.

Shiotani, T., Ohtsu, H., Momoki, S., Chai, H.K., Onishi, H., & Kamada, T. (2012). Damage Evaluation for Concrete Bridge Deck by Means of Stress Wave Techniques, *Journal of Bridge Engineering*, 17 (6), 847-856.

Shiotani, T., Shigeishi, M., & Ohtsu, M. (1999). Acoustic emission characteristics of concrete-piles. *Construction and Building Material*, 13, 73-85.

Shiotani, T., Yuyama, S., Li, Z., & Ohtsu, M. (2001). Application of AE improved b-value to quantitative evaluation of fracture process in concrete materials. *Journal of Acoustic Emission*, 19, 118-133.

Shiotani, T., Yuyama, S., Li, Z., & Ohtsu, M. (2000). Quantitative evaluation of fracture process in concrete by the use of improved b-value. *5th Int Symposium Non-Destructive Testing in Civil Engineering: ELSEVIER SCIENCE, Amsterdam*, 293-302.

Sohn, B.H, Czarnecki, J.A., & Farrar CR. (2000). Structural health monitoring using statistical process control. *Journal of Structural Engineering*, 126, 1356-1363.

Soulioti, D., Barkoula, N. M., Paipetis, A., Matikas, T., Shiotani, T. & Aggelis D.G. (2009). Acoustic emission behavior of steel fiber reinforced concrete under bending. *Construction and Building Materials*, 23(12), 3532-3536.

Soulioti, D., Barkouta, N.M., Paipetis, A., Matikas, T.E., Shiotani, T., & Aggelis, D.G. (2009). Acoustic emission behavior of steel fiber reinforced concrete under bending. *Construction and Building Material*, 23, 3532-3536.

Svec, O., Ziregulis, G., Bolander, J.E., & Stang, H. (2014). Influence of formwork surface on the orientation of steel fibres within self-compacting concrete and on the mechanical properties of cast structural elements. *Cement and Concrete Composite*, 50, 60-72.

Topçu, I., & Bilir, T. (2009). Experimental investigation of some fresh and hardened properties of rubberized self-compacting concrete. *Materials and Design*, 30, 3056-3065.

Uppal, A., Yoshino, D., & Dunegan, H.L. (2002). *Using acoustic emission to monitor fatigue cracks on the bridge at FAST*. Technology Digest, Transportation Technology Center, Inc, Association of American Railroads.

Wang, C., Zhang, Y., & Ma, A. (2010). Investigation into the Fatigue Damage Process of Rubberized Concrete and Plain Concrete by AE Analysis. *Journal of Materials in Civil Engineering*, 23, 953-960.

Weibull WA. (1951). A statistical distribution function of wide applicability. *Journal of Applied Mechanics*. 18, 292-297.

Wu, Z., Xie, W., Yu, J. (2003). Fuzzy c-means clustering algorithm based on kernel method. In: *Proc. Int. Conf. Computational Intelligence and Multimedia Applications*, 49-54.

Yerramala, A., Ramachandurdu, C., & Desai, B. (2013). Flexural strength of metakaolin ferrocement. *Composites: Part B*, 55, 176-183.

Yoon, D.J., Weiss, W.J., & Shah, SP. (2000). Assessing damage in corroded reinforced concrete using acoustic emission. *Journal Engineering Mechanics*, 126, 273-83.

Yuyama, S., Li, Z.W., Yoshizawa, M., Tomokiyo, T., & Uomoto, T. (2002). Evaluation of fatigue damage in reinforced concrete slab by acoustic emission. *NDT & E International*, 34, 381-7.

Yuyama, S., Li, Z.w., Ito, Y., & Arazoe, M. (1999). Quantitative analysis of fracture process in RC column foundation by moment tensor analysis of acoustic emission. *Construction and Building Material*, 13, 87-97.

Yuyama, S., Okamoto, T., Shigeishi, M., & Ohtsu, M. (1995). Acoustic emission generated in corners of reinforced concrete rigid frame under cyclic loading. *Materials Evaluation*, 53, 409-412.

Yuyama, S., Yokoyama, K., Niitani, K., Ohtsu, M., & Uomoto, T. (2007). Detection and evaluation of failures in high-strength tendon of prestressed concrete bridges by acoustic emission. *Construction and Building Material*, 21, 491-500.

Ziehl, P., & Ridge, A. (2006). Evaluation of Strengthened RC Beams: Cyclic Load Test and Acoustic Emission Methods. *ACI Structural Journal*, 103 (6), 832-841.